UNIVERSITY OF SOUTHAMPTON

FACULTY OF ENGINEERING AND THE ENVIRONMENT

Institute of Sound and Vibration Research

Mid-frequency Local Active Control of Road Noise

by

Woomin Jung

Thesis for the degree of Doctor of Philosophy

June 2018

UNIVERSITY OF SOUTHAMPTON

ABSTRACT

FACULTY OF ENGINEERING AND THE ENVIRONMENT
Institute of Sound and Vibration Research

Doctor of Philosophy

MID-FREQUENCY LOCAL ACTIVE CONTROL OF ROAD NOISE

by Woomin Jung

Interior road noise in vehicle cabins is mainly random and broadband, and can potentially be controlled using either passive or active methods. Previous active noise control systems have typically used secondary loudspeakers that are remote from a listener's ears, however, and this has limited their useful frequency range to below about 300 Hz. An active headrest system, with closely-spaced secondary loudspeakers and error sensors, may be a practical method of increasing this frequency range, using local active sound control. This thesis presents developments of the local active control strategy, with the aim of improving the attenuation performance and the convergence stability of active headrest systems in vehicles.

An active headrest system is first investigated via simulation, to understand the fundamental characteristics of local active control in enclosures. The application of a head-tracking device to the active headrest system is then investigated initially to allow the active headrest system to use an appropriate plant response in order to maintain stability. The remote microphone technique is then investigated, which uses the output from fixed monitoring microphones to estimate the signals at virtual error microphones at the listener's ears, via an observation filter. It is shown that the geometry of the monitoring microphone array should be chosen considering both the spatial correlation of the primary field and the condition number of the inversion associated with the design of the observation filter.

The head-tracking device and the remote microphone technique have been integrated in an active headrest system. A real-time implementation is presented of the nearfield estimation and integrated active headrest system for controlling either tonal or broadband sounds. In particular, the effects of using the head-tracking device during the control have been investigated with a human listener. Measurements of the road noise and acoustic response in a large SUV have also been conducted, and these are used to predict the performance of an active headrest system under various practical conditions, with promising results.

Contents

List of Figures

List of Tables

Declaration of Authorship

I, Woomin Jung , declare that the thesis entitled *Mid-frequency Local Active Control of Road Noise* and the work presented in the thesis are both my own, and have been generated by me as the result of my own original research. I confirm that:

- this work was done wholly or mainly while in candidature for a research degree at this University;
- where any part of this thesis has previously been submitted for a degree or any other qualification at this University or any other institution, this has been clearly stated;
- where I have consulted the published work of others, this is always clearly attributed;
- where I have quoted from the work of others, the source is always given. With the exception of such quotations, this thesis is entirely my own work;
- I have acknowledged all main sources of help;
- where the thesis is based on work done by myself jointly with others, I have made clear exactly what was done by others and what I have contributed myself;
- parts of this work have been published as:
  - Elliott, S. J., Jung, W., & Cheer, J. (2015). The spatial properties and local active control of road noise. Paper presented at *EuroNoise*, Netherlands.
  - Cheer, J., Elliott, S., & Jung, W. (2015). Sound field control in the automotive environment. Paper presented at *3rd International ATZ Automotive Acoustics Conference*, Switzerland.
  - Elliott, S., Simon, M., Cheer, J., & Jung, W. (2015). Head tracking for local active noise control. Paper presented at *12th Western Pacific Acoustics Conference*, Singapore.
  - Jung, W., Elliott, S., & Cheer, J. (2016). The effect of remote microphone technique and head-tracking on local active sound control. Paper presented at *ICSV23: 23rd International Congress on Sound and Vibration*, Athens.
  - Jung, W., Elliott, S., & Cheer, J. (2016). Identifying of interior noise sources

in a vehicle cabin using the inverse method. Paper presented at *ICSV23: 23rd International Congress on Sound and Vibration*, Athens.

- Jung, W., Elliott, S., & Cheer, J. (2017). Local active sound control using the remote microphone technique and head-tracking for tonal and broadband noise sources. Paper presented at *ICSV24: 24th International Congress on Sound and Vibration*, London.

- Jung, W., Elliott, S. J. & Cheer, J. (2017). Combining the remote microphone technique with head-tracking for local active sound control. *Journal of the Acoustical Society of America*, 142(1), 298-307.

- Elliott, S. J., Jung, W. & Cheer, J. (2018). Head tracking extends local active control of broadband sound to higher frequencies. *Scientific Reports*, 8(1), 5403.

- Jung, W., Elliott, S. J. & Cheer, J. (2018). Estimation of the pressure at a listener's ears in an active headrest system using the remote microphone technique. *Journal of the Acoustical Society of America*, 143(5), 2858-2869.

- Jung, W., Elliott, S. J. & Cheer, J. (2018). Local active control of road noise inside a vehicle. *Mechanical Systems and Signal Processing*, In review.

Signed:.....

Date:.....

Acknowledgements

This PhD research is jointly funded by an Engineering and Physical Sciences Research Council (EPSRC) industrial CASE studentship (Award no. 14220108) with Jaguar Land Rover (JLR). Permission to reproduce Fig. 5.1 has been granted by Dr Danielle Joy Moreau.

First and foremost, I am deeply grateful to my academic supervisor, Stephen J. Elliott, who has given me the opportunity to be involved in last MSc project and this PhD project. He has always offered me valuable guidance and support with great knowledge and insight. All the interesting discussions with him have inspired me to enjoy my PhD work. A most sincere thank you.

I also offer my heartfelt thanks to my academic supervisor, Jordan Cheer, for always giving me beneficial ideas and suggestions. He has greatly helped me in conducting various acoustic measurements by offering his valuable time and efforts.

Marcos Felipe Simon Galvez. Thank you for his initial help in developing the active control system with head-tracking.

I would like to thank all people in the University of Southampton and ISVR for their support, particularly those that helped me in taking measurements; especially Hogun Kim, Hongseok Jeong and Dahyun Yoon.

I feel thankful to Dr Delphine Nourzad and Mr Xavier Vinamata of JLR for their support as industrial supervisors and Mr You Hooi Tan for supporting the in-vehicle measurements.

Many thanks to everyone that I have met and experienced during my wonderful UK life.

Finally, my deepest gratitude goes to my wife (Sanga), two sons (Seunghoon and Yonghoon), parents (Yunkoo and Insuk) and rest of the family. They have always supported and prayed for me with their infinite love and patience to complete this PhD work.

List of Symbols

$A_{lmn}(\omega)$	Complex resonance term
a_{lmn}	Complex amplitude of lmnth mode
B	Bore of a engine cylinder in mm
c_0	Speed of sound in the medium
$\mathbf{d}$	Vector of complex disturbance signals at error sensors
$\boldsymbol{d}(n)$	Vector of disturbance signals in the time domain
$\mathbf{d}_e$	Vector of complex disturbance signals at virtual error sensors
$\hat{\mathbf{d}}_e$	Vector of estimated complex disturbance signals at virtual error sensors
$\boldsymbol{d}_e(n)$	Vector of disturbance signals at virtual error sensors in the time domain
$\mathbf{d}_m$	Vector of complex disturbance signals at monitoring sensors
$\hat{\boldsymbol{d}}'_m(n)$	$JN_m \times 1$ vector of estimated current and past disturbances at the monitoring sensors
d	Complex disturbance signal in the frequency domain
$d(n)$	Disturbance signal in the time domain
E	Expectation operator
E_p	Acoustic potential energy after control
E_{p_0}	Acoustic potential energy before control
$\mathbf{e}$	Vector of complex error signals
$\hat{\mathbf{e}}$	Vector of estimated complex error signals
$\boldsymbol{e}(n)$	Vector of error signals in the time domain
e	Complex error signal in the frequency domain
$e(n)$	Error signal in the time domain
$\mathbf{F}$	Matrix of transfer responses between primary sources and reference sensors
f	Frequency
f_0	Fundamental frequency
$\mathbf{G}$	Matrix of plant responses
$\mathbf{G}$	Matrix of effective plant responses (Chapter 6)
$\hat{\mathbf{G}}$	Matrix of estimated plant responses
$\mathbf{G}_e$	Matrix of plant responses between the secondary sources and virtual error sensors
$\mathbf{G}_m$	Matrix of plant responses between the secondary sources and monitoring sensors

G	Plant response
$\hat{G}$	Estimated plant response
$g_{n_e n_u k}$	kth coefficient of FIR plant response between n_uth secondary source and n_eth error sensor
$^{\mathrm{H}}$	Hermitian, complex conjugate transpose of a vector or matrix
$H(\omega)$	Hilbert transform filter
$\mathbf{I}$	Identity matrix
I	Number of FIR filter coefficients for controller
J	Number of FIR filter coefficients for observation filter
j	$\sqrt{-1}$
K	Number of FIR filter coefficients for plant response
k	Wavenumber
L	Separation between monitoring microphones
L_ϵ	Normalised mean squared estimation error level at the virtual microphone
lmn	Acoustic modal integers in the three coordinate directions
$\mathbf{m}$	Vector of complex controlled signals at monitoring sensors
$\boldsymbol{m}(n)$	Vector of controlled signals at monitoring sensors in the time domain
N	Engine rotational speed in rev/min
N_e	Number of error sensors
N_m	Number of monitoring sensors
N_u	Number of secondary sources
N_v	Number of primary sources
N_x	Number of reference sensors
n	sample time
$\mathbf{O}$	Matrix of complex observation filters in the frequency domain
$\hat{\mathbf{O}}$	Matrix of complex estimated observation filters in the frequency domain
$\boldsymbol{O}$	Matrix of observation filter coefficients in the time domain
$\hat{\boldsymbol{O}}$	Matrix of estimated observation filter coefficients in the time domain
$\mathbf{O}_{n_e n_m}$	Element of matrix of complex observation filters between the n_mth monitoring microphone and the n_eth error microphone
$\boldsymbol{O}_{\mathrm{D}}$	Matrix of delayed observation filter coefficients in the time domain
$\boldsymbol{O}_{n_e n_m}$	Vector of FIR filter coefficients of the observation filter between the n_mth monitoring microphone and the n_eth error microphone
O	Observation filter in the frequency domain
$\mathbf{P}$	Matrix of transfer responses between primary sources and error sensors
$\mathbf{P}_e$	Matrix of transfer responses between primary sources and virtual error sensors
$\mathbf{P}_m$	Matrix of transfer responses between primary sources and monitoring sensors
p	Acoustic pressure
$\boldsymbol{Q}$	Unitary matrix which is a set of orthonormal eigenvectors of the matrix $E[\hat{\boldsymbol{R}}^{\mathrm{T}}(n)\boldsymbol{R}(n)]$
q_i	Source strength

$\boldsymbol{R}(n)$	Matrix of filtered reference signals
$\hat{\boldsymbol{R}}(n)$	Matrix of estimated filtered reference signals
$\boldsymbol{R}_e(n)$	Matrix of filtered reference signals for virtual error sensors
$\hat{\boldsymbol{R}}_e(n)$	Matrix of estimated filtered reference signals for virtual error sensors
$\boldsymbol{R}_m(n)$	Matrix of filtered reference signals for monitoring sensors
$R(\Delta x)$	Spatial correlation
r	Euclidean distance
$r_{n_e n_u n_x}(n)$	$n_e n_u n_x$ filtered-reference signals
$\mathbf{S}_{dd}$	Power spectral density matrix for $\mathbf{d}$
$\mathbf{S}_{ee}$	Power spectral density matrix for $\mathbf{e}$
$\mathbf{S}_{vv}$	Power spectral density matrix for $\mathbf{v}$
$\mathbf{S}_{xd}$	Cross spectral density matrix between $\mathbf{x}$ and $\mathbf{d}$
$\mathbf{S}_{xx}$	Power spectral density matrix for $\mathbf{x}$
S	Stroke of a engine cylinder in mm
$^{\mathrm{T}}$	Transpose of a vector or matrix
$\mathbf{u}$	Vector of complex source strengths of secondary sources
$\mathbf{u}_\infty$	Steady state vector of control signals after the convergence
$\boldsymbol{u}(n)$	Vector of control signals in the time domain
V	Vehicle speed
$\mathbf{v}$	Vector of complex source strengths of primary sources
$\boldsymbol{v}(n)$	Vector of source signals in the time domain
$\mathbf{W}$	Matrix of complex control filters
$\boldsymbol{w}(n)$	Vector of control filter coefficients
$\boldsymbol{w}_\infty$	Steady state vector of control filter coefficients after the convergence
$w_{n_u n_x i}$	ith coefficient of FIR controller between n_xth reference sensor and n_uth actuator
$\boldsymbol{X}_v(n)$	moving virtual locations
$\mathbf{x}$	Vector of complex reference signals
$\boldsymbol{x}(n)$	Vector of reference sensor signals in the time domain
x	Complex reference signal in the frequency domain
$x(n)$	Reference signal in the time domain
x_0, y_0, z_0	Dimensions of the rectangular enclosure
$Z(r)$	Acoustic transfer response in the free field
α	Convergence coefficient
β	Positive real regularising parameter for the observation filter
γ^2	Multiple coherence function
Δ	Number of sample delays
Δ_{d_m}	Acoustical uncertainty
Δr_ϵ	Diameter of a sphere of the zone of quiet
Δx	Euclidean distance between $\mathbf{x}_1$ and $\mathbf{x}_2$
ϵ	Reduction factor (Chapter 2)

ϵ	$d_e - \hat{d}_e$ at a single virtual microphone (Chapter 5)
$\epsilon_l, \epsilon_m, \epsilon_n$	Normalisation factors
ζ_{lmn}	Damping ratio
$\mathbf{\Lambda}$	Matrix that has eigenvalues of the matrix $E[\hat{\boldsymbol{R}}^{\mathrm{T}}(n)\boldsymbol{R}(n)]$
λ	Wavelength
λ_{Nu}	Eigenvalues of $\hat{\mathbf{G}}_e^{\mathrm{H}}\mathbf{G}$
$\lambda_{n_u n_x i}$	$n_u n_x i$-th complex eigenvalue of the matrix $E[\hat{\boldsymbol{R}}^{\mathrm{T}}(n)\boldsymbol{R}(n)]$
μ	Positive filter coefficient-weighting parameter
ω	Angular frequency
ω_{lmn}	Natural frequency of the lmnth mode in a rectangular enclosure
ρ	Positive real regularising parameter for the controller
ρ_0	Density in the medium
$\rho(\Delta x)$	Normalized spatial correlation
σ	Normalised rms random variation
ψ_{lmn}	Mode shape
$<\ >$	Operation of spatial averaging
$\langle \lvert p(x) \rvert^2 \rangle$	Local space-averaged modulus squared pressure
$\| \ \|_F$	Frobenius matrix norm
$\{\ \}'$	$JN_m \times 1$ vector from the J current and past samples corresponding to the the signals in the braces
FIR	Finite Impulse Response
LMS	Least Mean Square
ISVR	Institute of Sound and Vibration Research
MIMO	Multi-Input Multi-Output
PSD	Power Spectral Density
SISO	Single-Input Single-Output
rms	Root mean square
rpm	Revolution per minute
SUV	Sport Utility Vehicle

Chapter 1

Introduction

1.1 Motivation

Although many passive methods have been utilised to control NVH (Noise, Vibration and Harshness) in vehicle cabins, research and development of electronic devices such as DSP (Digital Signal Processor), sensors and actuators may allow cost-effective and practical implementations of active sound control [1–8]. Active sound control in vehicles has been widely studied [9–12]. Research into the active control of sound for vehicle interior noise is mainly concerned with two areas: powertrain noise control and road-tyre induced noise control.

Powertrain noise is mainly tonal and recently several systems for the active control of the low frequency components of this noise have been implemented by manufacturers [2, 5, 7, 13]. The active control of the random road noise in vehicles has also been investigated [1, 4, 14, 15], but the performance is limited to low frequencies, typically below 300 Hz if the loudspeakers and microphones used for control are remote from the listener's head. Control of higher-frequency road noise may be possible with local control systems, such as those using loudspeakers and microphones in the headrests, which are often referred to as active headrest systems [16–19]. The close proximity between the secondary loudspeakers and the error sensors in the local active headrest system can provide several advantages over an active control system with remote loudspeakers and microphones, including low noise enhancement at other positions, short acoustic propagation delays in the control path and simpler plant responses between the secondary loudspeakers and the error sensors.

The practical application of advanced local active noise control is the motivation for this thesis, with the aim of increasing the controllable frequency range and the attenuation performance of the active headrest system in the automotive road noise control problem

1.2 Research objectives

The primary aim of this thesis is to present a study of the performance of a feedforward active headrest system for locally controlling road-induced noise in the car cabin, with the objective of increasing the controllable frequency range and the attenuation performance. The project aims to improve the fundamental understanding of how the characteristics of the sound field affect the control limitations, and also to facilitate the development of novel control strategies and geometries.

In particular, since head movements of an occupant can reduce the performance or cause instability in local active control systems, a new technique is investigated to improve the accuracy of the estimation of the signals at the control-targeted region. In addition, since the error signals cannot be directly measured at the ear positions for practical reasons, improved, virtual, sensing methods are necessary to estimate the error signals with accuracy. Finally the performance of the optimized active headrest system will be evaluated in a car, to determine how effectively this system might control the road noise. The ability to actively control noise to higher frequencies would have a significant impact on the NVH development of vehicles, and may allow lighter passive methods to be used, with the potential for more fuel efficient vehicles.

1.3 Project outline

This project is mainly divided into three stages as shown in Fig. 1.1.

In the initial stage, simulations focusing on the spatial properties of primary noise sources, secondary sources and error sensors have been conducted, in order to investigate the limitations on the conventional active headrest system in the automotive environment, and introduce the systematically limiting physical factors. Novel strategies for the improved active headrest system have then been studied. First of all, the use of head-tracking has been investigated when the position of the physical error microphones is changed along with the head movements of a listener. In addition, the availability of the remote microphone technique for virtually sensing error signals at the human ears has been investigated through a number of numerical simulations.

The second stage has focused on a laboratory based study of the remote microphone technique. The observation filters, necessary to estimate the virtual error signals from those at the fixed monitoring microphones, are calculated from measured acoustic transfer responses, and the accuracy of the nearfield estimation is considered in both an anechoic chamber and a more reverberant room. The tonal disturbance signals at the ears of a dummy head have also been estimated in real-time. In addition, the use of a head-tracking device has been considered together with the nearfield estimation using the

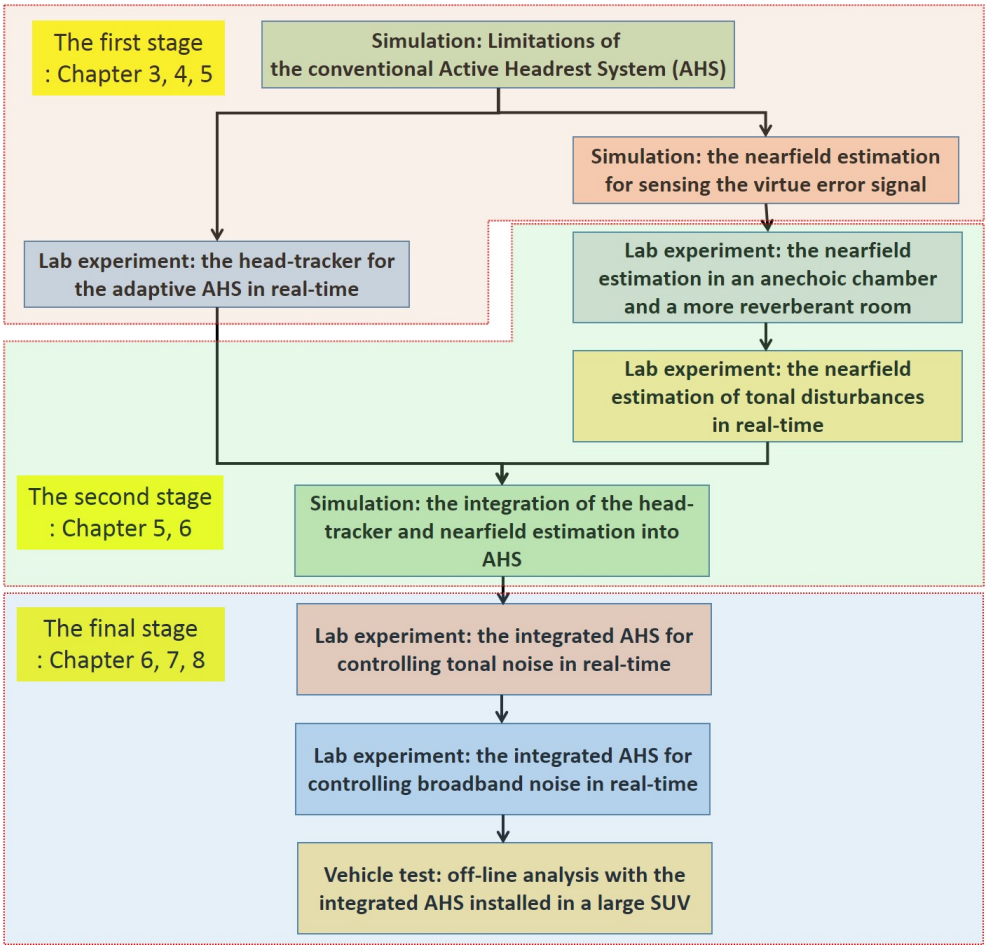

Figure 1.1: The overall structure of the PhD theis.

remote microphone technique, and these are simultaneously integrated into an active headrest system.

In the final stage, an integrated active headrest system has been studied to reduce either tonal or broadband random noise through real-time experiments. In particular, since the causal constraint should be considered to control broadband random noise, filters for active control and the remote microphone technique have been investigated in the time domain. Finally, since the active headrest system is intended to be applied in the automobile interior, the integrated active headrest system with a number of monitoring microphones has been installed in a large SUV and the acoustic responses, interior road noise and reference sensor signals have been measured. The nearfield estimation with the standard and improved remote microphone techniques in the time domain has been predicted. The optimal attenuation performance of the integrated active headrest system has also been investigated off-line using the measured data.

1.4 Thesis structure and contributions

1.4.1 Thesis structure

Chapter 2

This chapter presents a literature review on the theoretical background of local active control in the vehicle interior. First of all, the acoustic characteristics relating to vehicle NVH are reviewed with respect to powertrain noise, tyre-road noise and aerodynamic noise. A number of research results about global and local active control in the enclosure are then studied. The control strategies are classified into feedforward and feedback control and their aspects for active sound control are reviewed. Finally, the previous research about active noise control inside automobile cabins is divided into engine noise control and tyre-road noise control and a review of their applications is provided.

Chapter 3

This chapter describes simulation results on the optimal attenuation performance of the conventional active headrest system. It is investigated how the limitation of the active headrest system is influenced by different factors such as the properties of the primary sound field, the secondary source positions and the selection of error sensors. Simulations are implemented in a hypothetical automobile cabin and the acoustic responses in this cabin are calculated using either the monopole model in the acoustic free field or the modal model in the reverberant field. To understand the fundamental characteristics of local active control in the enclosures, the attenuation performance is described as not only a function of frequency but also a spatial distribution around the controlled area.

Chapter 4

The effects of head movements on adaptive active control and the integration of a head tracking system into the active headrest system are studied in this chapter. Changes in the plant responses, between secondary loudspeakers on the active headrest system and error microphones, are measured when a dummy head is moved in an active headrest. Using this measured data, the effects of the head movements on the stability of the filtered-reference LMS algorithm are investigated. Based on these findings, the application of the head-tracking system to active control is proposed. To verify the improvement of the adaptation stability, a combined active headrest system with the head-tracking is tested and the results of real-time operation with a human listener are presented.

Chapter 5

Virtual sensing algorithms offer a potential method of estimating error signals at virtual error microphones from remotely installed monitoring microphones. This chapter presents a review of the virtual sensing algorithms, and the remote microphone technique is considered as a way of estimating the error signals at a listener's ears in an active headrest system. A least-squares formulation for the optimal observation filter is presented, including a regularisation factor that is chosen to satisfy both the estimation

accuracy and robustness to uncertainties. The accuracy of the nearfield estimation is first investigated for a diffuse field via simulations. Simulations of a free field are also used to investigate the effect of the spatial directivity of the primary field. Finally, experiments in an anechoic chamber are conducted with 24 monitoring microphones around a dummy head positioned in an active headrest system. When six loudspeakers, driven by uncorrelated random disturbances, are used to generate the primary field, the best arrangement of monitoring microphones is considered, taking into account both accuracy and robustness. Appendix C presents experimental results when the same installation is used in a demonstration room at ISVR as an example of a more reverberant space.

Chapter 6

This chapter describes the integration of the remote microphone technique with the head-tracking system in a local active noise control system. The formulation is first studied for the attenuation performance and stability of an adaptive active headrest system combined with the remote microphone technique for tonal noise control. The effects of the head-tracking on the attenuation performance and stability are investigated off-line, using the measured acoustic responses in Chapter 5. The accuracy of the nearfield estimation and the effect of the head-tracking on the control performance are also investigated in real-time experiments. The integrated active headrest system is used to estimate and then attenuate the disturbance signals at a listener's ears from a single tonal primary source in the anechoic chamber, while a commercial head-tracking device detects and provides the real-time head position to the active headrest system whose responses are updated accordingly. Appendix C also presents experimental results from the ISVR demonstration room.

Chapter 7

In this chapter, the integrated active headrest system is used to control broadband random sound at the listener's ears. A time domain formulation of the optimal observation filter for the remote microphone technique and the optimal controller for active control is presented, to sense and control broadband random road noise. To improve the causality of the observation filter and the controller, an improved remote microphone technique, using a modeling delay, is also presented. Real-time control of broadband noise with the integrated active headrest system is implemented and the effect of the head-tracking is investigated. The integrated active headrest system employs the improved remote microphone technique when the primary source is located in front of the active headrest system. Appendix C also presents experimental results from the ISVR demonstration room.

Chapter 8

Based on the findings of Chapter 6 and Chapter 7, the performance of a multichannel feedforward active headrest system for the active control of interior road noise in a real vehicle cabin is investigated. The monitoring microphones and the active headrest

system with a dummy head are installed in the cabin and the acoustic responses, disturbance signals and reference signals are then measured. Using these measurement, the estimation accuracy of the causal remote microphone technique is investigated through simulations. The attenuation performance of the active headrest system using the remote microphone technique is also predicted offline. The effects of delays and head movements on the attenuation performance are also studied.

Chapter 9
The final chapter presents a summary of the work presented in the previous chapters. Suggestions for future work in this area are also provided.

1.4.2 Contributions

The main contributions of this thesis are:

1. A comprehensive understanding of the effects of the primary sound field on the performance of local active control systems and the design of secondary source and error sensor layouts. This has enabled the development of the optimised feedforward active control system to improve mid and high frequency performance.

2. The development of a local active control system with head tracking. This is the first practical demonstration of combining active control with head-tracking in the literature and has resulted in novel control strategies.

3. Understanding the behavior of the virtual sensing algorithm in different primary sound fields. In particular, the remote microphone technique has been studied through simulations and experiments. This has improved the accuracy and robustness of the remote microphone technique to estimate error signals at the targeted regions, and thus improved the performance and the stability of the control system.

4. The implementation of real-time active noise control using the integrated active headrest system under various conditions. Experimental methods for narrowband and broadband active noise control of the integrated system have been described and the test results have clearly demonstrated the achievable attenuation performance and the controllable frequency range. In addition, such active control has been conducted in both an anechoic enclosure and a more reverberant room and the results have been compared to each other.

5. The effects of the head-tracking device during real-time control have been investigated with a human listener. As actual head movements of the listener were used for real-time active control, the feasibility of the head-tracking has been validated.

6. The investigation of the performance of the integrated active headrest system in an automobile cabin. This study will allow the integrated active control system to be practically applied for controlling higher frequency interior noise in vehicles.

1.5 Publications

A number of publications and conference proceedings have arisen from both the work presented in this thesis and related work carried out during the same time period and these references are given in the following sections.

1.5.1 Journal papers

1. Jung, W., Elliott, S. J. & Cheer, J. (2017). Combining the remote microphone technique with head-tracking for local active sound control. *Journal of the Acoustical Society of America*, 142(1), 298-307. [20]

2. Elliott, S. J., Jung, W. & Cheer, J. (2018). Head tracking extends local active control of broadband sound to higher frequencies. *Scientific Reports*, 8(1), 5403. [21]

3. Jung, W., Elliott, S. J. & Cheer, J. (2018). Estimation of the pressure at a listener's ears in an active headrest system using the remote microphone technique. *Journal of the Acoustical Society of America*, 143(5), 2858-2869. [22]

4. Jung, W., Elliott, S. J. & Cheer, J. (2018). Local active control of road noise inside a vehicle. *Mechanical Systems and Signal Processing*, In review.

1.5.2 Conference papers

1. Jung, W., Elliott, S., & Cheer, J. (2017). Local active sound control using the remote microphone technique and head-tracking for tonal and broadband noise sources. Paper presented at *ICSV24: 24th International Congress on Sound and Vibration*, London. [23]

2. Jung, W., Elliott, S., & Cheer, J. (2016). Identifying of interior noise sources in a vehicle cabin using the inverse method. Paper presented at *ICSV23: 23rd International Congress on Sound and Vibration*, Athens. [24]

3. Jung, W., Elliott, S., & Cheer, J. (2016). The effect of remote microphone technique and head-tracking on local active sound control. Paper presented at *ICSV23: 23rd International Congress on Sound and Vibration*, Athens. [25]

4. Elliott, S., Simon, M., Cheer, J., & Jung, W. (2015). Head tracking for local active noise control. Paper presented at *12th Western Pacific Acoustics Conference*, Singapore. [26]

5. Cheer, J., Elliott, S., & Jung, W. (2015). Sound field control in the automotive environment. Paper presented at *3rd International ATZ Automotive Acoustics Conference*, Switzerland. [27]

6. Elliott, S. J., Jung, W., & Cheer, J. (2015). The spatial properties and local active control of road noise. Paper presented at *EuroNoise*, Netherlands. [28]

Chapter 2

Literature review

The aim of this chapter is to briefly review the literature on interior noise in vehicles and then to focus more on the use of active noise control in vehicles. In Section 2.1, the characteristics of interior noise inside automobile cabins are presented in terms of noise sources and transmission paths. In particular, powertrain noise, aerodynamic noise and tyre-road noise as main interior noises are reviewed in detail. In Section 2.2, the general features of global and local active sound control in an enclosure are described and previous research about these active sound control strategies is reviewed. In Section 2.3, the basic control structure of an active control system is classified into feedforward control and feedback control, and a brief overview of the two control structures is described. Finally, in Section 2.4, the application of active noise control to road vehicles is reviewed. Because active control approaches are dependent upon the type of noise source being controlled, the review is divided into reducing engine noise and reducing tyre-road noise.

2.1 Interior noise in road vehicles

Interior noise describes the acoustical characteristics that occupants of the vehicle cabin directly experience and thus well-designed interior noise can provide the occupants with comfort and enjoyment [29, 30]. The components of interior noise can be mainly categorised as engine noise, tyre-road noise, intake noise, exhaust noise, aerodynamic noise, and squeal and rattle noise from mechanical components [29, 31, 32]. Combinations of these noise sources contribute to an interior noise level for an average passenger car of around 45 dB(A) at the idle condition to around 78 dB(A) at maximum acceleration [32, 33]. The dominant sources of interior noise generally depend on speed and engine load conditions and noise from these sources is transmitted to the interior through both structure-borne and air-borne paths [29, 31, 32].

The interior noise spectrum is typically high in the low frequency range, below around 500 Hz, and noise levels are normally largest in the frequency range from 50 to 200 Hz

[32, 33]. The interior noise at this low- and mid-frequency range is mainly transmitted through structure-borne paths and the vibrating walls of the vehicle interior can radiate noise into the cabin, although the interior noise can also be attributed to the air-borne noise from the intake and exhaust system of the engine powertrain [29, 31–33]. In the range between 500 Hz and 1,000 Hz, the structure-borne and air-borne noise have similar levels and as the frequency increases, the contribution of the air-borne noise increases [32]. According to Lalor and Bharj [34], when a vehicle is driving at a speed of 100 km/h, so that it does not produce a significant level of wind noise, the front structure-borne, rear structure-borne and powertrain air-borne noise are the primary noise sources below 500 Hz. The front structure-borne noise is generally produced from vibrations of the engine powertrain and tyre-road interaction and the rear structure-borne noise is mainly due to the tyre-road interaction [29, 31, 33, 34]. In the 500 Hz and 1,000 Hz frequency range, the increased tyre-road air-bone noise becomes one of the primary noise sources. At this frequency range, although the front structure-borne noise and power train air-borne noise decrease, the rear structure-borne noise is still the dominant noise source [33, 34]. Therefore, noise from the interaction between the tyre and road is a main concern when attempting to control the interior noise in the frequency range up to 1,000 Hz. As well as powertrain noise and tyre-road noise, aerodynamic noise can be an important noise source as the vehicle velocity increases. This is because its sound power increases in proportion to the sixth power of the vehicle speed [29, 32, 35].

The following sections explain powertrain noise, aerodynamic noise and tyre-road noise, which are considered as the three primary sources for the interior noise.

2.1.1 Powertrain noise

The engine and its ancillaries such as the transmission, the mount system, the drive line, the intake system and the exhaust system are collectively called the powertrain [32]. Powertrain noise is one of the most important sources for interior noise [29–32]. Since traditional internal combustion engines generally produce their power using the four-stroke cycle, noise and vibration generated by combustion gas pressure, reciprocating and rotating motions of the engine components and the intake and exhaust processes are inevitable [29, 32].

Combustion gas pressure results in significant torsional vibration in the crankshaft and this vibration is transmitted to the mounting systems of the engine and its ancillaries. As a result, the vibration generates radiating noise through the vehicle body and walls. In addition, noise from the combustion process can also be directly transmitted through the engine block and covers as air-borne noise [29]. The frequency spectrum of the cylinder pressure can be a reliable indicator of the combustion induced noise [31]. The spectrum is mainly dominated by the fundamental firing frequency and its harmonics at low frequency ranges and is influenced by the stiffness-controlled response at mid

frequency ranges between around 500 and 3,000 Hz and additional components can be induced by the irregular combustion process [29, 32]. The amplitude of the spectrum at the mid frequency is proportional to the rate of combustion pressure rise. Pressure pulses at these frequencies can be the audible noise source that may influence the sound quality, which is the perceived level and characteristics of the noise [29, 30]. For example, since diesel compression ignition engines have more sudden pressure rises than spark ignition gasoline engines, diesel engines have more impulsive and higher frequency content [29, 30].

The other primary source from the engine is the mechanical excitation from the crank mechanism such as pistons, connecting rods, crankshafts and bearings [31]. Forces from the mechanical excitation are proportional to the engine speed in terms of amplitude and frequency and these forces are generated in all directions including translation, moments and torsion [29]. The transverse forces by the slider-crank mechanism generate piston impacts on the liner, which are called piston slap and the piston slap is typically the dominant source among the forces of the mechanical excitation [31, 32]. The excitation frequency spectrum from the piston impacts is much flatter than that of the combustion noise which is mainly dominated by the fundamental firing frequency and its harmonics [32]. Vibration from the transverses force is also transmitted to the vehicle body through the mounting systems and forces at low frequency can excite the structural vibration modes of the engine components and these resonances must be avoided [29, 31].

Since most motions of engine including the combustion process and the crank mechanism are closely related with engine rotation speed, the engine speed may be the most dominant factor for estimating engine noise [32]. With the engine rotation speed, the fundamental frequency, f_0, which is referred to as the dominant engine order, is given by [29, 31, 32]

$$f_0 = \frac{N}{2 \times 60} \times \text{no. of cylinders}, \tag{2.1}$$

where N is engine rotational speed in rev/min(rpm). For example, for a six-cylinder engine at 1,800 rpm, 90 Hz becomes the fundamental noise frequency and the third engine order becomes the dominant engine order because for a single engine rotation, three combustions are generated at three cylinders among six cylinders. Similarly, the fourth engine order becomes the dominant engine order for a eight-cylinder engine. Engine size is one of the important parameters for engine noise and so the approximate estimation of engine noise for petrol engines can be simplified by the engine speed and the engine size as

$$\text{dB(A)} = 50 \log_{10} N + 30 \log_{10} B + 40 \log_{10} S - 223.5, \tag{2.2}$$

where B and S are respectively the bore and stroke of a cylinder in mm [32].

An important type of powertrain interior noise is booming noise in the cabin. Booming noise is a drastic increase of specific low frequency tonal noise at certain engine speeds due to low orders of the engine firing frequency exciting low frequency acoustic resonances of the vehicle cavity [30, 35]. The booming noise degrades the sound quality perceived by the passengers, and is generally prevented by decoupling the acoustic modes from the excitation frequencies.

Noise from the intake and exhaust system is one of the most influential air-borne noise sources from the powertrain because these systems act as monopole sources and thus are efficient radiators [29]. When the engine continues to open and close engine intake valves, pressure pulses at the intake system are generated and these pressure pulses are radiated from the snorkel of the intake system [29]. In a similar way, when engine exhaust valves open and residual pressure from the combustion process is discharged, pressure pulses are generated and radiated at the tailpipe [32]. In addition, due to the high flow velocity in the exhaust process, high frequency flow noise with a broad band spectrum is also induced [29, 32]. Since the operating frequency of the intake and exhaust motion is the same as that of the combustion motion, the engine firing frequency is the primary frequency of the intake and exhaust noise which generally occurs at low frequencies below 500 Hz and the harmonic frequencies are also produced [29, 32].

To engineer the engine noise, the sound quality of the powertrain noise can be considerably influenced by manipulating intake and exhaust noise [29, 30, 32]. For instance, for a smooth and refined sound quality, intake and exhaust sound are tuned as the primary order sound and the harmonic sounds are less dominant [29, 30] and in contrast, the sporty sound requires modulations of the primary order and its harmonics and half orders [29, 30]. Intake and exhaust noise are tuned by reactive and dispersive attenuation components such as expansion chambers, Helmholtz resonators and absorption materials [29, 32].

2.1.2 Aerodynamic noise

Aerodynamic noise becomes one of the most dominant noise sources when vehicle speed is increased to more than 100 km/h because as mentioned, its sound pressure level rapidly increases as a function of speed (V), which typically is $60 \log_{10} V$ [29, 32, 35]. Therefore, vehicle tests for measuring aerodynamic noise are generally implemented at the vehicle speeds between 100 km/h and 160 km/h [30].

There are several noise generation mechanisms from turbulent flow such as turbulent boundary layers, flow separations and reattachments, cavity flows, leak flows and vortex shedding [29, 31, 32, 35]. The pressure fluctuations of the turbulent boundary layers on the surfaces of vehicle body panels and windows induce vibrations and thus generate

radiatied noise [29, 32]. However, noise from these vibrations is generally not dominant in terms of aerodynamic noise and a greater pressure fluctuations on the surfaces of the vehicles are generated by the flow separations and reattachments [29, 31, 32]. Vehicle body A-pillars and external sideview mirrors are one of the main causes of the separating and reattaching flows. Vortices from these flows generate broad band noise [29].

Cavity flows produce tonal noises via the fluid-dynamic resonance and the Helmholtz resonance. The fluid-dynamic resonance is caused by sound from vortices impinging on the downstream edge feeding back to the upstream edge, causing the formation of another vortex. This resonance produces strong tonal noise [29, 35]. In addition, when a certain volume of an enclosure is excited by the flow, the Helmholtz resonance can be produced [29].

Noise through leaks is produced by either net air flows between inside and outside or noise transmission by the movement of seals [29, 35]. Vortex shedding causing tonal air-borne noises is generated when flows pass through the long objects of circular or other sort of constant cross section such as car antennas, wipers and roof rack bars [29, 31, 32, 35].

2.1.3 Tyre-road noise

The influence of tyre-road noise on the interior noise is increasing important because noise from the powertrain is continuously being reduced, by either improved powertrain techniques or the application of the electric motor as an alternative of the internal combustion engine [30]. When a car is driving at a constant speed without acceleration, the tyre-road noise typically will dominate at more than 50 km/h but is also important at lower velocities, except in first gear [36].

Noise and vibration due to the interaction between the tyre and the road are generally transmitted by structure-borne paths from the tyres to the wheels and onwards via the suspensions to the body walls below around 500 Hz [30, 31]. Air-borne noise, above 500 Hz, can be transmitted from the tyres directly to the cabin through holes, leakage, and floors and doors which have a low transmission loss [30, 31]. Although the extent of the road induced noise depends on many factors, such as the vehicle speed and the roughness of roads, the largest sound level of interior road noise is typically around 60∼65 dB(A) at about 250 Hz and falls off as the frequency increases [31].

The tyre can act as both the noise source and transfer path [32, 37]. The air-borne noise from the tyre can be generated by air pumping in the tread and vibration of the tyre surfaces, such as the carcass or the sidewall [32, 37]. As the car moves along, tread segments are initially squashed and the air between the segments is emitted and then, the cavities of the treads are recovered and air is sucked back into the cavities. This air pumping can also be produced by cavities in the road surface. That is, when a tyre with

a smooth surface runs in to the rough road, air in the cavities of the road is emitted and sucked back [32].

Vibration of the tyre can be a cause of not only air-borne noise, as radiated noise from the tyre surface, but also structure-borne noise. Vibration can be produced by a number of mechanisms. First of all, the road roughness can deform the contact area of the tyre and the deformation can produce a mechanical force on the tyre. This excitation depends on how well the overall deformed area is isolated from the rest of the tyre area [37]. Therefore, the statistical properties of the road roughness can be used as the input and the radial vibration at low frequency is mainly created by this excitation [32, 37]. Secondly, when the tyre 'runs in', collisions between the tread blocks and the road are produced and these impacts vibrate the tyre tangentially. Finally, when the tyre 'runs out', adhesive tread blocks are separated from the road and block contractions create impacts [32, 37].

The excitation mechanisms for air-borne and structure-borne noise can be amplified by several phenomena, including the horn effect, mechanical resonances and acoustical resonances [32, 35, 37]. As the geometry between the threads and the road surface makes a horn shape, noise sources produce image sources and thus radiate more sound. This is called the horn effect and generally influences in the frequency range between 800 and 1200 Hz [32, 35, 37]. The tyre has a number of vibration modes like other mechanical systems [32, 37]. Below the first vertical mode of the tyre, the tyre acts as a rigid ring, without deformation, and a bounce mode is easily excited and thus the tyre transfers significant energy to the suspension. This first mode usually lies in the range of 80∼100 Hz. Above the first vertical mode, the tyre can isolate vibrations from the road roughness like an overdamped spring-mass and as frequency increases, higher modes of the radial belt mode are clearly dominant [37]. Acoustic resonance frequencies lie in the range of 190∼240 Hz, because the circular closed cavity of the tyre forms standing waves in that frequency range. That is, when the circumference of the tyre cavity matches with a wavelength, the first acoustic resonance is created by constructive interference of waves with the same phase. Due to the Doppler effect from the velocity of the rolling tyre, this acoustic resonance generates tonal and time-varying noise which is perceived as annoying [37].

The texture of the road surface can generally divided into three conditions - smooth asphalt surface, coarse chipping surface and rough surface with bumps and holes [37]. For the smooth asphalt surface, air-borne noise is mainly produced. For the coarse chipping surface, low frequency structure-borne noise is dominant and, for the rough surface with bumps and holes a constant cruising load with random impacts is produced. The amplitude of the road roughness spectrum usually decreases with frequency, but the roll-off slope can vary with the texture conditions. For the rough surface, the power spectrum of low frequency elements is largest and most rapidly decreases [37].

Transfer path analysis for road noise is complicated, compared to the case of the powertrain noise, because a single signal does not exist as a suitable reference signal. Therefore, grouped signals are utilized to provide a set of coherent signals [4, 14, 31]. A cruising mode is generally considered as the condition for measuring the tyre and road noise, because it can be regarded as time-invariant and the powertrain noise is not dominant compared to when the vehicle is accelerating [4, 11, 37]. Random signal processing using power spectral density and cross spectral density are typically used for the analysis of road noise [31].

2.2 Active noise control in enclosures

Active noise control in enclosures has been the subject of comprehensive research by [9, 38, 39] and can be divided into global active control and local active control. The analysis of Nelson and Elliott [9] is mainly reviewed here, to investigate these two methods of active control in an enclosure and other particular research is studied to provide examples.

2.2.1 Global active sound control in enclosures

According to Nelson and Elliott [9], global control can be achieved by minimizing the total acoustic potential energy in the enclosure and a sum of squared pressures can be used to estimate the acoustic potential energy. When the enclosure is harmonically excited, the energy in the enclosure can be approximately described as the summation of the acoustic modes and the strength of secondary sources can be optimised to minimise the sum of the squared pressures at every point in the enclosure.

Nelson and Elliott [9] show that the secondary source can suppresses the dominant modes, which are well coupled with both the primary and secondary sources, and significantly reduce the total acoustic potential energy. Thus the closer the secondary source is located to the primary source, the more modes that can be controlled. In addition, Nelson and Elliott [9] have investigated the case when multiple secondary sources are applied. Source strengths of the secondary sources have the form of a vector which minimises a quadratic cost function given by the acoustic potential energy and global control in a two-dimensional enclosure shows a similar tendency to the results in the one-dimensional enclosure. Finally, when the modal density and the modal overlap are large in the enclosure, an individual dominant mode does not exist but many modes contribute. Thus, global control by secondary sources remote from the primary source achieves very little attenuation. At the extreme condition when the sound field becomes diffuse, when two monopole sources separately act as the primary source and the secondary source and they are located close to each other in the enclosure, the fractional reduction in the acoustic potential energy can be expressed as

$$\frac{E_p}{E_{p_0}} = 1 - \left(\frac{\sin\, kr}{kr}\right)^2, \tag{2.3}$$

where E_{p_0} and E_p are the acoustic potential energy before and after control, k is the wavenumber and r is the distance between the primary source and secondary source. Therefore, this equation indicates that as either the frequency or the distance between the two sources increases, the reduction in the acoustic potential energy achieved by global control rapidly decreases to zero.

Cheer [11] has performed simulations of global control in an enclosure, using theoretical and measured impedances between sources and microphones, for different boundary conditions and different numbers of secondary sources. In these simulations, the global control performance in a rigid and non-rigid walled enclosure has been compared. It has been shown that for an internal acoustic primary source, the control performance is not significantly affected by the boundary condition and thus the research of Nelson and Elliott [9] about rigid walled enclosures can be valid for the non-rigid walled enclosure such as the vehicle cabin.

A number of researchers have shown that the maximum control frequency is limited to around 300 Hz in a vehicle cabin by the physical properties of the global control system [1, 5, 13, 40]. To investigate the effect of active control in a mining vehicle cabin, Stanef et al. [41] performed numerical simulations using a finite element model. In this research, the structural modes of the cabin boundary and the acoustic modes have been calculated by simulations to estimate acoustic properties of the cavity, and global and local active control have been applied to reduce the acoustic potential energy of this sound field. It was concluded that the location of the secondary sources with respect to the primary source plays an important role in the control performance and global control may not be possible using secondary sources remote from the primary source.

2.2.2 Local active sound control in enclosures

To control an enclosed sound field with a high modal density, Nelson and Elliott [9] suggest local active control, which provides control only at a targeted region in the enclosure. As the frequency increases, the modal density increases and the sound field can be considered as diffuse [42]. In this case, the contribution of the residual modes is substantial and thus control with the secondary sources remote from the primary source is expected to be ineffective, as discussed above. Gaussian random variables can be used to describe the spatial variations of the real and imaginary parts of the complex pressure in the diffuse sound field and the two parts are uncorrelated. Moreover, the spatial correlation, $R(\Delta x)$ of the complex pressures between different positions in diffuse sound fields is described as [9]

$$R(\Delta x) = \langle |p(x)|^2 \rangle \text{ sinc } k\Delta x, \tag{2.4}$$

where $\langle |p(x)|^2 \rangle$ is the local space-averaged modulus squared pressure and Δx is the distance between two positions. When the pressure at an error microphone is controlled to zero by a secondary source, the spatial distribution of the pressure around the error microphone position(x_0) is described as

$$\langle |p(x_0 + \Delta x)|^2 \rangle = \langle |p(x)|^2 \rangle [1 - \rho^2(\Delta x)], \tag{2.5}$$

where $\langle |p(x_0 + \Delta x)|^2 \rangle$ is the space-averaged modulus squared pressure at $x_0 + \Delta x$, $\rho(\Delta x)$ is the normalized spatial correlation as $R(\Delta x)$ / $\langle |p(x)|^2 \rangle$. Therefore, Elliott et al. [43] showed that the zone of quiet in which at least 10 dB of attenuation is achieved is formed as a sphere that has a diameter of about one-tenth of a wavelength.

Local active control in the near field of the secondary source has been also investigated by [9, 44]. When one secondary source and one error microphone are located close to each other, attenuation at the error microphone is mainly implemented by the direct field of the secondary source. In this case a diameter(Δr_ϵ) of a sphere of the zone of quiet is given by [9, 44]

$$\Delta r_\epsilon = \frac{\sqrt{\epsilon}}{\pi} \lambda, \tag{2.6}$$

where ϵ is the reduction factor, by which the space averaged square pressure is reduced, for example, $\epsilon = 0.1$ for 10 dB reduction and λ is the wavelength. Eq. (2.6) gives a result for the 10 dB zone of quiet as $\Delta r_{0.1} \approx 0.1 \times \lambda$ and this result is similar to the results of Elliott et al. [43].

The effect of the diffraction due to the secondary source and the human head on the formation of the zone of quiet has been investigated by Garcia-Bonito and Elliott [45]. This research shows that at low frequency, a shell-shaped zone of quiet is generated around the secondary source and as the frequency increases, the area of the zone of quiet becomes smaller. In addition, the analytical and experimental estimates of the effect of the diffraction by the secondary source and the head show that the zone of quiet is slightly enlarged by the diffraction.

Elliott and Cheer [46] have shown that the diffuse sound field can be generated by a diagonal matrix of spectral densities for a set of primary sources. The optimal least-squares controller for local active control in both frequency and time domains can then be formulated to simulate the performance of single-input and single-output (SISO) control and multiple-input and multiple-output (MIMO) control systems. The results of the SISO system correspond to the simulation results by Garcia-Bonito and Elliott [45]

and the results of the MIMO simulations show how the performance can be improved using a multichannel practical system.

Gonzalez et al. [47] have shown how noise reduction by active control is related to the improvement in the perceived sound quality, by using a local control system in the car seat with recorded vehicle engine noise and synthesized noise. In this research, tonal noises from the engine below 250 Hz around the human ears were mainly attenuated and thus the loudness, roughness and tonality were improved, even though the sharpness with respect to high frequency noise was deteriorated. Rafaely [48] has presented the use of a spherical loudspeaker array with 12 loudspeakers, to expands the area of the 10 dB zone of quiet at 500 Hz and the shape of the zone of quiet can be modified as the controlled area is moved. This research suggests that if the regularisation parameter is used appropriately to prevent the enhancement of sound level outside the zone of quiet, the spherical loudspeaker array could be used as a practical method for an improved local active control system.

Local active control using a parametric array loudspeaker has also been investigated to prevent the secondary sources from enhancing the sound pressure at regions outside of the controlled regions [49–51]. The parametric array loudspeaker using a spatially focused beam has been proven to reduce sound pressure level at a desired location and prevent spillover into the whole sound field. In addition, a steerable parametric array loudspeaker based on a phased array scheme has shown that a moving zone of quiet can be generated with a fixed beamforming loudspeaker. There are, however, concerns over the damages that may be induced to human ears from the high levels of ultrasound used in such systems, particularly when they are located so close to the head [52, 53].

A local active control system with the virtual microphone arrangement has been developed by Diaz et al. [54] in order to reduce low-frequency broadband noise at ear positions on a bed in a sleeping car of a train, when this noise is generated by the wheel-rail interaction of a railway vehicle. In this research, since relatively low frequency noise was required to be controlled, the disturbance signals at the ear positions were assumed to be equal to those at the remotely installed microphones and pre-measured plant responses at the ear positions were used to estimate error signals at the ear positions. When the primary source at a single frequency of either 50 or 250 Hz was used for simulations and experiments, the 10 dB zones of quiet were effectively generated around the ear positions.

The remote microphone technique (RMT) and the Kalaman filter based virtual sensing algorithm (KVS) for local active noise control have been compared by Booij and Berkhoff [19]. In this research, it has been shown that the RMT with FIR filters more accurately estimates signals at the error microphones around the ears than the KVS with the state space model since the state space model order was limited by the numerical instability and the computational demand. When the ‘silent chair’, which has

a similar configuration to a MIMO active headrest system, was used with the RMT to reduce broadband noise up to 500 Hz, the spatial distribution of the 10 dB zone of quiet and the attenuation performance around the desired positions has shown that the performance of local active control with the RMT is comparable to that achieved using direct measurements of the error signals, which may not be practical.

2.3 Feedforward control and feedback control

The strategies for active control can generally be classified as either feedforward control or feedback control and these two strategies are distinguished by the method in which the reference signal is generated [38, 55–58]. Feedforward control requires reference sensors to measure signals that are correlated with the primary noise source, such as the engine speed signals for engine noise control [7, 11, 59]. The noise at the error microphone position, which is correlated with the reference sensor signals, is then reduced by feedforward control. The signals from the error sensors are used for the adaptation of the control filter to changes in the primary source.

Feedback control uses the signals at the error sensors to drive the secondary source through the controller without the reference sensor and thus feedback control is effective when the primary sound field is due to a large number of uncorrelated sources [55, 56, 60]. There is an inevitable trade-off between the stability and the performance with feedback control [10, 55, 56, 61, 62]. That is, a high loop gain, which is the product of the plant response and the controller transfer response, is necessary for good performance, but a low loop gain is necessary for good stability [55].

Elliott and Sutton [56] have presented the performance of feedforward and feedback control to reduce road noise in cars. With a single secondary loudspeaker and a single error microphone, accelerometers on the body near the suspension measured reference signals for feedforward control and with the identical system, except for the absence of the reference sensors, the feedback control was implemented. When only a small delay, of 1 ms, was present in the plant response, the feedback control produced better performance than feedforward control below 300 Hz. The error signal after feedback control was almost white noise, which indicates the nonselective attenuation of feedback control. When the delay increased to 5 ms, however, the performance of the feedforward system was only slightly influenced by the change in the delay, whereas the performance of the feedback system was significantly degraded.

Cheer and Elliott [4] have also investigated multichannel feedforward and feedback systems to control interior road noise in a car. In this research, four microphones were installed around a headrest and four other microphones were positioned on the floor. Four car audio loudspeakers were utilised as the secondary sources. For feedback control, all eight microphones provided the error signals and for feedforward control, the four

microphones around the headrest provided the error signals and the four microphones on the floor provided the reference signals. Formulations of the controllers were presented with limitations on extreme enhancements in the disturbance signals measured at the headrest microphones. The performance of these systems has been estimated in a small car with measured transfer responses. The results for different conditions such as plant variations, disturbance variations and delays in the plant response have shown that feedback control is, in particular, more effective for broadband control than feedforward control although feedback control is non-selective and much more sensitive to the delays in the plant response.

An algorithm combining feedforward and feedback control, which is often called 'hybrid control', has also been investigated [63–65]. Akhtar and Mitsuhashi [64] have shown that feedforward active control with the filtered-reference LMS algorithm can be perturbed by uncorrelated disturbance signals and the convergence of the algorithm can be improved by removing uncorrelated components from the error signals in the controller. Numerical simulations demonstrated that while feedforward control does not reduce sinusoidal disturbance signals that are uncorrelated with the reference signals, the hybrid control achieves better attenuation performance and faster convergence for both correlated and uncorrelated sinusoidal disturbance signals.

2.4 Active sound control in road vehicles

2.4.1 Active sound control for reducing engine noise in road vehicles

Powertrain noise is mainly tonal, which is directly related to the engine rotational speed, and low frequency components of this noise are thus suitable for treatments using active noise control. Therefore, a variety of active control systems have been proposed by [10, 47, 59, 66, 67]. In particular, several systems for the active control of the engine noise have been commercialised by manufacturers [1, 2, 5–7, 13].

Because it is relatively easy to obtain periodic reference signals directly from the engine, feedforward active control of engine noise was first implemented some time ago [59] and the physical arrangement of a typical feedforward active control system for engine noise is well described by Elliott [10]. In this system, four loudspeakers around the front seats were used as the secondary sources to control noise at the engine firing frequency and its harmonics at eight microphones installed in the head lining. Engine noise was globally controlled in a cabin and noise reductions in not only the front seats but also the rear seats were achieved. Using car audio loudspeakers, a cost effective engine noise control system has also suggested by [13].

Schirmacher et al. [2] have presented an application of active engine noise control to compensate for the change in sound quality due to switching between 8-cylinder and

4-cylinder operation. To increase fuel efficiency, Audi applied cylinder deactivation technology to their V-8 engine and it was found that when four cylinders are deactivated for operating at part load, interior noise at the second engine order of the engine firing frequency is significantly and rapidly increased and the sound quality of the interior noise is thus degraded. To solve this problem, an adaptive active noise controller was calculated as a notch filter that reduces tonal noise at the second engine order of the engine firing frequency. Various uncertainties such as the number of passengers, seating positions and product variations have been considered for modelling the plant response. The active control system integrated with the car audio system achieved about 10 dB attenuation during the 4-cylinder operation and thus contributed to improve the fuel efficiency.

2.4.2 Active sound control for reducing tyre-road noise in road vehicles

Since tyre-road noise is one of the most important interior noise sources in road vehicles, various methods of active sound control have been studied to reduce tyre-road noise in vehicle cabins [1, 14, 15, 28, 40, 60, 62, 63, 68, 69].

Oh et al. [15] have presented the development of the active control system to reduce road booming noise in the vehicle interior. Vibration generated by tyre-road interactions can excite low order acoustic modes of the vehicle cabin and thus interior noise at a specific low frequency range can be drastically increased. In this research, at around 250 Hz, 8 dB or more increase in the interior booming noise was found under different road conditions and vehicle speeds. A feedforward active control system was thus applied to control the road booming noise. The positions of reference transducers on the suspension system were firstly considered, to increase the multiple coherence between the reference sensors of the suspension and error sensors around the front seats. This is because the optimal attenuation of the non-causal controller for feedforward active control has an upper limit determined by the multiple coherence function [4, 14, 55]. Therefore, the closer a multiple coherence is to unity, the more attenuation performance is possible to achieve. Because the four wheels vibrate independently, a single triaxial reference transducer produced poor coherence. When 2 triaxial reference transducers were installed on the right and left suspensions, a maximum attenuation of around 6 dB was achieved for the road booming noise at around 250 Hz. In addition, in this research, it was considered that nonuniform road surface and changing vehicle speed can produce time-varying vibrations between tyre and road and thus the general filtered-x LMS algorithm, which assumes that the control filter slowly adapts, can degrade the performance. Therefore, a leaky constraint filtered-x LMS algorithm was suggested for the fast convergence of the controller and releasing the constraint of time-invariance. Conclusively, around 5∼6

dB reduction in the road booming noise was achieved, when the car was driven at a constant speed of 60 km/h.

A cost-effective active control system for reducing low frequency road noise over a narrow bandwidth has been studied by Sano et al. [1]. In this research, to reduce the additional cost of active control, the car audio system speakers were used as the secondary sources and the narrow band drumming road noise at around 40 Hz was controlled by fixed feedback and feedforward controllers with analogue circuits. The drumming noise at the front seat was controlled by the feedback controller and the error microphone for the feedback control was used as the reference microphone for the feedforward control, which is necessary for preventing noise enhancements at the rear seats. The error microphone was located at the nodal line of the acoustic first order mode in the cabin, which allows the error microphone to measure in-phase signals of the drumming noise. In addition, when the error microphone signals are extremely large, due to the opening of windows or driving on very rough surface, the application of a limiter circuit prevents the audio speakers from distorting. Because the reference microphone for the feedforward control is located in the cabin, signals from the secondary sources can affect the reference signals and thus the howling effect can be generated. To prevent howling, feedforward control signals, filtered by the pre-measured plant responses between the secondary sources and the reference microphone, were used to cancel the effect of the unwanted feedback from the secondary sources to the reference microphone. Because the feedback control nonselectively attenuates the sound measured by the error microphone, the desired audio system signals should also be compensated, by adding the estimation of the reduced signals in advance. This cost-effective active control system has achieved about 10 dB noise reduction of the narrowband drumming noise, without undue enhancement of the noise level at the rear seat.

Duan et al. [63] have also presented a combined feedforward-feedback active control system to reduce broadband road noise in a car interior. This research suggests that when disturbance signals uncorrelated with reference signals are present for feedforward control, an additional feedback controller is used to attenuate the uncorrelated noise. A simulation showed that more than 6 dB of uncorrelated noise in the frequency range of 100∼170 Hz is additionally attenuated due to the combined feedback controller. In addition, because an excessive convergence factor of filtered-reference LMS algorithm for the adaptive feedforward control system can produce divergence, the small convergence factor for low frequency ranges is also applied to control higher frequency noise. This seems to be inefficient at controlling broadband road noise. Therefore, subband filtered-reference LMS algorithm (SFXLMS) was suggested to apply optimal convergence factors to decomposed frequency bands and as a result, 4 dB larger attenuation in the frequency range of 300∼360 Hz was achieved by SXLMS.

An implementation of active control for multiple narrowband road noise sources has been presented by Sakamoto and Inoue [40]. In this research, multiple notch filters were

designed to reduce narrowband components of interior noise up to 200 Hz, which are produced by tyre-road interactions. By integrating the proposed active control system with a commercialised engine booming noise control system, results have shown that it is possible to simultaneously reduce narrowband peaks of road noise at the low frequencies together with the engine booming noise.

Chapter 3

Optimal performance of a conventional local active sound control system in an enclosure

The objective of local active sound control in enclosures is generally to reduce the acoustic potential energy at particular locations, which produces localised zones of quiet around controlled error sensors [9, 44]. Previous research on active headrest systems, as a practical configuration of local control, has shown that this system potentially extends the controllable frequency range and the attenuation performance at the desired positions, such as at the ears of a listener, compared to global active sound control [16–19, 54, 70, 71]. In the active headrest system, secondary control sources and error sensors are installed around the headrests of the seats to control the interior noise around the driver and passengers.

The advantages of a local active headrest system, over a global active control system, may be listed as [9, 44]:

- The secondary loudspeakers and error sensors are acoustically well-coupled and so the loudspeakers do not have to drive too hard to control the error signals. As a result, noise enhancement at other positions can be low.

- The proximity between the secondary loudspeakers and error sensors can reduce the acoustic propagation delay in the control path, so that it is shorter than the propagation time associated with the primary disturbance signals and this may allow the active control process to remain causal despite electrical delays in the control system. The small delay between the secondary loudspeakers and the error sensors can improve the performance and tracking speed of adaptive control algorithms

- The plant response, which is the acoustic transfer response between the secondary loudspeakers and error sensors, is relatively simple and largely determined by the local

geometry since the direct field of the secondary source is dominant over the reverberant field. Consequently, ill-conditioning can be avoided and the control system can be more robust to small perturbations in the response of the enclosure.

The performance of such a local control system depends on the geometry of the system, but also on the spatial properties of the primary sound field [28, 46]. This chapter is concerned with understanding these factors including the geometry and the spatial properties and their effects on feedforward local active control systems. A general formulation is presented that allows the performance of such a local control system to be predicted from the calculated properties of the sound field. Therefore, the optimal attenuation performance of a local active control system is calculated through numerical simulations. The simulations allow a straightforward investigation of the effects of different factors for local active control.

In Section 3.1, theories for the optimal performance of the feedforward local active control system are studied and the simulation setup is described to realise acoustical conditions of a vehicle cabin. In Section 3.2, it is investigated how the optimal performance of an active headrest system in a free field is influenced by the positions of primary sources. In Section 3.3, similar simulations are implemented in a reverberant acoustic field which is modelled by the summation of a series of acoustic modes. In Section 3.4, methods to improve the optimal performance in the reverberant field are investigated. Finally, Section 3.5 presents the summary of this chapter.

3.1 Optimal feedforward active control in the frequency domain and simulation setup

3.1.1 Optimal feedforward active control in the frequency domain

Theories for feedforward active control have been widely investigated in the previous research [9, 38, 46, 55, 57] and this section mainly provides a review of the work on the optimal performance of a feedforward active control system in the frequency domain as in [46, 55]. Analysis in the frequency domain allows a straightforward assessment of the behaviour of the active control system in terms of the geometrical limitations of control for relatively narrowband disturbances. For generality, all signals are initially assumed to be stationary random, so that they can be described as their spectral densities, but their frequency dependence is suppressed for notational convenience.

A block diagram of the feedforward active control system is shown in Fig. 3.1. The N_v primary sources, which for random disturbances have a vector of complex source strengths in a single frequency bin of $\mathbf{v} = [v_1, v_2 \ \ldots \ v_{N_v}]^{\mathrm{T}}$, produce a vector of N_e complex disturbance signals, $\mathbf{d} = [d_1, d_2 \ \ldots \ d_{N_e}]^{\mathrm{T}}$ at the error microphones and a

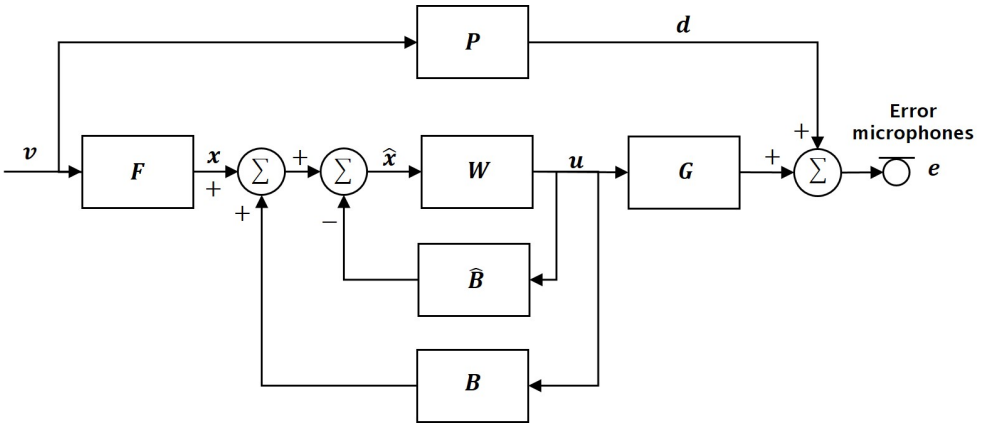

Figure 3.1: Block diagram of a feedforward active control system.

vector of N_x reference signals, $\mathbf{x} = [x_1, x_2 \ \ldots \ x_{N_x}]^{\mathrm{T}}$ at the reference microphones via the matrices of transfer responses $\mathbf{P}$ and $\mathbf{F}$, respectively. A matrix of control filters, $\mathbf{W}$, produces a vector of N_u control signals, $\mathbf{u} = [u_1, u_2 \ \ldots \ u_{N_u}]^{\mathrm{T}}$, which are transmitted to the error microphones, via the matrix of complex plant responses, $\mathbf{G}$, to minimise the disturbance signals, $\mathbf{d}$. The control signals may be fed back to the reference sensor via the matrix of transfer responses, $\mathbf{B}$ but it is assumed here that any feedback is cancelled out by a perfect model, $\hat{\mathbf{B}}$, so that the estimated reference signals, $\hat{\mathbf{x}}$ is equal to $\mathbf{x}$. This assumption may also be valid in a case in which reference sensors are installed on the body and suspension of a vehicle and secondary sources are installed around a headrest of a seat inside the vehicle, so that feedback from the secondary sources to the reference signals is negligible. The vector of complex error signals, $\mathbf{e}$, at the error microphones after control can thus be defined as

$$\mathbf{e} = \mathbf{d} + \mathbf{G}\mathbf{u} = \mathbf{d} + \mathbf{G}\mathbf{W}\mathbf{x} = \mathbf{P}\mathbf{v} + \mathbf{G}\mathbf{W}\mathbf{F}\mathbf{v}, \tag{3.1}$$

By minimising the cost function, which is defined as

$$J_1 = \mathrm{trace}\Big\{ E\left[\mathbf{e}\ \mathbf{e}^{\mathrm{H}}\right] \Big\}, \tag{3.2}$$

where $E[\ ]$ is the expectation operator, $^{\mathrm{H}}$ is the Hermitian or complex conjugate transpose, the optimal active controller, $\mathbf{W}_{\mathrm{opt}}$ can be obtained using the derivation detailed in Appendix A as

$$\mathbf{W}_{\mathrm{opt}} = -(\mathbf{G}^{\mathrm{H}}\mathbf{G})^{-1}\mathbf{G}^{\mathrm{H}}\mathbf{S}_{xd}\mathbf{S}_{xx}^{-1} = -(\mathbf{G}^{\mathrm{H}}\mathbf{G})^{-1}\mathbf{G}^{\mathrm{H}}\mathbf{P}\mathbf{S}_{vv}\mathbf{F}^{\mathrm{H}}(\mathbf{F}\mathbf{S}_{vv}\mathbf{F}^{\mathrm{H}})^{-1}, \tag{3.3}$$

where $\mathbf{S}_{xd} = E[\mathbf{d}\mathbf{x}^{\mathrm{H}}]$ is the cross spectral density matrix between $\mathbf{x}$ and $\mathbf{d}$ and $\mathbf{S}_{xx} = E[\mathbf{x}\mathbf{x}^{\mathrm{H}}]$ and $\mathbf{S}_{vv} = E[\mathbf{v}\mathbf{v}^{\mathrm{H}}]$ are the power spectral density matrices for $\mathbf{x}$ and $\mathbf{v}$, respectively. The spectral density matrix of the signals at the error microphones, $\mathbf{S}_{ee}$, after optimal control can then be obtained by substituting Eq. (3.3) into Eq. (3.1), so that

$$\begin{aligned}\mathbf{S}_{ee} &= E\left[(\mathbf{d} + \mathbf{G}\mathbf{W}_{\mathrm{opt}}\mathbf{x})(\mathbf{d} + \mathbf{G}\mathbf{W}_{\mathrm{opt}}\mathbf{x})^{\mathrm{H}}\right] \\ &= \mathbf{S}_{dd} + \mathbf{G}\mathbf{W}_{\mathrm{opt}}\mathbf{S}_{xd}^{\mathrm{H}} + \mathbf{S}_{xd}\mathbf{W}_{\mathrm{opt}}^{\mathrm{H}}\mathbf{G}^{\mathrm{H}} + \mathbf{G}\mathbf{W}_{\mathrm{opt}}\mathbf{S}_{xx}\mathbf{W}_{\mathrm{opt}}^{\mathrm{H}}\mathbf{G}^{\mathrm{H}},\end{aligned} \tag{3.4}$$

where $\mathbf{S}_{dd} = E[\mathbf{d}\mathbf{d}^{\mathrm{H}}]$ is the power spectral density matrix for $\mathbf{d}$. The optimal attenuation performance at the error microphones can then be obtained by dividing the sum of diagonal terms of $\mathbf{S}_{ee}$ by the corresponding term for $\mathbf{S}_{dd}$. Therefore, when the transfer responses and the primary source signals of the controlled acoustic field are either calculated or premeasured, the optimal control filter and the attenuation performance of the active control system can be estimated.

3.1.2 Simulation setup

The following simulation setup is used to study the performance of the feedforward local active control system in the car cabin, in terms of the controllable frequency range and the spatial distribution of the zone of quiet. The simulations are initially carried out for in a free field, since the results are then easier to understand. All simulations in this chapter are implemented by calculation in the frequency domain The dimensions of the interior space used in these simulations are 3 m×1.8 m×1.2 m, which are the approximate interior dimensions of the ISVR test car, which is a Ford S-MAX [11]. The primary sources are assumed to be potentially located at 560 different positions on the interior cabin walls and the separation between the primary sources is set as 0.2 m as shown in Fig. 3.2. The position number of the primary sources are described in Table 3.1.

Table 3.1: The position number of primary sources on the enclosure walls.

Surfaces	Floor	Roof	Front wall	Rear wall	Left wall	Right wall
Primary source Position No.	1-160	161-320	321-370	371-420	421-490	491-560

Two secondary sources, which represent a hypothetical two channel active headrest system, are approximately located at the headrest of the front passenger seat. In addition, an array of 25 microphones, which are separated by 75 mm, is located on a 0.3 m×0.3m grid at the head position of the passenger to visualise the sound field and the effects of the active headrest system near the head. The error microphones, whose outputs

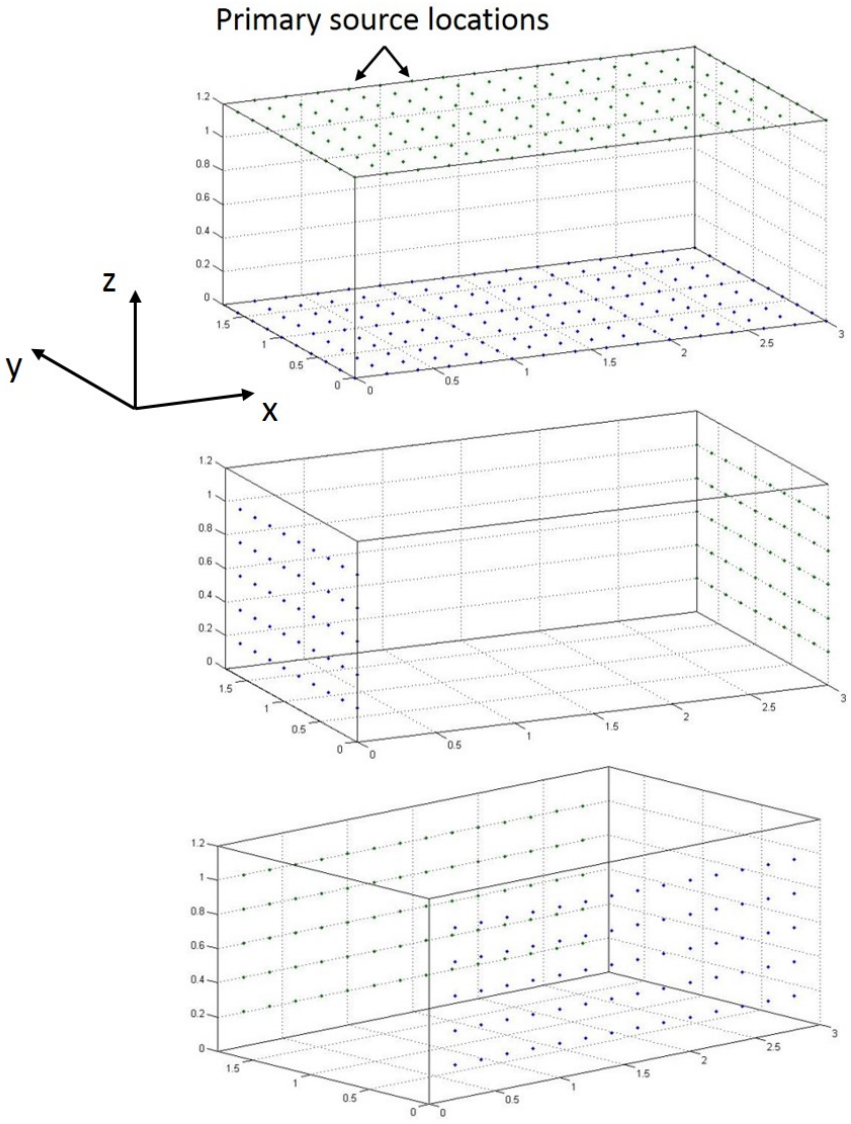

Figure 3.2: Primary source positions on the enclosure walls.

are controlled, are selected from these 25 microphones. The detailed locations of the secondary sources and microphones are shown in Fig. 3.3.

With the setup shown in Fig. 3.2 and Fig. 3.3, the performance of the active headrest system for different frequencies and different primary source positions are estimated. For the simple interpretation of the acoustical performance of the active headrest system, it is assumed that each primary source and secondary source acts as a monopole source and the influence of the head is not considered. The results of previous research [45, 72], suggest that the existence of the head can improve the performance of local active control systems, since the pressure gradient on the rigid sphere is zero and thus the acoustic field near the sphere is spatially more uniform. A dummy head will be used for experiments in the following chapters, so that the influence of the head will then be accounted for.

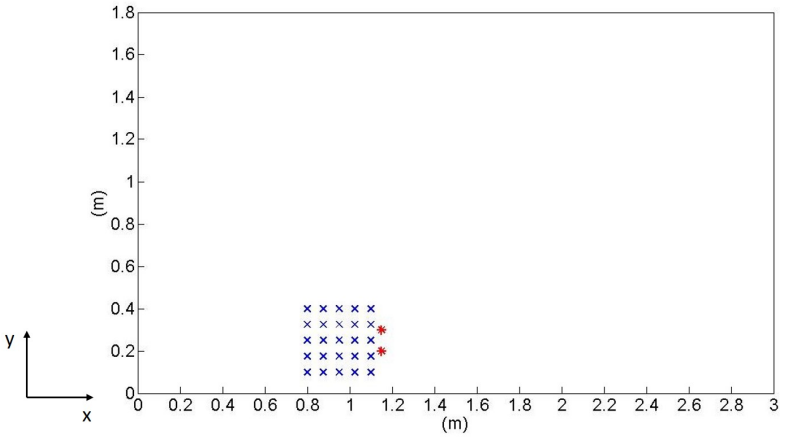

Figure 3.3: Locations of two secondary sources (*) and 25 microphones (×) viewed from above. The height of all devices is 0.9 m.

The causality and coherence between the reference and error sensors are very important in determining performance in the active control of broadband and random acoustic fields in a vehicle. For example, when the reference sensors are in the vicinity of the error sensors, the coherence between these sensors can be improved and thus better attenuation is achievable. However, because the control filter produces inevitable time delays due to a digital implementation, this delay can significantly degrade the attenuation performance. Vice versa, when the reference sensors measures the primary source signals in advance, at positions remote from the error sensors to maintain causality, the coherence between the reference and error sensors may be decreased. In this chapter, it is assumed that the reference sensors are perfectly collocated with the error sensors and the controller is not constrained to be causal, so that $\mathbf{S}_{xd}\mathbf{S}_{xx}^{-1}$ in Eq. (3.3) becomes the identity matrix and Eq. (3.4) can then be written as [28]

$$\mathbf{S}_{ee} = (\mathbf{I} + \mathbf{G}\mathbf{W}_{\text{opt}})\mathbf{S}_{dd}(\mathbf{I} + \mathbf{G}\mathbf{W}_{\text{opt}})^{\text{H}}. \tag{3.5}$$

where $\mathbf{I}$ is the identity matrix. In this case, the effect of the primary source and the relative geometry between the secondary source and the error sensor can be straightforwardly studied. The effects of causality and coherence on active control performance will be studied in Chapter 8, when causal controllers are considered for the reduction of broadband random disturbances using reference signals in a vehicle.

3.2 Estimations of the effect of the local active control system in the free field

3.2.1 Simulations of the performance of the local active control system for different frequencies in the free field

In this section, the performance of local active control for different frequencies under free field conditions is investigated. Since both primary source and secondary source are assumed to be monopole sources in the free field, all the acoustic transfer responses can be defined as [9, 73]

$$Z(r) = \frac{j\omega\rho_0 e^{-jkr}}{4\pi r}, \tag{3.6}$$

where $Z(r)$ is the acoustic transfer response, ω is the angular frequency, ρ_0 is the density in the medium, k is the wavenumber and r is the distance between the monopole source and a single microphone. Therefore, the amplitude and phase of the response at the sensors at a single frequency are only determined by the distances between the sources and the sensors. The sum of the diagonal elements of $\mathbf{S}_{dd}$ and $\mathbf{S}_{ee}$ is used as an overall measure of the mean square pressure over the error microphones before and after control.

When the primary source is assumed to be at a position, #331 on the front wall as detailed in Table 3.1, which suggests a position near the engine, and all 25 microphones are selected as the error microphones to be controlled by a two channel local active control system, Fig. 3.4 shows the sum of the diagonal elements of $\mathbf{S}_{dd}$ and $\mathbf{S}_{ee}$. The attenuation performance in the sum of the power spectral densities at the 25 error microphones is also plotted in the narrow band in Fig. 3.5(a) and in octave bands in Fig. 3.5(b). From Fig. 3.4 and Fig. 3.5, it is found that as the frequency increases, the performance of the active headrest system gradually decreases, as expected. The two secondary loudspeakers attempt to reduce disturbance signals at all 25 error microphones distributed widely around a head position, and so the relative distances from the primary source to the error microphones are quite different from each other, which produces phase differences between the disturbance signals. This limits the attenuation that can be achieved. In the following chapters, smaller regions, around the ears of the head are controlled, to improve the attenuation performance but for now this larger region of control will be retained.

Fig. 3.6 shows the attenuation at each position of the 25 error microphones ($= 10\log_{10}(S_{ee}/S_{dd})$). The performance of local active control is thus visualized around all the 25 microphones and it is found again that as the frequency increases, the performance decreases. It is also found that at the region that is closer to the secondary

sources, a better attenuation is generally achieved, except for the enhancement in the sound pressure in the very near field of the secondary sources at 150 Hz.

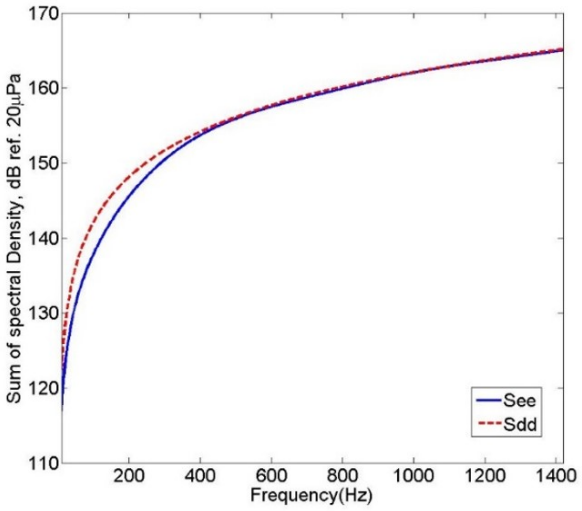

Figure 3.4: Comparison of the sum of the diagonal elements of $\mathbf{S}_{dd}$ and $\mathbf{S}_{ee}$ at all 25 microphones either with/without a two channel local active control system when disturbance signals are driven from a single primary source, #331 at the front wall of Table 3.1 and the 25 microphones are controlled in the free field.

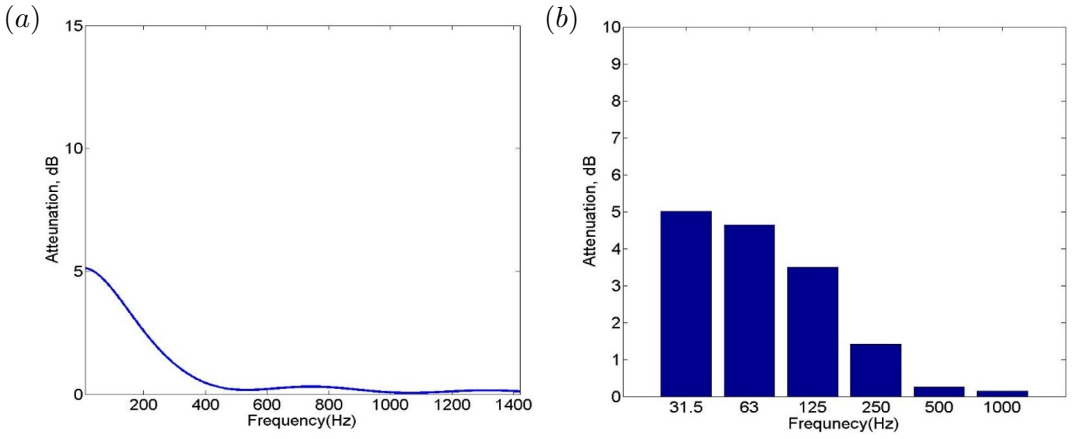

Figure 3.5: Attenuation in the sum of the diagonal elements of $\mathbf{S}_{dd}$ and $\mathbf{S}_{ee}$ at all 25 microphones when disturbance signals are driven from a single primary source, #331 at the front wall of Table 3.1 and the 25 microphones are controlled by a two channel local active control system in the free field : (a) narrow band and (b) octave band

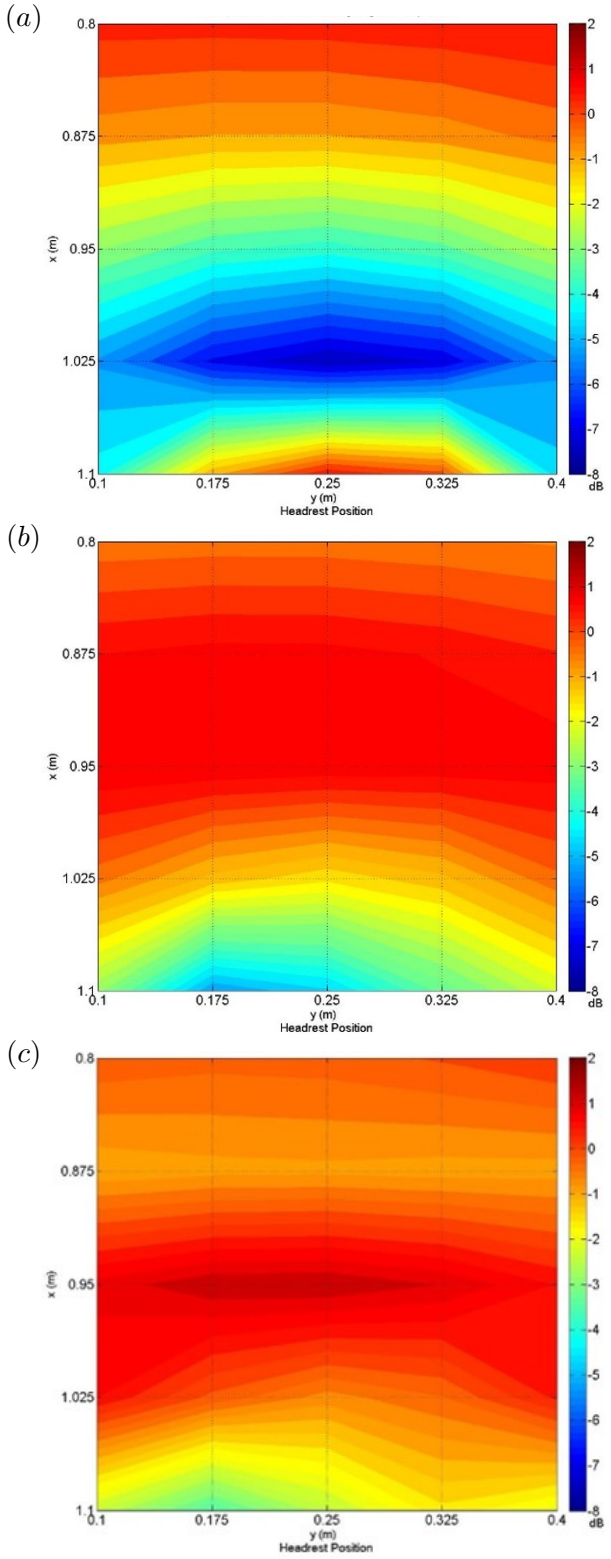

Figure 3.6: Attenuation performance ($= 10\log_{10}(S_{ee}/S_{dd})$) around 25 microphones when a two channel local active system is used to control all 25 error microphones with a single primary source, #331 at the front wall in the free field : (a) 150 Hz, (b) 300 Hz, (c) 450 Hz, The 25 microphones are located at the intersections of the grid in these figures.

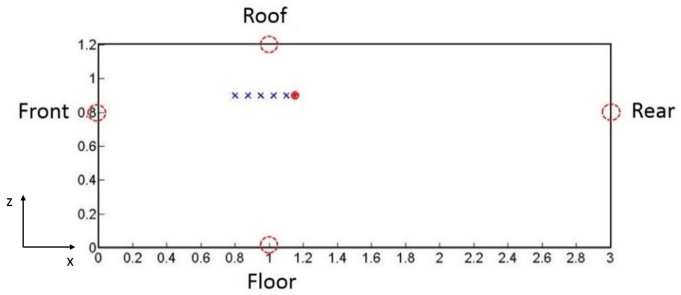

Figure 3.7: Locations of 4 different primary sources viewed from left side. The plane of the 25 microphones and the secondary sources can also be seen.

3.2.2 Simulations of the performance of the local active control system for different primary source positions in the free field

The change in the performance of the local active control system is now studied as the position of the primary source is varied. The primary source is located at 4 different positions, at the front, rear, roof and floor as shown in Fig. 3.7.

The attenuation in the sum of the power spectral densities at the 25 error microphones are compared in Fig. 3.8, which shows that the attenuation performance is significantly affected by the position of the primary source. The largest difference in attenuation is found between the primary sources positioned at the front wall and rear wall. This is because when the primary source is located at the front, the propagating direction of the primary source is opposite to that of the secondary sources and thus the phases between the primary source and the secondary are not well matched. Conversely, in the case of the rear wall primary source, since the propagating directions from the primary source and the secondary sources are similar, the signals are comparatively well matched. This result indicates that the relative positions of the primary and secondary sources and the control region is an important factor governing the control performance in the free field.

Fig. 3.9 shows the performance of the control system when either the frequency or the position of the primary source was changed. As shown in Fig. 3.9, as frequency increases, the attenuation values for all primary source positions are decreased but the extent of this decrease varies significantly for different positions of the primary sources.

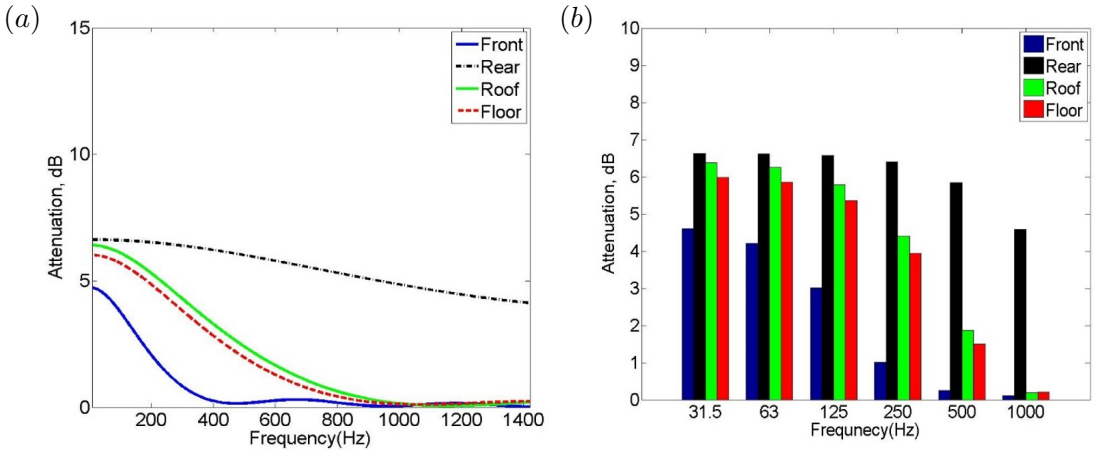

Figure 3.8: Attenuation in the sum of the diagonal elements of $\mathbf{S}_{dd}$ and $\mathbf{S}_{ee}$ at all 25 microphones when disturbance signals are driven from a single primary source among four different primary sources in Fig. 3.7 and the 25 microphones are controlled by a two channel local active control system in the free field : (a) narrow band and (b) octave band

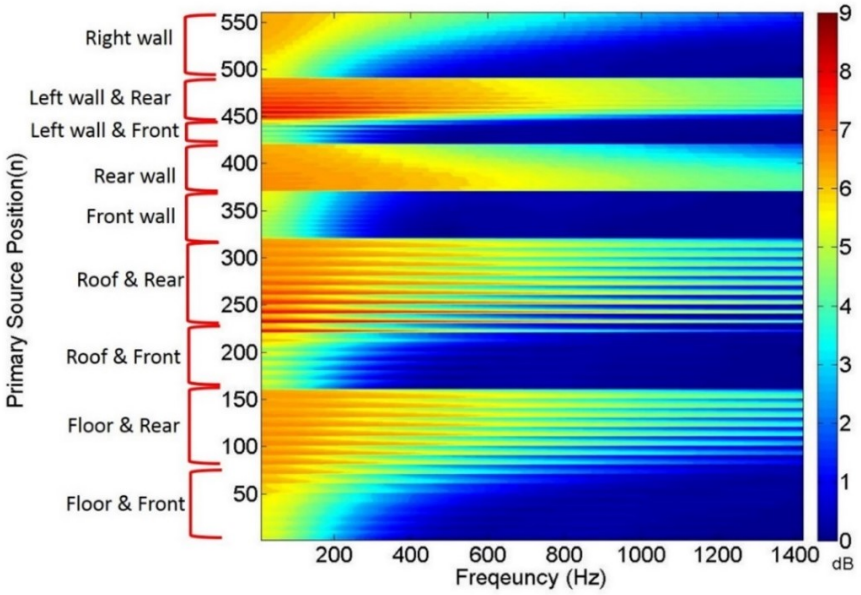

Figure 3.9: A contour map of the attenuation in the sum of the diagonal elements of $\mathbf{S}_{dd}$ and $\mathbf{S}_{ee}$ at all 25 error microphones using the two headrest secondary loudspeakers in the free field as a function of frequency and the location of a single primary source, as was shown in Fig. 3.2.

3.3 Estimations of the effect of the local active control system in a reverberant enclosure

3.3.1 Modeling of a reverberant enclosure using a modal model

In the previous section, the vehicle interior was assumed, for simplicity, to act as an acoustic free field, which means that the sound at the walls of the enclosure is perfectly absorbed. However, since sound reflection exists at the walls in an actual vehicle interior, the interior should be considered as a reverberant sound field. The sound field of a reverberant enclosure can be approximated at relatively low frequencies by the modal model [9, 74]. According to Nelson and Elliott [9], the pressure, $p(x, y, z)$, at a position in an enclosure can be obtained as the summation of a series of acoustic mode shapes as

$$p(x,y,z) = \sum_{l=0}^{\infty}\sum_{m=0}^{\infty}\sum_{n=0}^{\infty} a_{lmn}\ \psi_{lmn}(x,y,z), \tag{3.7}$$

where a_{lmn} is the complex amplitude of lmnth mode and ψ_{lmn} is the mode shape. For a rectangular enclosure, a_{lmn} can be described as

$$a_{lmn} = \frac{\rho_0 c_0^2}{x_0 y_0 z_0} A_{lmn}(\omega)\ \psi_{lmn}(x_i, y_i, z_i) q_i, \tag{3.8}$$

where c_0 is the speed of sound in the medium, the dimensions of the rectangular enclosure are x_0, y_0, z_0, $A_{lmn}(\omega)$ is the complex resonance term, $\psi_{lmn}(x_i, y_i, z_i)$ is the mode shape excited by a monopole source positioned at $x = x_i, y = y_i, z = z_i$ and q_i is the source strength [74]. The complex resonance term, $A_{lmn}(\omega)$ is defined as

$$A_{lmn}(\omega) = \frac{\omega}{2\zeta_{lmn}\omega_{lmn}\omega - j(\omega_{lmn}^2 - \omega^2)}, \tag{3.9}$$

where ζ_{lmn} is the damping ratio and ω_{lmn} is the natural frequency of the lmnth mode in a rectangular enclosure, which is defined as

$$\omega_{lmn} = \pi\ c_0 \sqrt{(\frac{l}{x_0})^2 + (\frac{m}{y_0})^2 + (\frac{n}{z_0})^2}. \tag{3.10}$$

The mode shape, $\psi_{lmn}(x, y, z)$ in the rectangular enclosure can be expressed as [9, 29, 74]

$$\psi_{lmn}(x,y,z) = \sqrt{\epsilon_l \epsilon_m \epsilon_n}\cos(\frac{lx\pi}{x_0})\cos(\frac{my\pi}{y_0})\cos(\frac{nz\pi}{z_0}). \tag{3.11}$$

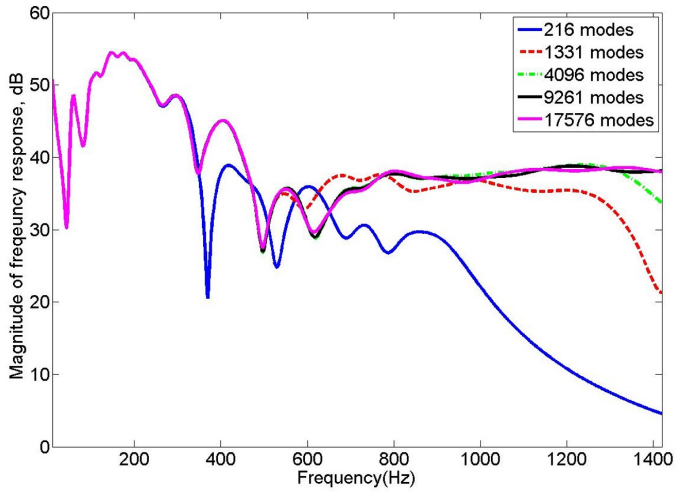

Figure 3.10: Magnitude of frequency response between the primary source #331 at the front wall of the enclosure and a single microphone among the 25 microphones at the head position in the modal modeled enclosure.

where $\epsilon_l, \epsilon_m, \epsilon_n$ are normalisation factors that are equal to one if the subscript is zero and are equal to two if the subscript is greater than zero.

The modal model of the enclosure in Fig. 3.2 has been implemented using various numbers of modes, as shown in Fig. 3.10, which shows the magnitude of the frequency response between the primary source #331 at the front wall of the enclosure and a single microphone. At low frequencies, below about 300 Hz, the frequency response can be approximated by a small number of modes. However, as the frequency increases, a larger number of modes are required to model the frequency responses. It is found that when 9,261 modes, with a maximum natural frequency of about 4,087 Hz, are employed, the frequency response up to 1,400 Hz converges to that for a larger number of modes. The damping ratio, ζ_{lmn} of the enclosure walls is set to 0.1, which has been considered as a typical damping ratio of the automobile interior [11, 14]. A peak in the response can be seen at a frequency of about 58 Hz, which corresponds to the $(1, 0, 0)$ mode of this rectangular enclosure. However, due to the high damping and model overlap, other peaks are not distinguishable. Responses between sources and sensors calculated using this modal model have been used in the following simulations of local active control in the reverberant acoustic field.

3.3.2 Simulations of the performance of the local active control system for different frequencies in the reverberant enclosure

In this section, acoustic responses from both the primary source and the two secondary sources to the microphones are simulated by the modal model. The same two-channel local active control system and 25 microphones to those in Section 3.2 are again used.

When the disturbance signals from the primary source at a position, #331 on the front wall are reduced by the control system, the sum of the diagonal elements of $\mathbf{S}_{dd}$ and $\mathbf{S}_{ee}$ at the all 25 microphones is shown in Fig. 3.11. In addition, the attenuation performance in the sum of the power spectral densities at the 25 error microphones is plotted in the narrow band in Fig. 3.12(a) and in octave bands in Fig. 3.12(b).

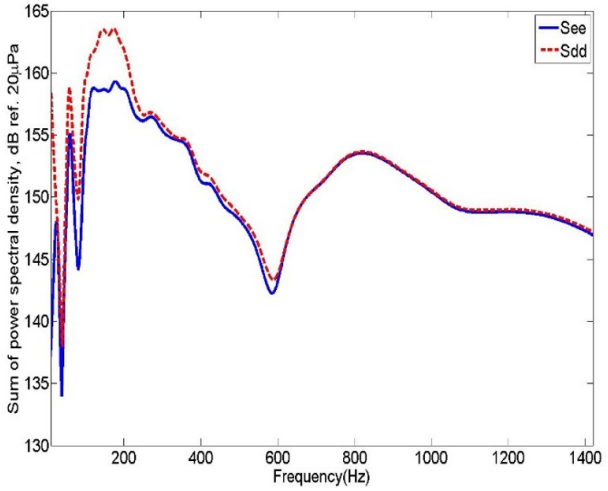

Figure 3.11: Comparison of the sum of the diagonal elements of $\mathbf{S}_{dd}$ and $\mathbf{S}_{ee}$ at all 25 microphones either with/without a two channel local active control system when disturbance signals are driven from a single primary source, #331 at the front wall of Table 3.1 and the 25 microphones are controlled in the reverberant field simulated by the modal model.

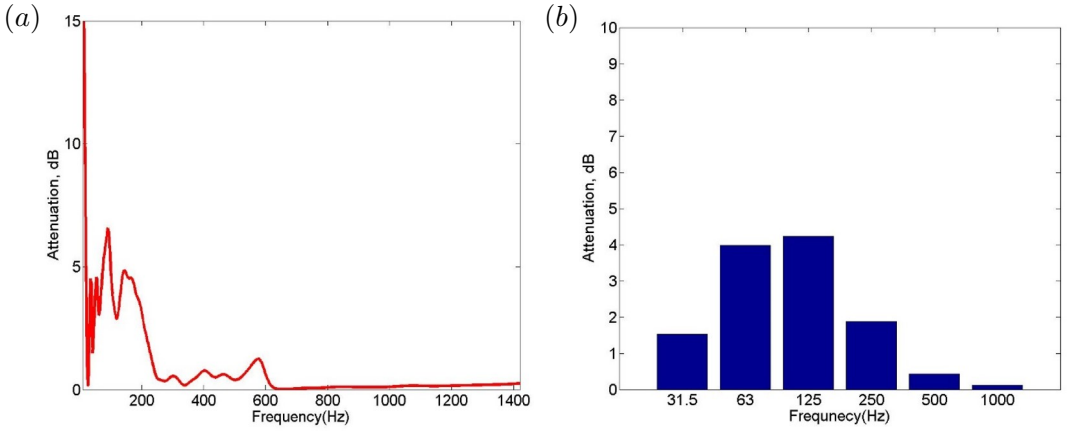

Figure 3.12: Attenuation in the sum of the diagonal elements of $\mathbf{S}_{dd}$ and $\mathbf{S}_{ee}$ at all 25 microphones when disturbance signals are driven from a single primary source, #331 at the front wall of Table 3.1 and the 25 microphones are controlled by a two channel local active control system in the reverberant field simulated by the modal model : (a) narrow band and (b) octave band

As shown in Fig. 3.11 and Fig. 3.12, a more complex performance characteristic is obtained for different frequencies, compared with the performance in the free field shown in Section 3.2. Under the free field condition, as frequency increases, the attenuation

value gradually decreases. However, under the reverberant field condition, in the 31.5 Hz octave band, very low attenuation value is obtained. This is because the secondary sources are located near the nodal line of the (1, 0, 0) mode, such that the secondary sources are not well coupled with the acoustic field and therefore poor control is achieved.

Fig. 3.13 shows contour plots which describe the attenuation performance around each position of the 25 error microphones ($= 10 \log_{10}(S_{ee}/S_{dd})$). By comparing Fig. 3.13 with Fig. 3.6, which shows the results of the attenuation performance under the free field condition, it can be seen that the distribution of the attenuation is more complicated in the reverberant case.

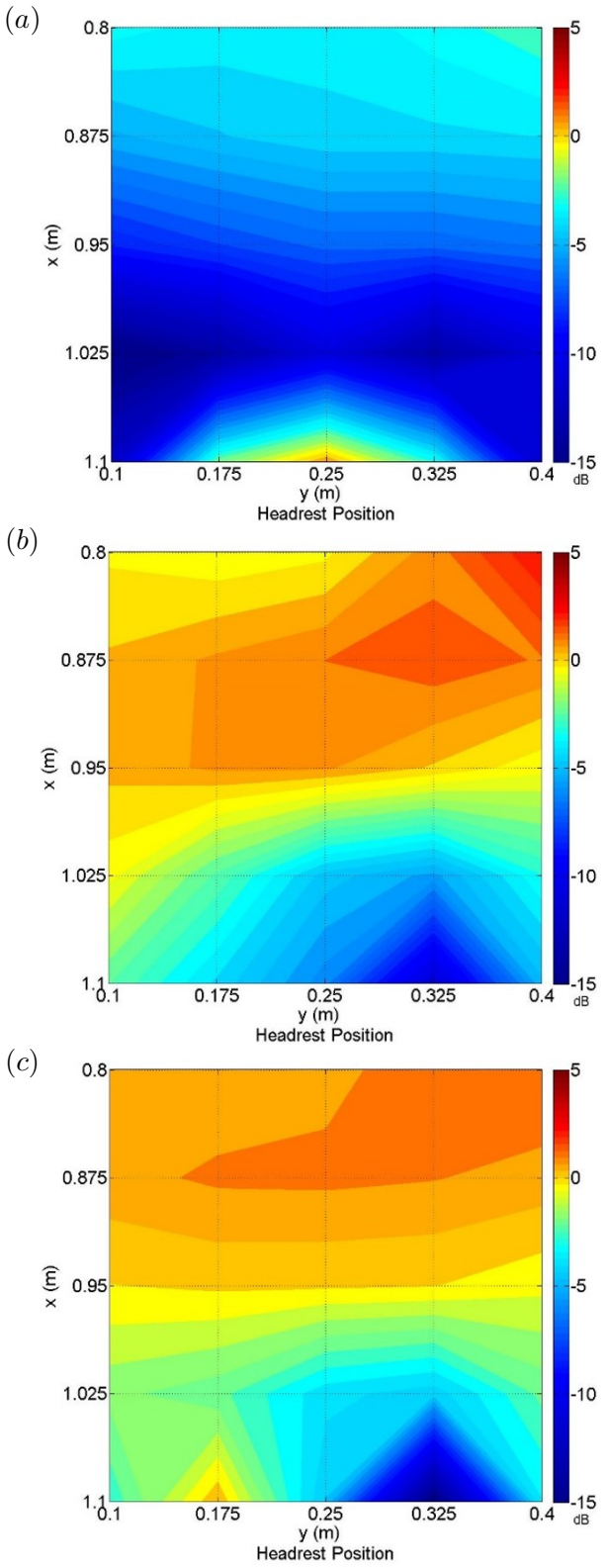

Figure 3.13: Attenuation performance ($= 10\log_{10}(S_{ee}/S_{dd})$) around 25 microphones when a two channel local active system is used to control all 25 error microphones with a single primary source, #331 at the front wall in the reverberant field simulated by the modal model : (a) 150 Hz, (b) 300 Hz, (c) 450 Hz, The 25 microphones are located at the intersections of the grid in these figures.

3.3.3 Simulations of the performance of the local active control system for different primary source positions in the reverberant enclosure

To analyse how the spatial character of the primary source affects local active control under the reverberant condition, the primary source is again located at the 4 different primary source positions as shown in Fig. 3.7. Fig. 3.14 shows the attenuation in the sum of the power spectral densities at the 25 monitoring microphones. When the primary source is located on the roof, the local active control system achieves the best performance in the first 2 octave bands. This fact may suggest that since the roof is closest to the control system, the primary sound field is dominated by the direct field of the primary source, rather than by the reverberant field and thus a more uniform sound field is produced at the monitoring region at low frequency, which makes the control more effective. In the third, fourth and fifth octave bands, the worst performance is obtained at the front and the best performance at the rear. This is similar to the free field results shown in Section 3.2, which suggests that the phase match between the primary source and the secondary source plays an import role in the performance in this frequency range.

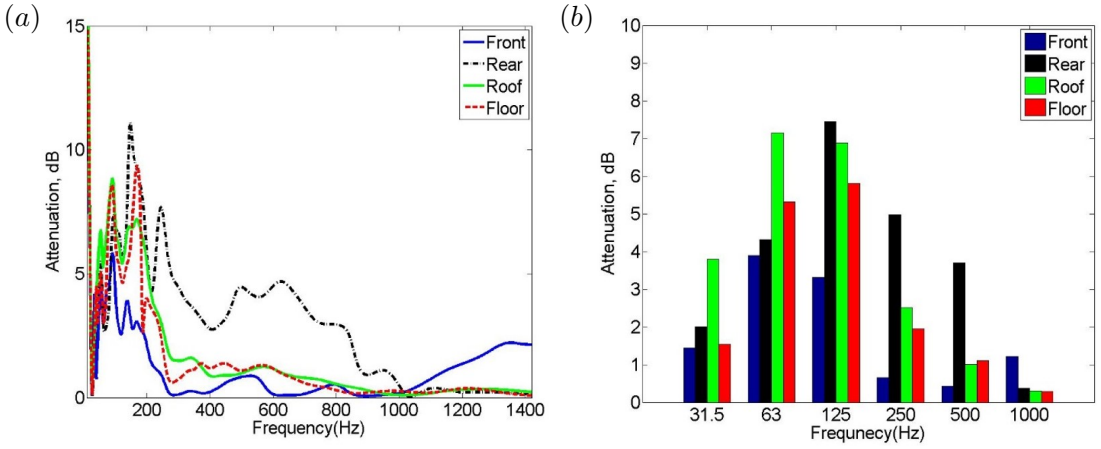

Figure 3.14: Attenuation in the sum of the diagonal elements of $\mathbf{S}_{dd}$ and $\mathbf{S}_{ee}$ at all 25 microphones when disturbance signals are driven from a single primary source among four different primary sources in Fig. 3.7 and the 25 microphones are controlled by a two channel local active control system in the reverberant field simulated by the modal model : (a) narrow band and (b) octave band

Fig. 3.15 again shows the performance for different frequencies and different primary source positions. Although the contour map in Fig. 3.15 seems to be more complex than that in Fig. 3.9 for the free field, the general trend is similar. That is, when the primary source is located in the rear areas, the attenuation is larger than when the primary is in the front area. In addition, the closer the distance between the primary source and the active headrest system, the better the attenuation that is achieved. Fig. 3.15 also shows that as frequency increases, the performance generally tends to decrease.

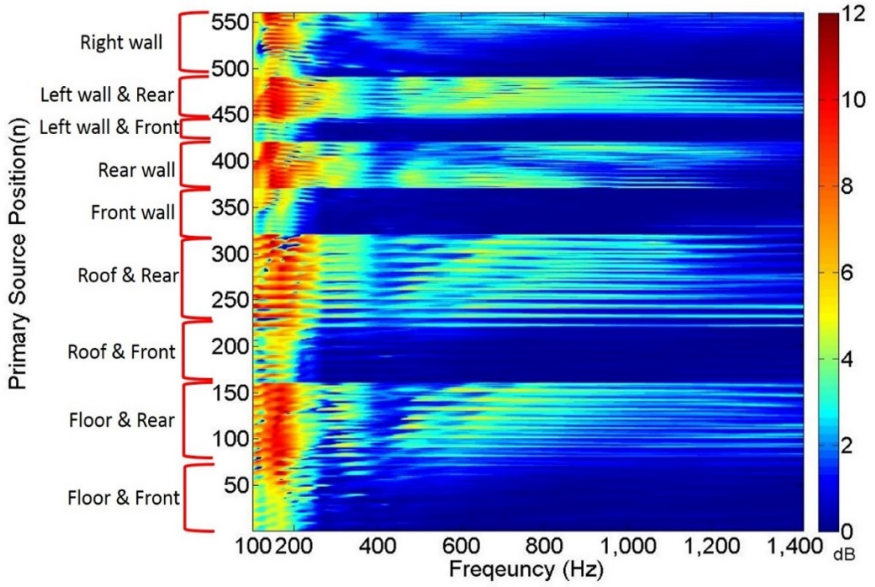

Figure 3.15: A contour map of the attenuation in the sum of the diagonal elements of $\mathbf{S}_{dd}$ and $\mathbf{S}_{ee}$ at all 25 error microphones using the two headrest secondary loudspeakers in the reverberant field simulated by the modal model as a function of frequency and the location of a single primary source, as was shown in Fig. 3.2.

3.4 Investigation of the effect of the secondary sources positions

3.4.1 Location of the error microphones and secondary sources

In the previous two sections, the effect of the active headrest system was estimated by the attenuation values of the 25 error microphones around the anticipated position of a human head. Since the region of these error microphones is relatively large, it is difficult for the active headrest system to achieve significant performance at high frequency. In this section, only eight microphones, which are closely located near the left and right ears are used as the error microphones to be controlled, as shown in Fig. 3.16.

With the error microphone array shown in Fig. 3.16(b), 5 configurations of the secondary sources are considered, as shown in Fig. 3.17 and listed in Table 3.2, to understand the effect of position on performance. The secondary source position #1 is the original position, considered in the previous sections, and, in the case of positions #3, #4 and #5, the secondary sources are located on the roof of the vehicle interior.

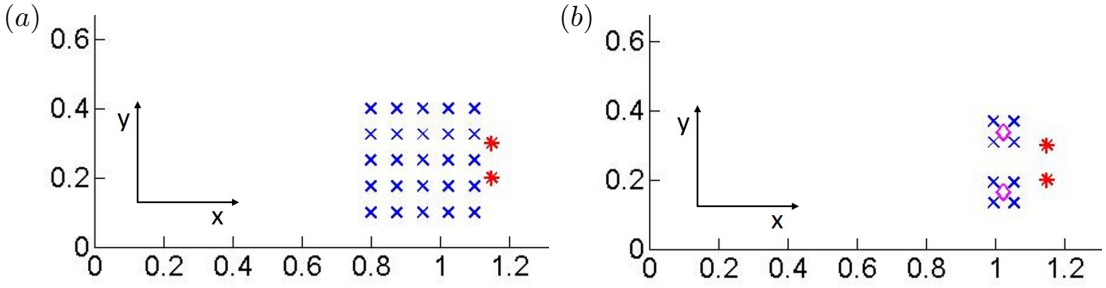

Figure 3.16: The error microphone arrays (×) to be controlled with two secondary sources (*), and left and right ear positions (♢) viewed from above, the height of all devices is 0.9 m: (a) 25 error microphones / (b) 8 error microphones around the ear positions

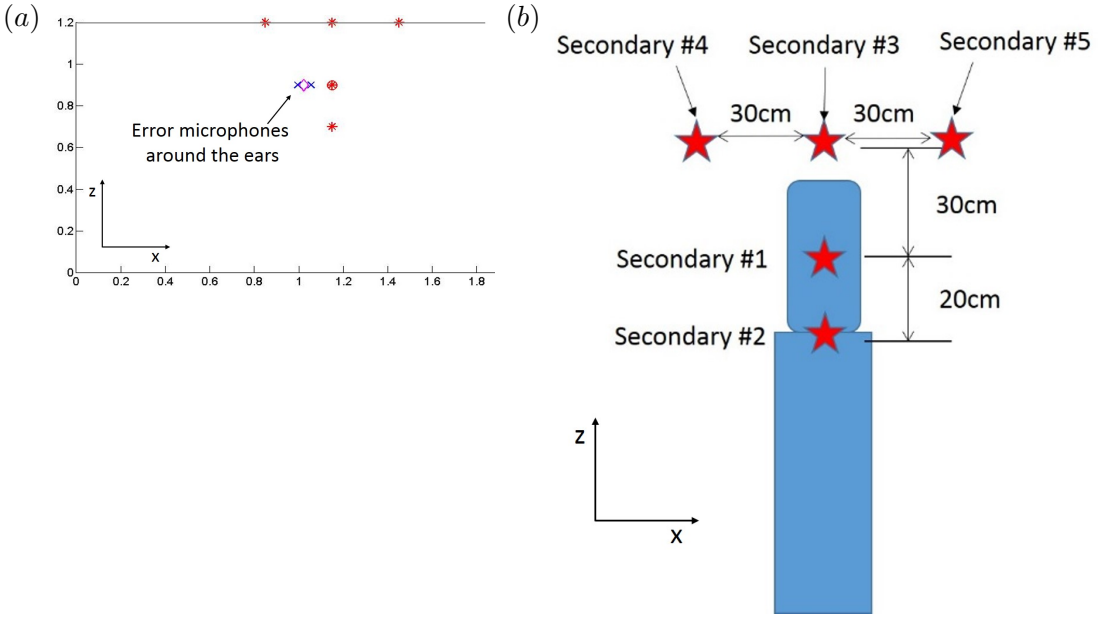

Figure 3.17: Locations of 5 different secondary source pairs (a) and the schematic design (b). Both figures are viewed from left.

Table 3.2: The coordinates of the 5 different secondary sources.

	X coordinate (m)	Y coordinate (m)	Z coordinate (m)
Secondary source #1	1.15	Left: 0.2 Right: 0.3	0.9
Secondary source #2	1.15		0.7
Secondary source #3	1.15		1.2
Secondary source #4	0.85		1.2
Secondary source #5	1.45		1.2

3.4.2 Estimation of the effect of the different secondary source positions

Based on the setup in the previous section, and the application of the modal model described in Section 3.3, the effect of the different secondary source positions on the control performance of the local active control system are calculated and shown in Fig. 3.18. In this calculation, it is assumed that the primary source #331 of the front wall is used. Fig. 3.18 shows that the attenuation value is significantly increased using only 8 error microphones, compared with the results of Section 3.3, where 25 error microphones were used covering a larger area. Fig. 3.18 also shows that the best result is obtained when the secondary sources are located at position #4. Since these secondary sources are positioned in front of the error sensors, the signals from the primary source and the secondary sources are particularly well-matched.

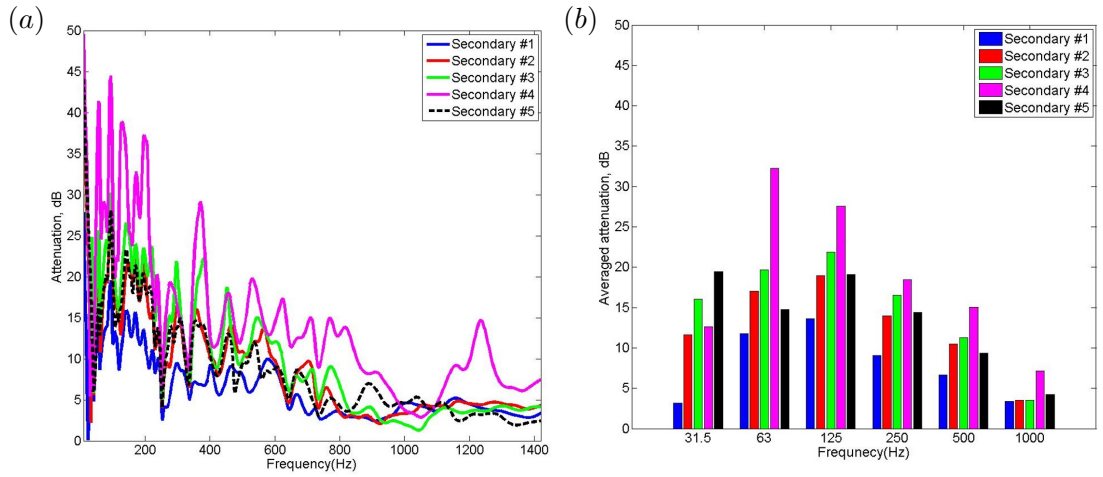

Figure 3.18: Attenuation in the sum of the diagonal elements of $\mathbf{S}_{dd}$ and $\mathbf{S}_{ee}$ at 8 microphones in Fig. 3.16(b) when disturbance signals are driven from a single primary source, #331 at the front wall of Table 3.1 and the 8 microphones are controlled by a two channel local active control system which is located at 5 different locations in Fig. 3.17 in the reverberant field simulated by the modal model : (a) narrow band and (b) octave band

For the four different primary source positions at the front, the rear, the roof and the floor, the control performance with the secondary sources at position #4 is investigated, as shown in Fig. 3.19. In this case it is found that the worst attenuation value is achieved when the primary source is located at the rear. This investigation again shows that the relative position of the primary and the secondary sources significantly affects the control performance.

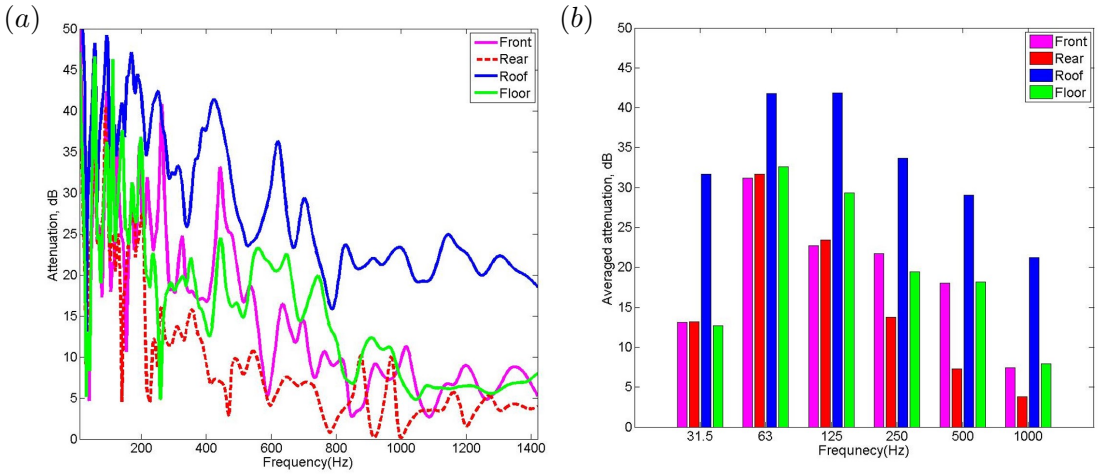

Figure 3.19: Attenuation in the sum of the diagonal elements of $\mathbf{S}_{dd}$ and $\mathbf{S}_{ee}$ at 8 microphones, using secondary source #4, when disturbance signals are driven from a single primary source among four different primary sources in Fig. 3.7 and the 8 microphones are controlled by a two channel local active control system in the reverberant field simulated by the modal model : (a) narrow band and (b) octave band

3.5 Summary

The optimal attenuation performance of a feedforward active headrest system has been studied to investigate the effects of different factors including: primary acoustic fields, geometries of the active headrest system and controlling targeted areas. By employing the theory in [46] for numerical simulations, the performance of the active headrest system has been straightforwardly estimated for the control of random noise. Measured acoustic responses in actual acoustic fields will be later utilized, with this theory, for off-line calculation of the active control performance.

Because this project focuses on controlling interior road noise in a vehicle, a rectangular enclosure with similar dimensions to those of an actual multi-purpose vehicle has been set up. It has also been assumed that primary noise sources for interior noise are distributed around the walls of the rectangular enclosure and are represented as 560 monopole sources. A hypothetical active headrest system, which has 2 secondary sources at a headrest and 25 monitoring microphones at a head position, was initially assumed to be installed at a front passenger seat. The performance of the active headrest system in a free field was initially studied. It has been shown that when the primary source is in the rear, the best attenuation is achieved and conversely, when the primary source is in the front, the worst attenuation is achieved. Therefore, it has been concluded that when pressure fields from the primary and secondary sources are well-matched, the attenuation can be significantly improved. The performance of the active headrest system has also been investigated in a reverberant field, which is modeled using a modal model. The

attenuation performance of the active control system is more complicated, compared with the results of the free field but shows similar trends. By changing the number of error microphones from 25 to 8 microphones more closely spaced around the ears, active control can be focused on smaller areas and it is shown that the best performance is obtained when the secondary sources are closest to the error microphones.

The results of this chapter help to understand the fundamental limitations of local active control in enclosures, and can be used as a guideline for the installation of the active headrest system in a vehicle. In all of these simulations the positions of the error microphones are assumed to be fixed, even though the position of the listener's head may move. In the following chapters the performance of local control systems is explored when the location of the error microphones are assumed to move with the head position.

Chapter 4

The use of head-tracking in local active sound control with physical error sensors

Although active sound control headphones, which can reduce noise levels for frequencies up to about 1 kHz, are now widely available [75, 76], their use is not convenient in many applications. Examples are when the listener is driving, or when sound control is required over long periods of time, in which case headphones can become uncomfortable. As mentioned in Chapter 3, local active control of sound is also possible using an active headrest system with loudspeakers and microphones remote from the ears [16–18, 77, 78]. However, a practical issue concerning local active control is the effect of listener head movements on the control performance. When local control is implemented around a listener's ears, head movements during control can introduce changes to the sound field and the acoustic responses, and as a result, the attenuation performance and stability of the adaptive algorithm can be reduced.

To overcome this problem, the application of a head-tracking device to local active control has been suggested [20, 26, 79]. That is, as the head-tracking device detects a change in the head position, this information can be used to update the controller using pre-calculated responses, which are required to implement an adaptive local active control system. In this chapter, a system is described in which the listener's head movements are tracked optically and this information is used by a local active control system to ensure that the attenuation performance and the stability of the active headrest system are maintained in real-time. It is assumed that the error microphones move with the position of the listener's head in this chapter, but the remote microphone technique, which does not make this assumption, will be discussed in following chapters.

In Section 4.1, a theoretical study is presented of how differences between the actual and the pre-modelled plant responses influence the stability of adaptive active control. In

Section 4.2, when a dummy head and an active headrest system are installed, the plant responses for different positions of the dummy head are measured to show changes in the plant response. In Section 4.3, when an adaptive active headrest system is used to control tonal noise, a commercial head-tracking device is applied to detect head movements and update the plant response accordingly. Finally, Section 4.4 presents the summary of this chapter.

4.1 Plant response and stability of adaptive feedforward control

In Chapter 3, the optimum steady-state filter for feedforward active control in the frequency domain is obtained as Eq. (3.3). However, in practical applications, a real-time controller is required to adapt to changes in the disturbance and reference signals and, therefore, time domain controllers are generally used. The adaptive feedforward controller has been comprehensively investigated by Elliott [55] and this section thus provides a review of the work that has been conducted about the stability of the adaptive algorithm.

For the feedforward active control algorithm in Fig. 3.1, a vector of N_x reference sensor signals in the time domain, at the nth sample time is expressed as $\boldsymbol{x}(n) = [x_1(n), x_2(n) \ \dots \ x_{N_x}(n)]^{\mathrm{T}}$ and a vector of control signals for the N_u secondary sources is $\boldsymbol{u}(n) = [u_1(n), u_2(n) \ \dots \ u_{N_u}(n)]^{\mathrm{T}}$. Therefore, the signal at the n_uth actuator from the Ith order FIR controller with coefficient $w_{n_u n_x i}$ can be expressed as

$$u_{n_u}(n) = \sum_{n_x=1}^{N_x} \sum_{i=0}^{I-1} w_{n_u n_x i} \ x_{n_x}(n-i). \tag{4.1}$$

The vectors of error signals and disturbance signals for the N_e error sensors are written as $\boldsymbol{e}(n) = [e_1(n), e_2(n) \ \dots \ e_{N_e}(n)]^{\mathrm{T}}$ and $\boldsymbol{d}(n) = [d_1(n), d_2(n) \ \dots \ d_{N_e}(n)]^{\mathrm{T}}$ respectively. After control, signals at the n_eth error microphone, $e_{n_e}(n)$ can be written as

$$e_{n_e}(n) = d_{n_e} + \sum_{n_u=1}^{N_u} \sum_{k=0}^{K-1} \sum_{n_x=1}^{N_x} \sum_{i=0}^{I-1} g_{n_e n_u k} \ w_{n_u n_x i} x_{n_x}(n-i-k), \tag{4.2}$$

where the matrix of plant responses, $\mathbf{G}(z)$, is described by the Kth order FIR filters with arbitrary accuracy and the impulse response from the n_uth secondary source to the n_eth error sensor is written as $g_{n_e n_u k}$.

When the $N_e N_u N_x$ filtered-reference signals for the error microphones are written as

$$r_{n_e n_u n_x}(n) = \sum_{k=0}^{K-1} g_{n_e n_u k}\; x_{n_x}(n-k), \tag{4.3}$$

by assuming that the plant response is linear time-invariant and that the controller filters are only slowly varying with respect to the delays in the system [55, 80], the effect of these filters on the reference signal can be transposed [55, 56]. Therefore, by substituting Eq. (4.3) into Eq. (4.2) and expressing Eq. (4.2) with the inner product, Eq. (4.2) can be written as

$$e_{n_e}(n) = d_{n_e} + \sum_{i=0}^{I-1} \boldsymbol{w}_i^{\mathrm{T}} \boldsymbol{r}_{n_e}(n-i), \tag{4.4}$$

where $\boldsymbol{w}_i = [w_{11i}\; w_{12i}\; \ldots\; w_{1N_xi}\; w_{21i}\; w_{22i}\; \ldots\; w_{N_uN_xi}]^{\mathrm{T}}$ and $\boldsymbol{r}_{n_e} = [r_{n_e11}\; r_{n_e12}\; \ldots\; r_{n_e1N_x}\; r_{n_e21}\; r_{n_e22}\; \ldots\; r_{n_eN_uN_x}]^{\mathrm{T}}$. Therefore $\boldsymbol{e}(n)$ can be expressed as

$$\boldsymbol{e}(n) = \boldsymbol{d}(n) + \boldsymbol{R}(n)\boldsymbol{w}(n), \tag{4.5}$$

where

$$\boldsymbol{R}(n) = \begin{pmatrix} \boldsymbol{r}_1^{\mathrm{T}}(n) & \boldsymbol{r}_1^{\mathrm{T}}(n-1) & \cdots & \boldsymbol{r}_1^{\mathrm{T}}(n-I+1) \\ \boldsymbol{r}_2^{\mathrm{T}}(n) & \boldsymbol{r}_2^{\mathrm{T}}(n-1) & \cdots & \boldsymbol{r}_2^{\mathrm{T}}(n-I+1) \\ \vdots & \vdots & \ddots & \vdots \\ \boldsymbol{r}_{n_e}^{\mathrm{T}}(n) & \boldsymbol{r}_{n_e}^{\mathrm{T}}(n-1) & \cdots & \boldsymbol{r}_{n_e}^{\mathrm{T}}(n-I+1) \end{pmatrix}, \tag{4.6}$$

and $\boldsymbol{w} = [\boldsymbol{w}_0^{\mathrm{T}}\; \boldsymbol{w}_1^{\mathrm{T}}\; \ldots\; \boldsymbol{w}_{I-1}^{\mathrm{T}}]^{\mathrm{T}}$ which is a $N_uN_xI \times 1$ vector of control filter coefficients.

To adapt the FIR filter coefficients of the controller, the steepest descent algorithm is widely used, which adjusts the filter coefficients in proportion to the negative of the local gradient of the cost function with respect to the filter coefficients, so that the coefficients converge towards the values that correspond to the global minimum of the cost function. Using this philosophy with the instantaneous gradient of the mean-squared error signals, the filtered-reference LMS algorithm can be defined as [55, 81–83]

$$\boldsymbol{w}(n+1) = \boldsymbol{w}(n) - \alpha \boldsymbol{R}^{\mathrm{T}}(n)\boldsymbol{e}(n). \tag{4.7}$$

where α is a convergence coefficient.

Since the true matrix of the plant responses for the filtered-reference signals cannot be perfectly obtained in practice, a matrix of estimated filtered-reference signals, $\hat{\boldsymbol{R}}(n)$,

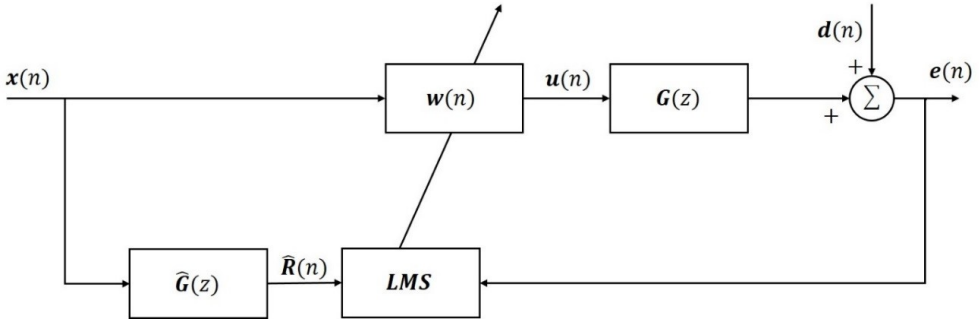

Figure 4.1: Block diagram of the practical form of the filtered-reference LMS algorithm for the feedforward active control system.

which is obtained from an estimate of the matrix of plant responses, $\hat{\mathbf{G}}(z)$, is used instead of $\boldsymbol{R}(n)$ and in this case the practical form of the filtered-reference LMS algorithm is written as

$$\boldsymbol{w}(n+1) = \boldsymbol{w}(n) - \alpha \hat{\boldsymbol{R}}^{\mathrm{T}}(n)\boldsymbol{e}(n). \tag{4.8}$$

A block diagram of the practical form of the filtered-reference LMS algorithm is shown in Fig. 4.1.

By substituting Eq. (4.5), Eq. (4.8) can be expressed as

$$\boldsymbol{w}(n+1) = \boldsymbol{w}(n) - \alpha[\ \hat{\boldsymbol{R}}^{\mathrm{T}}(n)\boldsymbol{d}(n) + \hat{\boldsymbol{R}}^{\mathrm{T}}(n)\boldsymbol{R}(n)\boldsymbol{w}(n)\ ]. \tag{4.9}$$

To converge to a set of control filter coefficients, the expectation of the term in square brackets should be equal to zero and thus at the converged state, the control filter coefficients, $\boldsymbol{w}_{\infty}$(n) can be written as

$$\boldsymbol{w}_{\infty}(n) = -\{E[\hat{\boldsymbol{R}}^{\mathrm{T}}(n)\boldsymbol{R}(n)]\}^{-1}E[\hat{\boldsymbol{R}}^{\mathrm{T}}(n)\boldsymbol{d}(n)]. \tag{4.10}$$

By subtracting Eq. (4.10) from both sides of Eq. (4.9) and again assuming that the control filter coefficients are changing slowly compared with the timescale of the filtered reference dynamics and so the variation of $\boldsymbol{w}$(n) is statistically independent of $\hat{\boldsymbol{R}}^{\mathrm{T}}(n)\boldsymbol{R}(n)$, Eq. (4.9) can be written as

$$E[\boldsymbol{w}(n+1) - \boldsymbol{w}_{\infty}] = \Big\{\boldsymbol{I} - \alpha E[\hat{\boldsymbol{R}}^{\mathrm{T}}(n)\boldsymbol{R}(n)]\Big\}E[\boldsymbol{w}(n) - \boldsymbol{w}_{\infty}]. \tag{4.11}$$

By simplifying Eq. (4.11) with the singular value decomposition [55, 84, 85],

$$\boldsymbol{v}(n+1) = \{\mathbf{I} - \alpha\boldsymbol{\Lambda}\}\boldsymbol{v}(n), \tag{4.12}$$

where $\boldsymbol{v}(n) = \boldsymbol{Q}^{\mathrm{T}} E[\boldsymbol{w}(n) - \boldsymbol{w}_{\infty}]$ and $E[\hat{\boldsymbol{R}}^{\mathrm{T}}(n)\boldsymbol{R}(n)] = \boldsymbol{Q}\boldsymbol{\Lambda}\boldsymbol{Q}^{\mathrm{T}}$ and $\boldsymbol{\Lambda}$ is a matrix that has eigenvalues of the matrix $E[\hat{\boldsymbol{R}}^{\mathrm{T}}(n)\boldsymbol{R}(n)]$ as the diagonal elements and $\boldsymbol{Q}$ is an unitary matrix which is a set of orthonormal eigenvectors of the matrix $E[\hat{\boldsymbol{R}}^{\mathrm{T}}(n)\boldsymbol{R}(n)]$. Since $\boldsymbol{\Lambda}$ is the diagonal matrix, Eq. (4.12) expresses a set of $N_u N_x I$ independent equations and the $n_u n_x i$-th independent equation can be expressed as

$$v_{n_u n_x i}(n+1) = (1 - \alpha\lambda_{n_u n_x i}) v_{n_u n_x i}(n), \tag{4.13}$$

where $\lambda_{n_u n_x i}$ is the $n_u n_x i$-th complex eigenvalue of the matrix $E[\hat{\boldsymbol{R}}^{\mathrm{T}}(n)\boldsymbol{R}(n)]$. Eq. (4.13) will converge to the optimum solution provided that

$$|1 - \alpha\lambda_{n_u n_x i}| < 1. \tag{4.14}$$

If the real and imaginary parts of $\lambda_{n_u n_x i}$ are written as $R_{n_u n_x i} + jX_{n_u n_x i}$, Eq. (4.14) can be expressed as

$$|1 - \alpha R_{n_u n_x i} + j\alpha X_{n_u n_x i}| < 1, \text{ or } (1 - \alpha R_{n_u n_x i})^2 + (\alpha X_{n_u n_x i})^2 < 1. \tag{4.15}$$

Therefore, the condition for stability is given by

$$0 < \alpha < \frac{2R_{n_u n_x i}}{R^2_{n_u n_x i} + X^2_{n_u n_x i}}. \tag{4.16}$$

For the convergence of all eigenvalues, Eq. (4.16) can be written as

$$0 < \alpha < \frac{2\mathrm{Re}(\lambda_{n_u n_x i})}{|\lambda_{n_u n_x i}|^2} \text{ for all } \lambda_{n_u n_x i}. \tag{4.17}$$

It is important to note in Eq. (4.17), when $\mathrm{Re}(\lambda_{n_u n_x i})$ has a negative value, the algorithm with any α value will not converge. Therefore, for a single tonal reference signal, the sufficient condition for the convergence at a single frequency can be written as [55, 86]

$$\mathrm{eig}[\ \hat{\mathbf{G}}^{\mathrm{H}}(e^{j\omega T})\mathbf{G}(e^{j\omega T}) + \mathbf{G}^{\mathrm{H}}(e^{j\omega T})\hat{\mathbf{G}}(e^{j\omega T})\ ] > 0 \text{ for all } \omega T, \tag{4.18}$$

where $\mathbf{G}(e^{j\omega T})$ and $\hat{\mathbf{G}}(e^{j\omega T})$ are the physical and modelled frequency responses of the plant at a single frequency. When $\mathbf{G}(e^{j\omega T})$ and $\hat{\mathbf{G}}(e^{j\omega T})$ are identical, the eigenvalues

are always positive and therefore, either uncertainty in the physical plant response or modelling errors in the modelled plant response determine the stability of the filtered-reference LMS algorithm. The stability may be improved using the leaky LMS algorithm, which is written as

$$\boldsymbol{w}(n+1) = (1-\alpha\mu)\boldsymbol{w}(n) - \alpha\hat{\boldsymbol{R}}^{\mathrm{T}}(n)\boldsymbol{e}(n), \tag{4.19}$$

where μ is a positive filter coefficient-weighting parameter. In practice, it is found that as positive values of μ are added to all the eigenvalues in Eq. (4.18), the stability of the adaptive algorithm can be improved [55].

4.2 Measurement of the plant response for different head positions within the active headrest system

When the feedforward active headrest system using the filtered-reference LMS algorithm attempts to adaptively reduce the noise at the listener's ears, excessive changes in the plant response may be produced by the displacement of the error microphones, due to movements of the listener's head, and as a result, the active headrest system may become unstable. That is, as the head position deviates from a supposed nominal position, the pre-modelled $\hat{\mathbf{G}}(e^{j\omega T})$ may become different from the physical plant response, $\mathbf{G}(e^{j\omega T})$, which varies with the head position and one of the eigenvalues in Eq. (4.18) can become negative in a specific frequency range.

To investigate the effect of changes in the plant response, the active headrest system, which has two secondary sources and two error microphones in the ears of a dummy head, was installed in a demonstration room for active noise control at ISVR, as shown in Fig. 4.2. Since the two secondary loudspeakers were located near the two error microphones in the ears of the dummy head, a matrix of plant responses is mainly dependent on the nearfield produced by the secondary loudspeakers. A reconstruction filter for the secondary loudspeakers was employed with a cut-off frequency of 1 kHz. A sample rate of 4 kHz has been used for all measurement and frequency responses are obtained up to 1 kHz. The secondary loudspeakers were driven by Gaussian white noise to measure the frequency responses. The frequency responses were obtained from the estimator, $H_1(e^{j\omega T})$, which is defined as the cross spectral density between the sensor and drive signal divided by the power spectral density of the drive signal [87]. A series of experiments was conducted when the dummy head was located at 16 possible positions on a 5×4 grid of points spaced 5 cm apart, as shown in Fig. 4.3(a), to investigate the potential changes of the plant responses when a listener's head is moved. Position #12 in Fig. 4.3(a) is considered to be the nominal position of the dummy head, i e. when the dummy head has no movement. The distances between the nominal head position and

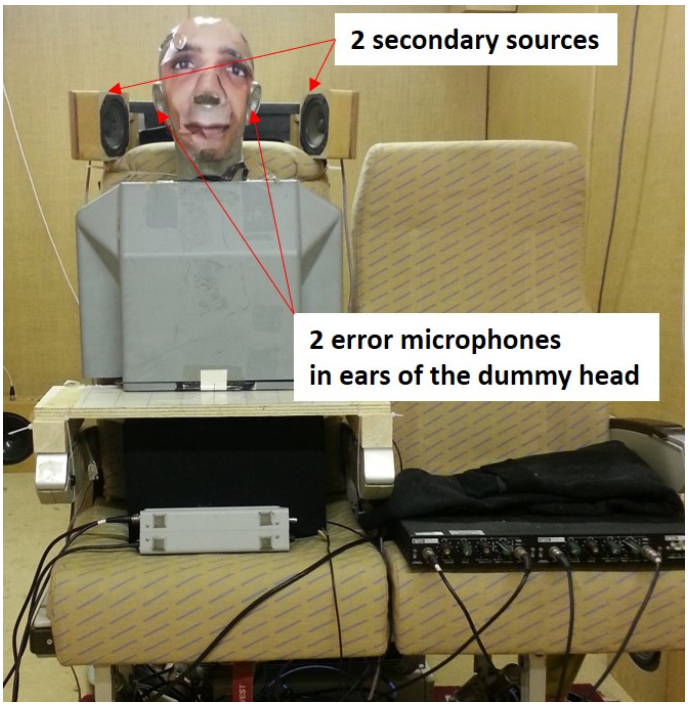

Figure 4.2: The installation of the active headrest system with the dummy head.

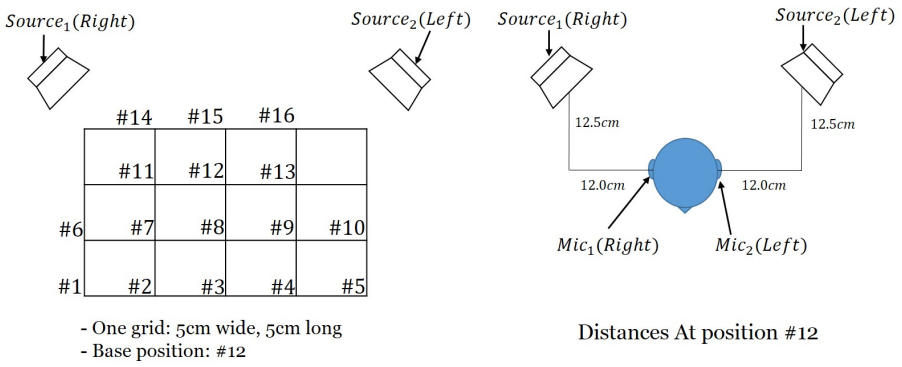

Figure 4.3: The grid of different head positions (left) and the distances between the secondary sources and the error microphones at position #12, the assumed nominal position (right).

the secondary loudspeakers are shown in Fig. 4.3(b). This installation will also be used for real-time active control in the following section. The equipment used is detailed in Appendix D.

At head position #12, the plant response and coherence measured between Mic 1 (right error micro-phone) and Mic 2 (left error microphone) and Source 1 (right secondary source) are shown in Fig. 4.4 and Fig. 4.5. Because Mic 1 is located closer to Source 1 and the dummy head blocks the sound propagation to Mic 2, the amplitude at Mic 1 is larger than that at Mic 2 and also both the amplitude and phase for Mic 1 have less variation than those for Mic 2. Fig. 4.5 shows that the coherence for both the

error microphones is almost 1 at frequencies between about 100 Hz and 1 kHz, which indicates that signals at the error microphones have linear association with the drive signals for the right secondary loudspeaker within this frequency range. The secondary loudspeaker does not operate efficiently below around 100 Hz, due to the small size of the loudspeaker and the small volume of its enclosure.

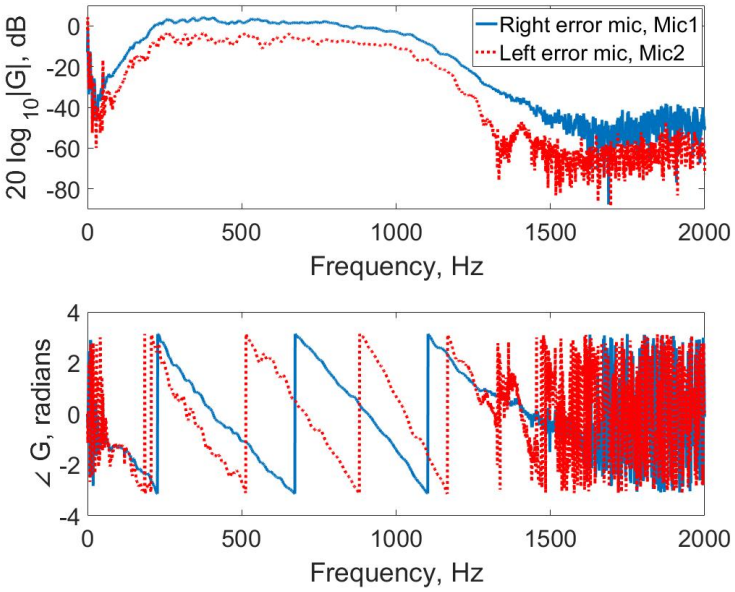

Figure 4.4: The amplitude (above) and phase (below) of the plant response between the right secondary loudspeaker and the right (solid line) and left (dashed line) error microphones at head position #12 in Fig. 4.3.

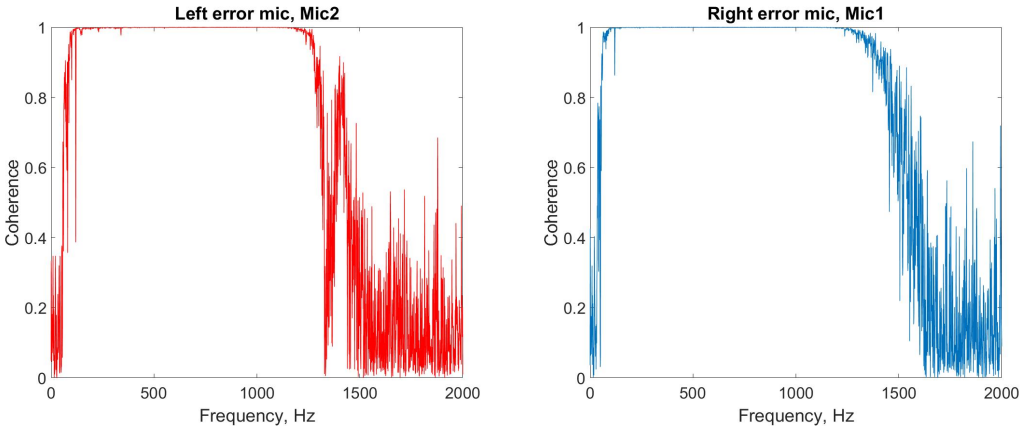

Figure 4.5: The coherence between the left error microphone, Mic 1 (left) and the right error microphone, Mic 2 (right) and Source1 (right secondary source) at head position #12 in Fig. 4.3.

When the head moves to position #5, #9 and #14 in Fig. 4.3, changes in the plant responses at Mic 1, which are defined as $\Delta G = G_{\text{moved position}} \,/\, G_{\#12}$, were measured and are shown in Fig. 4.6. The changes in the plant responses can be approximately described by the changes in the response of a monopole source in free field, as in Eq. (3.6). If the acoustic response for the nominal position #12 is defined as $Z(r_0)$, then the change in the plant response due to a variation in the head position can be predicted as

$$Z(r)/Z(r_0) = \frac{e^{-jk(r-r_0)}}{r/r_0}, \tag{4.20}$$

where r_0 is the distance between the monopole source and Mic 1 at the nominal position, position #12 and r is the distance to the moved head position. In Eq. (4.20), when the distance from the secondary source is increased as the head moves to position #5, the magnitude of $Z(r)\,/\,Z(r_0)$ is less than one and independent of frequency and the phase of $Z(r)\,/\,Z(r_0)$ decreases in proportional to the frequency. This theoretical characteristic of the monopole source is well matched with the measured data, as shown in Fig. 4.6 in the frequency range between around 100 Hz and 1,000 Hz. Changes in the response at other positions, such as position #9 and position #14, also correspond well to that of the monopole source model. However, when the dummy head is moved, changes in the plant responses at Mic 2 seem rather different, as shown in Fig. 4.7. That is, the magnitude of the changes are almost independent of the distance moved and the phase has a less linear relationship to the frequency compared to that shown in Fig. 4.6. The plant response at Mic 2 is more influenced by other effects including the scattering effect of the dummy head rather than the nearfield of the secondary source, and therefore the changes in the response at Mic 2 are not well predicted by the monopole model.

The changes in the plant responses at all 15 displaced positions are summarised in Fig. 4.8 and Fig. 4.9, which show the changes in the magnitude and phase of the plant responses as a function of $k\Delta r$ where k is the wavenumber and Δr is $r - r_0$. It can be seen that once again the phase changes are reasonably well explained by the monopole model. Fig. 4.9 shows the variation in the response to Mic 2 on this scale, which is much more random. Changes in the plant responses between Source 2 (left loudspeaker) and Mic 1 & Mic2 are symmetrically similar to the results shown above and therefore they are not described here.

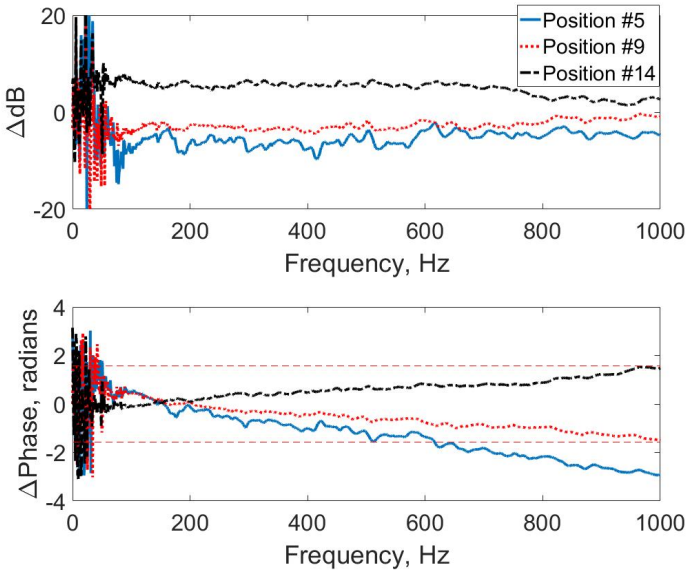

Figure 4.6: The changes in the plant response between Mic 1 and Source 1 when the head moves from position #12 to position #5, #9 and #14 in Fig. 4.3.

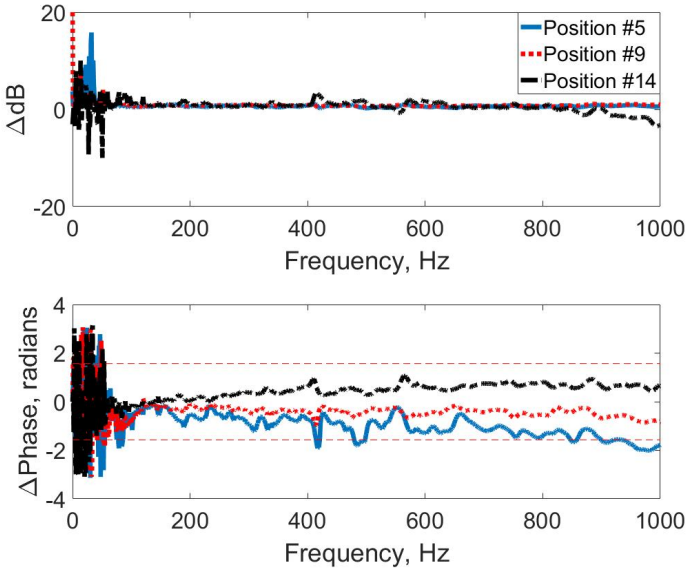

Figure 4.7: The changes in the plant responses between Mic 2 and Source 1 when the head moves from position #12 to position #5, #9 and #14 in Fig. 4.3.

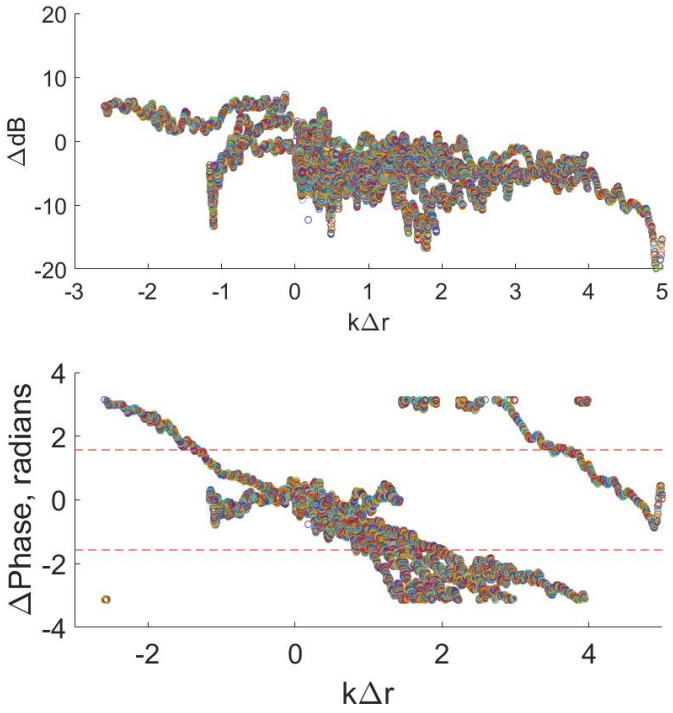

Figure 4.8: The changes in the plant responses against $k\Delta r$ between Mic 1 and Source 1 for the 15 difference positions relative to the response of position #12

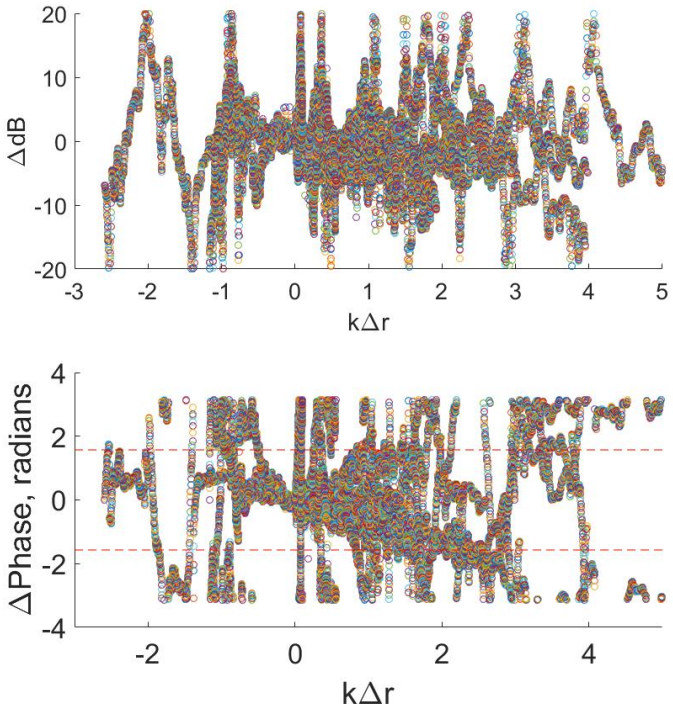

Figure 4.9: The changes in the plant responses against $k\Delta r$ between Mic 2 and Source 1 for the 15 difference positions relative to the response of position #12

4.3 Application of the head-tracking system to local active sound control

In Section 4.2, the plant responses measured at 16 different positions and the changes in these plant responses compared to the nominal position were investigated. This measured data is utilised here to assess the stability of the feedforward active headrest system in Fig. 4.2 with the filtered-reference LMS algorithm.

For a single input single output (SISO) system as a simple case, the sufficient condition for the stability, which is equivalent to Eq. (4.18), can be expressed as [55]

$$-90^\circ < \text{phase}\Big(\frac{\hat{G}(e^{j\omega T})}{G(e^{j\omega T})}\Big) < 90^\circ. \tag{4.21}$$

Therefore, when $\hat{G}(e^{j\omega T})$ is the pre-modeled plant response at the nominal position #12, and $G(e^{j\omega T})$ is the physical plant response when the head is moved to the different positions, the phase difference provides a measure of the stability of the SISO system. For instance, in Fig. 4.6, as $\pm 90^\circ$ are indicated by the red dotted lines, when the head moves to position #5, the control system would become unstable for frequencies above about 600 Hz and when the head moves to either position #9 or #14, the control system would become unstable from around 1 kHz.

For the MIMO system with the two secondary loudspeakers, the eigenvalue stability condition given by Eq. (4.18) is assessed for the 15 moved positions and the results are shown in Fig. 4.10. Although the real parts of both eigenvalues remain positive up to 1 kHz when the head is moved to position #8, 5 cm from the nominal position, it is clear that the real part of one of the eigen values becomes negative above 600 Hz at position #1, which is 14 cm from the nominal position, indicating that the active headrest system is expected to become unstable above this frequency. Similarly at position #2, the stability limit is about 672 Hz.

To ensure the stability of the control system with head movements, a head tracking system is suggested to update the plant response as the head moves, as shown in Fig. 4.11. The head tracker can give location information in order for an active control system to select an appropriate plant response from a look-up table of the pre-modelled plant responses and thus the controller could be adapted with suitable filtered-reference signals. To verify this strategy, a commercial tracking system, the Microsoft Kinect, was used as the head tracker. The Kinect is positioned in front of the active headrest system, as shown in Fig. 4.12. During real-time control, the head tracker is used to measure the head position, 30 times per seconds, and the closest pre-calculated head position is identified. The information from the Kinect was decoded in real-time using plug-in software implemented in MaxMSP and this was passed to a dSPACE-based adaptive

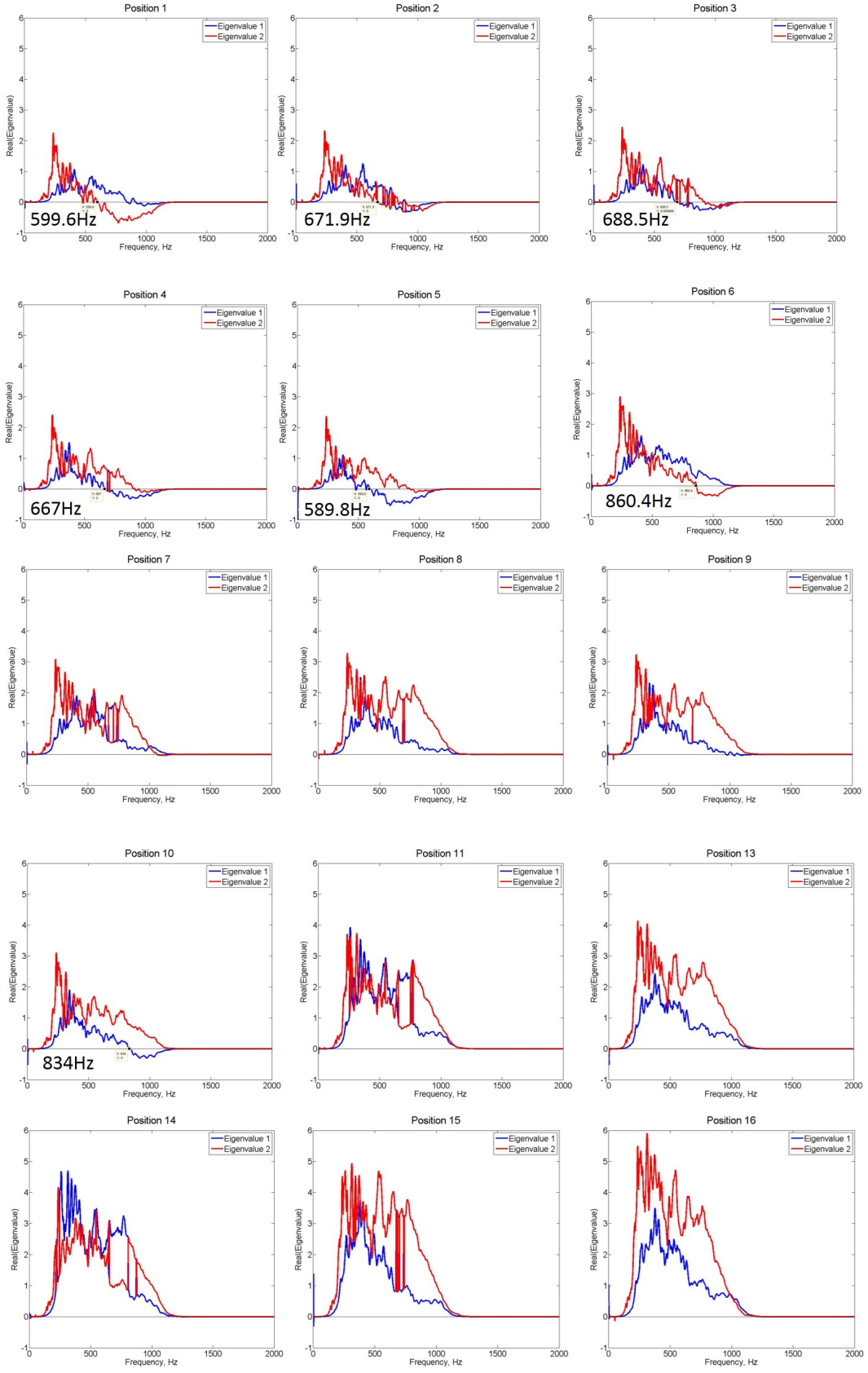

Figure 4.10: Eigenvalues of [$\hat{\mathbf{G}}^H(e^{j\omega T})\mathbf{G}(e^{j\omega T}) + \mathbf{G}^H(e^{j\omega T})\hat{\mathbf{G}}(e^{j\omega T})$] of the MIMO system for different 15 positions, with respect to the nominal position #12 in Fig. 4.3.

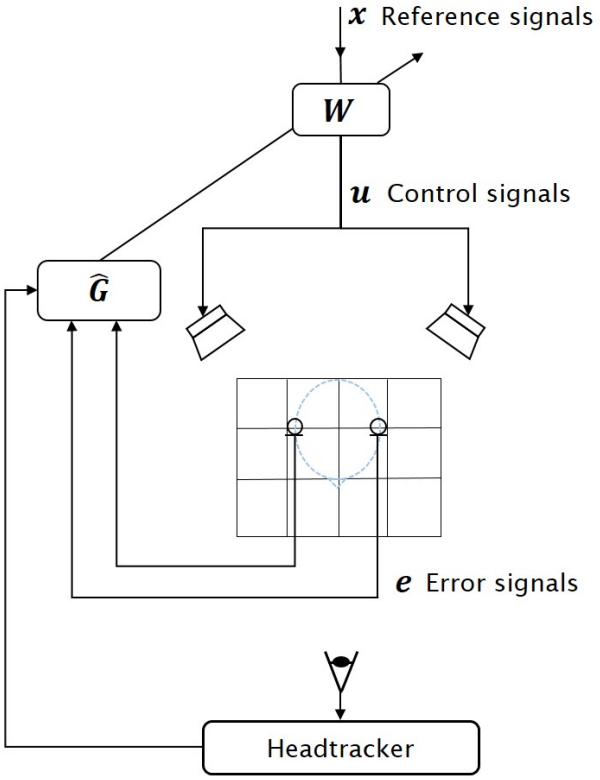

Figure 4.11: The use of a tracker to determine the position of the head in a local active sound control system and hence update the estimate of the plant response, $\hat{\mathbf{G}}(z)$, between the secondary loudspeakers and error microphones.

controller, which already had stored in it the various plant responses for the 16 head positions. A single primary source was installed behind the active headrest system and driven by a single frequency signal. Since tonal disturbances are being controlled, external reference sensors are not required in this system as the reference is obtained directly from the tonal generator. The equipment used in this set of experiments is detailed in Appendix D.

The performance of the active headrest system using the head tracker was tested with a human listener moving their head within the area defined by the grid above, when they were wearing in-ear microphones acting as the error sensors in this control system, as shown in Fig. 4.13(a). Fig. 4.13(b) shows the time history of the error signal, measured in the right ear of the subject, during the course of a tracking experiment. In the first time interval, from 0 to 5 seconds, only the single frequency disturbance at 650 Hz from the primary source is measured, without control. In the second time interval, from 5 to 14 seconds, the active control system is turned on and the error signal is reduced. In the third time interval, from 14 to 22 seconds, the listener starts to move with the head tracking off, until the control system becomes unstable, approximately when it reaches position #3 in Fig. 4.3. From the analysis of the eigenvalues of the plant response in Fig. 4.10, it is predicted that when the dummy head is moved to position #3 without

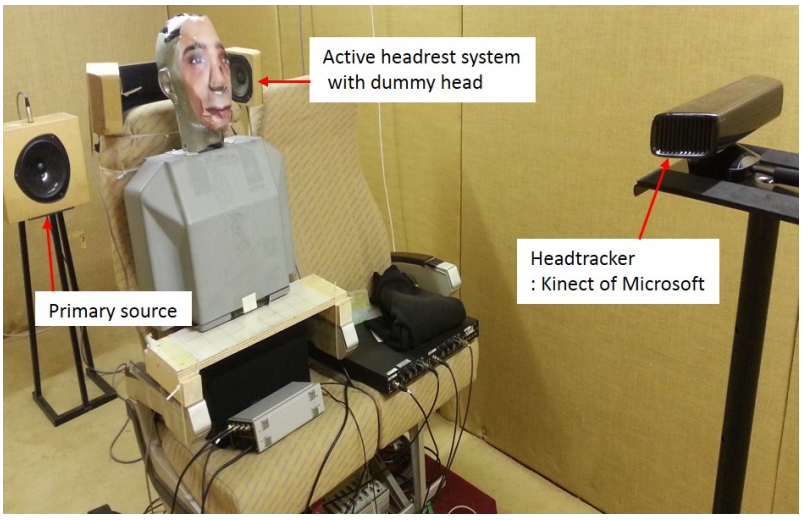

Figure 4.12: The installation of the active headrest system with the head tracker.

headtracking, the active headrest system becomes unstable at around 690 Hz. In the final step, the head tracker is turned on and rapidly acquires the current head position and corrects the estimate of the plant response, so that the active control system again becomes stable and reduces the disturbance signals.

The main objective of this experiment is to demonstrate the capacity for head tracking to improve the stability of active sound control, and so these initial experiments are deliberately rather idealised. In a number of possible practical applications for such a local active system, several issues may need to be addressed, which are not considered in detail in this chapter. The most significant assumption is that the listener is prepared to wear microphones in their ears, and the use of remotely installed microphones to avoid this is discussed in the following chapters. In addition there are a number of issues whose solutions are likely to be rather application-specific. In particular, the head tracking has been achieved here using a commercial system and we have only tracked the translational motion of the head due to the limitations of time. In practice the head will probably have rotational as well as translational motion, which will also need to be tracked.

The control filters have to adapt when there is a change in the head position. The time taken for the head tracker to acquire a new position is about 1/30 second [88]. This was significantly greater than the adaptation time of the filter used to control tonal sound in this chapter, which had a sample frequency of 4 kHz. Actual head movements of a listener in a vehicle cabin is investigated in Appendix F. Therefore, although the speed of the head tracking system may be important in following rapid head movement in some applications, an active headrest system with a headtracker still appears to be practicable to reduce interior noise inside a vehicle during normal operating conditions.

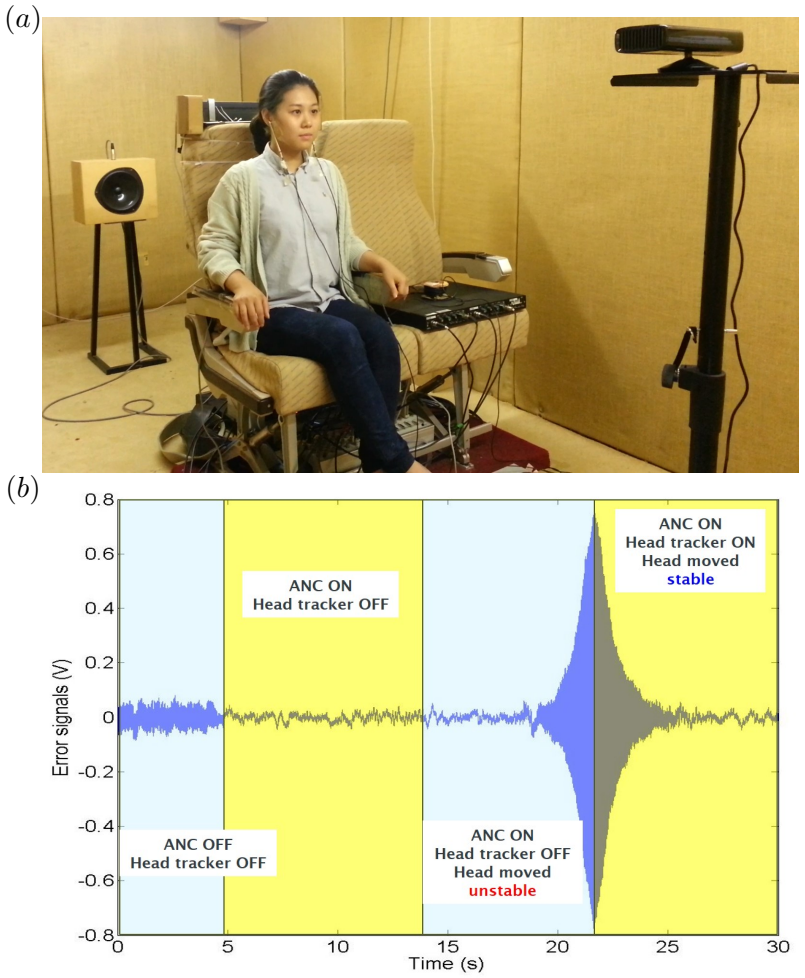

Figure 4.13: Active control of an active headrest system combined with a head tracker with a human listener for reducing 650 Hz tonal disturbance signals in real-time: (a) The test installation, in which the participant has two physical error microphones in their ears for evaluation purposes and (b) the measured signals at the right of these error microphones during active control and head-tracking.

4.4 Summary

This chapter has verified how a head tracker can improve the stability of an adaptive local active control system. The sufficient condition for the filtered-reference LMS algorithm depends on the difference between the pre-modelled and physical plant response. The plant response matrix has been measured when the error microphones in a dummy head are installed in an active headrest system and moved to 16 different positions on the seat. The changes in the plant response between the right error microphone and the right secondary source are similar to those of a monopole source but the response to the left error microphone is more random, due to the scattering effect of the dummy head. When the dummy head is moved too far from the nominal head position, negative real eigenvalues are generated. For instance, when the dummy head has been moved by 14

cm to position #1 in Fig. 4.3, the real parts of the eigenvalues become negative from around 600 Hz.

To prevent the divergence of the adaptive active headrest system, a head-tracking system has been applied. The head-tracking system detects the moved head position and this information is used to update a plant response matrix. The test result with a human listener has shown that when a single primary source produces a 650 Hz tonal noise, a diverging adaptive active system becomes stable when the plant response matrix is updated. This result agrees reasonably well with what is observed in the analysis of the eigenvalues.

The changes in the plant responses at the different positions suggest that to ensure stability and to increase the attenuation performance of the active headrest system at the occupant's ears, the plant response should be updated depending on the head position. In order to avoid the need to have error microphones in the listener's ears, Chapter 5 will consider the estimation of the error signals at the ears using the remote microphone technique. In Chapter 6 and Chapter 7 the head tracking system will be combined with the remote microphone technique for spatially moving virtual error microphones.

Chapter 5

Nearfield estimation using the remote microphone technique

An estimate of the error signals in the desired control regions is required to adapt a local active control system. However, the direct installation of error sensors in the desired positions significantly limits the practical application of active headrest systems. For example, passengers in a car are unlikely to accept the need to wear in-ear microphones over long periods of time for local active control. The zone of quiet around a fixed error sensor, within which more than 10 dB of attenuation is achieved, is also limited to a diameter of about 1/10 of an acoustic wavelength in a single frequency diffuse field, which is about 3.4 cm at 1 kHz [43]. Therefore, any separation between the positions of the error sensors and the targeted control regions can lead to the zone of quiet being outside of the desired region of control, and the noise at the ears may even be enhanced due to the constructive interference between the disturbance and control signals.

A wide variety of virtual sensing algorithms [72, 79, 89–91] have been proposed to overcome this problem, by estimating the pressures that would be measured at microphones located in the control-targeted regions, which are referred to as virtual error sensors, from remotely installed physical sensors, which are referred to as monitoring sensors. The first of these algorithms, called the virtual microphone arrangement, assumed that the disturbance signal at the virtual error sensors was equal to that at the monitoring microphones [72], but a later technique, called the remote microphone technique [89], applies a specific filter, called the observation filter here, to estimate the disturbance signals at the virtual error sensors by filtering the disturbance signals at the monitoring sensors. This chapter considers the remote microphone technique, with an observation filter calculated using the least-squares method, when different arrays of monitoring microphones are used in different sound fields, since the accuracy of the nearfield estimation is mainly determined by the spatial properties of the primary acoustic field.

In Section 5.1, previous research about the virtual sensing algorithms is reviewed and the optimal observation filter for the remote microphone technique is formulated in the frequency domain. Section 5.2 describes the results of numerical simulations of nearfield estimation, with either a single or multiple monitoring sensors, in a single frequency diffuse field. Section 5.2 also presents simulation results for the remote microphone technique in a free field. The effects of using the remote microphone technique in practical acoustic fields in an anechoic chamber are considered in Section 5.3. Loudspeakers are used to generate primary sources and a number of microphones are installed around an active headrest system with a dummy head. The observation filters are then calculated from measured acoustic transfer responses and the accuracy of the nearfield estimation can be estimated. Appendix C reports a similar study, with the active headrest installed in a more reverberant room. Finally, Section 5.4 presents the summary of this chapter.

5.1 Virtual sensing algorithms for local active sound control

In this section, several virtual sensing algorithms are reviewed, all of which estimate the error signal at the virtual error sensor. In particular, the optimal observation filter for the remote microphone technique is formulated in the frequency domain. The disturbances are assumed to be random and stationary and can thus be described by their power and cross spectral densities. If the disturbances are broadband random, the causality of an observation filter needs to be considered and the corresponding formulation in the time domain will be considered in chapter 7. However, if the disturbance signals have a narrowband spectrum, the frequency domain formulation can be applied without the causality constraint. The formulation of the observation filter in the frequency domain can provide an efficient tool to investigate the nearfield estimation performance of different sensor geometries for various acoustic fields using either a numerical model of the acoustic field or measurements in a practical arrangement.

5.1.1 A review of virtual sensing algorithms

Virtual sensing algorithms have been extensively investigated to overcome the limitations of positioning a physical error sensor at a desired cancellation position [19, 72, 79, 89–93]. The virtual error sensing can be conceptually distinguished from the physical error sensing as shown in Fig. 5.1. If control is only achieved at the physical sensor, the sound at the ears of the listener may not be reduced. Therefore, when the physical error microphones cannot be located at the targeted cancellation positions, the estimation of the error signals at the virtual error sensors remotely installed from the physical monitoring sensors is necessary.

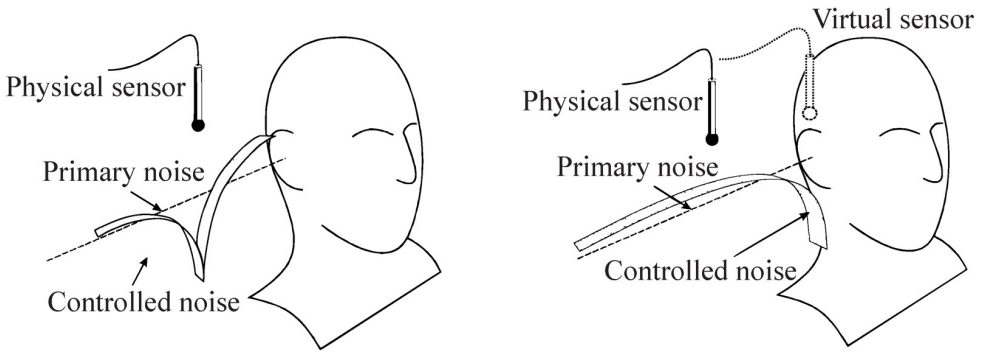

Figure 5.1: The concepts of the physical error sensing (left) and the virtual error sensing (right). [79]

The virtual microphone arrangement, [18, 72, 77], assumes that the disturbance signals at the virtual error sensors are almost equal to those at the monitoring sensors although the plant responses from the secondary sources to the monitoring and virtual sensors are significantly different due to the nearfield of the secondary sources. With this assumption, Garcia-Bonito *et al.* [72] have shown, in the context of the attenuation performance of an active headrest system in a diffuse sound field, that at frequencies, below about 500 Hz, the attenuation performance achieved using the virtual microphone arrangement is comparable to that achieved when error signals at the ears of a dummy head are used directly, since the primary acoustic fields at the virtual and monitoring sensors are similar. At frequencies from 500 Hz to 1 kHz, however, there is a substantial difference between the primary acoustic fields at the virtual and monitoring sensors and this limits the attenuation performance achieved with the virtual microphone arrangement.

The forward difference extrapolation technique has been suggested for virtual sensing in [90, 94]. In the forward difference extrapolation technique, pressure and pressure gradient at the virtual error sensor are estimated by fitting a spatial polynomial to the signals measured at a number of monitoring sensors. This technique has several advantages over other virtual sensing algorithms. Firstly, it is not required to assume equal disturbance signals at the virtual error and monitoring microphones. Moreover, a fixed gain prediction allows the nearfield estimation to be more robust to any physical system changes and the observation filter is not required to be modelled. However, the estimation accuracy is limited to low frequencies, for which the distance between the virtual and monitoring sensors is smaller than the wavelength. Although higher-order finite difference estimation is used to improve the prediction accuracy of this algorithm, the accuracy of this higher-order estimation was found to be degraded by sensitivity and phase mismatches and relative position errors between microphones [94, 95]. Kestell *et al.* [94] have shown that when a single source is used to reduce a 400 Hz sinusoidal noise from a single primary source in an anechoic chamber, 10 dB of attenuation is achieved at a desired position which is separated 10 cm from a single monitoring microphone by using the first-order estimation. However, with the second-order estimation,

no improvement in attenuation is produced compared to results obtained from the conventional control without the virtual sensing algorithm, because the accuracy of the second-order estimation is very sensitive to spatial uncertainty.

The Kalman filtering virtual sensing method [19, 91, 96] uses Kalman filtering theory to model an active control system as a state-space system. A Kalman filter is formulated to calculate estimates of the plant states and the nearfield estimation can include a known or measured noise covariance on the sensors. However, this method is only suitable for systems of relatively low order. To demonstrate the performance of this method, real-time feedforward experiments have been conducted to reduce broadband random noise between 50 and 500 Hz in an acoustic duct [91]. The state space model was first modelled using the preliminary measurement and the filtered-x LMS algorithm with the Kalman filtering virtual sensing method achieved an overall attenuation of 19.7 dB at the virtual microphone.

5.1.2 The remote microphone technique

The remote microphone technique was initially suggested by Roure and Albarrazin [89] and has also been widely investigated in the literature [46, 79, 97–100]. To overcome the limitation of the virtual microphone arrangement at higher frequencies, the remote microphone technique applies the observation filter to estimate the disturbance signals at the virtual error sensors by optimally weighting the disturbance signals at the monitoring sensors. In a preliminary identification stage, physical error sensors are typically installed at the positions of the virtual error sensors and the disturbance signals are simultaneously measured at both the error sensors and monitoring sensors. From these signals, the observation filter can be designed in either the frequency or time domain [46, 79, 101]. After this initial training, the physical error sensors can be removed and the disturbance signals at the virtual error sensors are estimated by filtering the disturbance signals at the monitoring sensors with the observation filter. The attenuation performance of an active headrest system using either the virtual microphone arrangement or the remote microphone technique has been compared by Das *et al.* [97] who showed that about 20 dB more reduction is achieved with the remote microphone technique, compared with the virtual microphone arrangement, with a tonal primary noise with a frequency of around 196 Hz and a feedback active headrest system. Although a relatively low frequency tonal noise was controlled in this study, it was clear that a more accurate estimation of the virtual error signals, using the remote microphone technique, can significantly improve the attenuation performance because the feedback control system is particularly affected by inaccurate error signals. The accuracy of the remote microphone technique depends on the spatial properties of the primary acoustic field, however, and this needs to be investigated to determine the attenuation performance of the active control system in different applications.

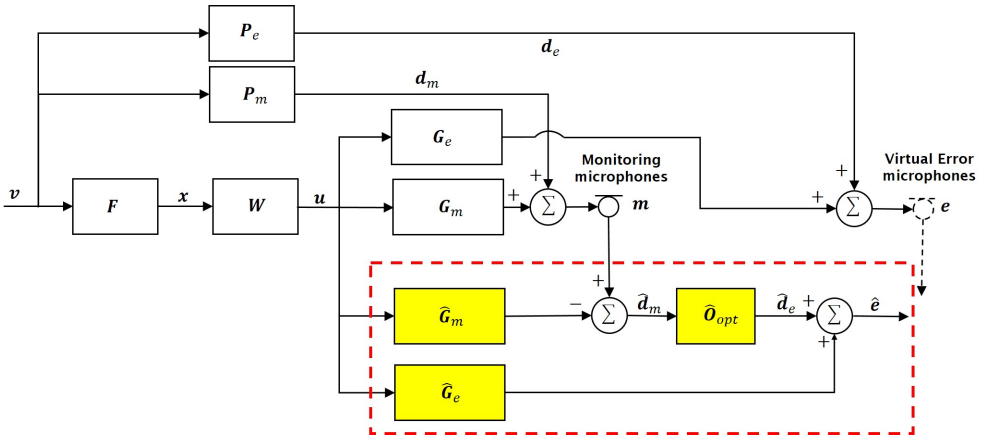

Figure 5.2: Block diagram of the feedforward active control algorithm, combined with the standard remote microphone technique in a dashed rectangle.

The remote microphone technique, which estimates virtual error signals from the signals measured at the remote monitoring microphones, can be combined with a feedforward active control system, as shown in Fig. 5.2 [23, 79]. The N_v primary sources, which for random disturbances have a vector of complex source strengths in a single frequency bin of $\mathbf{v} = [v_1, v_2 \ \dots \ v_{N_v}]^{\mathrm{T}}$, produce a vector of N_e complex disturbance signals, $\mathbf{d}_e = [d_{e1}, d_{e2} \ \dots \ d_{eN_e}]^{\mathrm{T}}$ at the virtual error microphones and a vector of N_x reference signals, $\mathbf{x} = [x_1, x_2 \ \dots \ x_{N_x}]^{\mathrm{T}}$ at the reference microphones via the matrices of transfer responses $\mathbf{P}_e$ and $\mathbf{F}$, respectively. The reference signals drive the matrix of control filters, $\mathbf{W}$, to produce a vector of N_u control signals, $\mathbf{u} = [u_1, u_2 \ \dots \ u_{N_u}]^{\mathrm{T}}$, which are transmitted to the virtual error microphones, via the matrix of complex plant responses, $\mathbf{G}_e$, to minimise these disturbance signals. The vector of complex error signals, $\mathbf{e}$, at the virtual error microphones after control can thus be defined as

$$\mathbf{e} = \mathbf{d}_e + \mathbf{G}_e\mathbf{u} = \mathbf{d}_e + \mathbf{G}_e\mathbf{W}\mathbf{x} = \mathbf{P}_e\mathbf{v} + \mathbf{G}_e\mathbf{W}\mathbf{F}\mathbf{v}, \tag{5.1}$$

where the dependence on frequency of all of these signals and responses has been suppressed for notational convenience. Any feedback from the secondary sources to the reference sensors is assumed to be negligible, which can be ensured through the use of feedback cancellation filters for example. When the direct measurement of the virtual error signals, $\mathbf{e}$, is infeasible, they can be estimated from the N_m complex monitoring microphone signals, $\mathbf{m} = [m_1, m_2 \ \dots \ m_{N_m}]^{\mathrm{T}}$, which are equal to

$$\mathbf{m} = \mathbf{d}_m + \mathbf{G}_m\mathbf{u} = \mathbf{d}_m + \mathbf{G}_m\mathbf{W}\mathbf{x} = \mathbf{P}_m\mathbf{v} + \mathbf{G}_m\mathbf{W}\mathbf{F}\mathbf{v}, \tag{5.2}$$

where $\mathbf{d}_m = [d_{m1}, d_{m2} \ \dots \ d_{mN_m}]^{\mathrm{T}}$ is a vector of disturbance signals measured at the monitoring microphones and $\mathbf{G}_m$ is the matrix of plant responses between the secondary

sources and the monitoring microphones. In practice, true matrices of plant responses, $\mathbf{G}_e$ and $\mathbf{G}_m$ are not usually available and therefore estimates of the plant responses are used in the controller, as denoted by $\hat{\mathbf{G}}_e$ and $\hat{\mathbf{G}}_m$. Similarly $\mathbf{d}_m$ and $\mathbf{d}_e$ are estimated in practice as $\hat{\mathbf{d}}_m$ and $\hat{\mathbf{d}}_e$.

If $\hat{\mathbf{O}}$ is the estimated observation filter used to calculate $\hat{\mathbf{d}}_e$ from $\hat{\mathbf{d}}_m$, the estimated error signals, $\hat{\mathbf{e}}$, at the virtual error microphones can be written as

$$\hat{\mathbf{e}} = \hat{\mathbf{d}}_e + \hat{\mathbf{G}}_e\mathbf{u} = \hat{\mathbf{O}}\hat{\mathbf{d}}_m + \hat{\mathbf{G}}_e\mathbf{u} = \hat{\mathbf{O}}(\mathbf{m} - \hat{\mathbf{G}}_m\mathbf{u}) + \hat{\mathbf{G}}_e\mathbf{u}. \tag{5.3}$$

The observation filter in Eq. (5.3) will influence how accurately $\hat{\mathbf{d}}_e$ is estimated, and the estimation error between $\hat{\mathbf{d}}_e$ and $\mathbf{d}_e$ is an important factor in determining the performance of the control system. The optimal observation filter, $\mathbf{O}_{\text{opt}}$, can be derived by minimising the mean squared estimation error between $\mathbf{d}_e$ and $\hat{\mathbf{d}}_e$. In practice, however, it is also necessary to include a term in the cost function that is proportional to the mean squared magnitude of all the coefficients in the observation filter, to improve the robustness of this filter. If $\mathbf{d}_e$ and $\mathbf{d}_m$ are measured in preliminary experiments before active control, so that in this case $\mathbf{d}_m$ is known, $\mathbf{O}_{\text{opt}}$ can be obtained by minimising the cost function [46],

$$J_2 = \text{trace}\Big\{ E\left[(\mathbf{d}_e - \mathbf{O}\mathbf{d}_m)(\mathbf{d}_e - \mathbf{O}\mathbf{d}_m)^{\text{H}} + \beta\ \mathbf{O}\mathbf{O}^{\text{H}}\right] \Big\} \tag{5.4a}$$

$$= \text{trace}\Big\{ \mathbf{S}_{d_e d_e} - \mathbf{S}_{d_m d_e}\mathbf{O}^{\text{H}} - \mathbf{O}\mathbf{S}_{d_m d_e}^{\text{H}} + \mathbf{O}(\mathbf{S}_{d_m d_m} + \beta\mathbf{I})\mathbf{O}^{\text{H}} \Big\}, \tag{5.4b}$$

where $E[\,]$ is the expectation operator, $^{\text{H}}$ is the Hermitian or complex conjugate transpose and β is a positive real regularising parameter, $\mathbf{I}$ is the identity matrix, $\mathbf{S}_{d_e d_e} = E[\mathbf{d}_e\mathbf{d}_e^{\text{H}}]$ and $\mathbf{S}_{d_m d_m} = E[\mathbf{d}_m\mathbf{d}_m^{\text{H}}]$ are the power spectral density matrices for $\mathbf{d}_e$ and $\mathbf{d}_m$ respectively, and $\mathbf{S}_{d_m d_e} = E[\mathbf{d}_e\mathbf{d}_m^{\text{H}}]$ is the cross spectral density matrix between $\mathbf{d}_m$ and $\mathbf{d}_e$. In a stationary random sound field, when the number of monitoring microphones (N_m) is larger than the number of error microphones (N_e), the problem of minimising Eq. (5.4) is mathematically overdetermined. The term, $\beta\ \mathbf{O}\mathbf{O}^{\text{H}}$, in Eq. (5.4a) always ensures that the matrix, $\mathbf{S}_{d_m d_m} + \beta\mathbf{I}$, in Eq. (5.4b) is positive definite, and hence invertible. As a result, the cost function J_2, which is a quadratic function of the real and imaginary parts of each element in $\mathbf{O}$, has a unique minimum value. The optimal value, $\mathbf{O}_{\text{opt}}$, is derived in Appendix A to give

$$\mathbf{O}_{\text{opt}} = \mathbf{S}_{d_m d_e}(\mathbf{S}_{d_m d_m} + \beta\mathbf{I})^{-1} = \mathbf{P}_e\mathbf{S}_{vv}\mathbf{P}_m^{\text{H}}(\mathbf{P}_m\mathbf{S}_{vv}\mathbf{P}_m^{\text{H}} + \beta\mathbf{I})^{-1}, \tag{5.5a,b}$$

where $\mathbf{S}_{vv}$ is the power spectral density matrix of the primary source strengths, $\mathbf{v}$, and $\mathbf{P}_e$ and $\mathbf{P}_m$ are the matrices of acoustical transfer responses from the primary sources to the error microphones and monitoring microphones respectively, as shown in Fig. 5.2. When practical estimates of $\mathbf{P}_e$ and $\mathbf{P}_m$ are used to calculate the observation filter in Eq. (5.5b), this is denoted $\hat{\mathbf{O}}_{\text{opt}}$, as used in Eq. (5.3).

Although the term, $\mathbf{S}_{d_m d_m} + \beta\mathbf{I}$ in Eq. (5.5a) is positive definite, it can be ill-conditioned, so that $\mathbf{O}_{\text{opt}}$ is sensitive to both physical and numerical uncertainties. A reduction in the condition number can be obtained by the appropriate selection of the regularisation factor, β. As β increases, the solution for the optimal observation filter becomes more robust to practical uncertainties [102], but an excessively large regularisation factor can produce a biased solution, with a higher estimation error. Therefore, to select an appropriate regularisation factor, it is necessary to consider the trade-off between the robustness and the accuracy with which $\hat{\mathbf{d}}_e$ estimates $\mathbf{d}_e$.

The normalised mean squared estimation error level at the virtual microphone, L_ϵ, can be defined as

$$L_\epsilon = 10 \log_{10} \left| \frac{S_{\epsilon\epsilon}}{S_{d_e d_e}} \right|, \tag{5.6}$$

where ϵ is defined as $d_e - \hat{d}_e$ at a single virtual microphone location.

The remote moving microphone technique has also been investigated to estimate the moving virtual error sensor signal under the head movements [103]. In this research, it is assumed that the moving virtual locations, $\boldsymbol{X}_v(n)$, are defined as

$$\boldsymbol{X}_v(n) = [\ \boldsymbol{x}_{v1}(n)\ \boldsymbol{x}_{v2}(n)\ \ldots\ \boldsymbol{x}_{vN_e}(n)\ ], \tag{5.7}$$

where N_e is again the number of virtual error sensors and $\boldsymbol{x}_{vn_e}(n)$ is defined by three dimensional coordinates as

$$\boldsymbol{x}_{vn_e}(n) = [\ x_{vn_e}(n)\ y_{vn_e}(n)\ z_{vn_e}(n)\ ]^{\mathrm{T}}. \tag{5.8}$$

The remote moving microphone technique estimates the error signals at the spatially fixed virtual sensor positions, $\overline{\boldsymbol{X}}_v(n)$ by utilizing the algorithm of the remote microphone technique in Eq. (5.5). The error signals at $\boldsymbol{X}_v(n)$ are then interpolated from the estimated error signals at $\overline{\boldsymbol{X}}_v(n)$. However, since this method assumes that $\boldsymbol{X}_v(n)$ is known at each time step, additional devices such as a headtracker are necessary to monitor the head position, for example.

5.2 Simulation study for nearfield estimation using the remote microphone technique

5.2.1 Estimating disturbance signals at a single virtual error microphone in a single frequency diffuse field

When the complex disturbance signal, $d_m(\mathbf{x}_1)$, at a single monitoring microphone at a point described by the coordinate vector, $\mathbf{x}_1$, is used to estimate the complex disturbance signal, $d_e(\mathbf{x}_2)$, at a single error microphone at a point, $\mathbf{x}_2$, the accuracy depends on the spatial cross-correlation function between the two signals, which for a diffuse primary field, as derived in [9, 104], can be written as

$$< d_e(\mathbf{x}_2)d_m^*(\mathbf{x}_1) >=< |p|^2 > [\sin(k\Delta x)]/(k\Delta x) =< |p|^2 > \text{sinc } k\Delta x. \tag{5.9}$$

where $<\ >$ denotes the operation of spatial averaging by taking samples of the pressure field over a volume of space with dimensions much larger than an acoustic wavelength, * indicates complex conjugation, $< |p|^2 >$ is the space-averaged mean squared pressure in the diffuse field, k is the wavenumber and Δx is the Euclidean distance between $\mathbf{x}_1$ and $\mathbf{x}_2$.

If only a single monitoring microphone is used, $\mathbf{S}_{d_m d_m}$ is a positive scalar and thus Eq. (5.5) can be used with β set to zero, with Eq. (5.9), to give the space-averaged optimal observation filter, $\mathrm{O}_{\mathrm{opt}}(\Delta x)$ in a single frequency diffuse field as

$$\mathrm{O}_{\mathrm{opt}}(\Delta x) =< d_e(\mathbf{x}_2)d_m^*(\mathbf{x}_1) >< d_m(\mathbf{x}_1)d_m^*(\mathbf{x}_1) >^{-1}= \text{sinc } k\Delta x. \tag{5.10}$$

Using Eq. (5.10) for the nearfield estimation, the space-averaged estimation error between $d_e(\mathbf{x}_2)$ and $\hat{d}_e(\mathbf{x}_2)$ is given by

$$\begin{aligned} L_\epsilon &= 10\log_{10}\left(\frac{< |d_e(\mathbf{x}_2) - \mathrm{O}_{\mathrm{opt}}(\Delta x)d_m(\mathbf{x}_1)|^2 >}{< |d_e(\mathbf{x}_2)|^2 >}\right) \\ &= 10\log_{10}(1 - \text{sinc}^2\ k\Delta x). \end{aligned} \tag{5.11}$$

To confirm these predictions, a series of simulations have been implemented in a synthetic single frequency diffuse field, as in [46], using 642 uncorrelated monopole sources uniformly distributed over a sphere of radius 3 m around the monitoring and error microphones. The observation filter and estimation error are calculated from the disturbance

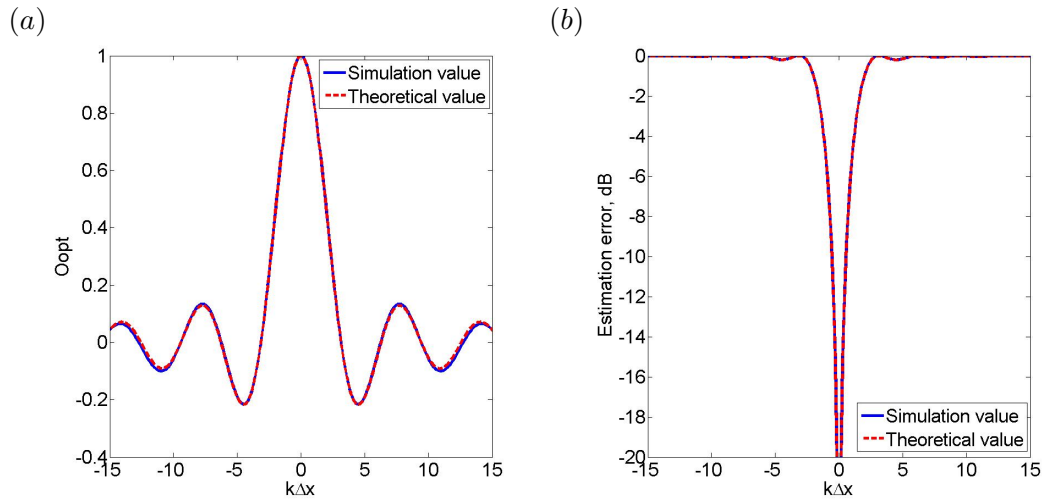

Figure 5.3: (a) The response of the observation filter and (b) the estimation error when a single monitoring microphone is used to estimate the disturbance signals at a single error sensor in a diffuse field. Simulation (solid line), Theoretical value (dashed line)

signals of a single monitoring microphone at the center of the sphere and a 51×51 grid of potential virtual error microphone locations, in the 1 m × 1 m region. The results of this simulation are presented in Fig. 5.3 and show that there is a good agreement between the analytical and simulation results. The estimation error is significantly greater than -10 dB as $k\Delta x$ is increased beyond about ± 0.55, so that Δx is greater than about 1/11.4 of a wavelength, which occurs when either the frequency is increased or the distance between the monitoring and virtual error microphones is increased.

To demonstrate the performance with multiple monitoring microphones, simulations were performed using four monitoring microphones to estimate the signal at a single virtual error microphone in a single frequency diffuse field. Assuming that there are four monitoring microphones arranged in a linear array, as in Fig 5.4, the elements of $\mathbf{S}_{d_m d_e}$ and $\mathbf{S}_{d_m d_m}$ can be calculated to show that

$$\mathbf{S}_{d_m d_e} =< |p|^2 > [\text{sinc } kr_1 \;\; \text{sinc } kr_2 \;\; \text{sinc } kr_3 \;\; \text{sinc } kr_4], \tag{5.12}$$

where $r_1,\ r_2,\ r_3$ and r_4 are the distances from the monitoring microphones to the virtual microphone, and

$$\mathbf{S}_{d_m d_m} =< |p|^2 > \begin{pmatrix} 1 & \text{sinc } kL & \text{sinc } 2kL & \text{sinc } 3kL \\ \text{sinc } kL & 1 & \text{sinc } kL & \text{sinc } 2kL \\ \text{sinc } 2kL & \text{sinc } kL & 1 & \text{sinc } kL \\ \text{sinc } 3kL & \text{sinc } 2kL & \text{sinc } kL & 1 \end{pmatrix}, \tag{5.13}$$

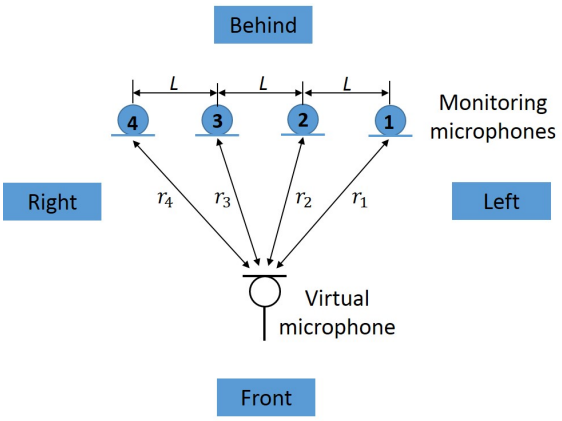

Figure 5.4: Geometry of a linear array with four monitoring microphones used to estimate the pressure at a given virtual microphone location.

where $< |p|^2 >$ is again the space-averaged mean squared pressure in the diffuse field and L is the separation distance between the monitoring microphones. So that with regularization,

$$\mathbf{O}_{\text{opt}} = [\text{sinc}\, kr_1 \;\; \text{sinc}\, kr_2 \;\; \text{sinc}\, kr_3 \;\; \text{sinc}\, kr_4] \begin{pmatrix} 1+\beta & \text{sinc}\, kL & \text{sinc}\, 2kL & \text{sinc}\, 3kL \\ \text{sinc}\, kL & 1+\beta & \text{sinc}\, kL & \text{sinc}\, 2kL \\ \text{sinc}\, 2kL & \text{sinc}\, kL & 1+\beta & \text{sinc}\, kL \\ \text{sinc}\, 3kL & \text{sinc}\, 2kL & \text{sinc}\, kL & 1+\beta \end{pmatrix}^{-1}. \tag{5.14}$$

In this overdetermined case it is important that the regularisation factor, β is carefully selected such that both the estimation error and condition number are acceptable. Fig. 5.5(a) shows the condition number and estimation error, as defined by Eq. (5.6), for different regularisation factors when a line array of four monitoring microphones, with a separation distance along the x-axis of $L = 0.1$ m, is used to estimate the disturbance signal at a single virtual error microphone at $x = 0$, $y = -2L$, i.e. in front of the microphone array in Fig. 5.4, in a single frequency diffuse field at a frequency of around 135 Hz, which corresponds to $kL = 0.25$. From these results, it can be seen that the condition number is significantly reduced for values of β above $\beta = 10^2$ and good nearfield estimation is maintained below $\beta = 10^4$. A good choice of the regularisation factor in this case is thus $\beta = 10^3$. It is clear from Eq. (5.14) that higher values of regularisation will be required at low frequencies, when $kL \ll 1$, whereas when $kL \gg 1$, the matrix that is being inverted tends to the identity matrix and no regularisation is required. The observation filter responses in the case considered here are shown in Fig. 5.5(c) as the location of the virtual error microphone is varied along the x-axis at $y = -2L$. For comparison, the observation filter responses with $\beta = 0$ are shown in Fig. 5.5(b). From these results, it can be seen that with regularisation, the amplitudes

of the observation filter responses are significantly reduced, and also the amplitude and phase of the responses change less with the position of the virtual microphone, which indicates that the estimation will be more robust to spatial uncertainties in the position of the virtual microphone.

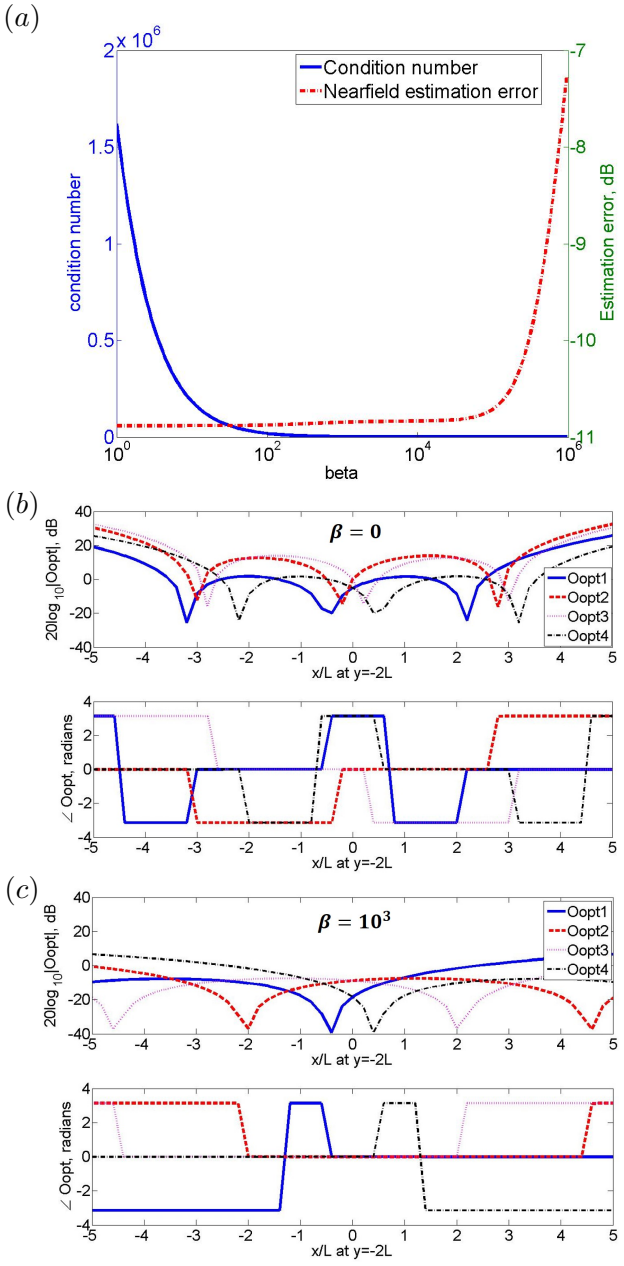

Figure 5.5: (a) Condition number of the inverse term in Eq. (5.5) (Solid line) and the nearfield estimation error (Dash-dot line), for the arrangement shown in Fig. 5.4 at a frequency such that $kL = 0.25$, with different regularisation factors in the observation filter used to estimate disturbance signals of a virtual error microphone at $x = 0$, $y = -2L$ from an array of four monitoring microphones in a diffuse field. The responses of the observation filter matrix, as the location of the single virtual error microphone is varied along x-axis, is also shown (b) without and (c) with the regularisation factor ($\beta = 10^3$).

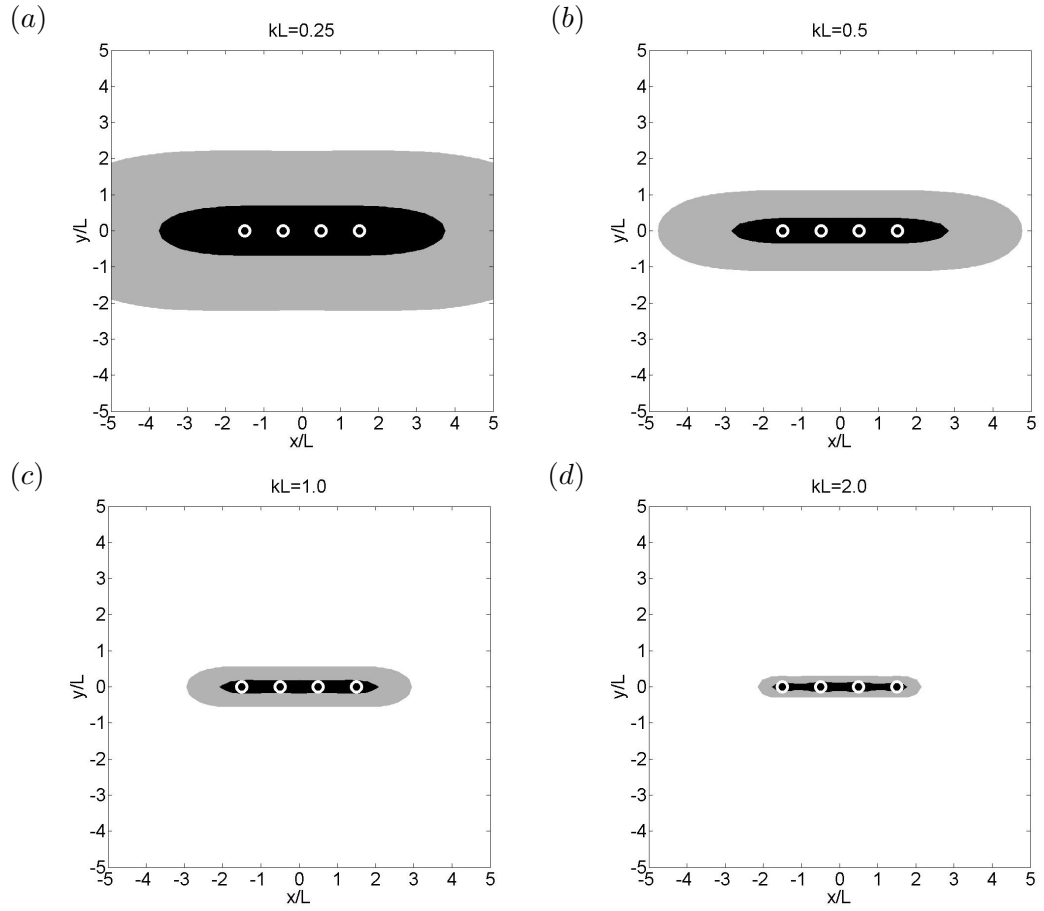

Figure 5.6: The 20 dB error zone (black area) in which the estimation error in Eq. (5.6) is less than -20 dB, and the 10 dB error zone (gray area) in which an estimation error between -20 dB and -10 dB is achieved when the **line** array of four monitoring microphones at $y = 0$ (white circles) is used to estimate the disturbance at different virtual error microphone locations in a single frequency ***diffuse*** field: (a) $kL = 0.25$ with $\beta = 10^3$, (b) $kL = 0.5$ with $\beta = 6.6 \times 10^3$, (c) $kL = 1$ with $\beta = 6.6 \times 10^4$ and (d) $kL = 2$ with $\beta = 0$.

Fig. 5.6 shows contour plots of the estimation error area for different positions of the virtual error microphone on a $\pm 5L$ grid, at different frequencies, with four monitoring microphones positioned as in Fig. 5.4. For these results, the regularisation factors for different frequencies are determined via the process illustrated in Fig. 5.5, giving $\beta = 10^3$ at $kL = 0.25$, $\beta = 6.6 \times 10^3$ at $kL = 0.5$, $\beta = 6.6 \times 10^4$ at $kL = 1$ and $\beta = 0$ at $kL = 2$ and the detailed process of calculating along with responses of the observation filters for $kL = 0.5$ and $kL = 1$ are investigated in Appendix B but at $kL = 2$ the regularisation factor is not required due to sufficiently small conditioning number. In these plots, the black area (20 dB error zone) indicates the zone in which the estimation error is -20 dB or less and the gray area (10 dB error zone) indicates the zone in which the estimation error is between -20 dB and -10 dB. Comparing the results in Fig. 5.6 to the results presented for the single monitoring microphone case, it can be seen that the

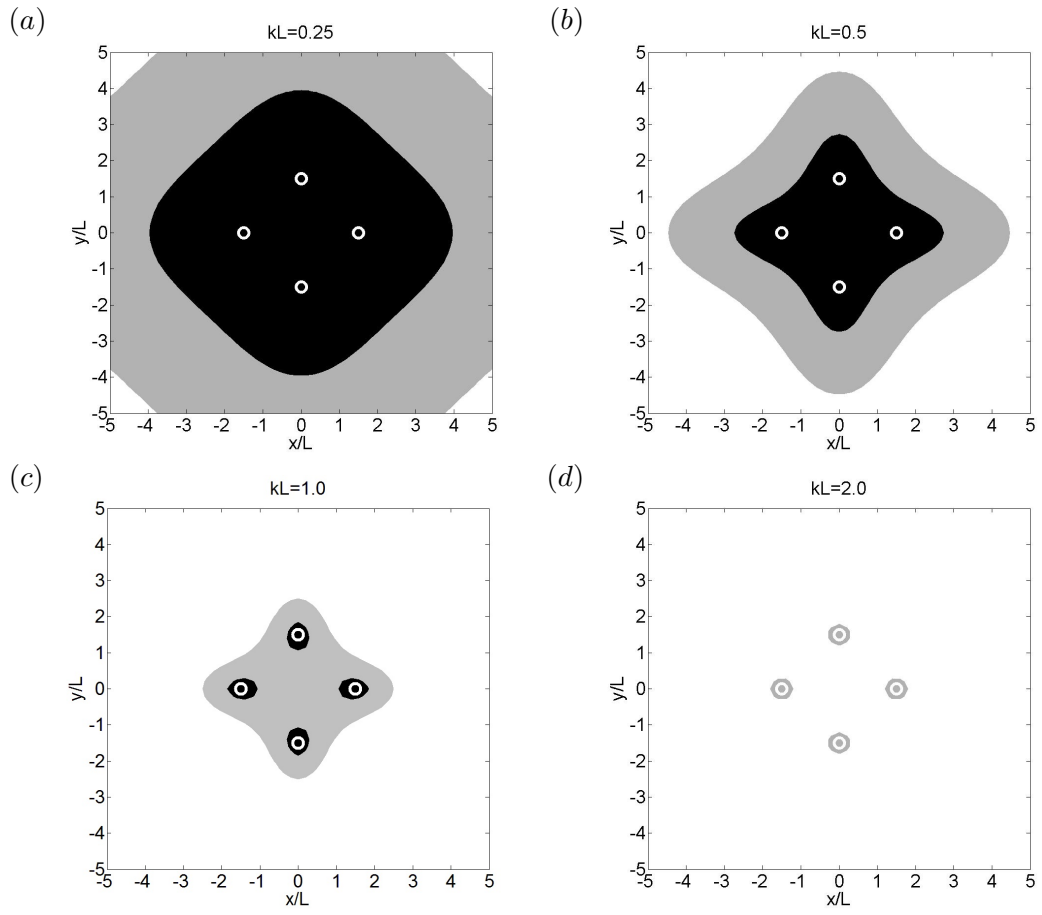

Figure 5.7: The 20 dB error zone (black area) in which the estimation error in Eq. (5.6) is less than -20 dB, and the 10 dB error zone (gray area) in which an estimation error between -20 dB and -10 dB is achieved when the **circular** array of four monitoring microphones (white circles), which has a diameter of $3L$, are used to estimate the disturbance at different virtual error microphone locations in a single frequency ***diffuse*** field: (a) $kL = 0.25$ with $\beta = 10^3$, (b) $kL = 0.5$ with $\beta = 0$, (c) $kL = 1$ with $\beta = 0$ and (d) $kL = 2$ with $\beta = 0$.

shapes of the zones depend on the geometry of the multiple monitoring microphones. Additionally, although the size of the zones reduces as the frequency increases, the use of the multiple monitoring microphones can clearly extend the size of the zones within which the virtual microphone signal can be accurately estimated, compared to a single monitoring microphone. For example, at $kL = 0.5$, with a single monitoring microphone, the 10 dB error zone is generated as a sphere of diameter $\lambda/5.7(= 2.2L)$, from Eq. (5.11), but with four monitoring microphones, the length of the 10 dB error zone is still $\lambda/5.7(= 2.2L)$ in the y direction but is about $\lambda/1.3(= 9.6L)$ in the x direction, as shown in Fig. 5.6(b).

Fig. 5.7 shows the corresponding results when the four monitoring microphones are placed in a circle of radius $1.5L$. This corresponds to moving the central two microphones in the line array to positions in the y direction that are symmetric with those of the

Table 5.1: The results of the nearfield estimation at the position $x = 0$, $y = -2L$ using the two different arrays (line array and circular array) of 4 monitoring microphones in a diffuse sound field.

kL	Freq. (Hz) with $L = 0.1$m	Line array of 4 monitoring microphones	
		Estimation error (dB)	Condition number before and after regularisation
0.25	135	-10.8	$1.2 \times 10^7 \rightarrow 1{,}863$ ($\beta = 10^3$)
0.5	271	-5.4	$1.9 \times 10^5 \rightarrow 1{,}042$ ($\beta = 6.6 \times 10^3$)
1.0	541	-1.3	$2{,}164 \rightarrow 283$ ($\beta = 6.6 \times 10^4$)
2.0	1,082	-0.5	15 ($\beta = 0$)

kL	Freq. (Hz) with $L = 0.1$m	Circular array of 4 monitoring microphones	
		Estimation error (dB)	Condition number before and after regularisation
0.25	135	-33.0	$2{,}796 \rightarrow 1{,}104$ ($\beta = 10^3$)
0.5	271	-29.4	168 ($\beta = 0$)
1.0	541	-16.6	8 ($\beta = 0$)
2.0	1,082	-5.6	3 ($\beta = 0$)

remaining microphones in the x direction. It can be seen that the circular array can estimate disturbance signals at a virtual error microphone in the diffuse field more effectively up to $kL = 1$, compared to the line array in Fig. 5.6. However, at $kL = 2$, since the distance between the monitoring microphones is then relatively large compared with an acoustic length, each monitoring microphone acts like a single monitoring microphone with the result that the 10 dB error zones are similar to those shown in Fig. 5.3. It is also found that because the distance between the monitoring microphones in the circular array is larger than that of the line array, the condition number is significantly improved and the regularisation factor is not required for this circular array, except at $kL = 0.25$. A detailed process to find a proper regularisation factor for the circular array is also described in Appendix B.

To compare the results of the line array in Fig. 5.6 and the circular array in Fig. 5.7, the estimation errors at a single virtual microphone at $x = 0$, $y = -2L$ and the condition numbers before and after regularisation are shown in Table 5.1. Table 5.1 again shows that the estimation error at the virtual microphone is improved using the circular array of monitoring microphones, compared to the line array. The main reason for the improvement is that the nearfield estimation position used in Table 5.1 is much closer to one of the monitoring microphones in the circular array than to any monitoring microphone in the linear array. It is also found that due to the separation between the monitoring microphones, the condition number is significantly reduced. Therefore, by identifying the characteristics of the primary acoustic field, an appropriate array of monitoring microphones can be designed.

5.2.2 Estimating the disturbance signals with the primary sources located on one side of the monitoring microphones in the free field

In the previous section, the performance of the remote microphone technique in a diffuse field has been investigated via a number of numerical simulations using 642 uncorrelated primary sources surrounding the microphone array. It is also interesting to investigate the influence of the spatial directivity of the primary field on the accuracy of the nearfield estimation. Therefore, this section presents simulation results of nearfield estimation obtained with the same arrays of four monitoring microphones as used in the previous section, but excited by a number of primary sources operating at more specific locations in a free field environment.

The line array of monitoring microphones, as shown in Fig. 5.6 are first used for the following two simulations in the free field. The locations of the primary sources, however, are different. Fig. 5.8 shows contour plots of the estimation error at different virtual error microphone locations when 6 primary sources driven by uncorrelated signals and with an inter-source spacing of $8L$ are located at $y = 30L$, i.e. behind the microphone array in Fig. 5.4 if this is a plan view. If only a single primary source is assumed for these simulations, the spatial correlation is unity at all points in the sound field and so perfect estimation can, in principle, be achieved. The regularisation factors for different frequencies are again obtained through consideration of a trade-off between the nearfield estimation and the robustness to uncertainties, and the regularisation factors used are: $\beta = 15$ at $kL = 0.25$, $\beta = 60$ at $kL = 0.5$, $\beta = 200$ at $kL = 1$, $\beta = 0$ at $kL = 2$ and detailed responses of the observation filters are investigated in Appendix B. From the results shown in Fig. 5.8, it can be seen that both the 20 dB error zone and 10 dB error zone in the free field are significantly larger than those in the diffuse field, since the spatial correlation between the monitoring microphones and the virtual error microphone in the free field is improved. Even at the highest frequency of about 1,082 Hz with $L = 0.1$m, which corresponds to $kL = 2$, the 10 dB error zone extends to more than $10L$ in the y-direction. This result suggests that when fixed monitoring microphones are installed on a headrest of a seat, for example, the pressure at the ears of a listener, which may be up to around 0.5 m away from the monitoring microphones, could be accurately estimated for primary fields propagating from this direction.

Fig. 5.9 shows the results of the nearfield estimation using the same monitoring microphones, but when the line array of primary sources is located at $x = -30L$, i.e. on the right of the microphone array in Fig. 5.4 if this is a plan view. From these results, it can be seen that the 20 dB error zone and the 10 dB error zone in the y direction in this case are smaller than those in Fig. 5.8 since the relative geometry between the primary sources and the monitoring microphones in Fig. 5.8 maintains a higher spatial correlation between the virtual error microphone and monitoring microphones over a broader

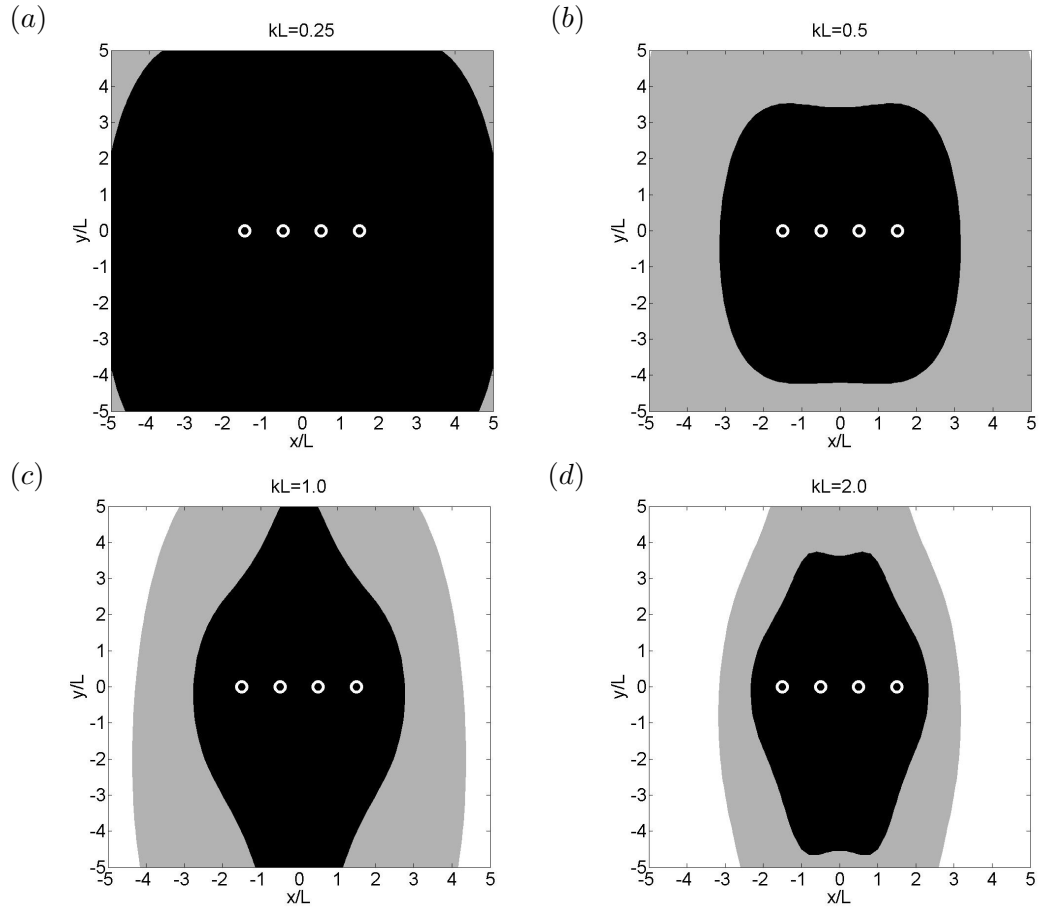

Figure 5.8: The 20 dB error zone (black area) in which the estimation error in Eq. (5.6) is less than -20 dB, and the 10 dB error zone (gray area) in which an estimation error between -20 dB and -10 dB is achieved when the **line** array of four monitoring microphones at $y = 0$ (white circles) are used to estimate the disturbance at different virtual error microphone locations, with 6 primary sources separated by $8L$ at $y = 30L$, ***behind*** the microphone array in Fig. 5.4, producing disturbances in the free field: (a) $kL = 0.25$ with $\beta = 15$, (b) $kL = 0.5$ with $\beta = 60$, (c) $kL = 1$ with $\beta = 200$ and (d) $kL = 2$ with $\beta = 0$.

area, compared to the results in Fig. 5.9. It is interesting that the two error zones in the diffuse field in Fig. 5.6 can be approximately generated by the intersection of the corresponding zones in Fig. 5.8 and Fig. 5.9, even though the diffuse field consists of an infinite number of plane waves emanating from all possible propagation directions.

The results for the circular array of monitoring microphones with the primary sources behind the array are shown in Fig. 5.10. Fig. 5.10 (a) and (b) shows that the circular array in the free field achieves a better nearfield estimation up to 271 Hz, which corresponds to $kL = 0.5$, compared to the line array in Fig. 5.8 (a) and (b). This is because the regularisation factors required for the circular array are smaller than those required for the line array because the distance between the monitoring microphones is larger than that of the line array. However, at 1,082 Hz($kL = 2$), the accuracy of the

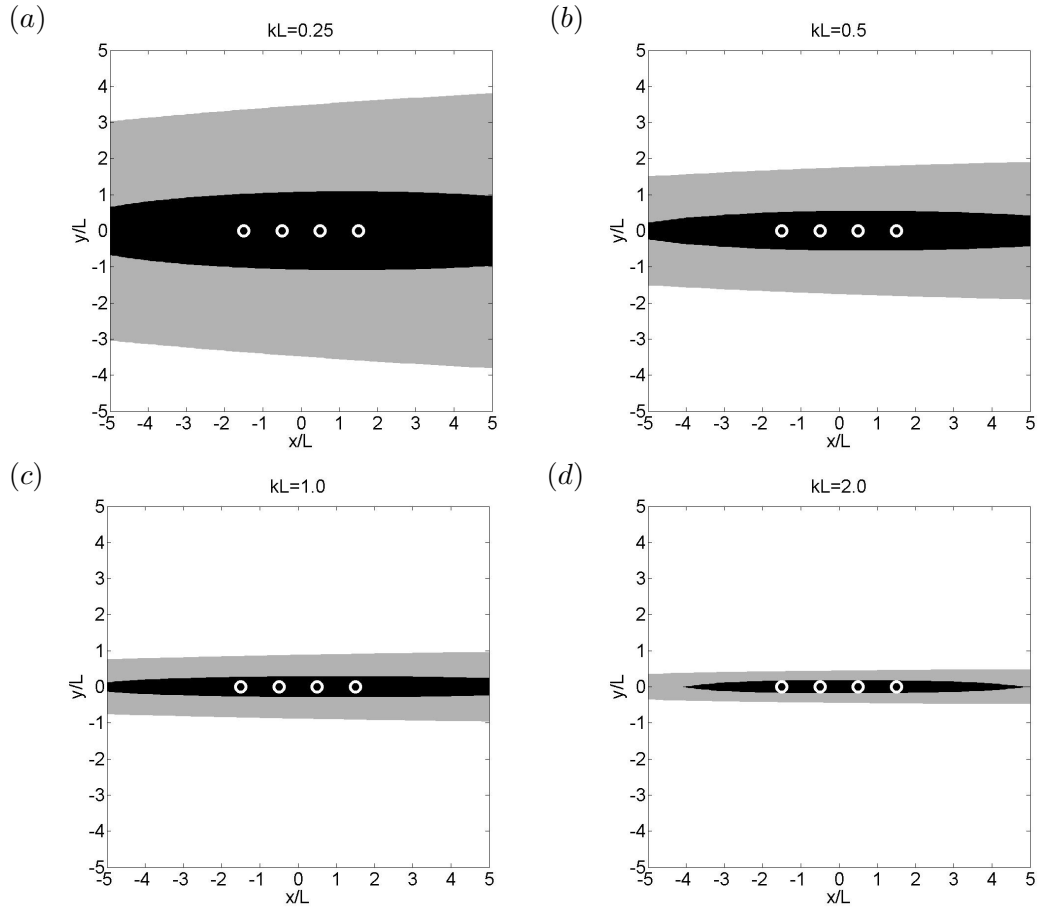

Figure 5.9: The 20 dB error zone (black area) in which the estimation error in Eq. (5.6) is less than -20 dB, and the 10 dB error zone (gray area) in which an estimation error between -20 dB and -10 dB is achieved when the **line** array of four monitoring microphones at $y = 0$ (white circles) are used to estimate the disturbance at different virtual error microphone locations with 6 primary sources separated by $8L$ at $x = -30L$, on the ***right*** of the microphone array in Fig. 5.4, producing disturbances in the free field: (a) $kL = 0.25$ with $\beta = 15$, (b) $kL = 0.5$ with $\beta = 60$, (c) $kL = 1$ with $\beta = 240$ and (d) $kL = 2$ with $\beta = 955$.

nearfield estimation is degraded, compared to the line array in Fig. 5.8(d) because a larger regularisation factor is used and the circular array is not well-matched with the spatial distribution of the sound field in this frequency range. Results with primary sources to the right are just rotated versions of Fig. 5.10 due to symmetry.

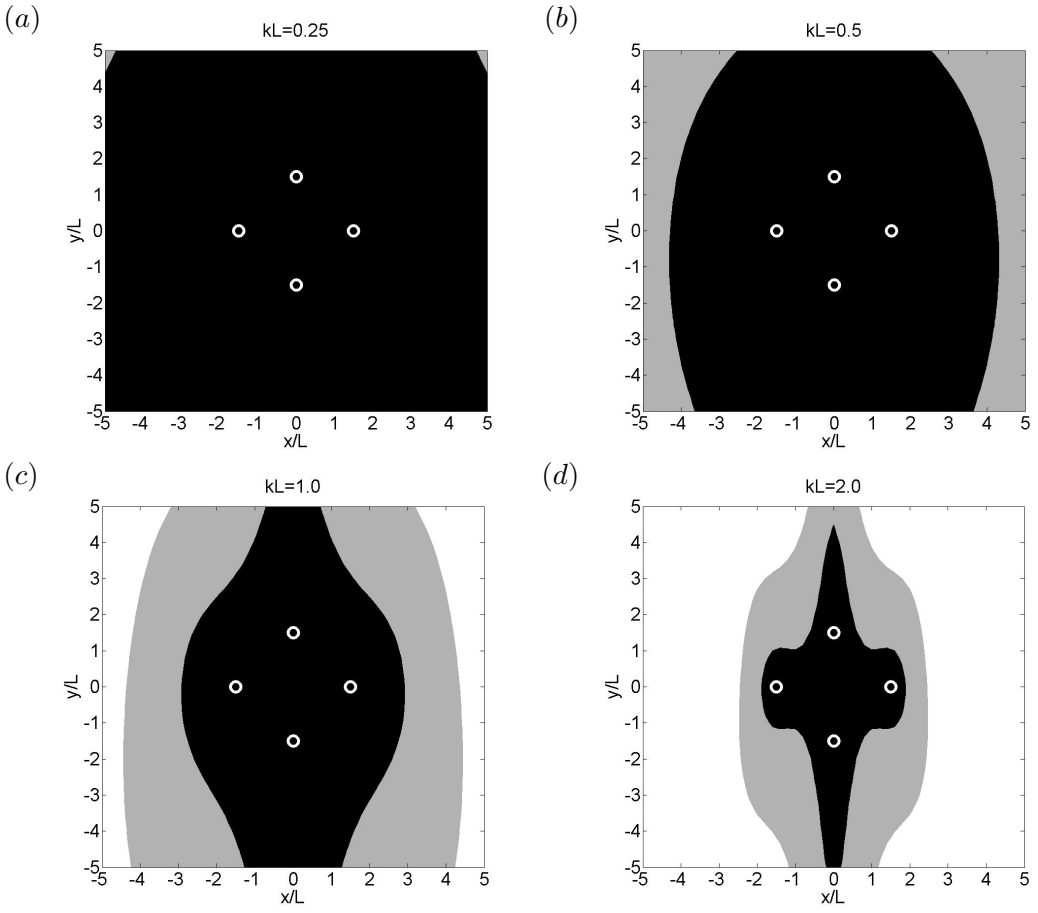

Figure 5.10: The 20 dB error zone (black area) in which the estimation error in Eq. (5.6) is less than -20 dB, and the 10 dB error zone (gray area) in which an estimation error between -20 dB and -10 dB is achieved when the **circular** array of four monitoring microphones (white circles), which has a diameter of $3L$, are used to estimate the disturbance at different virtual error microphone locations, with 6 primary sources separated by $8L$ at $y = 30L$, ***behind*** the microphone array in Fig. 5.4, producing disturbances in the free field: (a) $kL = 0.25$ with $\beta = 14$, (b) $kL = 0.5$ with $\beta = 55$, (c) $kL = 1$ with $\beta = 200$ and (d) $kL = 2$ with $\beta = 436$.

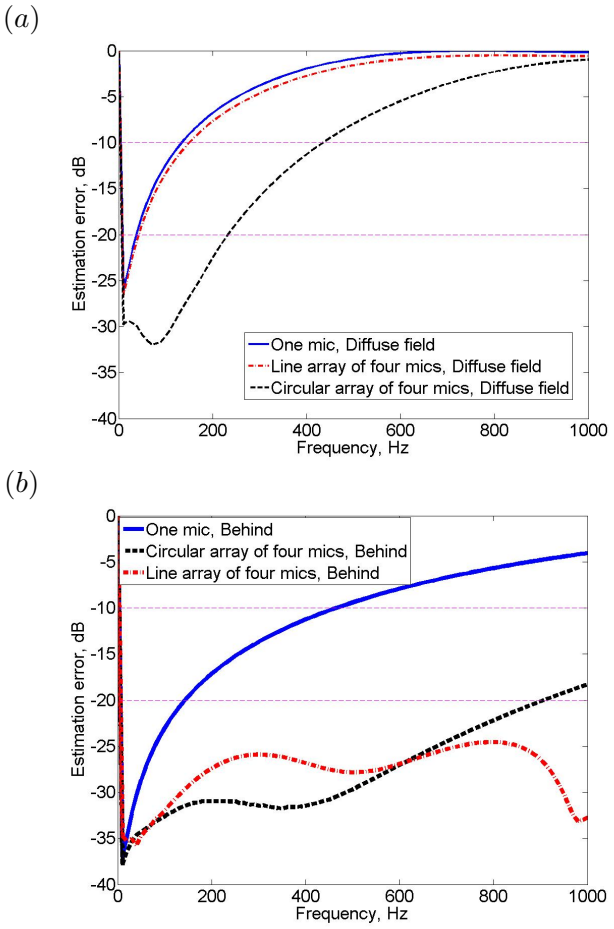

Figure 5.11: The estimation error as a function of frequency when disturbance signals at a single virtual error microphone located at $x = -L$, $y = -2L$ with $L = 0.1$m, which is an approximate location of the right ear of the dummy head in the following experiment, are estimated using: (a) in the ***diffuse*** field, a single monitoring microphone(thin solid line), a line array of four monitoring microphones(thin dashed dot line) and a circular array of four monitoring microphones(thin dashed line), and (b) in the free field with an array of six primary sources ***behind*** the monitoring microphone array, a single monitoring microphone(bold solid line), a line array of four monitoring microphones(bold dashed dot line) and a circular array of four monitoring microphones(bold dashed line).

An alternative way of looking at these results is to plot the normalised estimation error at a particular point as a function of frequency, as in Fig. 5.11. The virtual microphone in this case is located at position $x = -L$, $y = -2L$ with $L = 0.1$m, which corresponds approximately to the location of the right ear of the dummy head used in the following experiments. The results in Fig. 5.11 are shown for the numerical simulations with both the line and circular arrays of four monitoring microphones in a diffuse field and with 6 uncorrelated primary sources located to the rear of the monitoring microphone array. Results when using a single monitoring microphone at the origin to estimate the disturbance at the virtual error microphone are also shown. From these results it

can be seen that in general, the estimation error increases with frequency, as expected. Although the results with the line array of the four monitoring microphones are only slightly better than with the single monitoring microphone in the diffuse field, with the normalised error being below -10 dB up to around 200 Hz in both cases, the estimation error with the circular array is improved, in which case the error is below -10 dB up to 400 Hz. If the primary sources are behind of the array, the estimation errors with the monitoring microphone arrays are much less than those in the diffuse field. In particular, with the line array, the error is below -20 dB up to 1 kHz. The incident wave from the primary sources located to the rear is accurately detected by the line array of the monitoring microphones before it reaches the virtual microphone position, so that its waveform can be accurately estimated. When the primary sources are behind of the array, the circular array achieves better estimation than the line array up to around 600 Hz, but at higher frequencies, the error with the line array is less. The results for the primary sources on the right of the monitoring microphones are similar to those for the diffuse field in this case and so are not shown.

The effect of head movements on the nearfield estimation is also investigated. The near field estimation error for different head positions, at $x = -L$, $y = -1.6L$ or $x = -L$, $y = -3L$ have also been calculated, for a diffuse field for the circular array and for the primary sources behind the array for the line array, as shown in Fig. 5.12. Fig. 5.12 shows that as the head moves further from the monitoring microphones, the estimation error is degraded, as expected, even though a reasonable accuracy in the nearfield estimation is still achieved at $x = -L$, $y = -3L$ in Fig. 5.12(b), when the line array of four monitoring microphones is used in the free field with an array of six primary sources behind the monitoring microphone array.

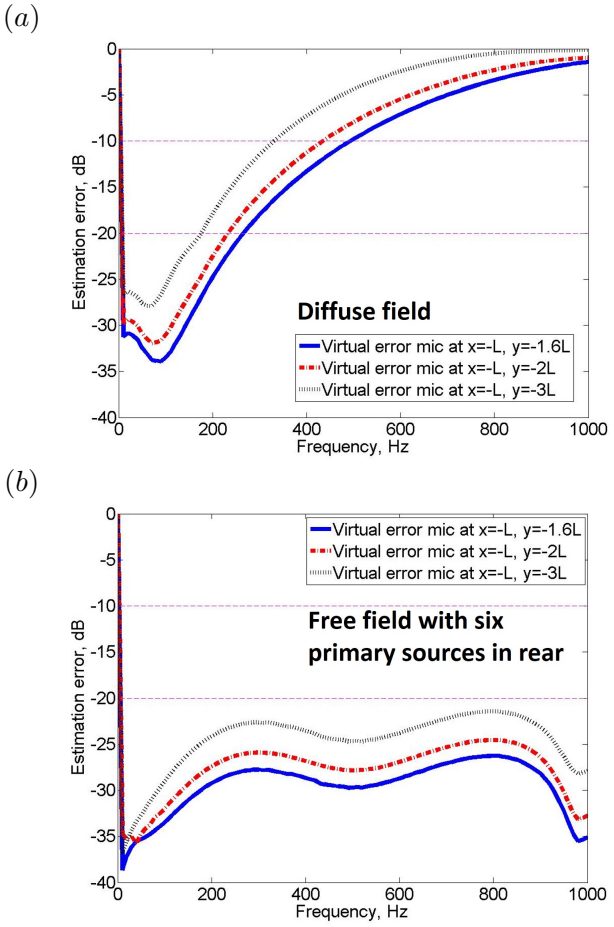

Figure 5.12: The estimation error as a function of frequency when disturbance signals at a single virtual error microphone located at different positions (solid line: $x = -L$, $y = -1.6L$, dashed dot line: $x = -L$, $y = -2L$, as in Fig. 5.11 and dot line: $x = -L$, $y = -3L$), which are approximate moved locations of the right ear of the dummy head in the following experiment, are estimated using: (a) a circular array of four monitoring microphones in the ***diffuse*** field, and (b) a line array of four monitoring microphones in the free field with an array of six primary sources ***behind*** the monitoring microphone array.

5.3 Experimental study using the active headrest in an anechoic chamber

5.3.1 Test installation in an anechoic chamber

To estimate the effect of using the remote microphone technique in practical acoustic fields, the active headrest was installed in the small anechoic chamber at ISVR. Six loudspeakers, which function as primary sources, were installed behind the active headrest system with a dummy head, together with 24 monitoring microphones, as shown in Fig. 5.13. Fig. 5.13(b) and (c) show how these 24 monitoring microphones, located at different positions on a mounting structure and the headrest, were numbered. Fig. 5.13(d) shows how the primary loudspeakers were numbered. A similar arrangement was also installed in a more reverberant room, which is the ANC demo room at ISVR, and the results of the experimental study are reported in Appendix C. The equipment used is detailed in Appendix D.

The aim of the experimental study was to select four monitoring microphones for the nearfield estimation, out of the 24 possible monitoring microphones, in order to investigate the relationship between the geometry of the monitoring microphone array and the accuracy of the nearfield estimation. To compare the estimated disturbance signals at the virtual error microphone with the actual disturbance signals, two microphones in the ears of the dummy head were used as the physical error sensors, in order to identify the observation filter. To be consistent with the above simulations, the six loudspeakers used as the primary sources were positioned behind the active headrest, as shown in Fig. 5.13, and driven with uncorrelated white noise signals. A grid was installed to move the dummy head to different head positions as shown in Fig. 5.14. A series of experiments was conducted when the dummy head was located at 18 different positions on a 5×4 grid of points spaced 5 cm apart, as shown in Fig. 5.14. Measurements of the various acoustic transfer responses were taken and these were used to calculate the optimum observation filters for the various combinations of monitoring microphones and the different head positions, using Eq. (5.5). The potential accuracy of the remote microphone technique was then estimated.

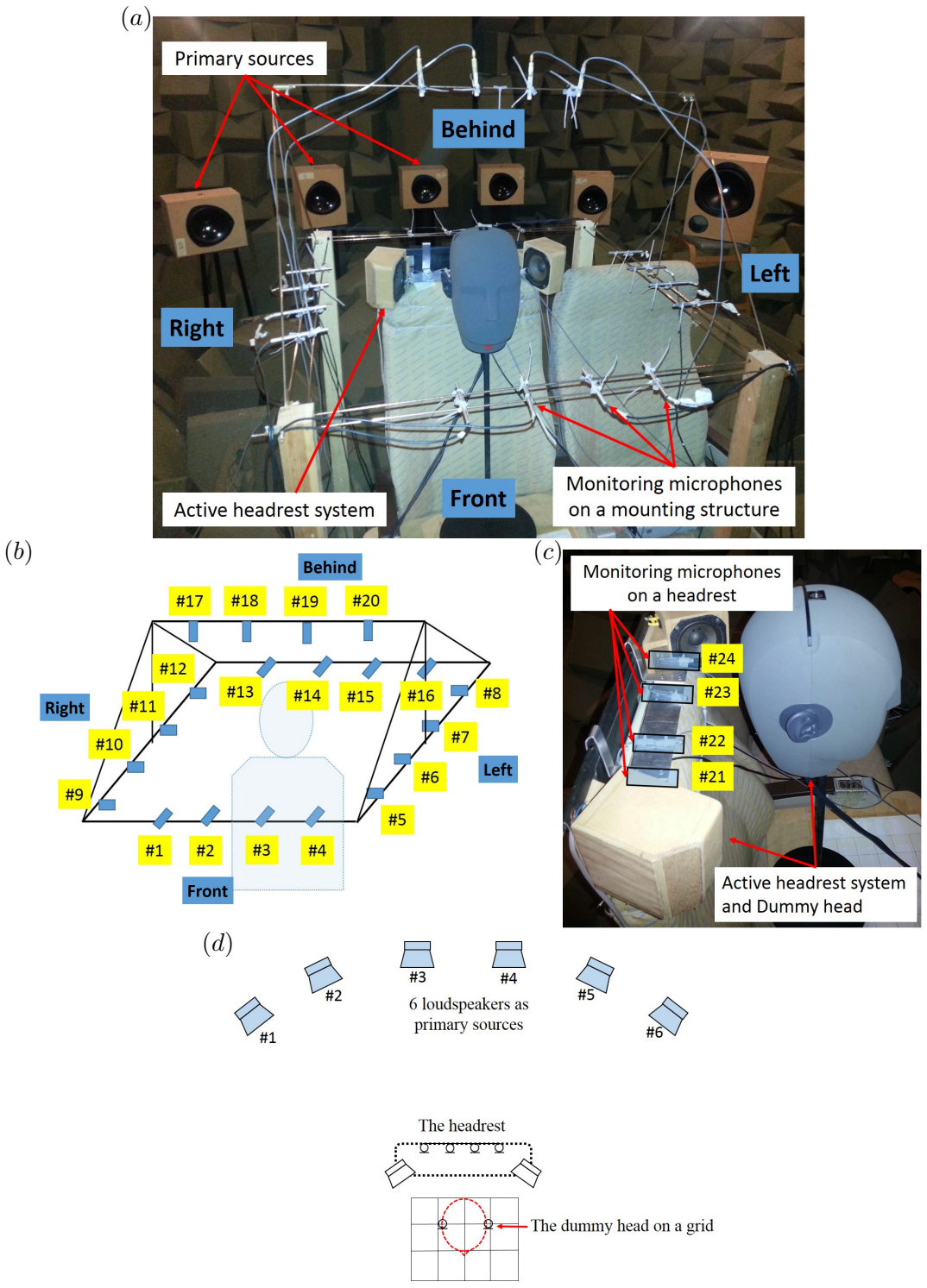

Figure 5.13: (a) The overall installation for the nearfield estimation experiments when six primary sources produce uncorrelated random disturbance signals and with monitoring microphones installed around an active headrest system to estimate the disturbance signals at two error microphones in the ears of a dummy head in an anechoic chamber. (b) 20 potential monitoring microphones on a mounting structure. (c) four monitoring microphones on the headrest and two error microphones in the dummy head. (d) six primary sources behind the headrest.

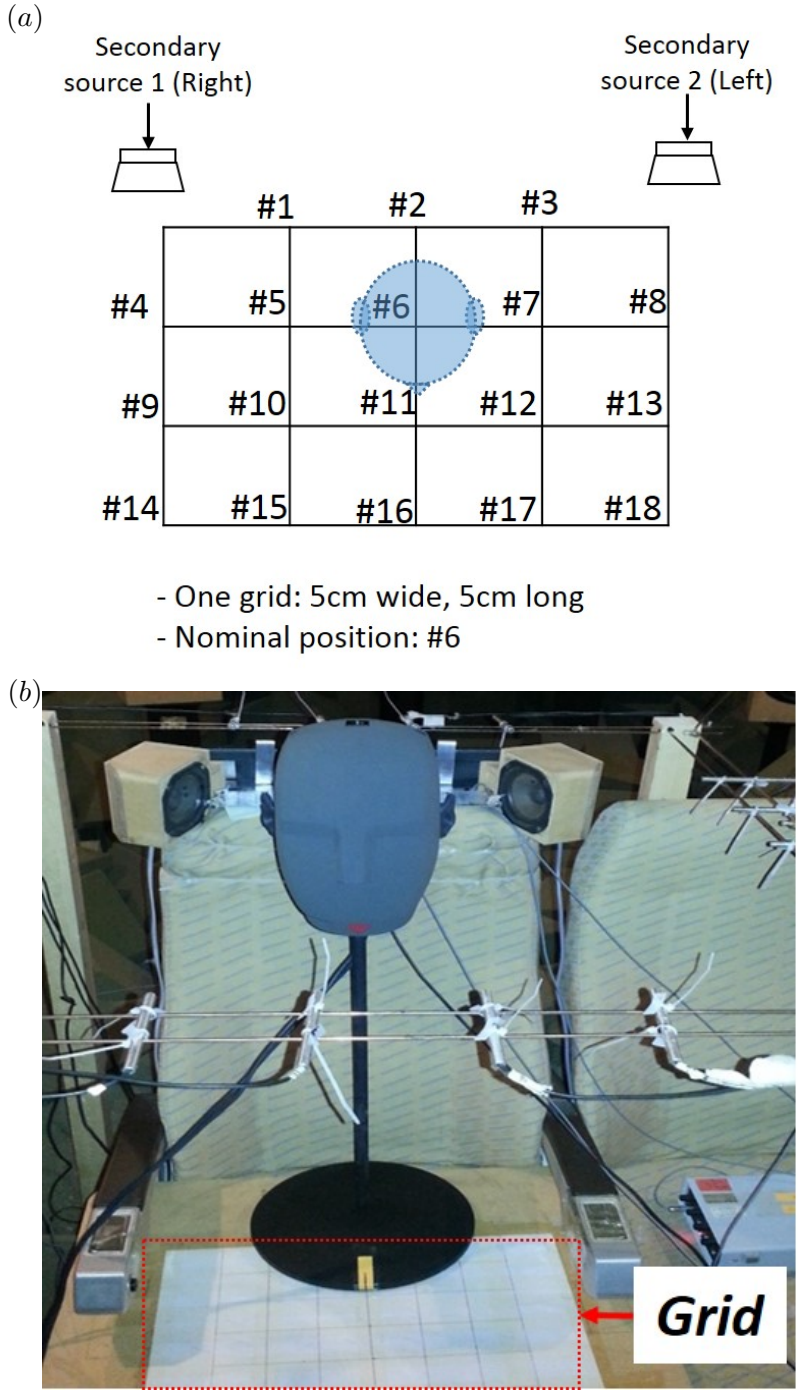

Figure 5.14: The grid for different head positions: a schematic draft, with the head in the nominal position, #6, (a) and an installation of the grid on the seat (b).

5.3.2 Measurement of the acoustic transfer response and coherence

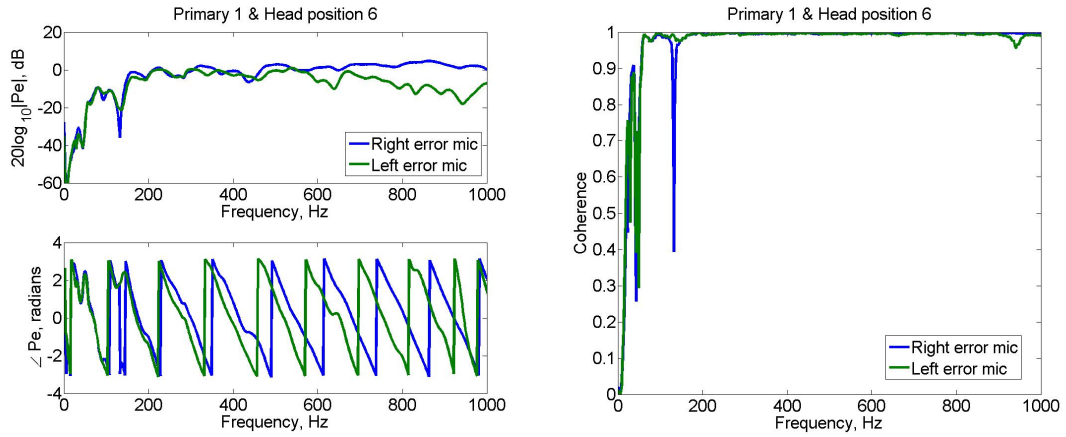

Figure 5.15: The transfer response, $\mathbf{P}_e$ (Left) and coherence (Right) between the primary source #1, operating alone, and the left and right error microphones at head position #6.

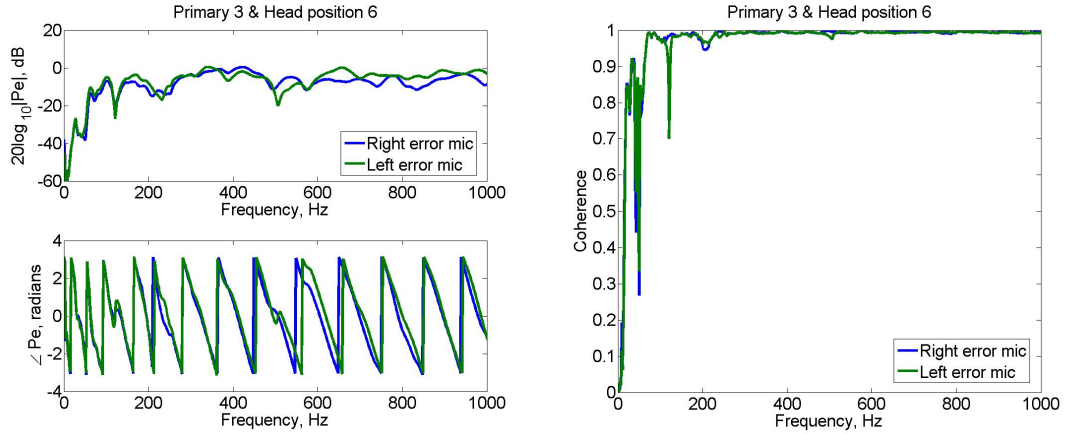

Figure 5.16: The transfer response, $\mathbf{P}_e$ (Left) and coherence (Right) between the primary source #3, operating alone, and the left and right error microphones at head position #6.

The matrix of transfer responses from primary sources to error microphones is denoted $\mathbf{P}_e$ and the matrix of transfer responses from primary sources to monitoring microphones is denoted $\mathbf{P}_m$ as in Fig. 5.2. When the primary source #1 and #3, as numbered in Fig. 5.13(d), are separately driven, the acoustic transfer responses, $\mathbf{P}_e$ and $\mathbf{P}_m$ at the error microphones and the monitoring microphones #21, #22, #23, #24, as numbered in Fig. 5.13(c), are shown in Fig. 5.15, Fig. 5.16, Fig. 5.17 and Fig. 5.18. The relative position between the source and microphones clearly influences in the details of the responses. This is because sound is reflected and scattered by structures around the dummy head, such as the seat and panels for mounting the secondary loudspeakers and monitoring microphones, as well as the head itself. In addition, certain dips in coherence

are also found at low frequencies, where the response of the loudspeakers is poor, and at dips in the transfer responses. However, since good coherence is generally obtained between 70 Hz and 1 kHz, the transfer responses, $\mathbf{P}_e$ and $\mathbf{P}_m$ have the appropriate linear association in this frequency range.

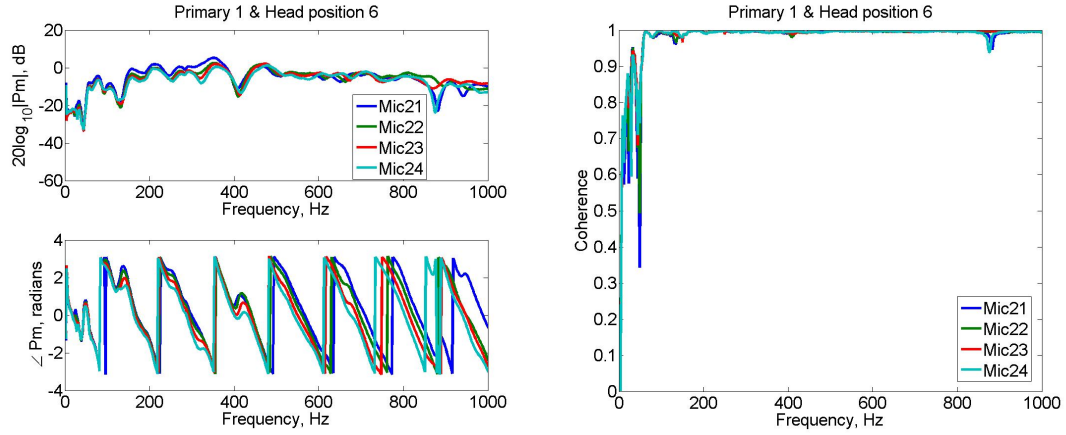

Figure 5.17: The transfer response, $\mathbf{P}_m$ (Left) and coherence (Right) between the primary source #1, operating alone, and the monitoring microphones #21, #22, #23 and #24 at head position #6.

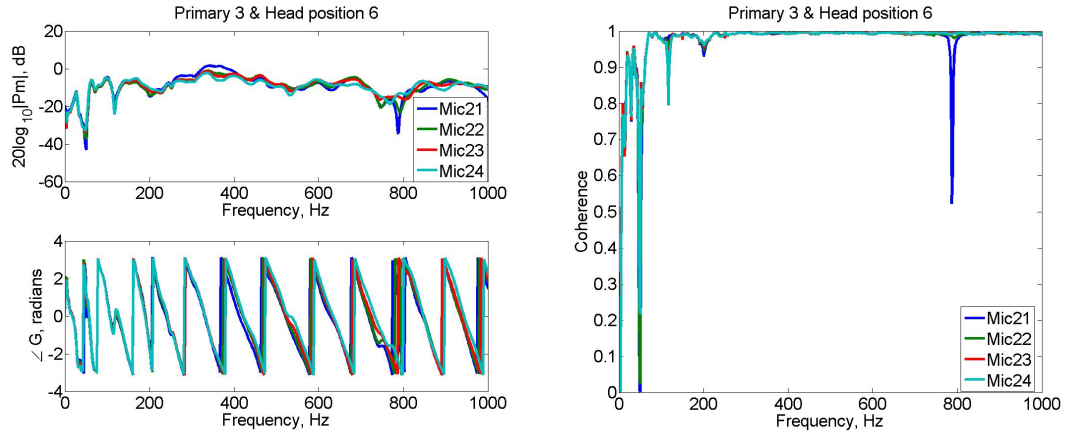

Figure 5.18: The transfer response, $\mathbf{P}_m$ (Left) and coherence (Right) between the primary source #3, operating alone, and the monitoring microphones #21, #22, #23 and #24 at head position #6.

5.3.3 Nearfield estimation for different monitoring microphones array and different head positions in an anechoic chamber

Measurements of the various acoustic transfer responses in section 5.3.2 were used to calculate optimum observation filters for the various combinations of monitoring microphones, using Eq. (5.5). The potential accuracy of the remote microphone technique has also been estimated. Regularisation factors for different combinations of monitoring

microphones were obtained by a consideration of the trade-off between the estimation accuracy and the robustness, as in the previous sections. The dummy head is initially located in the nominal head position #6.

Fig. 5.19 shows the estimation error at the two ears of the dummy head, calculated with regularisation, and the condition numbers of the inverted term in Eq. (5.5) with and without regularisation, as a function of frequency, when using monitoring microphones #21, #22, #23 and #24, which are located on the headrest. This estimation error may be compared with the simulation results in Fig. 5.11(b), which has a similar but more idealised geometry. The difference between the experimental results and the simulation results in the free field is mainly due to reflections from the seat, the headrest system and the dummy head. A -10 dB estimation error can be considered to be the limit for a sufficiently accurate practical estimation, because the active headrest system can then achieve 10 dB attenuation with this estimation error, if $\mathbf{G}_e$ and $\mathbf{G}_m$ in Fig. 5.2 are almost identical to $\hat{\mathbf{G}}_e$ and $\hat{\mathbf{G}}_m$ [25]. Therefore, the experimental results in Fig. 5.19 show that this monitoring microphone array can accurately estimate the disturbance up to about 400 Hz, apart from a narrow band at around 250 Hz.

To investigate the effect of different selections of monitoring microphone positions on the accuracy of the nearfield estimation, the estimation error for other sets of four monitoring microphones was also investigated. When monitoring microphones #3, #7, #10, #14 were selected, which form a ring around the headrest, the results are shown in Fig. 5.20. It can be seen that the estimation error with these monitoring microphones, at frequencies below 700 Hz, is better than those shown in Fig. 5.19 but the estimation error in the frequency range above 700 Hz is degraded compared to the result in Fig. 5.19. It was found, through an exhaustive search of all sets of four monitoring microphones, however, that with monitoring microphones #13, #22, #23, #16, i.e. with two microphones on the headrest and two on the rear supporting structure, the best nearfield estimation is achieved, as shown in Fig. 5.21. It is clear from the results in Fig. 5.19, 5.20 and 5.21 that selection of the monitoring microphone positions needs to be considered with regard to both the spatial correlation of the primary field and the condition number of the inverted term in Eq. (5.5). For instance, in the case shown in Fig. 5.19, although the monitoring microphones are located to match with the spatial characteristics of the primary acoustic field, the small distance between the monitoring microphones results in a large condition number, which suggests that the observation filter will be strongly influenced by the physical and numerical uncertainties in the inverted term. To improve the robustness of this microphone array, a larger regularisation factor is required up to 700 Hz, which degrades the nearfield estimation error in this frequency range. Conversely, in Fig. 5.20, although the condition number is lower due to the larger spacing between the microphones, the formation of the microphones is not well-matched with the spatial distribution of the sound field and therefore the nearfield estimation accuracy in the frequency range above 700 Hz is not improved. In conclusion,

the monitoring microphone array in Fig. 5.21 achieves a good trade-off between spatial matching of the acoustic field and the condition number associated with the inversion. Slight asymmetries in the geometric arrays give rise to differences in the nearfield estimation error at the two ears of the dummy. If the primary sources are located at different locations, different combinations of monitoring microphones need to be considered to achieve the best trade-off between the spatial properties of the primary acoustic field and the condition number.

Fig. 5.22 shows the estimation error at the left and right error microphones when the dummy head is located at 3 different positions on the grid shown in Fig. 5.14(a): position #6 (the nominal position), position #2 (5 cm backward from the nominal position) and position #16 (10 cm forward from the nominal position). In Fig. 5.22, it can be seen that as the distance from the monitoring microphones to the error microphones increases, the estimation performance between about 200 Hz and 800 Hz is degraded, as expected. This trend is well matched to the previous simulation results shown in Fig. 5.12.

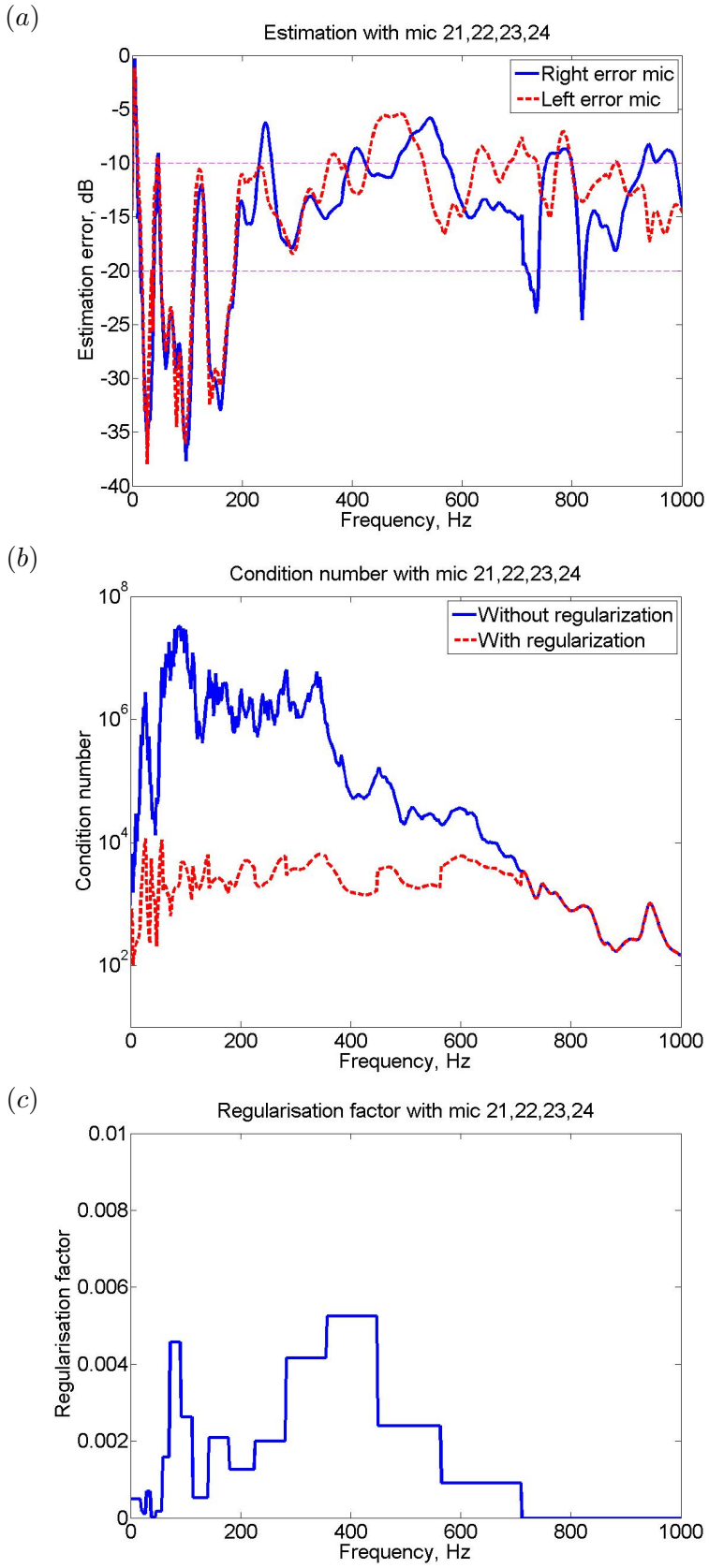

Figure 5.19: The nearfield estimation error (a), condition number (b) and regularisation factor (c) calculated from the measured data when four monitoring microphones, #21, #22, #23, #24, are selected from the monitoring array in Fig. 5.13 to estimate the disturbance signals at the ears of the dummy head when 6 primary sources located at the rear of the headrest are driven with uncorrelated white noise.

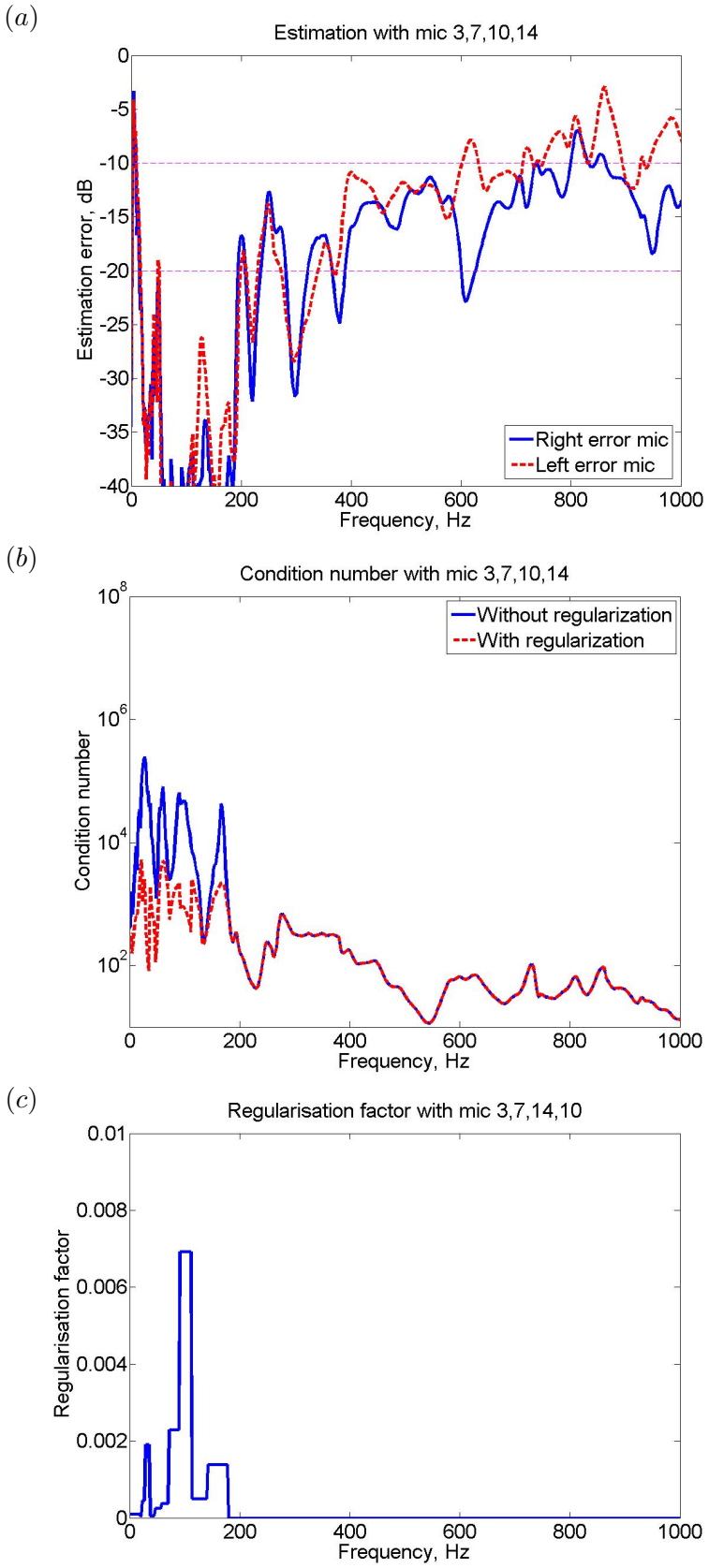

Figure 5.20: The nearfield estimation error (a), condition number (b) and regularisation factor (c) calculated from the measured data when four monitoring microphones, #3, #7, #10, #14, are selected from the monitoring array in Fig. 5.13 to estimate the disturbance signals at the ears of the dummy head when 6 primary sources located at the rear of the headrest are driven with uncorrelated white noise.

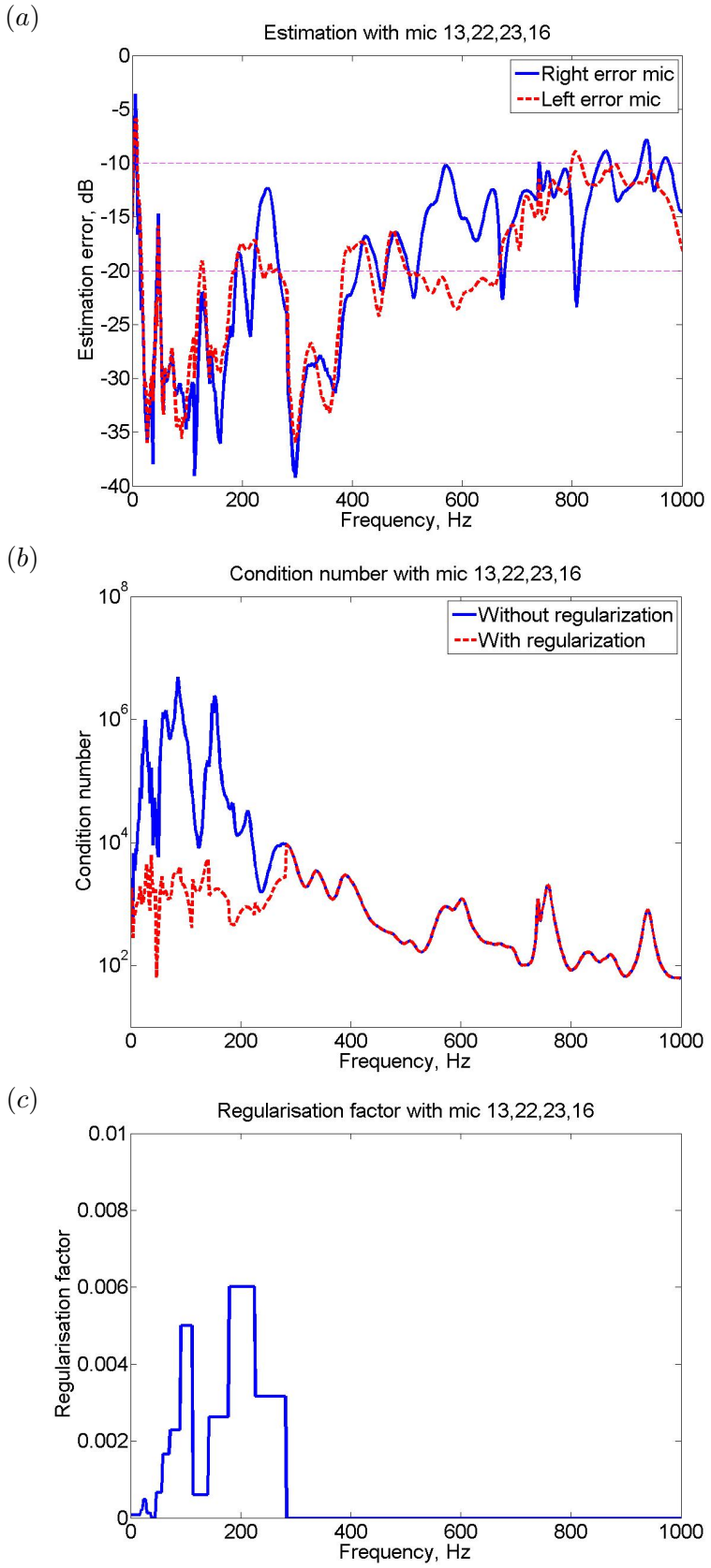

Figure 5.21: The nearfield estimation error (a), condition number (b) and regularisation factor (c) calculated from the measured data when four monitoring microphones, #13, #22, #23, #16, are selected from the monitoring array in Fig. 5.13 to estimate the disturbance signals at the ears of the dummy head when 6 primary sources located at the rear of the headrest are driven with uncorrelated white noise.

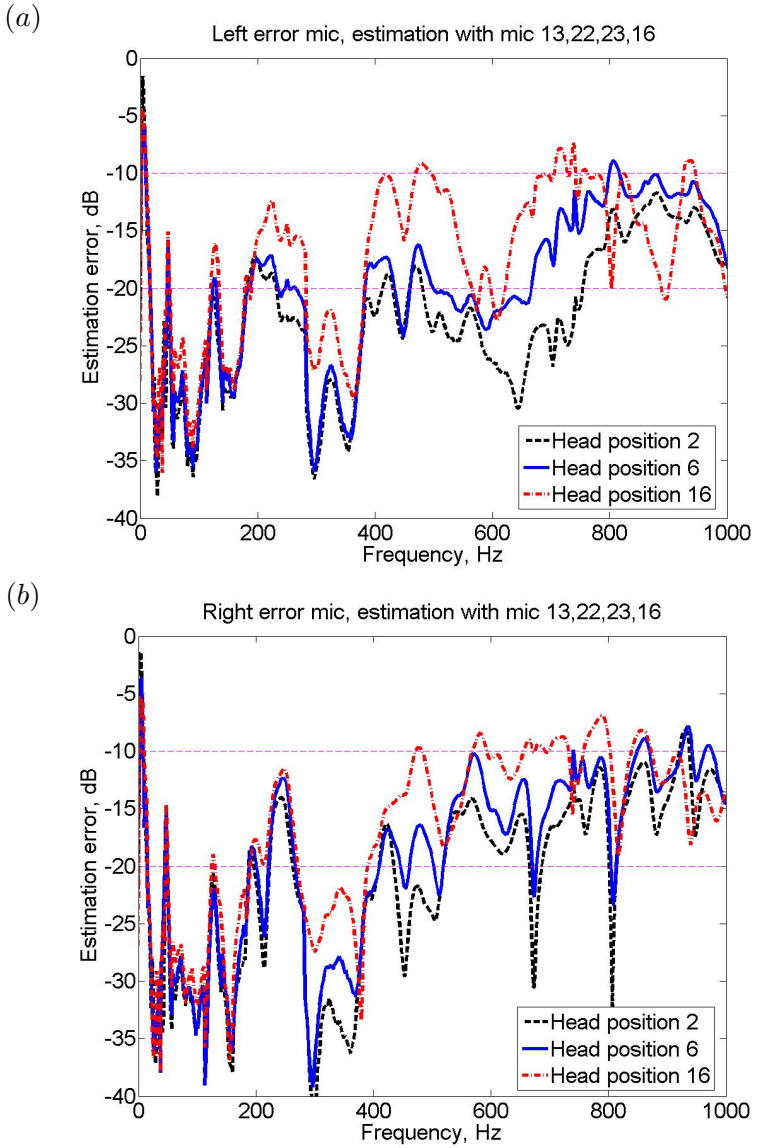

Figure 5.22: The comparison of the nearfield estimation error for the different head positions with the monitoring microphones, #13, #22, #23, #16 when 6 uncorrelated random primary sources are behind the active headrest: (a) the left error microphone, (b) the right error microphone.

5.3.4 The response of the observation filter in the frequency and time domain

The response of the observation filter, $\mathbf{O}_{\text{opt}}$ was investigated when the disturbance signals at the error microphones from the 6 primary sources in the rear are estimated using the monitoring microphones #13, #22, #23 and #16, as used in Fig. 5.21. From Eq. (5.5), the frequency responses of $\mathbf{O}_{\text{opt}}$, used to estimate the signals at the left and right error microphones, are calculated and shown in Fig. 5.23 and Fig. 5.24. Fig. 5.23 shows that to estimate the signal at the left error microphone, the monitoring microphones #22 and #23 in Fig. 5.13(c) are more weighted than the monitoring microphones #13 and #16 in Fig. 5.13(b). This is because microphones #22 and #23 are closer to the left error microphone than microphones #16 and particularly, #13. In Fig. 5.24 for the right ear, monitoring microphones #22 and #23 are again more heavily weighted but now the observation filter for microphone #16 generally has the smallest amplitude, due to its farther distance from the right-hand microphone.

If it is not constrained to be causal, the time domain response of the observation filter can be obtained from the inverse Fourier transform of $\mathbf{O}_{\text{opt}}$, calculated in the frequency domain. The impulse responses of the observation filter for the left-hand ear from monitoring microphones #13, #22, #23 and #16 are shown in Fig. 5.25. As expected, the impulses responses for the monitoring microphones #22 and #23 have larger amplitudes than the monitoring microphones #13 and #16. Non-casual components are present in all four impulse responses. Since the non-causal filters must respond to future inputs, before the monitoring microphones detect disturbance signals, these filters are impractical to estimate the primary signal unless time-advanced reference signals are available. It is found that if the non-causal components of the impulses are windowed out, and the estimation error is again calculated, this is significantly higher than in Fig. 5.21. Therefore, the appropriate causal observation filter will be studied in the Chapter 7 for the practical implementation to random noise in the time domain.

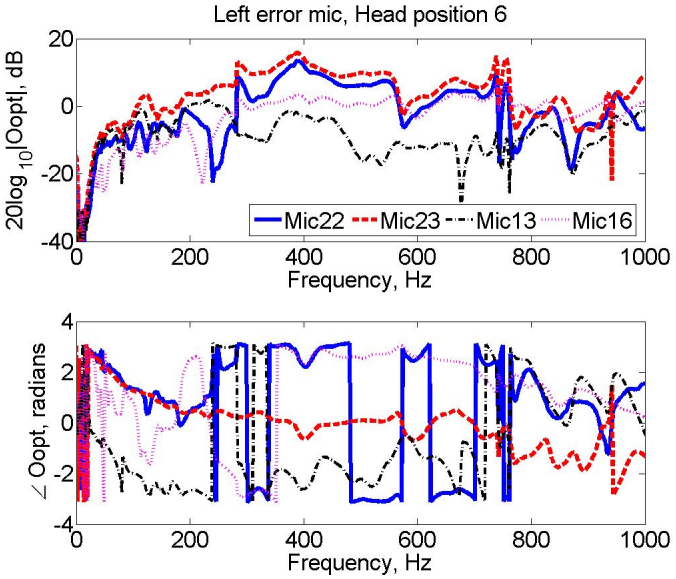

Figure 5.23: The frequency response of $\mathbf{O}_{\text{opt}}$ to estimate the signals of the ***left*** error microphone at the head position #6 by the monitoring microphones #13, #22, #23 and #16 when 6 uncorrelated primary sources are driven in rear.

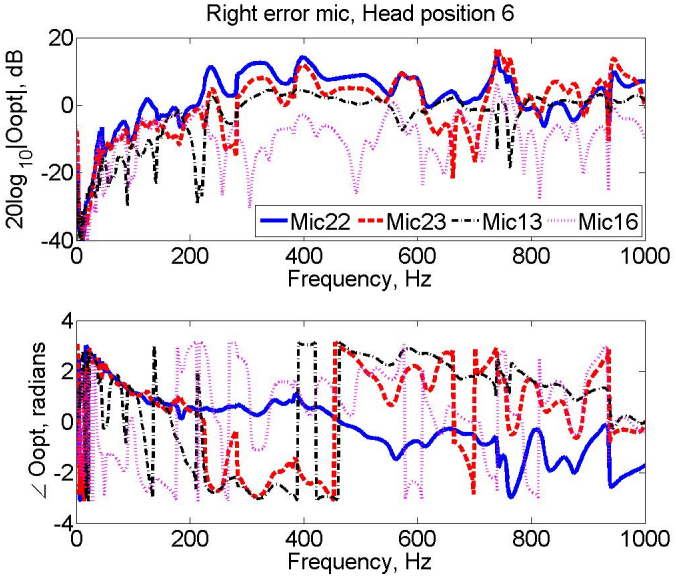

Figure 5.24: The frequency response of $\mathbf{O}_{\text{opt}}$ to estimate the signals of the ***right*** error microphone at the head position #6 by the monitoring microphones #13, #22, #23 and #16 when 6 uncorrelated primary sources are driven in rear.

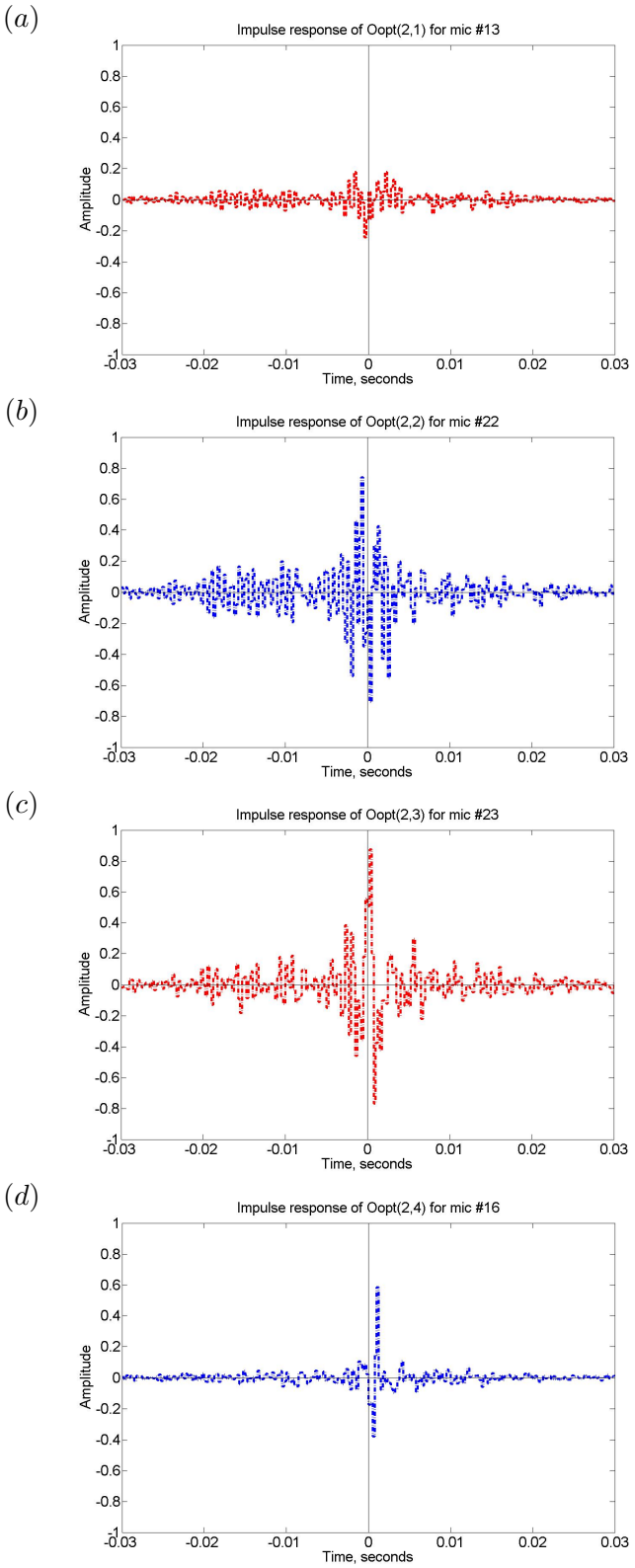

Figure 5.25: The impulse response of the observation filter to estimate the signals of the left error microphone at the head position #6 by the monitoring microphones #13, #22, #23 and #16, when six uncorrelated primary sources are driven in rear: (a) the observation filter, $\mathbf{O}_{\text{opt}}(2,1)$ for the monitoring microphone #13, (b) the observation filter, $\mathbf{O}_{\text{opt}}(2,2)$ for the monitoring microphone #22, (c) the observation filter, $\mathbf{O}_{\text{opt}}(2,3)$ for the monitoring microphone #23, (d) the observation filter, $\mathbf{O}_{\text{opt}}(2,4)$ for the monitoring microphone #16.

5.4 Summary

This chapter has investigated the potential for using the remote microphone technique in an active headrest system, to avoid the installation of physical error sensors at the ears of a listener. To estimate the signals at virtual error microphones from physical monitoring microphones, different virtual sensing algorithms have been suggested and these are reviewed. A general least-squares formulation in the frequency domain has been presented for the optimal observation filter in the frequency domain, using the power and cross spectral densities of the random and stationary disturbances. In this formulation, a regularisation factor has been included to improve the conditioning of the matrix that needs to be inverted, which is chosen using the trade-off between the accuracy of the nearfield estimation and the conditioning of the inversion. This formulation has been used to assess the accuracy of the nearfield estimation using both numerical and experimental investigation.

Simulations using this optimal observation filter have been implemented in a single frequency diffuse field. When a single monitoring microphone was used for the nearfield estimation, the observation filter is equal to the sinc $k\Delta x$ function, where k is the wavenumber and Δx is the distance from the monitoring microphone to the virtual error microphone. For simulations, an approximation to a diffuse field was synthesised using 642 uncorrelated monopole sources uniformly distributed over a sphere, and there was good agreement between the analytic results and those from simulations. Line and circular arrays of four monitoring microphones were also investigated to estimate the pressure at a single virtual error microphone in a single frequency diffuse field and the estimation regions were calculated within which a virtual microphone would have a mean-squared error of -10 dB or -20 dB. The circular array of four monitoring microphones achieved the better nearfield estimation than the line array because the circular array is more well-matched with the spatial distribution of the diffuse field. The shapes of these zones depend on the geometry of the monitoring microphone array and the primary source locations, although the area of the zones is generally reduced as the frequency increases, as expected.

To investigate the influence of the spatial distribution of the primary field, when a line array of six uncorrelated primary sources in the free field produces the disturbance signals, the same line and circular arrays of four monitoring microphones are used to estimate the signals at a single virtual error sensor. Simulations have shown that when the line array estimates disturbance signals due to the six primary sources behind the array in the free field, the estimation error is significantly reduced, compared to the results with the same array of the monitoring microphones in the diffuse field, because of the improved spatial correlation between the monitoring microphones and the virtual error microphones. Results with the circular array have shown that at lower frequency ranges up to 271 Hz($kL = 0.5$), better estimation is achieved due to the smaller condition

number with respect to the inversion, but at higher frequencies, 1,082 Hz($kL = 2.0$), worse estimation is achieved, because the circular array is not well-matched with the spatial distribution of the primary acoustic field.

The performance of the remote microphone technique on an active headrest has then been investigated via experiments in an anechoic chamber, using multiple uncorrelated primary sources to investigate the error at virtual microphones located at the ears of a dummy head. 24 monitoring microphones were installed on a mounting structure and on the headrest, and the dummy head was located in the seat and moved to 18 different positions. With these installations, acoustical transfer responses were measured to calculate observation filters for different combinations of monitoring microphones. With six uncorrelated primary sources behind the active headrest, off-line experimental results of 3 different monitoring microphone arrays have shown that the choice of the monitoring microphone positions should consider both the spatial correlation of the primary field and the condition number of the inverted term of the observation filter. In general, as the distance between the monitoring microphones and the dummy head is increased, the nearfield estimation gets worse. The responses of the observation filter in the frequency domain have shown that the closer the monitoring microphones are to the error microphones, the greater the amplitude of the filters. When the responses of the observation filter in the frequency domain were inverse Fourier transformed to give responses in the time domain, non-causal components have been shown to exist, which may affect their practicality in a real-time system.

In Appendix C, acoustical transfer responses for a similar installation to that used in the anechoic chamber have been measured in a more reverberant room. It has been found that the acoustical responses have more variation than in the anechoic chamber, due to resonances and reflections. The nearfield estimation in the more reverberant chamber is degraded compared with the results in the anechoic chamber. The results with the 3 different monitoring microphone arrays have shown a similar tendency to those in the anechoic chamber, however. The choice of the monitoring microphones again requires a trade-off between the spatial distribution of the acoustic field and the conditioning number for the inversion. The responses in the time domain show that the observation filters for the more reverberant chamber have similar non-causal components to those for the anechoic chamber.

This chapter has thus investigated the performance of the remote microphone technique under ideal and practical conditions, using both numerical models and measurements in practical arrangements. The results provide an insight into the use of the remote microphone technique in several potential applications, particularly in an active headrest system. In the following chapters, the nearfield estimation will be combined with adaptive active control of both tonal and broadband noises and thus virtual error signals will be estimated for adaptation. Moreover, the head-tracking will also be applied to enable updating of the relevant transfer responses when a listener moves their head.

Chapter 6

Combining the remote microphone technique and head-tracking for local active control of tonal noise

In Chapter 4, the head-tracking device was used with the active headrest system and error microphones in the ears, so that when the listener moves the head, the head-tracking can maintain the stability of the active headrest system. In addition, in Chapter 5, the nearfield estimation of the remote microphone technique was investigated through both the simulations and experiments and it was concluded that the virtual error signals can be accurately estimated from the monitoring microphone signals. In this chapter, the head-tracking and the remote microphone technique are simultaneously integrated into the active headrest system to reduce disturbances from tonal noise sources. Therefore, as the head-tracking device detects a change in the head position, this information can be utilised to update the controller and the observation filter using pre-calculated responses, which are required to implement an adaptive local active control system and maintain the stability of the system. This chapter discusses how the remote microphone technique can be used in practice and the condition for the stability of the overall tonal adaptive control system with integrated head-tracking. Moreover, a complete experimental implementation, which includes practical head-tracking, is presented and is used to validate the performance and stability analysis.

In section 6.1, a theoretical analysis of the integrated active headrest system is presented. In section 6.2 from the measured acoustic transfer responses of Chapter 5, the stability and the optimal performance of the integrated active headrest system are investigated off-line. In section 6.3, the real-time implementation of the nearfield estimation and integrated active headrest system for controlling tonal sounds in an anechoic chamber

is presented. In Appendix C, the real-time implementation of the nearfield estimation and integrated active headrest system for controlling tonal sounds in a more reverberant room is also investigated. Finally, section 6.4 presents the summary of this chapter.

6.1 The optimal and adaptive control of tonal disturbances with the integrated local active control system

In this section, the optimised control signals and attenuation performance are formulated in the frequency domain. In addition, a condition for the stability of an adaptive feedforward active control system combined with the remote microphone technique is derived. Analysis in the frequency domain allows a straightforward assessment of the behaviour of the active control system when it aims to control tonal noise. For generality, all signals are initially assumed to be stationary random, with spectral densities [46], but their frequency dependence is suppressed for notational convenience.

Since the combined active control system attempts to reduce the estimated error signals, $\hat{\mathbf{e}}$, the optimal control signals, $\mathbf{u}_{\text{opt}}$, can be obtained by minimising $\hat{\mathbf{e}}$ using the cost function defined as

$$J_3 = \text{trace}\Big\{ E\left[\hat{\mathbf{e}}\,\hat{\mathbf{e}}^{\text{H}}\right] \Big\}. \tag{6.1}$$

To describe Eq. (6.1) in terms of $\mathbf{u}$, we first substitute Eq. (5.2) into Eq. (5.3) and use the optimal observation filter, $\hat{\mathbf{O}}_{\text{opt}}$, so Eq. (5.3) can be expressed as

$$\hat{\mathbf{e}} = \hat{\mathbf{O}}_{\text{opt}}\mathbf{d}_m + \left[\hat{\mathbf{G}}_e + \hat{\mathbf{O}}_{\text{opt}}(\mathbf{G}_m - \hat{\mathbf{G}}_m)\right]\mathbf{u}. \tag{6.2}$$

In Eq. (6.2), the term, $\hat{\mathbf{G}}_e + \hat{\mathbf{O}}_{\text{opt}}(\mathbf{G}_m - \hat{\mathbf{G}}_m)$ can be defined as the effective plant response, $\mathbf{G}$, between $\mathbf{u}$ and $\hat{\mathbf{e}}$, and only if both $\hat{\mathbf{G}}_e$ is equal to $\mathbf{G}_e$ and $\hat{\mathbf{G}}_m$ is equal to $\mathbf{G}_m$, will this plant response be equal $\mathbf{G}_e$. By substituting Eq. (6.2) into Eq. (6.1), the cost function can be written as

$$J_3 = \text{trace}\Big\{ E\left[(\hat{\mathbf{O}}_{\text{opt}}\mathbf{d}_m + \mathbf{G}\mathbf{u})(\hat{\mathbf{O}}_{\text{opt}}\mathbf{d}_m + \mathbf{G}\mathbf{u})^{\text{H}}\right] \Big\}. \tag{6.3}$$

where again

$$\mathbf{G} = \hat{\mathbf{G}}_e + \hat{\mathbf{O}}_{\text{opt}}(\mathbf{G}_m - \hat{\mathbf{G}}_m). \tag{6.4}$$

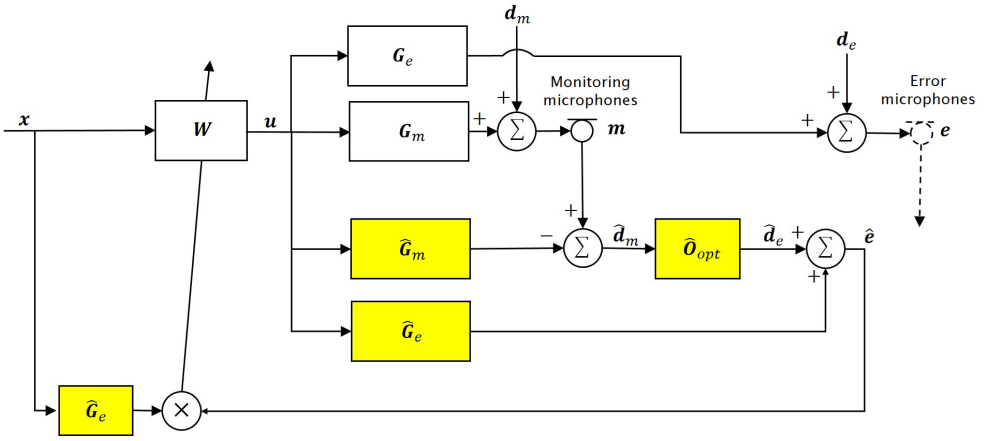

Figure 6.1: Block diagram of the filtered-reference LMS algorithm for adaptive feedforward control, combined with the remote microphone technique.

The optimal control signals, $\mathbf{u}_{\text{opt}}$, that minimise Eq. (6.3) can be obtained using the derivation detailed in Appendix A as

$$\mathbf{u}_{\text{opt}} = -(\mathbf{G}^{\text{H}}\mathbf{G})^{-1}\mathbf{G}^{\text{H}}\hat{\mathbf{O}}_{\text{opt}}\mathbf{d}_m. \tag{6.5}$$

The spectral density matrix of the signals at the error microphones, $\mathbf{S}_{ee}$, after optimal control can then be obtained by substituting Eq. (6.5) into Eq. (5.1), so that

$$\begin{aligned}\mathbf{S}_{ee} &= E\left[(\mathbf{d}_e + \mathbf{G}_e\mathbf{u}_{\text{opt}})(\mathbf{d}_e + \mathbf{G}_e\mathbf{u}_{\text{opt}})^{\text{H}}\right] \\ &= \mathbf{S}_{d_e d_e} - \mathbf{G}_e(\mathbf{G}^{\text{H}}\mathbf{G})^{-1}\mathbf{G}^{\text{H}}\hat{\mathbf{O}}_{\text{opt}}\mathbf{S}_{d_m d_e}^{\text{H}} - \mathbf{S}_{d_m d_e}\hat{\mathbf{O}}_{\text{opt}}^{\text{H}}\mathbf{G}(\mathbf{G}\mathbf{G}^{\text{H}})^{-1}\mathbf{G}_e^{\text{H}} \\ &\quad + \mathbf{G}_e(\mathbf{G}^{\text{H}}\mathbf{G})^{-1}\mathbf{G}^{\text{H}}\ \hat{\mathbf{O}}_{\text{opt}}\mathbf{S}_{d_m d_m}\hat{\mathbf{O}}_{\text{opt}}^{\text{H}}\mathbf{G}(\mathbf{G}\mathbf{G}^{\text{H}})^{-1}\ \mathbf{G}_e^{\text{H}}.\end{aligned} \tag{6.6}$$

The optimal attenuation performance at the error microphones can then be obtained by dividing the sum of diagonal terms of $\mathbf{S}_{ee}$ by the corresponding term for $\mathbf{S}_{d_e d_e}$.

To use the remote microphone technique in practice, it can be combined with the filtered-reference LMS algorithm for feedforward control, and the block diagram of the combined algorithm is shown in Fig. 6.1. In this figure, the error signals, estimated using the remote microphone technique with the optimal observation filter, are multiplied by the filtered-reference signals to update the control filter coefficients. To investigate the conditions for the convergence of the adaptive algorithm, when a single tonal reference signal is assumed, the vector of complex control signals, $\mathbf{u}$, at the $(n+1)$-th iteration can be written as

$$\mathbf{u}(n+1) = \mathbf{u}(n) - \alpha\hat{\mathbf{G}}_e^{\text{H}}\hat{\mathbf{e}}(n), \tag{6.7}$$

where α is the convergence coefficient and $\hat{\mathbf{e}}(n)$ is the vector of sampled estimated error signals at the nth sample time. In Eq. (6.7), the internal plant model, $\hat{\mathbf{G}}_e$, is used instead of the effective plant response, $\mathbf{G}$, since the difference between $\mathbf{G}_m$ and $\hat{\mathbf{G}}_m$ is not known and so is assumed to be zero. From Eq. (6.2), the vector of sampled estimated error signals at the nth sample time, $\hat{\mathbf{e}}(n)$, can be written as

$$\hat{\mathbf{e}}(n) = \hat{\mathbf{O}}_{\text{opt}}\mathbf{d}_m(n) + \left[\hat{\mathbf{G}}_e + \hat{\mathbf{O}}_{\text{opt}}(\mathbf{G}_m - \hat{\mathbf{G}}_m)\right]\mathbf{u}(n) = \hat{\mathbf{O}}_{\text{opt}}\mathbf{d}_m(n) + \mathbf{G}\mathbf{u}(n). \tag{6.8}$$

By substituting Eq. (6.8) into Eq. (6.7), Eq. (6.7) can be expressed as

$$\mathbf{u}(n+1) = \mathbf{u}(n) - \alpha\left[\hat{\mathbf{G}}_e^{\text{H}}\hat{\mathbf{O}}_{\text{opt}}\mathbf{d}_m(n) + \hat{\mathbf{G}}_e^{\text{H}}\mathbf{G}\mathbf{u}(n)\right]. \tag{6.9}$$

The expression in square brackets in Eq. (6.9) is zero after convergence, if convergence can be achieved. Therefore, the steady state vector of control signals after the convergence, $\mathbf{u}_\infty$, is defined to be

$$\mathbf{u}_\infty = -(\hat{\mathbf{G}}_e^{\text{H}}\mathbf{G})^{-1}\hat{\mathbf{G}}_e^{\text{H}}\hat{\mathbf{O}}_{\text{opt}}\mathbf{d}_m. \tag{6.10}$$

By subtracting Eq. (6.10) from both sides of Eq. (6.9), Eq. (6.10) can be written as

$$(\mathbf{u}(n+1) - \mathbf{u}_\infty) = \left[\mathbf{I} - \alpha\hat{\mathbf{G}}_e^{\text{H}}\mathbf{G}\right](\mathbf{u}(n) - \mathbf{u}_\infty). \tag{6.11}$$

When the eigenvalues of $\hat{\mathbf{G}}_e^{\text{H}}\mathbf{G}$ are denoted by λ_{Nu}, from the singular value decomposition discussed in Chapter 4, the condition for the stability of the adaptive algorithm is given by

$$0 < \alpha < \frac{2\text{Re}(\lambda_{Nu})}{|\lambda_{Nu}|^2} \quad \text{for all } \lambda_{Nu} \tag{6.12}$$

Therefore, a sufficient condition for the convergence is that the real parts of all the eigenvalues must be positive. In the case considered here, when the remote microphone method is combined with the filtered-reference LMS algorithm, and using the definition of the effective plant response, $\mathbf{G}$, in Eq. (6.4), the sufficient condition becomes [26]

$$\text{Re}(\text{eig}[\hat{\mathbf{G}}_\mathbf{e}^{\text{H}}\hat{\mathbf{G}}_\mathbf{e} + \hat{\mathbf{G}}_\mathbf{e}^{\text{H}}\ \hat{\mathbf{O}}_{\text{opt}}(\mathbf{G}_\mathbf{m} - \hat{\mathbf{G}}_\mathbf{m})]) > 0. \tag{6.13}$$

In Eq. (6.13), because the real parts of the eigenvalues of $\hat{\mathbf{G}}_e^{\text{H}}\hat{\mathbf{G}}_e$ are always positive, the stability is determined by the term, $\hat{\mathbf{G}}_e^{\text{H}}\hat{\mathbf{O}}_{\text{opt}}(\mathbf{G}_m - \hat{\mathbf{G}}_m)$. This would be zero if $\hat{\mathbf{G}}_m$

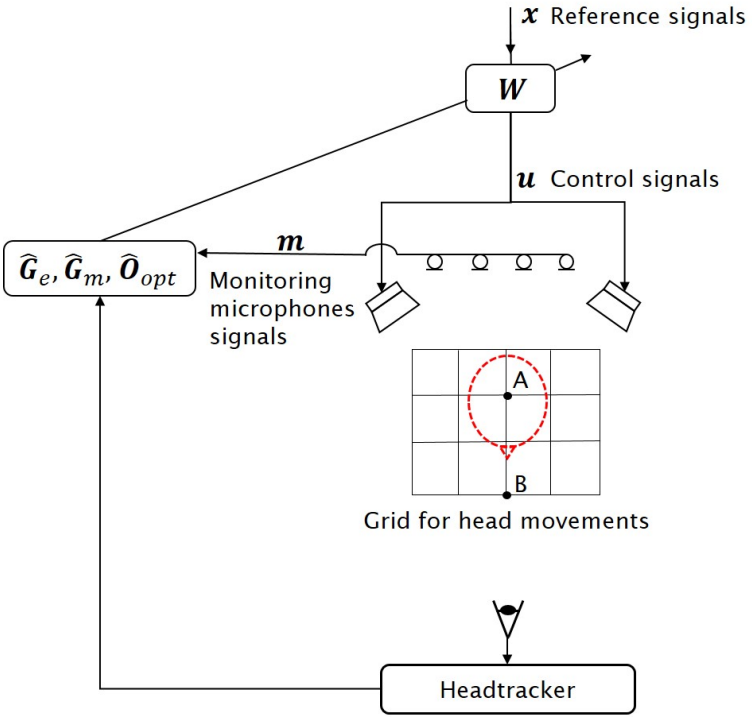

Figure 6.2: The active headrest system integrated with the headtracker and monitoring microphones of the remote microphone technique.

was exactly equal to $\mathbf{G}_m$, but in practice small differences between these matrices can be amplified by $\hat{\mathbf{O}}_{\text{opt}}$ if the elements of this observation filter are large. This reinforces the need for regularisation in the calculation of $\hat{\mathbf{O}}_{\text{opt}}$ since regularisation will reduce the magnitude of the elements, as seen in Fig. 5.5 for example.

When the sound at the ears of a listener is locally controlled, $\mathbf{G}_m$, $\mathbf{G}_e$ and $\mathbf{d}_e$ will all be modified by head movements. Therefore, if $\hat{\mathbf{G}}_m$, $\hat{\mathbf{G}}_e$ and $\hat{\mathbf{O}}_{\text{opt}}$ were pre-modelled and fixed at a nominal head position, the stability and performance of the active headrest system would be influenced by differences between the pre-modelled responses and the physical responses that will be introduced due to head movements. To overcome this problem, a head tracking device can be integrated with the active headrest system, which uses the remote microphone technique and adaptive control algorithm shown in Fig. 6.1. The integrated active headrest system is shown in Fig. 6.2. The head tracking device detects changes in the listener's head position and provides this information to the adaptive algorithm employing the remote microphone technique. The control system can then use this position information to update $\hat{\mathbf{G}}_m$, $\hat{\mathbf{G}}_e$ and $\hat{\mathbf{O}}_{\text{opt}}$ dynamically, as the head position is changed, by using a pre-calculated lookup table, for example.

6.2 Off-line investigation of the stability and performance of the integrated system

To investigate the effects of the integrated active headrest system in an actual acoustic field, measured acoustic transfer responses from the installation in Fig. 5.13 in Chapter 5 have been used for the off-line analysis based on the theory developed in the previous section. The plant response matrix between the virtual error microphones at the dummy head and the secondary sources, $\mathbf{G}_e$ was obtained. At head position #6 which was defined as a nominal position of the dummy head in Fig. 5.14, the transfer responses and coherences between the error microphones and the secondary source 1 (right) are shown in Fig. 6.3(a). The phase is almost linearly proportional to frequency due to the distance between the secondary source and sensor. The plant response matrix between the monitoring microphones #13, #22, #23, #16, which were selected to achieve the better nearfield estimation in Chapter 5, and the secondary sources 1(right), $\mathbf{G}_m$ is similar with the trend of $\mathbf{G}_e$, as shown in Fig. 6.3(b).

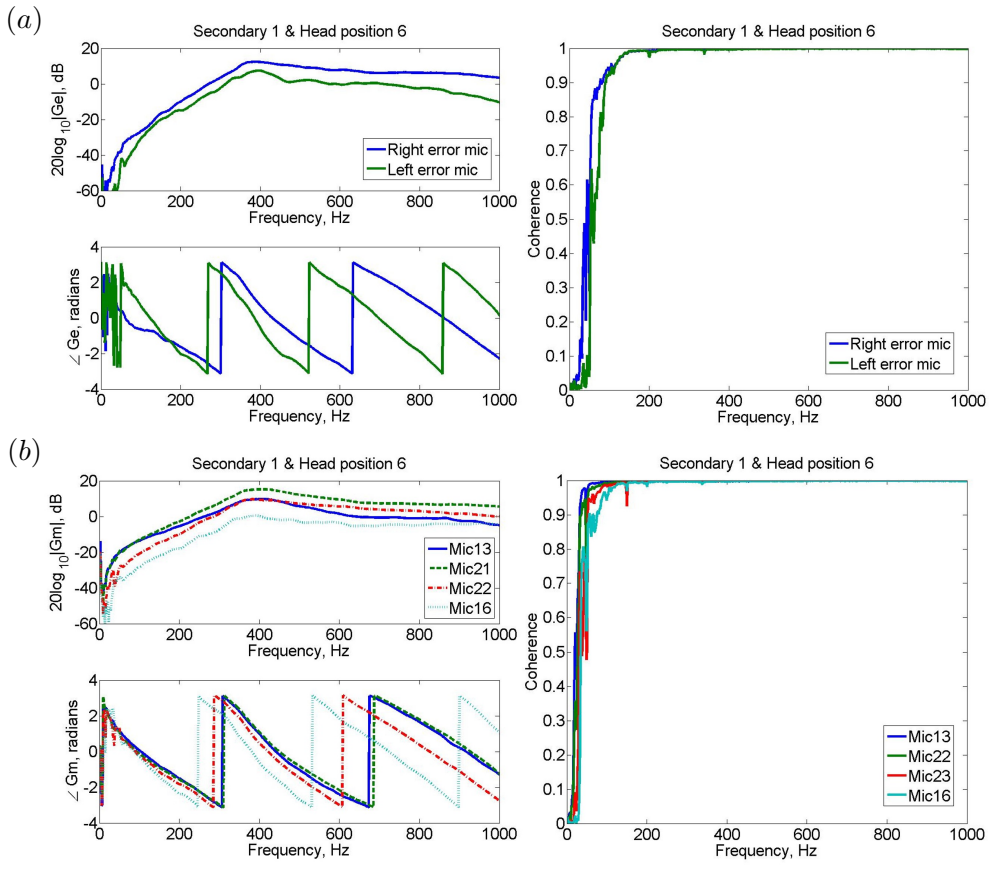

Figure 6.3: (a) The plant response, $\mathbf{G}_e$ (left) and coherence (right) between the secondary source 1(the right secondary loudspeaker) and the physical error microphones in the dummy head at head position #6. (b) The plant response, $\mathbf{G}_m$ (left) and coherence (right) between the secondary source 1 and the monitoring microphones #13, #22, #23 and #16 at head position #6.

The attenuation performance and stability were investigated when the active headrest system is combined with the monitoring microphones, #13, #22, #23 and #16. It was again assumed that the six primary sources are driven by uncorrelated white noise sources. To show the effect of the head-tracking, it was assumed that the dummy head is moved from position 'A' to position 'B' in Fig. 6.2, which correspond to position #6 and #16 in Fig. 5.14, with and without the head-tracking device. The head-tracking device was simulated by updating the filters, $\hat{\mathbf{G}}_m$, $\hat{\mathbf{G}}_e$ and $\hat{\mathbf{O}}_{\text{opt}}$ for position 'B'. From Eq. (6.5) and Eq. (6.6), the optimal attenuation performance of the active headrest system with and without the headtracker is calculated and shown in Fig. 6.4. It can be seen that the optimal attenuation can be significantly improved with the headtracker and also considerable attenuation can be achieved even in higher frequencies, However, the attenuation performance of the active control system without the headtracker is much less and in higher frequency ranges, enhancements in the sound level are produced.

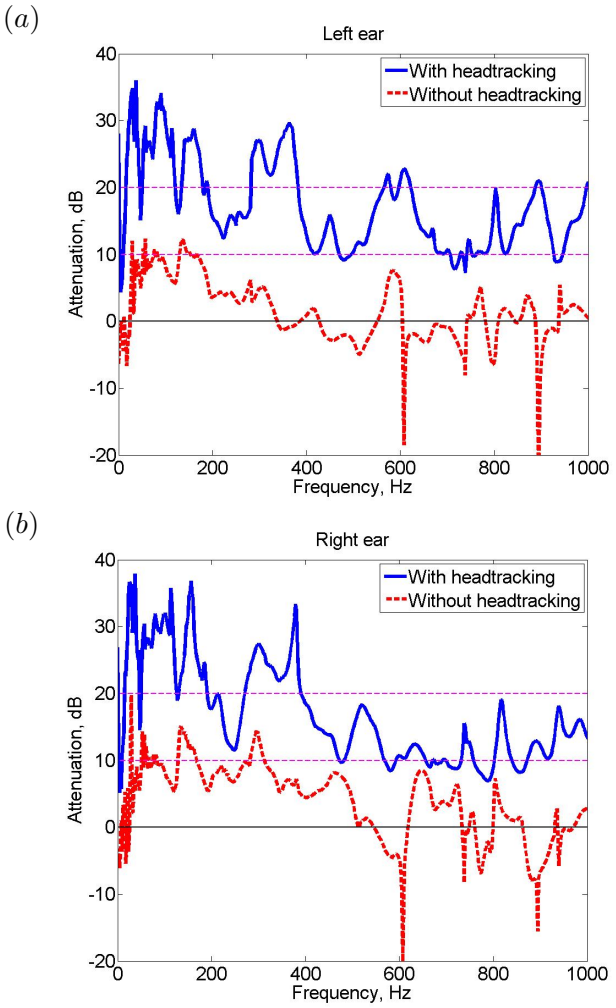

Figure 6.4: The optimal attenuation performance of the integrated active headrest system simulated with and without the headtracker when the head is moved from position 'A' to position 'B' in the anechoic chamber: at the left ear(a) and at the right ear(b).

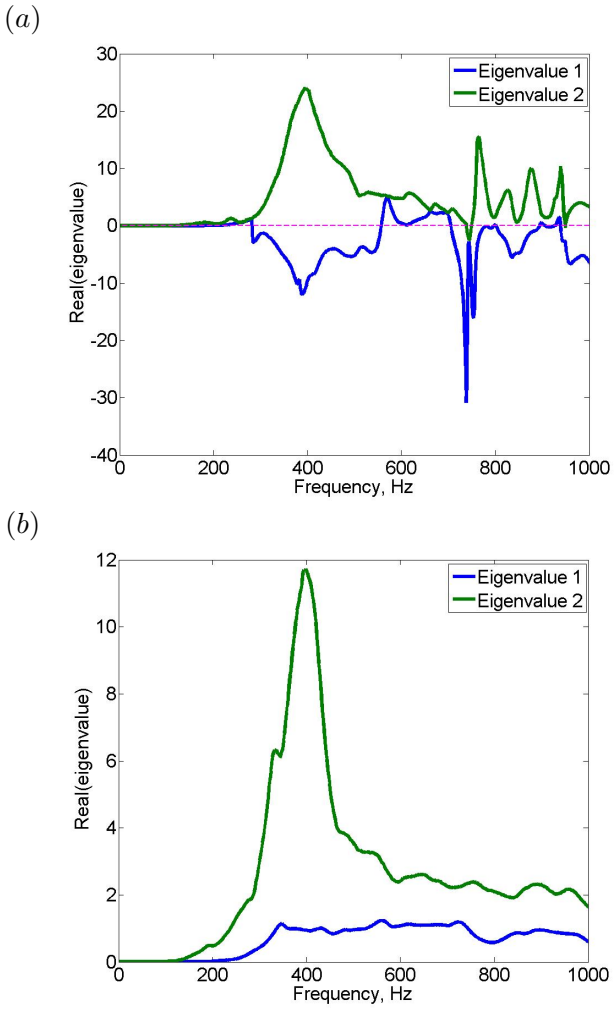

Figure 6.5: The real parts of the eigenvalues of $\hat{\mathbf{G}}^H\mathbf{G}$ in Eq. (6.13) when the head is moved from position A' to position B': (a) without the headtracker and (b) with the headtracker.

To investigate the stability of the adaptive active headrest system, changes in the eigenvalues due to head movements both with and without the headtracker are compared using Eq. (6.13), as shown in Fig. 6.5. In Fig. 6.5(a), without the headtracker, the real eigenvalue becomes negative from around 280 Hz, due to the difference between $\mathbf{G}_m$ and $\hat{\mathbf{G}}_m$. Therefore, it is expected that the integrated active headrest system can be unstable from this frequency. However, in Fig. 6.5(b), with the headtacker updating $\hat{\mathbf{G}}_m$ for position 'B', the real eigenvalues are always positive and the active headrest system can maintain the stability.

Therefore, based on the results of Fig. 6.4 and Fig. 6.5, it is anticipated that the head tracking system can improve both the stability and attenuation performance of the active headrest system in the anechoic chamber. In Appendix C, the effects of the headtracker on the active control system in the more reverberant room are also analysed off-line.

6.3 Real-time implementation for active control of tonal disturbances and experimental investigation

To investigate the real-time performance of the integrated active headrest system, several experiments have been conducted. In this section, the optimised observation filters have been calculated by off-line analysis of the measured acoustic transfer responses, based on the theory developed in Chapter 5. Experiments have then been conducted to investigate the performance of the active headrest system using the remote microphone technique and head-tracking in real-time, when the primary sound field is produced by a single tonal source.

6.3.1 Experiment arrangement

Fig. 6.6 shows the experimental installation used for the real-time implementation and testing in an anechoic chamber. Four monitoring microphones were installed, with two on the back of the headrest and two on the supporting structure, as shown in Fig. 6.6. In Chapter 5, the positions of these monitoring microphones were selected through a series of preliminary experiments to obtain an accurate nearfield estimation of the disturbance signals at the virtual error sensors, which are located at the same positions of monitoring microphones, #13, #22, #23 and #16 in Fig. 5.13.

To compare the estimated disturbance signals at the virtual error microphones with the actual disturbance signals, two microphones were also installed in the ears of a dummy head. The dummy head and physical error microphones can be removed after the preliminary measurements and the system can be used by a real listener. After calculating the observation filter, the active headrest system with the adaptive algorithm shown in Fig. 6.1 was applied using the measured plant responses, to reduce the disturbance signals in real-time. The full set of transfer responses between the primary and secondary sources and the monitoring and physical error microphones was measured when the dummy head was located at 18 different positions on a 5 x 4 grid of points spaced 5 cm apart, which has already described in Fig. 5.14.

The control system was implemented on a dSPACE system at a sampling rate of 4 kHz, with reconstruction filters having a cut-off frequency of 1 kHz. The complex values of $\hat{\mathbf{G}}_m$, $\hat{\mathbf{G}}_e$ and $\hat{\mathbf{O}}_{\text{opt}}$ at a single frequency were used to adapt the complex components of the control signal. A single loudspeaker was installed behind the active headrest system to act as the primary source, driven by a single frequency signal.

Finally, a commercial device, the Microsoft Kinect, was installed in front of the dummy head and used to track the head position. During real-time control, the head tracker is used to measure the head position and the closest pre-calculated head position is identified. The information from the Kinect was decoded in real-time using plug-in software

implemented in MaxMSP and this was passed to a dSPACE-based adaptive controller, which already had stored in it the various plant responses and pre-calculated observation filters for the 18 head positions. The equipment used is detailed in Appendix D and the structures of MATLAB SIMULINK and MaxMSP used here are detailed in Appendix E.

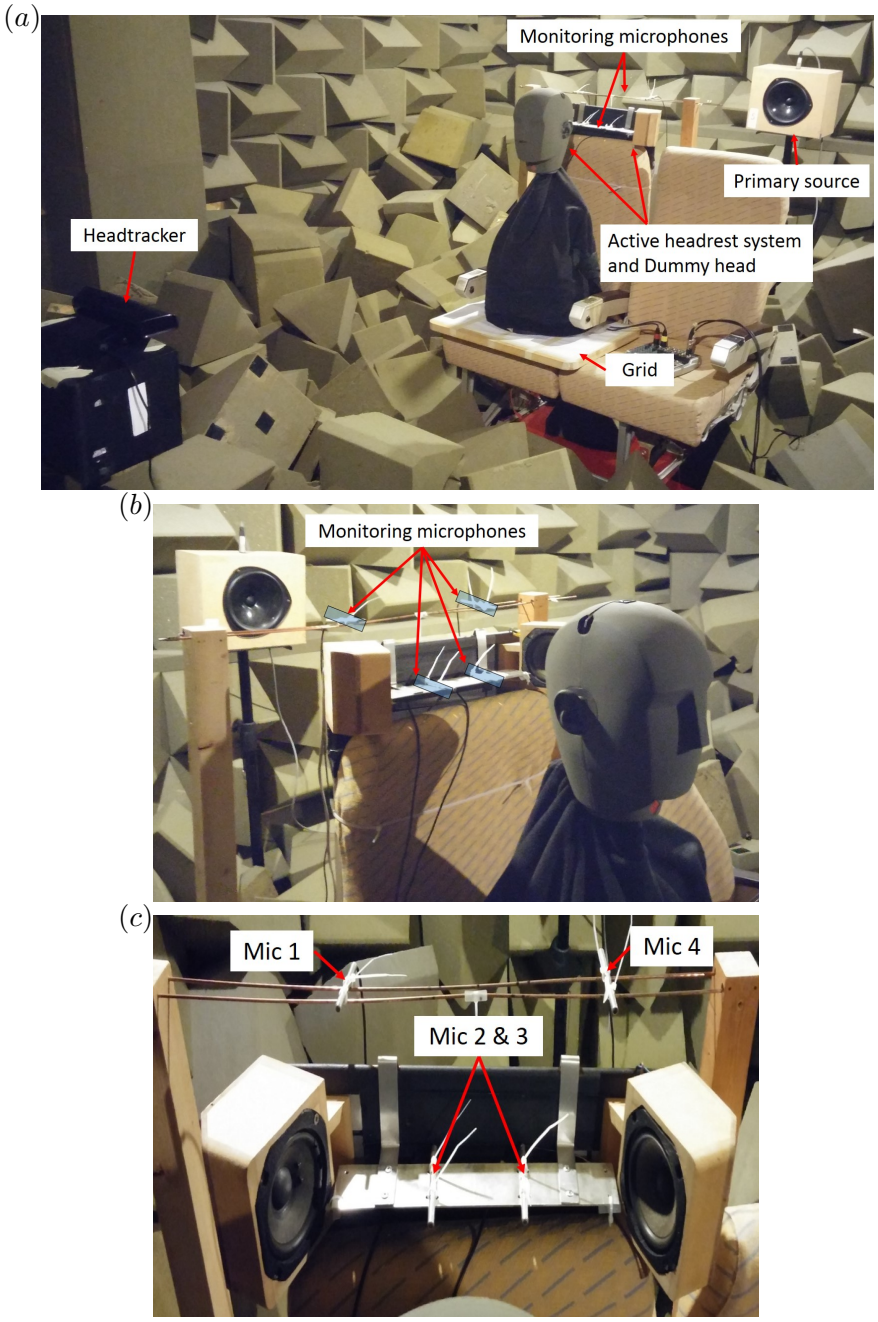

Figure 6.6: (a) The overall installation for the real-time operation of both the nearfield estimation and the integrated active headrest system for controlling tonal disturbance signals, (b) the dummy head with 2 error microphones, one in each ear, and 4 monitoring microphones to the rear and (c) the monitoring microphones on both a mounting structure and the headrest.

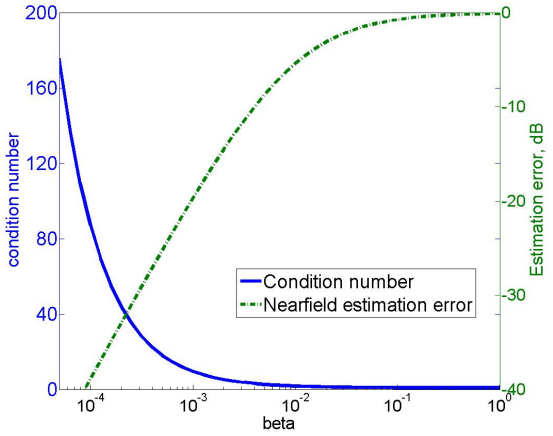

Figure 6.7: Condition number of the inverse term in Eq. (5.5) (Solid line) and off-line nearfield estimation error (Dash-dot line) with different regularization factors to estimate the disturbance signals at the right error microphone at the nominal head position using the monitoring microphones at 600 Hz.

6.3.2 The nearfield estimation of tonal sounds in real-time

As mentioned in Chapter 5, the observation filter must be pre-calculated using Eq. (5.5) and the pre-measured acoustic responses. In addition, an appropriate regularisation factor is necessary in order to achieve both accurate estimation and robustness to practical uncertainties. An estimate of the robustness of the observation filter can be obtained from the condition number of the matrix being inverted in Eq. (5.5). Fig. 6.7 shows that for an excitation frequency of 600 Hz, a regularization factor between 10^{-4} and 10^{-2} appears to give a reasonable trade-off between the condition number and the estimation error if an attenuation of at least 10 dB is to be achieved. The estimation accuracy was analysed off-line using the data measured in the installation shown in Fig. 6.6 with the disturbance signals at the error microphones estimated from the monitoring microphone array using the observation filters given by Eq. (5.5). The estimation error at each microphone, L_ϵ, has been defined in Eq. (5.6).

In order to determine an appropriate regularisation factor for the real-time implementation, values in the range of 10^{-4} to 10^{-2} were investigated through off-line calculation of the estimation accuracy and the robustness to uncertainty. Following the related analysis presented by Elliott et al. [102], the acoustical uncertainty, Δ_{d_m} in the power spectral density matrix of $\mathbf{d}_m$ can be included in Eq. (5.5) as

$$\mathbf{O}_{\text{opt}} = \mathbf{S}_{d_m d_e}(\mathbf{S}_{d_m d_m} + \Delta_{d_m} + \beta\mathbf{I})^{-1}, \tag{6.14}$$

where Δ_{d_m} is defined as

$$\Delta_{d_m} = \sigma^2 \frac{\|\mathbf{S}_{d_m d_m}\|_F}{M^2}\mathbf{I}, \tag{6.15}$$

where σ is the normalised rms random variation, $\| \ \|_F$ is the Frobenius matrix norm defined in [55] and M is the number of monitoring microphones. The normalised rms random variation is set to either 0.05, 0.1 or 0.2, representing either 5 %, 10 %, or 20 % variation in the measured estimation of the pressure at the monitoring microphones. If different regularisation factors are applied under these different levels of variation, changes in the nearfield estimation error indicate the robustness of the observation filter. Fig. 6.8 shows the nearfield estimation error for different levels of acoustical uncertainty for three different regularisation factors. From the results in Fig. 6.8, it can be seen that when different levels of acoustical uncertainty exist, the nearfield estimation error with $\beta = 10^{-4}$ is influenced by the acoustical uncertainty, although a reasonably accurate estimation is achievable even with 20% uncertainty. That is, the acoustic uncertainty including measurement noise is not included in the sensor signals, but this would be amplified by the inversion in Eq. (6.14) without sufficient regularisation. However, the influence of the acoustical uncertainty is decreased as the regularisation factor is increased such that with $\beta = 10^{-3}$ the variation in the estimation error for different levels of uncertainty is less than 1 dB . From the results shown in Fig. 6.7 and Fig. 6.8, a regularisation factor, $\beta = 10^{-3}$ was selected as appropriate for the real-time estimation. It can be seen from Fig. 6.8 that in the frequency range below 100 Hz, the nearfield estimation error is significantly increased because the primary loudspeaker does not generate sound efficiently in this frequency range and so the measured pressures are dominated by background noise, giving poor coherence between the loudspeaker input and microphone output.

When tonal disturbance signals at the dummy head error microphones at different frequencies are measured and compared with those estimated from the monitoring microphones in real-time, with the pre-calculated observation filter using a regularisation of $\beta = 10^{-3}$, the results shown in Table 6.1 show that an estimation error of less than -15 dB estimation error is achieved at all frequencies between 300 and 700 Hz. Table 6.1 also shows that the off-line results, which are predicted from the measured acoustic responses, give a reasonable indication of the real-time performance, as measured in the following section.

6.3.3 Real-time adaptive control using the integrated active headrest system

The real-time performance of the integrated active headrest system was then tested when a single primary source in the anechoic chamber was driven to produce a tonal disturbance. For the estimation of the virtual error signals, the observation filters described

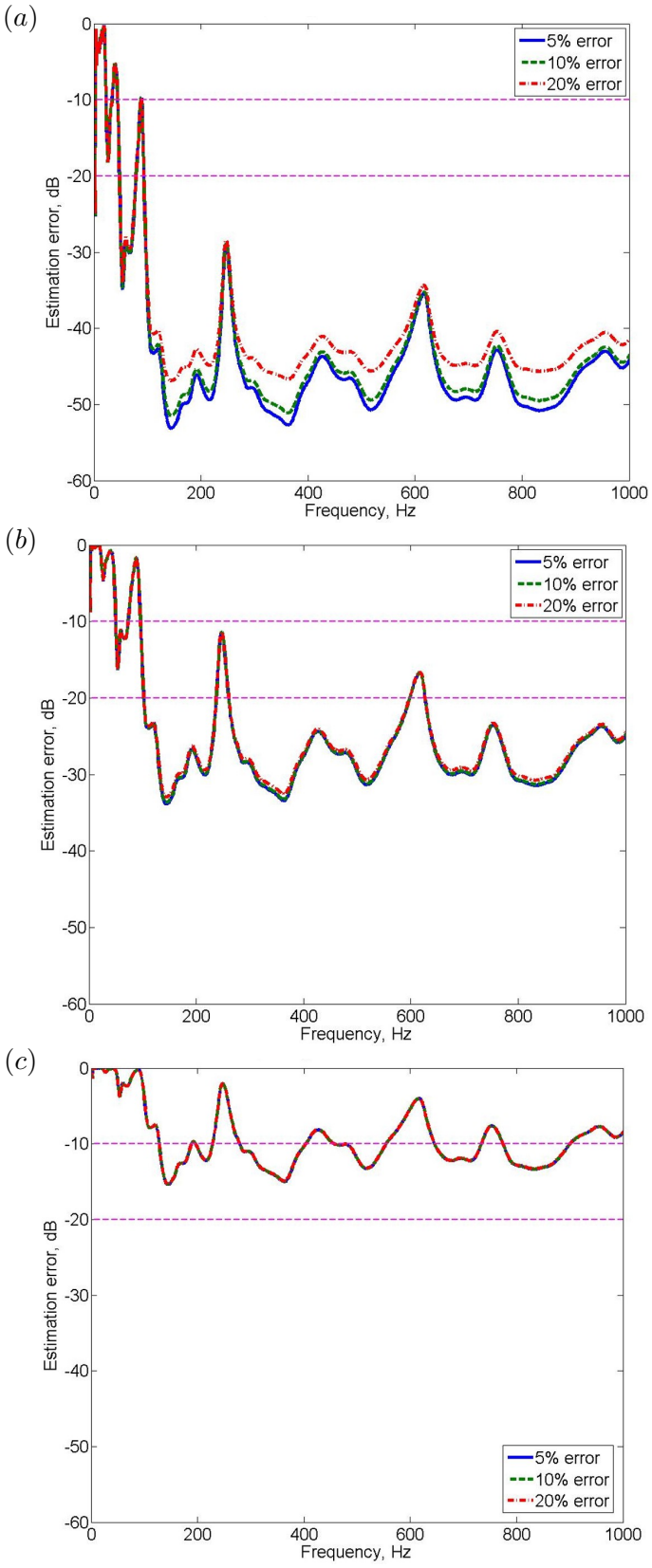

Figure 6.8: Changes in the nearfield estimation error for different acoustic uncertainties in the analysis of the monitoring microphones when the observation filter is applied with different regularization factors as: (a) β =10^{-4}, (b) β =10^{-3}, (c) β =10^{-2}

Table 6.1: Comparisons of the nearfield estimation error between the off-line and real-time test when tonal disturbance signals at the right error microphone of the dummy head are estimated by the 4 monitoring microphones around the headrest with the pre-calculated observation filter in the anechoic chamber.

Frequencies	Off-line estimation error (dB)	Real-time estimation error Magnitude (dB), Phase (radians)
300 Hz	-28.5	-29.4, -0.01π
400 Hz	-28.9	-32.1, -0.01π
500 Hz	-27.7	-19.3, -0.03π
600 Hz	-22.9	-21.1, -0.02π
700 Hz	-27.8	-17.0, -0.01π

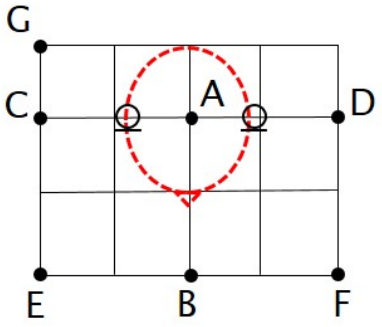

Figure 6.9: Location of the different head positions on the measuremnet grid.

in the previous section, with a regularisation factor of β =10^{-3}, were applied.

When the dummy head was located in the nominal position 'A' in Fig. 6.9, the attenuation performance was measured, as summarised in Table 6.2. The attenuation of the estimated error signals inside the control system, i.e. $\hat{\mathbf{e}}(n)$ in Eq. (6.8), is termed the "predicted" attenuation in this table, and this is almost perfectly cancelled by the adaptive controller since this calculation takes no account of background noise. The attenuation actually achieved at the microphones in the dummy head is degraded, because in the previous section, as the regularisation factor was applied to improve the robustness of the observation filter, the nearfield estimation error between the actual and estimated error signals was increased to between -20 and -30 dB. If a smaller regularisation factor for the observation filter is used, differences between the predicted and actual attenuation can be decreased. However, with β =10^{-3}, selected to give a trade-off between the robustness and accuracy of the nearfield estimation, although the achieved performance is lower than the predicted performance, an actual attenuation of greater than 15 dB is still achieved at all frequencies between 300 and 700 Hz. The real-time estimation error in Table 6.1 generally corresponds to the actual attenuation in Table 6.2 because when differences between $\mathbf{G}_e$ and $\hat{\mathbf{G}}_e$ and $\mathbf{G}_m$ and $\hat{\mathbf{G}}_m$ are negligibly small, the actual attenuation from Eq. (6.6) becomes similar to the nearfield estimation error in Eq. (5.6). Therefore, although the real-time adaptive control was implemented

between 300 and 700 Hz, a similar attenuation performance can be expected at higher frequencies based on the nearfield estimation error in Fig. 6.8.

Table 6.2: Predicted and achieved attenuation performance of the integrated active headrest system for tonal disturbances at different frequencies in the anechoic chamber when the dummy head is located in position 'A'.

Frequencies	Predicted attenuation right / left ear, (dB)	Achieved attenuation right / left ear, (dB)
300 Hz	75.9 / 78.0	22.4 / 26.1
400 Hz	94.2 / 94.8	23.3 / 30.3
500 Hz	99.1 / 98.3	23.9 / 20.4
600 Hz	82.0 / 80.7	15.9 / 28.6
700 Hz	87.1 / 87.9	15.0 / 26.0

The effect of the head-tracking device on the integrated active control system was then investigated by moving the dummy head from position 'A' to the different positions indicated in Fig. 6.9. Fig. 6.10 and Fig. 6.11 show changes in the acoustic transfer responses, $\mathbf{G}_e$, $\mathbf{G}_m$ and $\mathbf{P}_e$ for different head positions. In Fig. 6.10, $\mathbf{G}_e(1,1)$ and $\mathbf{G}_e(1,2)$ indicate the acoustic transfer responses between the microphone in the right ear of the dummy head and the right and left secondary loudspeakers, respectively. In addition, in Fig. 6.11, $\mathbf{G}_m(2,1)$ is the acoustic transfer response between the right secondary loudspeaker and monitoring microphone 2 and $\mathbf{P}_e(1,1)$ is the acoustic transfer response between the primary source and the right ear microphone. As the dummy head is moved, the acoustic responses, $\mathbf{G}_e$ and $\mathbf{P}_e$, which are directly related to the microphones in the dummy head, are significantly changed. It is also important to note, however, that the response from the secondary sources to the static monitoring microphones, $\mathbf{G}_m$ is also influenced by the head movement, due to the scattering effect of the dummy head. The use of the headtracker and the selection of accurate values for $\mathbf{G}_e$, $\mathbf{G}_m$ and $\mathbf{P}_e$ can thus significantly improve the attenuation performance and stability.

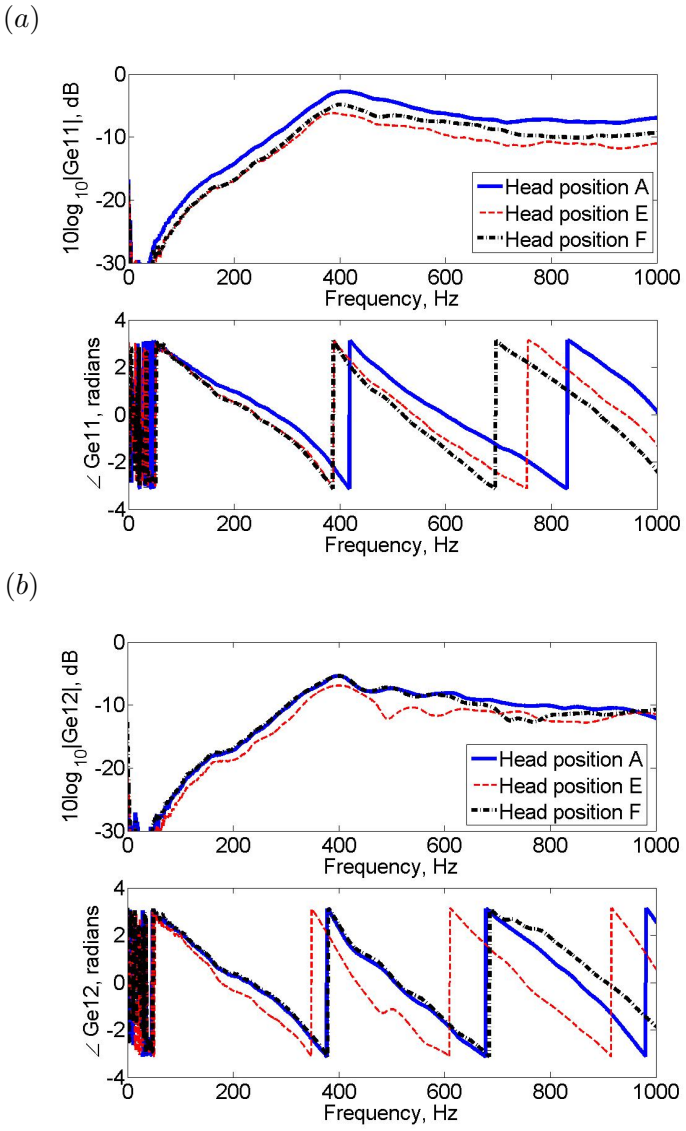

Figure 6.10: Examples of changes in acoustic transfer response, $\mathbf{G}_e$ for different dummy head positions in Fig. 6.9: (a) $\mathbf{G}_e(1,1)$ and (b) $\mathbf{G}_e(1,2)$ between the right and left secondary loudspeakers and the right error microphone at dummy head.

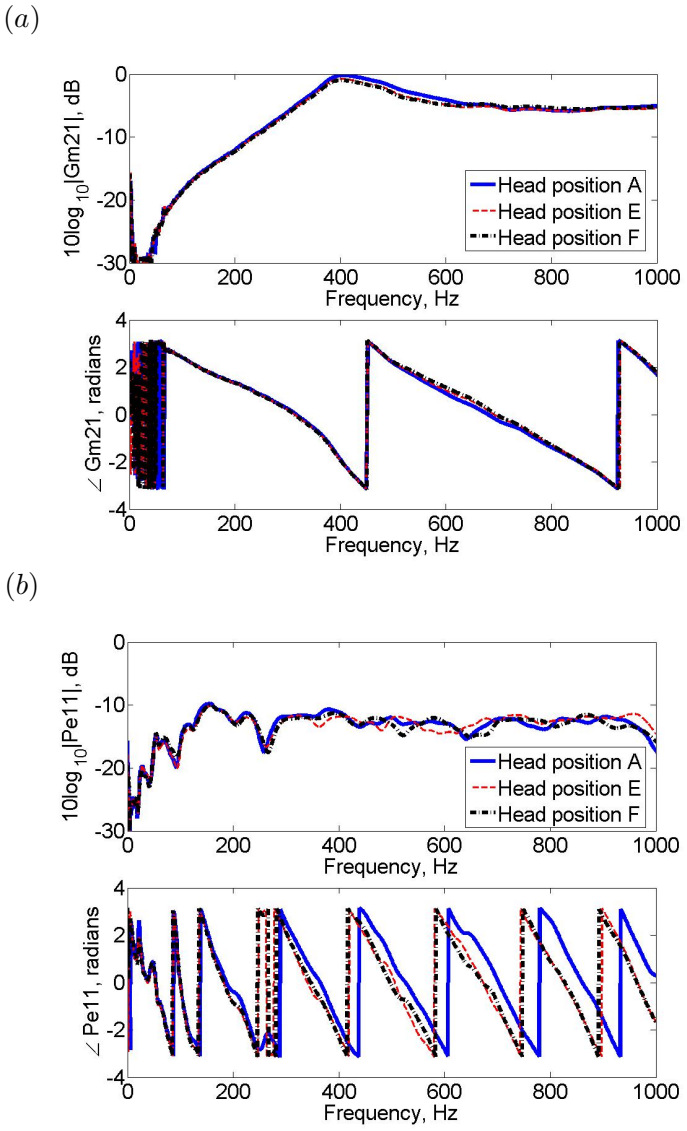

Figure 6.11: Examples of changes in acoustic transfer responses, $\mathbf{G}_m$ and $\mathbf{P}_e$ for different dummy head positions in Fig. 6.9: (a) $\mathbf{G}_m(2,1)$ between the right secondary loudspeaker and the monitoring microphone 2 and (b) $\mathbf{P}_e(1,1)$ between the primary source and the right ear microphone.

In Table 6.3, attenuation results for the active headrest system with and without the headtracker in operation are compared for the 5 different positions. When the head-tracking device is used to update the acoustic transfer responses for the different positions, the attenuation performance is generally improved for all positions. In particular, when the dummy head is moved to either position 'C', 'D' or 'E', noise enhancement, as indicated as negative attenuations, is generated without head-tracking at 700 Hz, but the performance of the active headrest system with the headtracker is significantly improved. Since the error signals are influenced by the combined effects of a number of different terms, as seen in Eq. (6.6), it is difficult to pin down the source of the variability seen in Table 6.3. Also, although in these experiments the control system remained stable as the dummy head was moved even without the head tracking, it was found in experiments at other frequencies that the control system became unstable without head-tracking and that the control system could change from being stable to being unstable even for relatively small changes in the disturbance frequency.

Fig. 6.12 shows the time history of the signal measured by the microphone in the dummy head as it is moved from position 'A' to 'D' for a disturbance frequency of either 600 Hz or 700 Hz. The measured signals can be divided into three time intervals. The first interval shows the disturbance signals without control when the dummy head is located at position 'D'. The second interval shows the error signals when the active headrest system is implemented without the head tracker. It can be seen that the disturbance signal at 600 Hz is slightly reduced but the disturbance signal at 700 Hz is enhanced due to the significant difference between the virtual and actual error signals. The head tracker is then in operation in the third time interval, and the attenuation performance is significantly improved at both frequencies.

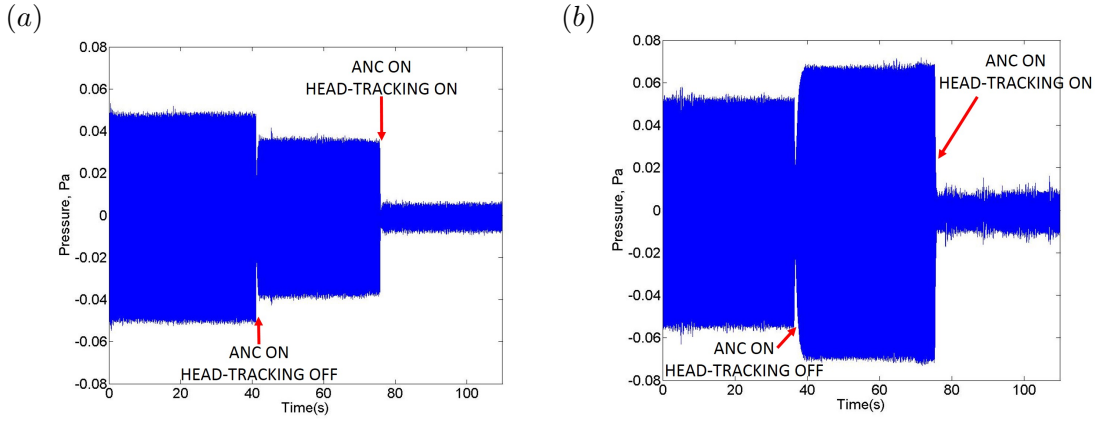

Figure 6.12: Measured signals at the right error microphone of the dummy head at position 'D' when the integrated active headrest system with the remote microphone technique and the head tracker reduces the tonal disturbance signals from a single primary source in the anechoic chamber: (a) 600 Hz, (b) 700 Hz

Table 6.3: Comparison between the actual attenuation performance of the integrated active headrest system with and without the head-tracking system when the dummy head is moved to different positions and a single loudspeaker produces a tonal disturbance at different frequencies in the anechoic chamber.

Frequencies	Position 'B', Actual attenuation, right/left ear (dB)		Position 'C', Actual attenuation, right/left ear (dB)	
	without head-tracking	with head-tracking	without head-tracking	with head-tracking
300 Hz	10.8 / 17.8	21.1 / 23.1	12.7 / 22.3	27.0 / 22.0
400 Hz	9.7 / 12.8	18.5 / 16.6	9.8 / 16.1	16.8 / 15.6
500 Hz	8.0 / 1.0	30.2 / 4.5	7.2 / 3.6	14.0 / 11.0
600 Hz	24.5 / 6.9	13.7 / 13.0	5.0 / 8.8	17.6 / 11.6
700 Hz	9.7 / 8.6	21.0 / 11.4	2.1 / -1.6	17.3 / 9.3

Frequencies	Position 'D', Actual attenuation, right/left ear (dB)		Position 'E', Actual attenuation, right/left ear (dB)	
	without head-tracking	with head-tracking	without head-tracking	with head-tracking
300 Hz	19.4 / 11.8	26.7 / 24.8	7.9 / 20.6	27.6 / 22.9
400 Hz	14.1 / 5.7	21.4 / 20.7	5.0 / 14.2	14.1 / 15.6
500 Hz	0.9 / 6.4	16.1 / 21.5	5.1 / 3.2	14.8 / 14.2
600 Hz	2.5 / 4.0	20.4 / 23.7	5.3 / 19.5	12.2 / 13.6
700 Hz	-2.5 / 4.6	16.9 / 23.2	4.0 / -0.6	22.1 / 16.0

Frequencies	Position 'F', Actual attenuation, right/left ear (dB)	
	without head-tracking	with head-tracking
300 Hz	21.5 / 12.3	28.8 / 25.2
400 Hz	15.0 / 6.1	16.1 / 14.1
500 Hz	4.3 / 14.3	22.8 / 9.5
600 Hz	13.2 / 1.1	11.0 / 19.1
700 Hz	0.8 / 3.4	39.7 / 18.9

The feasibility of this integrated active headrest system was also tested with a human listener moving their head. The installation shown in Fig. 6.6 was again used, but two physical error microphones were installed, for evaluation purposes, at the two ears of the human participant instead of in the dummy head. The active control system was implemented to reduce a 600 Hz tonal disturbance signal and the participant moved to different positions similar to those shown in Fig. 6.9. The resulting signals measured at the physical error microphones are shown in Fig. 6.13. In the second time interval, from about 10 to 20 seconds, the active headrest system is switched on and effectively attenuates the disturbance signals at the nominal position. However, it can be seen from the third time interval, from about 20 to 100 seconds, that as the listener then moves their head to different positions without the headtracker, the performance of the control system is significantly degraded. In the final step, from about 100 to 180 seconds, the

headtracker is switched on and the control system achieves an improved performance in spite of head movements. In a practical system the accuracy and speed of the response of the headtracker may be important, depending on the application, but the current system demonstrates the feasibility with a commercially available device, the Kinect, that was not specifically designed for this purpose.

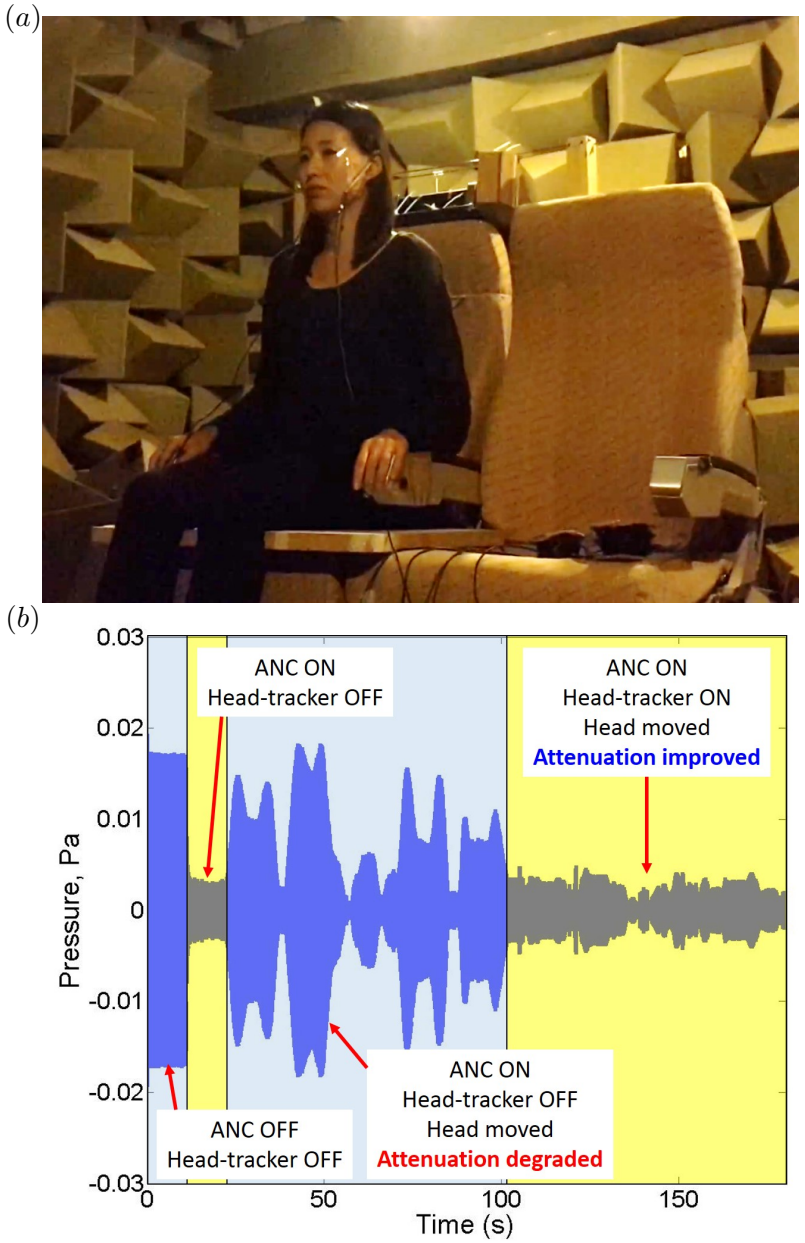

Figure 6.13: Active control of the integrated active headrest system with a human listener for reducing 600 Hz tonal disturbance signals in real-time: (a) The test installation, in which the participant has two physical error microphones in their ears for evaluation purposes and (b) the measured signals at these error microphones during active control and head-tracking.

6.4 Summary

In this chapter, the integration of both the remote microphone technique and head-tracking into an active headrest system has been investigated. An optimal feedforward active control system combined with the remote microphone technique has been formulated in the frequency domain. In addition, when the remote microphone technique is combined with an adaptive feedforward active control system, equations for the optimal attenuation performance and for the stability have also been derived. In terms of the stability, it has been concluded that in Eq. (6.13), when the effective plant response, $\mathbf{G}$, is $\hat{\mathbf{G}}_e + \hat{\mathbf{O}}_{\text{opt}}(\mathbf{G}_m - \hat{\mathbf{G}}_m)$, the eigenvalues of $\hat{\mathbf{G}}_e^{\text{H}}\mathbf{G}$ can influence the stability and thus the difference between $\mathbf{G}_m$ and $\hat{\mathbf{G}}_m$, as amplified by $\hat{\mathbf{G}}_e^{\text{H}}$ and $\hat{\mathbf{O}}_{\text{opt}}$, will threaten the stability. Moreover, the optimal performance will be degraded by differences between $\hat{\mathbf{G}}_m$, $\hat{\mathbf{G}}_e$, $\hat{\mathbf{O}}_{\text{opt}}\mathbf{d}_m$ and $\mathbf{G}_m$, $\mathbf{G}_e$, $\mathbf{d}_e$. Especially head movements can produce significant differences between the acoustic responses. Therefore, the use of a head-tracking device is investigated to improve the performance and stability when the head of a listener is moving, as $\hat{\mathbf{G}}_m$, $\hat{\mathbf{G}}_e$, $\hat{\mathbf{O}}_{\text{opt}}$ of a pre-calculated look-up table are updated.

Effects of the remote microphone technique and the head-tracking have been verified by using the measured acoustic responses at the installation in Fig. 5.13. Therefore, when the listener moved the head from position 'A' to position 'B' in Fig. 6.2, real eigenvalues of $\hat{\mathbf{G}}_e^{\text{H}}\mathbf{G}$ with and without the head-tracking have been investigated. Without the head-tracking, in the anechoic chamber, negative real eigenvalues were produced from around 280 Hz. Conversely, with the head-tracking, the real eigenvalues remained positive, which indicated the improvement of the stability. In addition, with the head-tracking, the optimal attenuation performance has been significantly improved. Without the head-tracking, enhancements of sound level have been generated at several frequencies.

The nearfield estimation achieved using the observation filter and the integration of the remote microphone technique and head-tracking have been verified through real-time experiments, when a single primary source produces tonal noise in an anechoic chamber. To find an appropriate regularisation factor for the observation filter calculation, changes in the accuracy and robustness of the nearfield estimation with different regularisation factors have been calculated. With an observation filter having the selected regularisation factor, the signals at the ears of a dummy head can be estimated in real-time from remotely installed monitoring microphones with less than -15 dB error. The adaptive active control system combined with the remote microphone technique also achieved more than 15 dB attenuation of the signals measured at the ears of the dummy head, which is located at a fixed nominal head position, for frequencies up to 700 Hz. When the dummy head was moved to different positions, the attenuation was degraded unless a headtracking device was used to update the acoustic responses using a look-up table containing pre-modelled responses.

The following chapter considers the extension of this combination of the remote microphone technique and head tracking to the active control of random broadband noise.

Chapter 7

Combining the remote microphone technique and head-tracking for local active control of broadband random noise

In the previous chapter, it has been shown that the combination of the remote microphone technique with head-tracking can significantly improve the stability and the attenuation performance of local active control of tonal noise. For stationary random broadband noise, it is required that the observation filter and the active controller are causally constrained. Therefore, in this chapter, we will investigate the nearfield estimation and attenuation performance in the time domain. The results presented here, for the active control of broadband noise, clearly demonstrate the range of frequencies over which such active control is possible.

In section 7.1, the formulation of such a control strategy in the time domain is considered first. In section 7.2, a single primary source behind the active headrest in an anechoic chamber is used to produce broadband random disturbance signals. In section 7.2, a primary source in front of the active headrest is also used. Since in the latter case, signals at the error microphones are detected in advance of signals at the monitoring microphones, the causality of the observation filter can be significantly degraded and thus an improved version of the remote microphone technique, which is referred to as the delayed remote microphone technique, is applied to overcome the non-causality from the relative geometry of the microphones to the primary source. The performance of the active headrest system with the delayed remote microphone technique is also investigated in real-time. In Appendix C, these experimental devices were also installed in the more

reverberant room and the performance of the integrated active headrest system was investigated for a more complex sound field. Finally, section 7.3 presents the summary of this chapter.

7.1 Time domain formulations for active control combined with the remote microphone technique

7.1.1 Optimal feedforward active control using the standard remote microphone technique

The block diagram of the combined algorithm, using the remote microphone technique and feedforward active control system, has been shown in Fig. 5.2. For stationary random broadband noise, it is required that the observation filter and the controller for active sound control are causally constrained. Therefore, we will investigate the nearfield estimation and attenuation performance in the time domain. In Fig. 5.2, N_v primary sources, which have a vector of source signals at the nth sample time, $\boldsymbol{v}(n) = [v_1(n), v_2(n) \ \ldots \ v_{N_v}(n)]^{\mathrm{T}}$, are assumed to produce a vector of N_e disturbance signals, $\boldsymbol{d}_e(n) = [d_{e1}(n), d_{e2}(n) \ \ldots \ d_{eN_e}(n)]^{\mathrm{T}}$ at the virtual error microphones and a vector of N_x reference sensor signals, $\boldsymbol{x}(n) = [x_1(n), x_2(n) \ \ldots \ x_{N_x}(n)]^{\mathrm{T}}$ via matrices of transfer responses, $\mathbf{P}_e$ and $\mathbf{F}$, respectively. A vector of control signals for the N_u secondary sources, $\boldsymbol{u}(n) = [u_1(n), u_2(n) \ \ldots \ u_{N_u}(n)]^{\mathrm{T}}$, is produced and the n_uth control signal, $u_{n_u}(n)$, is obtained from the sum of the contributions from the N_x reference sensor signals, each filtered by an Ith order FIR control filter with coefficients $w_{n_u n_x i}$, so that

$$u_{n_u}(n) = \sum_{n_x=1}^{N_x} \sum_{i=0}^{I-1} w_{n_u n_x i} \; x_{n_x}(n-i). \tag{7.1}$$

The control signals are transmitted to the virtual error microphones, via a matrix of plant responses, $\mathbf{G}_e$ to minimise the disturbance signals, $\boldsymbol{d}_e(n)$, and therefore, signals at the n_eth virtual error microphone, $e_{n_e}(n)$ can be written as [55]

$$e_{n_e}(n) = d_{en_e} + \sum_{n_u=1}^{N_u} \sum_{k=0}^{K-1} \sum_{n_x=1}^{N_x} \sum_{i=0}^{I-1} g_{e,n_e n_u k} \; w_{n_u n_x i} x_{n_x}(n-i-k), \tag{7.2}$$

where the matrix of plant responses, $\mathbf{G}_e$, is described by Kth order FIR filters with arbitrary accuracy and the impulse response from the n_uth secondary source to the n_eth virtual error microphone is written as $g_{e,n_e n_u k}$. Any feedback from the secondary sources to the reference sensors is assumed to be negligible, which can be ensured through the use of feedback cancellation filters, for example. When the $N_e N_u N_x$ filtered-reference signals for the error microphones are written as

$$r_{e,n_e n_u n_x}(n) = \sum_{k=0}^{K-1} g_{e,n_e n_u k}\; x_{n_x}(n-k), \tag{7.3}$$

Eq. (7.2) can be expressed by substituting Eq. (7.3) into Eq. (7.2) as

$$e_{n_e}(n) = d_{en_e} + \sum_{i=0}^{I-1} \boldsymbol{w}_i^{\mathrm{T}} \boldsymbol{r}_{en_e}(n-i), \tag{7.4}$$

where $\boldsymbol{w}_i = [w_{11i}\; w_{12i}\; \ldots\; w_{1N_xi}\; w_{21i}\; w_{22i}\; \ldots\; w_{N_uN_xi}]^{\mathrm{T}}$ and $\boldsymbol{r}_{en_e} = [r_{e,n_e11}\; r_{e,n_e12}\; \ldots\; r_{e,n_e1N_x}\; r_{e,n_e21}\; r_{e,n_e22}\; \ldots\; r_{e,n_eN_uN_x}]^{\mathrm{T}}$. Therefore, the vector of N_e error signals, $\boldsymbol{e}(n) = [e_1(n), e_2(n)\; \ldots\; e_{N_e}(n)]^{\mathrm{T}}$ at the virtual error microphones can be expressed as

$$\boldsymbol{e}(n) = \boldsymbol{d}_e(n) + \boldsymbol{R}_e(n)\boldsymbol{w}, \tag{7.5}$$

where

$$\boldsymbol{R}_e(n) = \begin{pmatrix} \boldsymbol{r}_{e1}^{\mathrm{T}}(n) & \boldsymbol{r}_{e1}^{\mathrm{T}}(n-1) & \cdots & \boldsymbol{r}_{e1}^{\mathrm{T}}(n-I+1) \\ \boldsymbol{r}_{e2}^{\mathrm{T}}(n) & \boldsymbol{r}_{e2}^{\mathrm{T}}(n-1) & \cdots & \boldsymbol{r}_{e2}^{\mathrm{T}}(n-I+1) \\ \vdots & \vdots & \ddots & \vdots \\ \boldsymbol{r}_{en_e}^{\mathrm{T}}(n) & \boldsymbol{r}_{en_e}^{\mathrm{T}}(n-1) & \cdots & \boldsymbol{r}_{en_e}^{\mathrm{T}}(n-I+1) \end{pmatrix}, \tag{7.6}$$

and $\boldsymbol{w} = [\boldsymbol{w}_0^{\mathrm{T}}\; \boldsymbol{w}_1^{\mathrm{T}}\; \ldots\; \boldsymbol{w}_{I-1}^{\mathrm{T}}]^{\mathrm{T}}$ which is a $N_uN_xI \times 1$ vector of control filter coefficients.

When the direct measurement of the virtual error signals, $\boldsymbol{e}(n)$ is infeasible, they can be estimated from a vector of N_m monitoring microphone signals, $\boldsymbol{m}(n) = [m_1(n), m_2(n)\; \ldots\; m_{N_m}(n)]^{\mathrm{T}}$, which is equal to

$$\boldsymbol{m}(n) = \boldsymbol{d}_m(n) + \boldsymbol{R}_m(n)\boldsymbol{w}, \tag{7.7}$$

where $\boldsymbol{d}_m(n) = [d_{m1}(n), d_{m2}(n)\; \ldots\; d_{mN_m}(n)]^{\mathrm{T}}$ is a vector of N_m disturbance signals at the monitoring microphones and $\boldsymbol{R}_m(n)$ has a similar form to $\boldsymbol{R}_e(n)$ in Eq. (7.6), except that the impulse response from the n_uth secondary source to the n_mth monitoring microphone, g_{m,n_mn_uk}, in the plant response, $\mathbf{G}_m$, is used in Eq. (7.3), instead of g_{e,n_en_uk}. In practice, the true plant responses, $\mathbf{G}_e$ and $\mathbf{G}_m$, are not usually available and therefore estimates of the plant responses are used in the controller, as denoted by $\hat{\mathbf{G}}_e$ and $\hat{\mathbf{G}}_m$, where the superscript $\hat{}$ represents an estimate of an actual value. Similarly $\boldsymbol{d}_m(n)$ and $\boldsymbol{d}_e(n)$ are measured in practice as $\hat{\boldsymbol{d}}_m(n)$ and $\hat{\boldsymbol{d}}_e(n)$.

If $\hat{\boldsymbol{O}}$ is the estimated observation filter used to calculate $\hat{\boldsymbol{d}}_e(n)$ from $\hat{\boldsymbol{d}}_m(n)$, then the estimated error signals at the virtual error microphones, $\hat{\boldsymbol{e}}(n)$, can be written as

$$\hat{\boldsymbol{e}}(n) = \hat{\boldsymbol{d}}_e(n) + \hat{\boldsymbol{R}}_e(n)\boldsymbol{w} = \hat{\boldsymbol{O}}\hat{\tilde{\boldsymbol{d}}}_m(n) + \hat{\boldsymbol{R}}_e(n)\boldsymbol{w} = \hat{\boldsymbol{O}}\{\boldsymbol{m}(n) - \hat{\boldsymbol{R}}_m(n)\boldsymbol{w}\}' + \hat{\boldsymbol{R}}_e(n)\boldsymbol{w}, \quad (7.8)$$

where $\hat{\boldsymbol{O}}$ is the matrix of observation filter coefficients in the time domain, $\hat{\tilde{\boldsymbol{d}}}_m(n)$ represents the $JN_m \times 1$ vector of estimated current and past disturbance signals at the monitoring microphones, and similarly $\{\ \}'$ represents the $JN_m \times 1$ vector, which is built up from the J current and past samples corresponding to the the signals in the braces.

The matrix of observation filter coefficients, $\hat{\boldsymbol{O}}$, is defined as

$$\hat{\boldsymbol{O}} = [\boldsymbol{O}_1^{\mathrm{T}}\ \boldsymbol{O}_2^{\mathrm{T}}\ \ldots\ \boldsymbol{O}_{N_e}^{\mathrm{T}}]^{\mathrm{T}}, \quad (7.9)$$

where

$$\boldsymbol{O}_{n_e} = [\boldsymbol{O}_{n_e1}^{\mathrm{T}}\ \boldsymbol{O}_{n_e2}^{\mathrm{T}}\ \ldots\ \boldsymbol{O}_{n_eN_m}^{\mathrm{T}}]^{\mathrm{T}}, \quad (7.10)$$

and $\boldsymbol{O}_{n_en_m}$ is a vector of coefficients defining the observation filter between the n_mth monitoring microphone and the n_eth error microphone, which is modelled by an FIR filter with J coefficients and expressed as

$$\boldsymbol{O}_{n_en_m} = [O_{n_en_m0}\ O_{n_en_m1}\ \ldots\ O_{n_en_m(J-1)}]^{\mathrm{T}}. \quad (7.11)$$

In addition, the $JN_m \times 1$ vector of estimated current and past disturbance signals at the monitoring microphones, $\hat{\tilde{\boldsymbol{d}}}_m(n)$, is defined as

$$\hat{\tilde{\boldsymbol{d}}}_m(n) = [\hat{\tilde{\boldsymbol{d}}}_{m1}^{\mathrm{T}}(n)\ \hat{\tilde{\boldsymbol{d}}}_{m2}^{\mathrm{T}}(n)\ \ldots\ \hat{\tilde{\boldsymbol{d}}}_{mN_m}^{\mathrm{T}}(n)]^{\mathrm{T}}, \quad (7.12)$$

where

$$\hat{\tilde{\boldsymbol{d}}}_{mn_m}(n) = [\hat{d}_{mn_m}(n)\ \hat{d}_{mn_m}(n-1)\ \ldots\ \hat{d}_{mn_m}(n-J-1)]^{\mathrm{T}}. \quad (7.13)$$

Since the active control system attempts to minimise the estimated error signals, $\hat{\boldsymbol{e}}(n)$, the accuracy of the nearfield estimation using the observation filter, $\hat{\boldsymbol{O}}$, can be an important factor in terms of the actual attenuation at the virtual error microphones. When

the number of monitoring microphones (N_m) is larger than the number of virtual error microphones (N_e), the problem is mathematically overdetermined and the equation for the optimal observation filter, $\boldsymbol{O}_{\text{opt}}$, can be obtained, using the derivation detailed in Appendix A, as

$$\boldsymbol{O}_{\text{opt}} = \left(\{E[\boldsymbol{d}_m^{'}(n)\boldsymbol{d}_m^{'\text{T}}(n) + \beta\mathbf{I}^{'}]\}^{-1}E[\boldsymbol{d}_m^{'}(n)\boldsymbol{d}_e^{\text{T}}(n)]\right)^{\text{T}}, \tag{7.14}$$

where $\boldsymbol{d}_m^{'}(n)$ again represents the $JN_m \times 1$ vector of current and past monitoring microphone disturbance signals, $E[\,]$ is the expectation operator, β is a positive real effort-weighting parameter to improve the robustness of the optimal observation filter, and $\mathbf{I}^{'}$ is the identity matrix having the same dimensions as $\boldsymbol{d}_m^{'}(n)\boldsymbol{d}_m^{'\text{T}}(n)$. The regularisation parameter, β, is chosen to give a reasonable trade-off between the accuracy with which the disturbance signals are estimated at the virtual microphone positions and the robustness of this estimate to small changes in these positions and to the locations of the primary sources. If $\boldsymbol{d}_m^{'}(n)$ and $\boldsymbol{d}_e(n)$ are measured in preliminary experiments before active control and it is assumed that $\boldsymbol{d}_m^{'}(n)$ and $\boldsymbol{d}_e(n)$ are known perfectly, $\boldsymbol{O}_{\text{opt}}$ can be calculated from Eq. (7.14) using the measured auto and cross correlation functions of these signals.

The causally constrained optimal controller, $\boldsymbol{w}_{\text{opt}}$, can be derived by minimising the estimated error signals, $\hat{\boldsymbol{e}}(n)$ at the virtual error microphones. In practice, however, it is also necessary to include a term in the cost function that is proportional to the effort required by the control filter, in order to improve the robustness of this control filter. Therefore, the cost function, J_5 can be written as

$$J_5 = \text{trace}\left\{E\left[\hat{\boldsymbol{e}}(n)\ \hat{\boldsymbol{e}}^{\text{T}}(n) + \rho\ \boldsymbol{w}\boldsymbol{w}^{\text{T}}\right]\right\}, \tag{7.15}$$

where ρ is a positive real effort-weighting parameter for the controller. To minimise this cost function, it is required that Eq. (7.8) is expressed in terms of $\boldsymbol{w}$ by substituting Eq. (7.7) into Eq. (7.8) to give

$$\hat{\boldsymbol{e}}(n) = \hat{\boldsymbol{O}}\boldsymbol{d}_m^{'}(n) + [\hat{\boldsymbol{O}}\Delta\boldsymbol{R}_m^{'}(n) + \hat{\boldsymbol{R}}_e(n)]\boldsymbol{w}, \tag{7.16}$$

where $\Delta\boldsymbol{R}_m^{'}(n)\boldsymbol{w} = \{[\boldsymbol{R}_m(n) - \hat{\boldsymbol{R}}_m(n)]\boldsymbol{w}\}^{'}$. Therefore, the causally constrained optimal controller, $\boldsymbol{w}_{\text{opt}}$, with the practical estimate of the optimal observation filter, $\hat{\boldsymbol{O}}_{\text{opt}}$, can be obtained, using the derivation detailed in Appendix A, as

$$\boldsymbol{w}_{\text{opt}} = -\{E[\boldsymbol{R}^{\text{T}}(n)\boldsymbol{R}(n) + \rho\mathbf{I}]\}^{-1}E[\boldsymbol{R}^{\text{T}}(n)\hat{\boldsymbol{O}}_{\text{opt}}\boldsymbol{d}_m^{'}(n)], \tag{7.17}$$

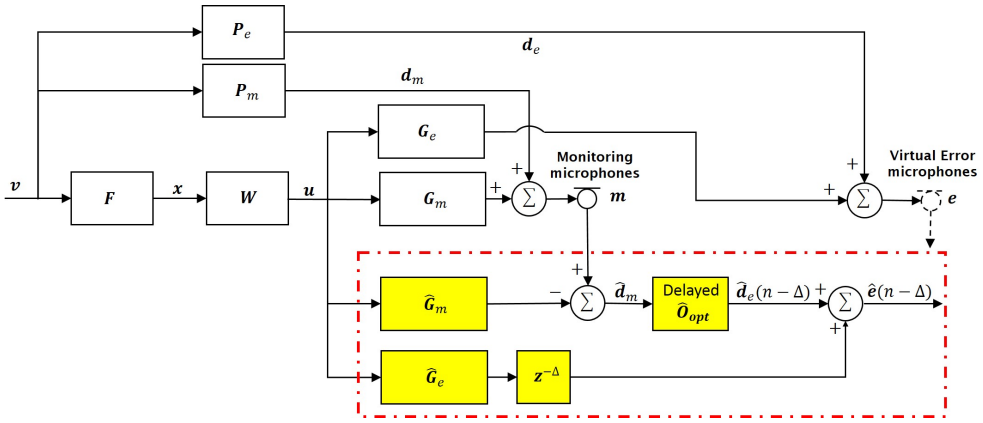

Figure 7.1: Block diagram of the feedforward active control algorithm, combined with the delayed remote microphone technique in a dashed dot rectangle.

where $\boldsymbol{R}(n) = [\hat{\boldsymbol{O}}_{\text{opt}}\Delta\boldsymbol{R}'_m(n) + \hat{\boldsymbol{R}}_e(n)]$ and $\mathbf{I}$ is the identity matrix having the same dimensions as $\boldsymbol{R}^{\text{T}}(n)\boldsymbol{R}(n)$.

7.1.2 Optimal feedforward active control using the delayed remote microphone technique

When the monitoring microphones can detect the disturbance signals in advance of the virtual error microphones, the causality between the virtual error microphones and the monitoring microphones can be maintained and the standard remote microphone technique in the previous section can be applied to estimate the virtual error signals accurately. However, when the disturbance signals arrive at the virtual error microphones earlier than at the monitoring microphones, due to the relative geometry of the virtual error microphones, the monitoring microphones and the primary sources, the causality between the virtual error and monitoring microphones would be significantly degraded. This is because the estimation of 'future' random signals at the virtual error microphones from the monitoring microphones may not be achievable.

To overcome this limitation, an improved remote microphone technique called the 'delayed' remote microphone technique, suggested in [105], is applied to the feedforward active control algorithm, as shown in Fig. 7.1. In the delayed remote microphone technique, the vector of N_m monitoring microphone signals, $\boldsymbol{m}(n)$, is used to estimate the disturbance signals at the virtual error microphones with a delay of Δ samples, $\hat{\boldsymbol{d}}_e(n-\Delta)$ with the delayed optimal observation filter, $\boldsymbol{O}_{\text{opt,D}}$ which is given by

$$\boldsymbol{O}_{\text{opt,D}} = \left(\{E[\boldsymbol{d}'_m(n)\boldsymbol{d}'^{\text{T}}_m(n) + \beta\mathbf{I}']\}^{-1}E[\boldsymbol{d}'_m(n)\boldsymbol{d}^{\text{T}}_e(n-\Delta)]\right)^{\text{T}}. \tag{7.18}$$

By minimising the cost function $J_5 = trace\left\{ E\left[\hat{\boldsymbol{e}}(n-\Delta)\ \hat{\boldsymbol{e}}^{\mathrm{T}}(n-\Delta) + \rho\ \boldsymbol{w}\boldsymbol{w}^{\mathrm{T}}\right] \right\}$, the causally constrained optimal controller with the delayed remote microphone technique, $\boldsymbol{w}_{\mathrm{opt,D}}$ is given by

$$\boldsymbol{w}_{\mathrm{opt,D}} = -\{E[\boldsymbol{R}_{\mathrm{D}}^{\mathrm{T}}(n)\boldsymbol{R}_{\mathrm{D}}(n) + \rho\mathbf{I}]\}^{-1}E[\boldsymbol{R}_{\mathrm{D}}^{\mathrm{T}}(n)\hat{\boldsymbol{O}}_{\mathrm{opt,D}}\boldsymbol{d}_m^{'}(n)], \tag{7.19}$$

where $\boldsymbol{R}_{\mathrm{D}}(n) = [\hat{\boldsymbol{O}}_{\mathrm{opt,D}}\Delta\boldsymbol{R}_m^{'}(n) + \hat{\boldsymbol{R}}_e(n-\Delta)]$. When the disturbance signals from the primary sources are stationary, $\boldsymbol{w}_{\mathrm{opt,D}}$ is almost identical to $\boldsymbol{w}_{\mathrm{opt}}$ and active control at the virtual error microphones can still be achieved. The selection of Δ in practice is discussed in the following section.

7.1.3 Adaptive control of broadband random sound

The filtered-reference LMS algorithm for feedforward control combined with the remote microphone technique has been investigated for control of tonal disturbance signals in Chapter 6 and the block diagram of the adaptive control algorithm was shown in Fig. 6.1. In contrast to the remote active control of tonal noise, where only the in phase and quadrature components of a single frequency reference signal have to be adapted to achieve control, the real-time control of broadband random noise requires digital filters for the controller, plant models and observation filter, in order to achieve control over a range of frequencies.

For the standard remote microphone technique, the generalised multichannel filtered-reference LMS algorithm [55] used to update the control signal filters is

$$\boldsymbol{w}(n+1) = \boldsymbol{w}(n) - \alpha\hat{\boldsymbol{R}}_e^{\mathrm{T}}(n)\hat{\boldsymbol{e}}(n). \tag{7.20}$$

To analyse the convergence properties of this algorithm, a similar way in section 6.1 is used and Eq. (7.8) is thus substituted into Eq. (7.20) to give

$$\boldsymbol{w}(n+1) = \boldsymbol{w}(n) - \alpha\left[\hat{\boldsymbol{R}}_e^{\mathrm{T}}(n)\hat{\boldsymbol{O}}_{\mathrm{opt}}\boldsymbol{d}_m^{'}(n) + \hat{\boldsymbol{R}}_e^{\mathrm{T}}(n)\boldsymbol{R}(n)\boldsymbol{w}(n)\right]. \tag{7.21}$$

If the algorithm is stable, the expectation value of the term in square brackets in Eq. (7.21) is zero after a set of control filter coefficients is converged. Therefore, the steady state vector of control signals after the convergence, $\boldsymbol{w}_\infty$, is defined to be

$$\boldsymbol{w}_\infty = -\{E[\hat{\boldsymbol{R}}_e^{\mathrm{T}}(n)\boldsymbol{R}(n)]\}^{-1}E[\hat{\boldsymbol{R}}_e^{\mathrm{T}}(n)\hat{\boldsymbol{O}}_{\mathrm{opt}}\boldsymbol{d}_m^{'}(n)]. \tag{7.22}$$

In general, $\hat{\boldsymbol{R}}_e$, which is the matrix of reference signals filtered by the internal model, $\hat{\mathbf{G}}_e$, is not same with $\boldsymbol{R}(n)$ and $\boldsymbol{w}_\infty$ would not be equal to $\boldsymbol{w}_{\text{opt}}$ with $\rho = 0$ in Eq. (7.17).

By subtracting Eq. (7.22) from both sides of Eq. (7.21) and assuming that the control filter coefficients are changing slowly compared with the timescale of the filtered reference dynamics and so the variation of $\boldsymbol{w}(n)$ is statistically independent of $\hat{\boldsymbol{R}}_e^{\text{T}}(n)\boldsymbol{R}(n)$ [55], Eq. (7.21) can be written as

$$E[\boldsymbol{w}(n+1) - \boldsymbol{w}_\infty] = \left[\boldsymbol{I} - \alpha E[\hat{\boldsymbol{R}}_e^{\text{T}}(n)\boldsymbol{R}(n)]\right] E[\boldsymbol{w}(n) - \boldsymbol{w}_\infty]. \tag{7.23}$$

When the potentially complex eigenvalues of $E[\hat{\boldsymbol{R}}_e^{\text{T}}(n)\boldsymbol{R}(n)]$ are denoted by λ_{R_e}, from the principal coordinates analysis presented by Elliott [55], the condition for the stability of the adaptive algorithm is given by

$$0 < \alpha < \frac{2\text{Re}(\lambda_{R_e})}{|\lambda_{R_e}|^2} \quad \text{for all } \lambda_{R_e}. \tag{7.24}$$

Therefore, a sufficient condition for the convergence is that the real parts of all the eigenvalues must be positive and using a frequency domain analysis, a sufficient condition for the stability of this adaptive algorithm can also be described as Eq. (6.13) [26, 55].

When the headtracker is used as suggested in Fig. 6.2, $\hat{\mathbf{G}}_m$, $\hat{\mathbf{G}}_e$ and $\hat{\boldsymbol{O}}_{\text{opt}}$ are identified as causal filters from a series of experiments conducted prior to control, as the dummy head is located at each of different positions. These filters are then stored in the control system.

For the filtered-reference LMS algorithm combined with the delayed remote microphone technique [105], the delayed filtered reference signals are multiplied with the delayed estimated error signals to adapt the controller, as illustrated in Fig. 7.2. The combined algorithm can thus be written as

$$\boldsymbol{w}_{\text{D}}(n+1) = \boldsymbol{w}_{\text{D}}(n) - \alpha\hat{\boldsymbol{R}}_e^{\text{T}}(n-\Delta)\hat{\boldsymbol{e}}(n-\Delta). \tag{7.25}$$

7.2 Real-time implementation for active control of broadband random disturbances

7.2.1 Experimental arrangement

A similar experimental arrangement to that for the active control of tonal noise in Fig. 6.6 has been used to reduce broadband random disturbances in an anechoic chamber. A headrest system is used for the demonstration, with two secondary loudspeakers

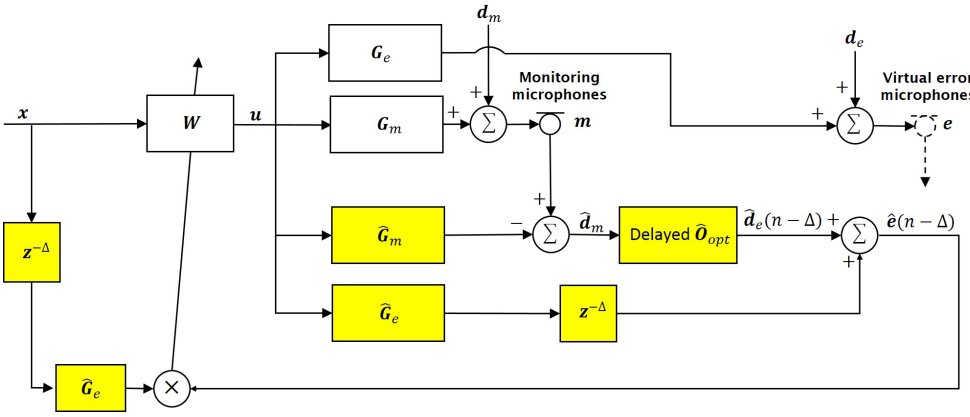

Figure 7.2: Block diagram of the filtered-reference LMS algorithm for adaptive feedforward control, combined with the delayed remote microphone technique.

at the sides of the headrest and a static array of four monitoring microphones, #13, #22, #23 and #16, as shown in Fig. 5.13. These microphones were about 18 cm and 27 cm, respectively, away from the centre of the dummy head when it was in the nominal position, which is shown as position‘ A’ on the grid in Fig. 6.9. The remote microphone technique was also used to estimate the pressures at the ears of the dummy head from those at the monitoring microphones. The responses from the loudspeakers to the microphones at the ear positions of a dummy head, which are required to implement this technique, were measured in an initial calibration phase, when the dummy head was moved to each of 20 pre-defined positions on the grid in Fig. 6.9.

In a series of experiments conducted prior to control, all of these three responses, $\hat{\mathbf{G}}_m$, $\hat{\mathbf{G}}_e$ and $\hat{\boldsymbol{O}}_{\text{opt}}$, are identified as FIR filters from measurements made with the dummy head in each of the 20 separate positions on the grid and these are then stored in the control system. The 8 individual observation filters in the matrix $\hat{\boldsymbol{O}}_{\text{opt}}$ that were used in the arrangement here each had 128 coefficients and both $\hat{\mathbf{G}}_m$ and $\hat{\mathbf{G}}_e$ were modelled here as 64 coefficient FIR filters, at each of the 20 dummy head positions. The control system used 128 coefficients for each of the four control filters and was implemented on a dSPACE system at a sampling rate of 3 kHz, with reconstruction filters having a cut-off frequency of 1 kHz. A Microsoft Kinect (Kinect 1.0 for Windows), was used for head tracking and positioned about 1.5 m away from the dummy head. The information from the Kinect was decoded in real-time using plug-in software implemented in MaxMSP and this was passed to the dSPACE controller, which already stored the various plant responses and pre-calculated observation filters for the 20 head positions. Reference signals related to the primary sources were assumed to be observed directly in these experiments. Therefore the usual causality issues associated with the time-advance of the reference signals and the coherence between the reference and disturbance signals are not considered in this experiment. However, in many practical applications, such as the control of road noise in cars [14], this is not realistic and the reference signals have to

be obtained from carefully located sensors placed on the vehicle. The type and position of the sensors is still a matter of active investigation in this and other applications. In Chapter 8, the effects of the choice of reference signals on the attenuation performance of active control are investigated from the measurement in a vehicle. The equipment used here is detailed in Appendix D.

7.2.2 Real-time adaptive control with the standard remote microphone technique and head-tracking

The loudspeaker acting as the primary source was initially located behind the headrest, as in Fig. 6.6, and driven by band-limited Gaussian white noise between 200 and 1,000 Hz. The dummy head was in the nominal position, 'A' in Fig. 6.9. For the remote microphone technique in the time domain, the optimal observation filter with the causality constraint was obtained from Eq. (7.14) with $\beta = 10^{-3}$, which was chosen based on the trade-off between the accuracy of the nearfield estimation and the robustness to any uncertainties, as studied in Chapter 5. The impulse responses of $\hat{\boldsymbol{O}}_{11}$ and $\hat{\boldsymbol{O}}_{12}$ among chosen from the 8 FIR filters of $\hat{\boldsymbol{O}}_{opt}$ in the time domain are shown in Fig. 7.3. The elements, $\hat{\mathbf{O}}(1,1)$ and $\hat{\mathbf{O}}(1,2)$, of the optimised observation filters in the frequency domain without the causality constraint are also transformed by inverse Fourier transform and compared with the impulse responses of $\hat{\boldsymbol{O}}_{11}$ and $\hat{\boldsymbol{O}}_{12}$ in Fig. 7.3. The impulse responses of $\hat{\boldsymbol{O}}_{11}$ and $\hat{\boldsymbol{O}}_{12}$ are similar to the causal response of $\hat{\mathbf{O}}(1,1)$ and $\hat{\mathbf{O}}(1,2)$ but the non-causal responses of $\hat{\mathbf{O}}(1,1)$ and $\hat{\mathbf{O}}(1,2)$ are excluded from the the impulse response of $\hat{\boldsymbol{O}}_{11}$ and $\hat{\boldsymbol{O}}_{12}$ due to the causality constraint.

The accuracy of the nearfield estimation of the causally constrained observation filter can be compared with that of the non-causal filter, as shown in Fig. 7.4. It can be seen that although the non-causal components are excluded from the the causal constrained observation filter and the nearfield estimation error is thus slightly increased compared to that of the non-causal filter, the remote microphone technique with the causality constraint still performs well. This is because the primary source was installed behind the headrest and so the monitoring microphones can detect disturbance signals in advance of the error microphones.

(*a*)

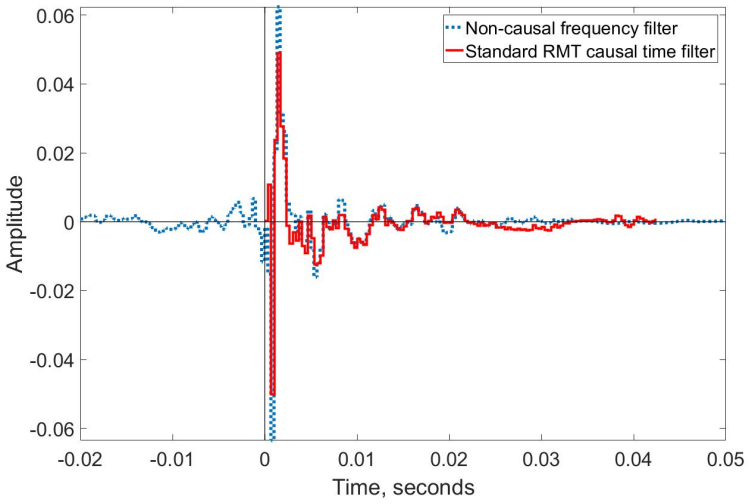

(*b*)

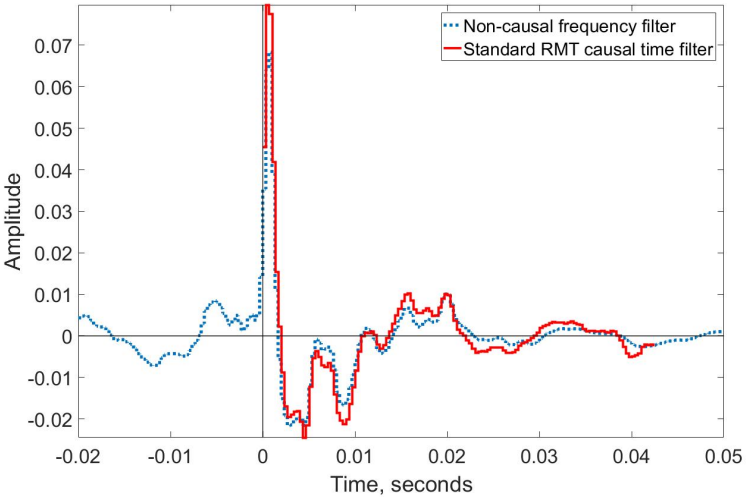

Figure 7.3: The impulse responses of $\hat{\boldsymbol{O}}_{11}$, upper graph, and $\hat{\boldsymbol{O}}_{12}$, lower graph, chosen from the 8 FIR filters of the causal constrained $\hat{\boldsymbol{O}}_{opt}$ (Solid line). Also shown are the inverse Fourier transformed $\hat{\mathbf{O}}(1,1)$, upper graph, and $\hat{\mathbf{O}}(1,2)$, lower graph, for $\hat{\mathbf{O}}_{opt}$ calculated in the frequency domain, without the causal constraint (Dashed line).

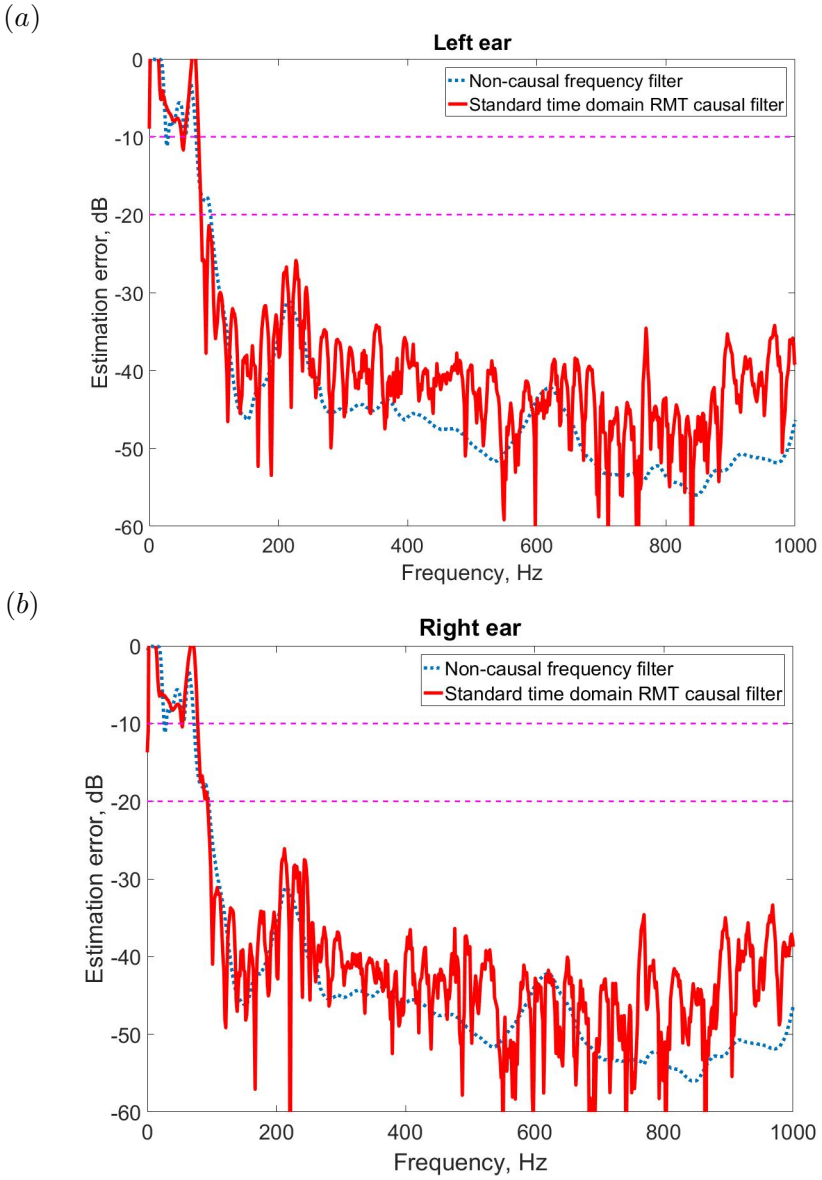

Figure 7.4: Comparison of the nearfield estimation of the standard remote microphone technique, RMT with the causality constraint (solid line) to that with the non-causal frequency filter (dashed line).

The attenuation performance of the causally constrained controller is also investigated. The power spectral density of the pressure signals from the microphones in the left and right-hand ear positions of the dummy head was measured, as shown by the solid lines in Fig. 7.5. The dummy head was also located at the nominal position, 'A' in Fig. 6.9 and this was identified by the head tracker before control and the appropriate set of observation filters and plant response filters was used in the control algorithm to attenuate the pressure at the two ears. As a benchmark for the best possible performance with this arrangement, control was also implemented using the signals from the microphones mounted in the dummy head directly as error signals, with the results also shown by the dot-dashed lines in Fig. 7.5. Reductions in pressure of about 20 dB are observed at the error microphones on both sides of the dummy head after active control, from about 300 Hz to about 1 kHz. Below 300 Hz, the small loudspeakers used as secondary sources are not very efficient and lower levels of control are achieved. The results obtained using the monitoring microphones and remote microphone technique, as shown by the dashed lines in Fig. 7.5, are almost as good as those obtained by directly minimising the signal from the error microphones in the dummy head in this configuration.

The head tracking performance was then tested by moving the dummy head from the nominal position to other head positions. Figure 7.6 shows the time history of the signal from the right-hand ear of the dummy head after it had been moved to position 'E' on the grid shown in Fig. 6.9, which is about 14 cm from the nominal head position, 'A'. During the first interval shown in Fig. 7.6(a), up to 30 seconds, the active control system is switched off, so that the measured pressure is just due to the disturbance from the loudspeaker acting as the primary source behind the headrest. The control system is then switched on, from 30 to 60 seconds, but with the observation filter and plant responses appropriate to the head position still being in the nominal head position, 'A'. The results shows some reduction in level, but this is not as great as when the head tracker was switched on, after 60 seconds. Fig. 7.6 shows that once the head tracking system is enabled at 60 seconds, the correct head position is acquired and the observation filter and plant responses are updated within a second or so to give good control.

The spectrum of the pressure at the right-hand ear of the dummy head is shown in Fig. 7.6(b) under these three conditions. It can be seen that without head tracking, attenuations of about 10 dB are achieved up to only about 600 Hz, whereas with head tracking enabled, attenuations similar to those achieved with the head at the nominal position, in Fig. 7.5, are obtained. Experiments have also been performed moving the dummy head to other locations. For instance, when the dummy is in position 'G' , the results are shown in Fig. 7.7, which have similar results to those shown in Fig. 7.6, except that the disturbance signal is actually enhanced at higher frequencies above around 700 Hz, before head tracking is implemented and the filters updated. If the head movement is too large, it is also possible for the control system to become unstable without head tracking.

(*a*)

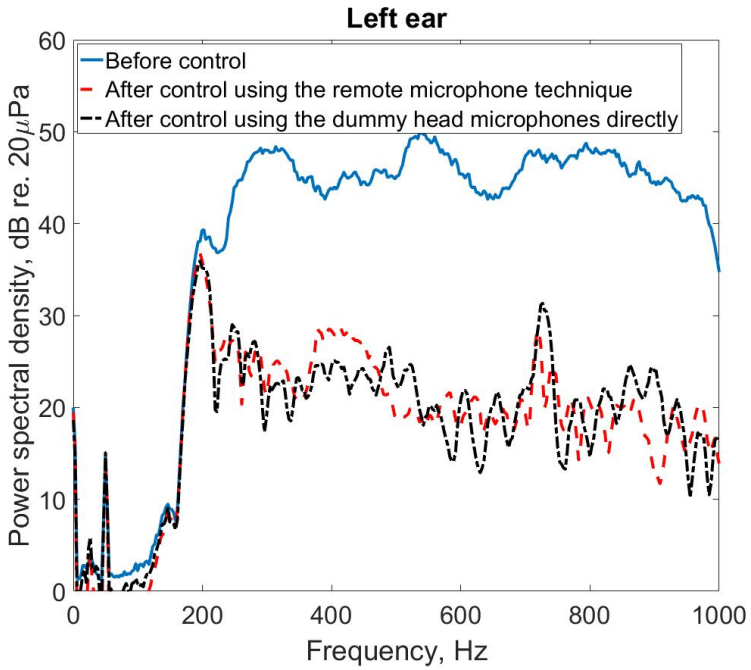

(*b*)

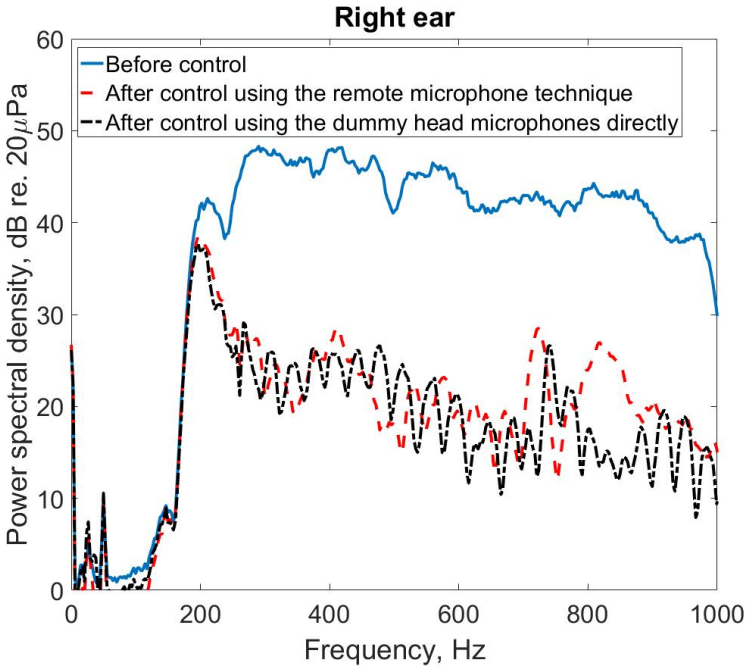

Figure 7.5: Power spectral density of the signal measured at the microphones in the left and right hand side of the dummy head when it was in the nominal position and the primary source was behind the headrest before control, solid line, after control using the monitoring microphones and observation filter to estimate the signal at the ear position using the remote microphone technique, dashed line, and, for reference, when the microphones in the dummy head themselves were used as the error signals in the control algorithm, dot-dashed line.

(*a*)

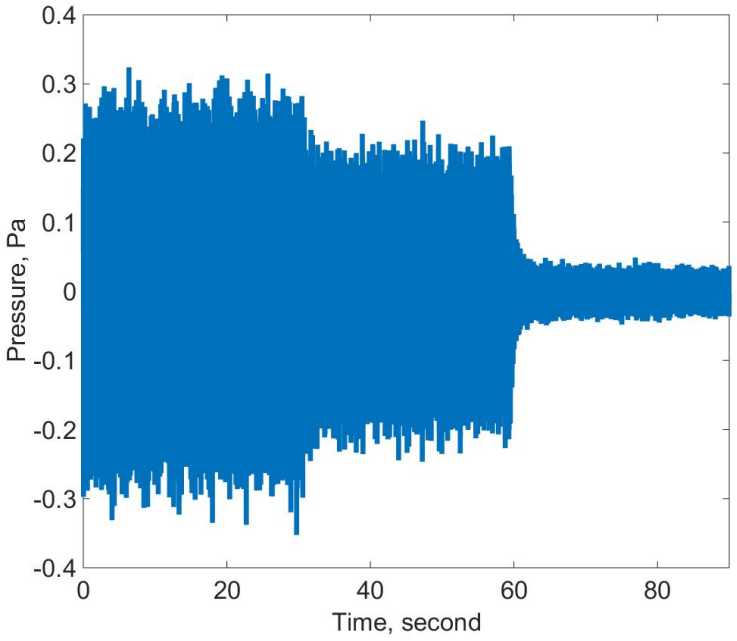

(*b*)

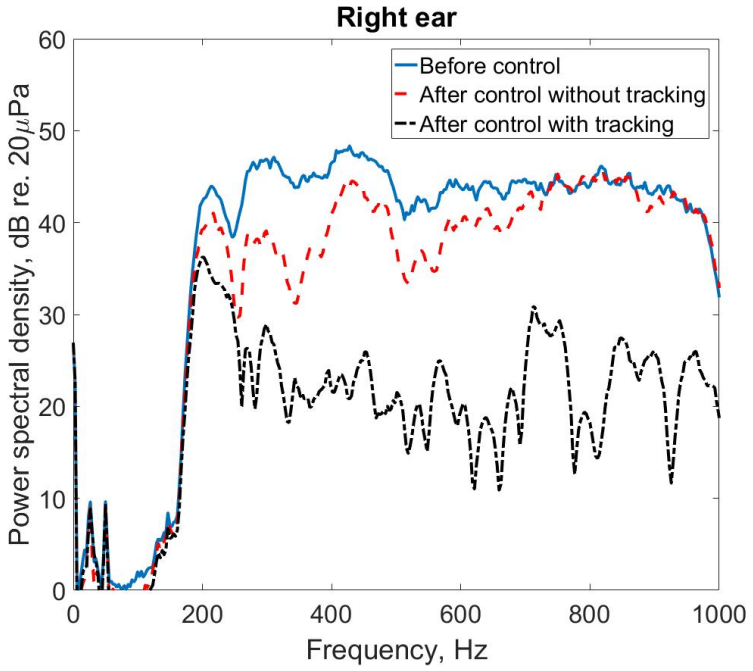

Figure 7.6: Time history of the pressure signal measured in the right-hand ear of the dummy head, (a), when in position 'E' before control, up to 30 seconds, when control is implemented with the observation filter and plant responses appropriate for the nominal head position, from 30 to 60 seconds, and when the head tracker is enabled so that the correct head position is identified, after 60 seconds. The power spectral density of the signal at this microphone is also shown, (b), before control, after control but without head tracking and after control with the head tracker enabled.

(*a*)

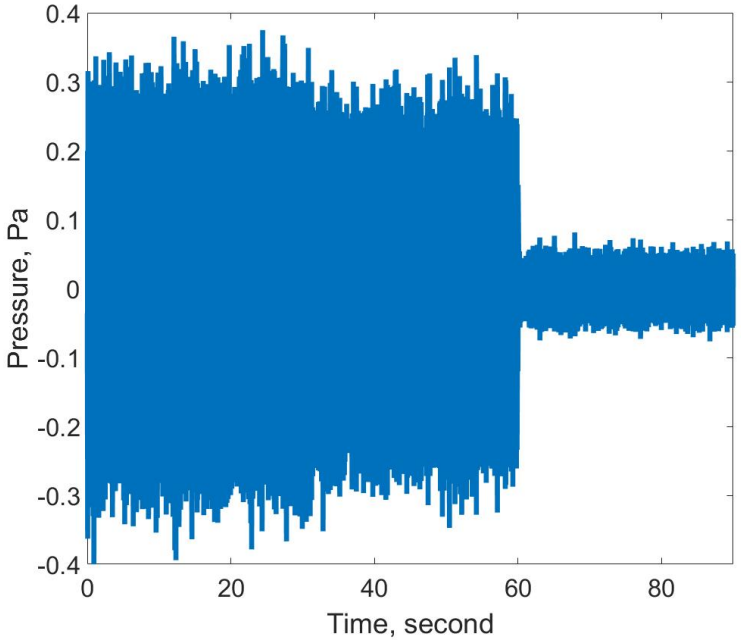

(*b*)

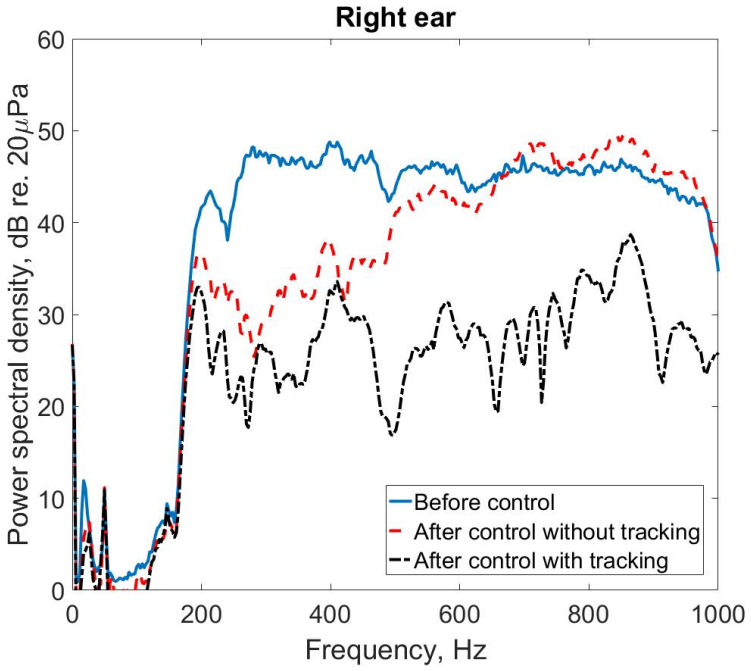

Figure 7.7: Time history of the pressure signal measured in the right-hand ear of the dummy head, (a), when in position 'G' before control, up to 30 seconds, when control is implemented with the observation filter and plant responses appropriate for the nominal head position, from 30 to 60 seconds, and when the head tracker is enabled so that the correct head position is identified, after 60 seconds. The power spectral density of the signal at this microphone is also shown, (b), before control, after control but without head tracking and after control with the head tracker enabled.

Further experiments have been conducted with a human listener moving their head slowly within the area defined by the grid above, when they were wearing in-ear microphones to monitor the pressure at their ear positions. The results are shown in Fig. 7.8.

Without head tracking, the zones of quiet are fixed, and the subjective impression of listening in the headrest is that of moving in and out of the zones of quiet, as the head is moved by 5 cm or so. With head tracking, the zones of quiet are moved with the ear locations as the head position is changed and good cancellation is maintained even during head motion. Control is achieved up to about 1 kHz, at which the theoretical size of the zone of quiet in a diffuse field, one tenth of a wavelength [43, 106], is about 3.4 cm. In the present arrangement, the spacing between the identified head positions is about 5 cm, which is slightly larger than the diffuse field zone of quiet but since these experiments are performed under anechoic condition, the zone of quiet is slightly larger [46] and so good control is maintained at positions between the identified head positions.

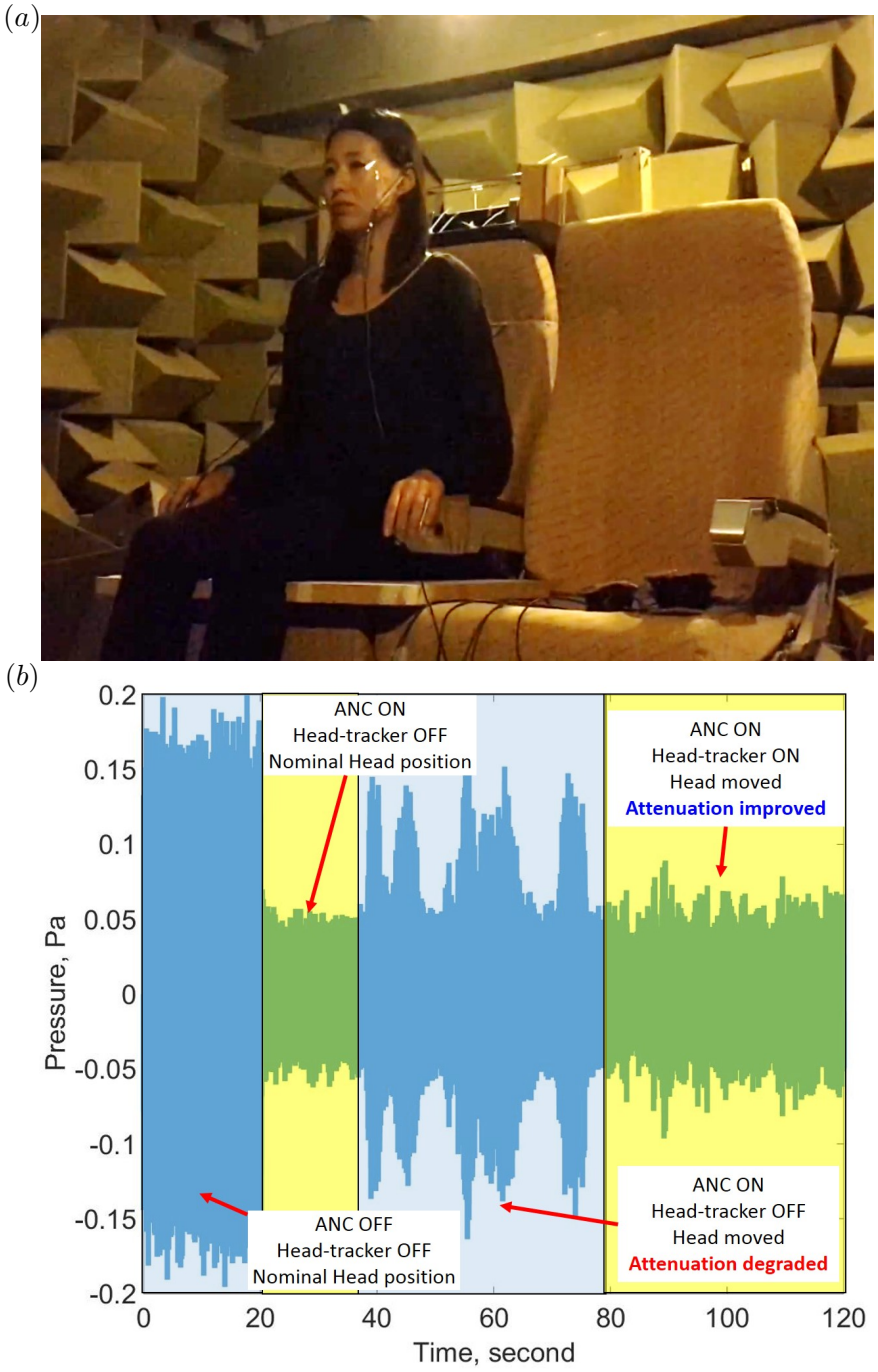

Figure 7.8: Active control with the integrated active headrest system with a human listener for reducing broadband random disturbance signals in real-time: (a) The test installation, in which the participant has two physical error microphones in their ears for evaluation purposes and (b) the measured signals at one of these error microphones during active control and head-tracking.

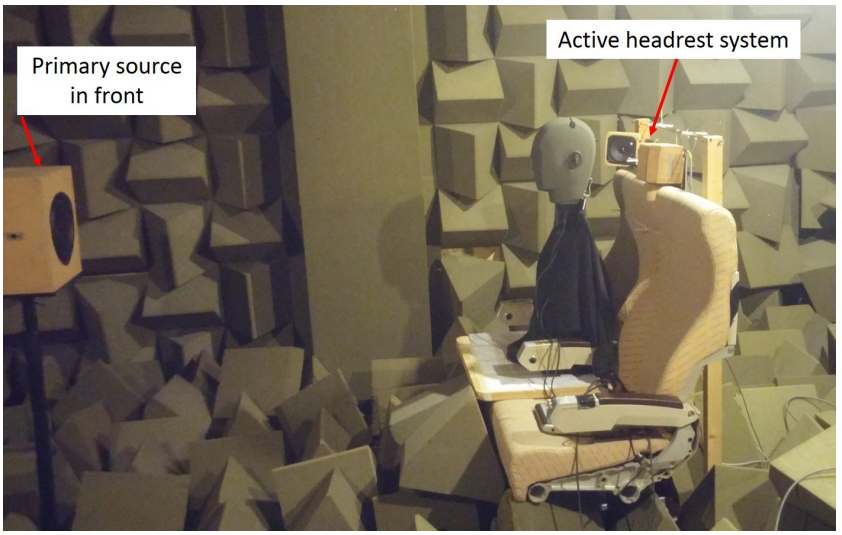

Figure 7.9: Experimental arrangement for local active control of broadband random noise driven from a single primary source in front.

7.2.3 Real-time adaptive control with the delayed remote microphone technique for the front primary source

In the previous sections, the primary source was located in the rear of the active headrest system and the causality between the error microphones and monitoring microphones can be thus maintained because the monitoring microphones can detect disturbance signals earlier than the error microphones. As a result, the standard time domain remote microphone technique can be used to accurately estimate the error signals. However, when the primary source is in front of the active headrest system, as shown in Fig. 7.9, the causality of the observation filter is lost because the estimation of 'future' random signals at the error microphones from the monitoring microphones may not be achievable. Therefore, to overcome this limitation, the 'delayed' remote microphone technique was used for active control of broadband random noise.

To investigate the effect of the delayed remote microphone technique, the impulse responses of the causally constrained observation filters are compared with those of the non-causal observation filters calculated using the standard method in the frequency domain. The dummy head was located at the nominal position 'A' and a modelling delay of about 0.7 ms, corresponding to 2 samples, is applied since the average distance from the dummy head to the monitoring microphones is around 225 mm so sound takes about 0.7 ms to travel from one to the other. Fig. 7.10 shows the responses of $\hat{\boldsymbol{O}}_{12}$ in this case. It can be seen that the impulse response corresponding to the causally constrained time domain filter calculated using the standard remote microphone technique is now significantly different from the causal part of the inverse Fourier transformed optimal observation filter calculated in the frequency domain, since important non-causal components of this response are not present in the causally constrained filter. In Fig. 7.10(b),

however, it can be seen that by using the delayed remote microphone technique, the important non-causal components of the response are included in the impulse response, which results in the improved nearfield estimation.

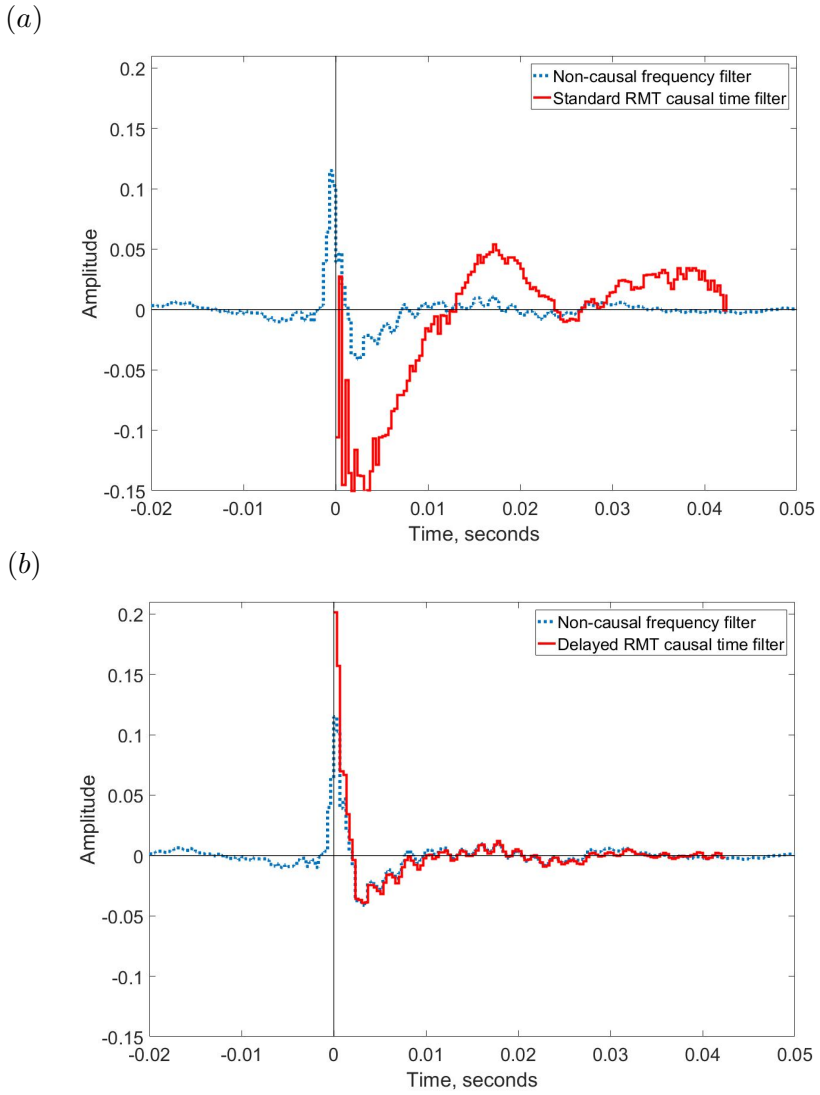

Figure 7.10: Comparison of the impulse response of $\hat{\boldsymbol{O}}_{12}$ among the FIR filters of the causal constrained time filter with the inverse Fourier transformed $\hat{\mathbf{O}}(1,2)$, which is among responses of the non-causal optimal observation filter in the frequency domain when broadband random disturbances are driven from a single primary source in front: (a) the standard remote microphone technique, (b) the delayed remote microphone technique.

The results of real-time active control are shown in Fig. 7.11 when the standard and the delayed remote microphone technique are used. It is clearly important to include a suitable modelling delay in the observation filters for the front primary source locations, since otherwise the attenuation is limited when the standard remote microphone technique, with no modelling delays, is used. The convergence time of the adaptive algorithm in equation (7.25) depends on the overall delay in the plant response, $\hat{\mathbf{G}}_e$, [26] which includes both the modelling delay and also the acoustic and electrical delays of the system. The modelling delay used for the observation filter in these experiments was 0.7 ms, which was not large compared with the delay due to the acoustic propagation between the loudspeaker and microphone and that due to the anti-aliasing and reconstruction filters in this case, which was about 1.3 ms in total. So although, in principle, the modelling delay will increase the convergence time of the adaptive control algorithm, this increase is small in the experiments reported here, since the overall delay is not dominated by the modelling delay and the disturbances is also stationary. The control filter thus only had to adapt when there was a change of head position, in which case the time taken for the head tracker to acquire a new position was significantly greater than the adaptation time of the filter. There may be some applications, with small acoustic delays and nonstationary disturbances, in which this modelling delay does become important in determining the convergence time and so limits the control performance.

(a)

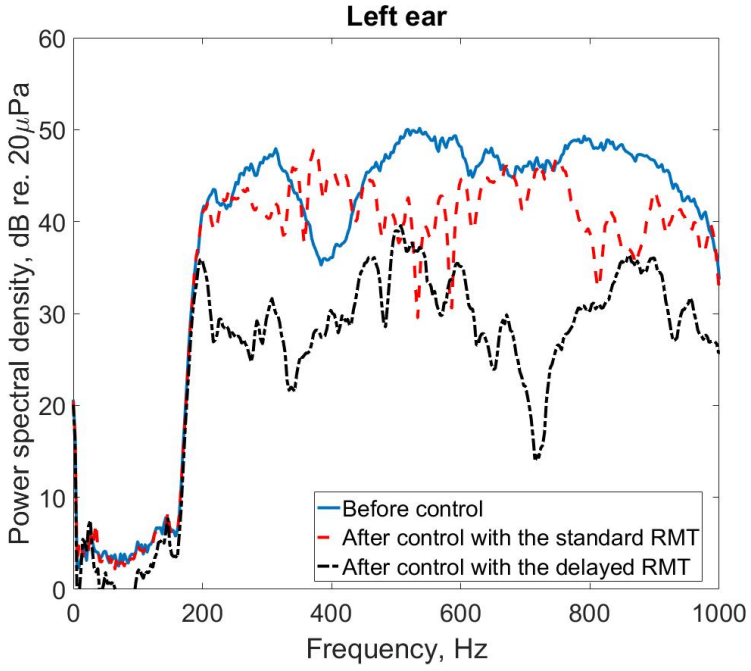

(b)

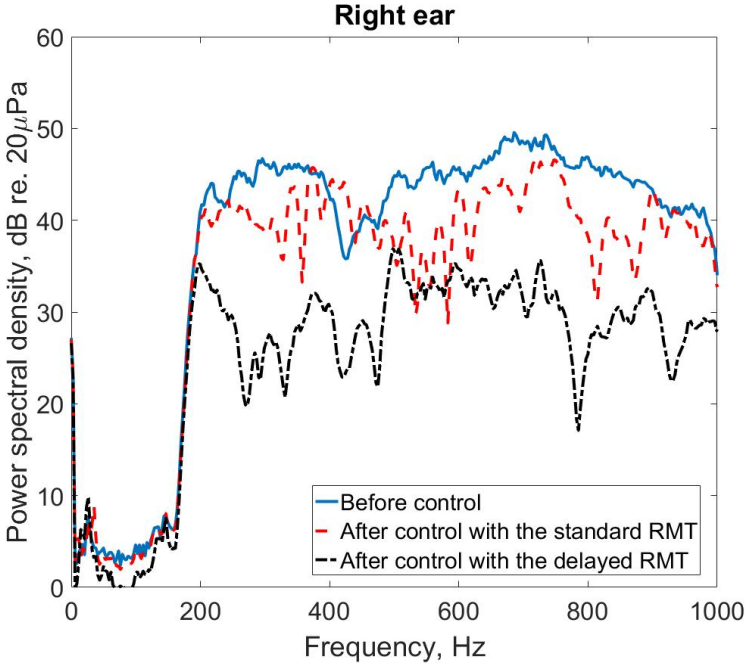

Figure 7.11: Power spectral density of the signal measured at the microphones in the left and right hand side of the dummy head when it was in the nominal position and the primary source was positioned in front of the headrest before control, solid line, after control using the standard remote microphone technique, RMT, dashed line, and after control using the delayed RMT, when it includes a modelling delay of 0.7 ms, dot-dashed line.

7.3 Summary

In this chapter, the attenuation performance of an active headrest system, using both the remote microphone technique and head-tracking, has been investigated to reduce broadband random disturbances at an anechoic chamber. The optimal observation filter and the control filter for active control with a causality constraint have been formulated in the time domain for the sensing and control of broadband random disturbances. To improve the performance of the active controller, the head-tracking has been used to optically track the listener's head movements and this information is employed by a local active control system to ensure that the broadband random sound at the listener's ears is attenuated at frequencies up to about 1 kHz. The nearfield estimation and noise reduction have been verified through real-time experiments with a similar installation to that in Chapter 6, with two secondary loudspeakers at the sides of the headrest and a static array of four monitoring microphones along the top of the headrest.

When the dummy head was located at a nominal position and the primary source is behind the active headrest, the four monitoring microphones with the causally constrained observation filter can accurately estimated the disturbance signals at the virtual error microphones of the dummy head, since the monitoring microphones can detect the disturbance signals in advance of the virtual error microphones. Real-time control with the remote microphone technique have demonstrated that disturbance signals at the error microphones were reduced to $20-30$ dB at the anechoic chamber up to about 1 kHz. In addition, with head tracking, when the position of the dummy head was changed, good cancellation has been maintained even during head motion. Without head tracking, the zones of quiet are fixed, and the subjective impression of listening in the headrest may be that of moving in and out of the zones of quiet but with head tracking, the zones of quiet are moved with the ear locations like steering the positions at which local active sound control is obtained to be close to the ears of the user.

Finally, when the primary source was in front of the active headrest system, the delayed remote microphone technique was applied to overcome the non-causal observation filter. A modelling delay of 0.7 ms, which was decided by the average distance between the monitoring and the virtual error microphones, has been used to improve the causality issue of the nearfield estimation. Since the accuracy of the nearfield estimation was improved and the modelling delay was not large compared with the inherent delay in the plant response, the attenuation performance of the integrated active headrest system was significantly improved compared with the standard remote microphone technique, without any modelling delay.

Chapter 8

Experimental investigation into the performance of the integrated active headrest system inside a vehicle

In the previous chapters, laboratory studies have shown that the stability, the attenuation and the controllable frequency range of a local active control system can be improved by the integration of the remote microphone technique and head-tracking. To investigate effects of such a local control algorithm on the automotive road noise control problem, this chapter investigates the performance of such system using direct measurements of the pressures and acoustic responses in a vehicle.

The nearfield estimation accuracy of the remote microphone technique is considered when the causal optimal observation filter is designed from measurements of the interior noise pressure at a number of monitoring microphones around a car cabin and two error microphones at the ears of a dummy head. It is then shown through simulations using measured responses that a multichannel active headrest system with a causal controller can be combined with the remote microphone technique to reduce broadband interior road noise. The effect of head-tracking on the nearfield estimation and the attenuation performance is also investigated, when the dummy head is located at different positions.

In section 8.1, the test installation and acoustic characteristics in a car cabin are presented. Measured signals from microphones positioned in the rear right seat of a large SUV are then used in section 8.2 to estimate the performance of the remote microphone technique in this application. Section 8.3 presents the predicted attenuation performance of the active headrest system combined with the remote microphone technique

to reduce broadband random road noise. Finally, section 8.4 presents the summary of this work.

8.1 Car cabin environment

8.1.1 Experimental arrangement in a car cabin

To estimate the effect of local active sound control with the remote microphone technique in a vehicle, an active headrest system with a dummy head was installed at the rear right seat of a large SUV, as shown in Fig. 8.1. In addition, 16 monitoring microphones were installed around the dummy head and Fig. 8.1 also shows how these 16 monitoring microphones, located at different positions in the vehicle cabin, are numbered for reference. The interior noise at the monitoring microphones and the virtual error microphones at the ears of the dummy head was measured when the car was driven under four different conditions: over a rough road at constant 30 mph, over a rough road at constant 50 mph, over a smooth road at constant 30 mph and over a smooth road at constant 50 mph. This measurement was then used to calculate the observation filters, from the measured signals from the monitoring and error microphones, and to analyse the accuracy of the standard and delayed remote microphone techniques. To compare the estimated disturbance signals at the virtual error microphones with the actual disturbance signals, two microphones in the ears of the dummy head were used in these measurements as the physical error sensors. The sampling frequency was 3 kHz and this gives a Nyquist frequency of 1.5 kHz and anti-aliasing and reconstruction filters had a cut-off frequency of 1 kHz. A series of experiments was conducted when the dummy head was located at 7 different positions on a 5×4 grid of points spaced 5 cm apart, as shown in Fig. 8.2, to investigate the potential accuracy of the remote microphone technique and the achievable attenuation of the active headrest system when a listener's head is moved. In this chapter, the nearfield estimation and the attenuation performance are investigated through off-line analysis due to the practical limitation of the processing devices available. That is, in a preliminary test, it was confirmed that when two reference sensors and four monitoring microphones are used with the sampling frequency of 3 kHz, a real-time controller of the dSPACE system is practicable with maximum 64 filter coefficients. Since more reference sensors and more monitoring microphones were used in the vehicle test, the off-line analysis with causal filters can provide more beneficial results. The equipment used here is detailed in Appendix D.

8.1.2 Acoustic response measurements inside the cabin

Disturbance signals at the 16 monitoring microphones and two error microphones have been measured when the car was driven under the four different conditions. Reference

Figure 8.1: The overall installation for the remote microphone technique and local active sound control experiments when interior road noise is measured at the rear right seat of a large SUV using 16 potential positions for monitoring microphones around the dummy head and two error microphones in the ears of a dummy head. Eight potential monitoring microphones are positioned on the headrest and ceiling (a), four monitoring microphones on the rear right seat (b) and four monitoring microphones on the front right seat (c).

signals from eight sensors installed around the four wheels were simultaneously measured along with the interior disturbance signals. A-weighted power spectral densities of the signals at the left and right error microphones of the dummy head located at position 'A' in Fig. 8.2, as the nominal position, are shown in Fig. 8.3. The A-weighting is commonly used by manufacturers to judge road noise components. It can be seen in Fig. 8.3 that although overall noise levels on the rough road are slightly louder than

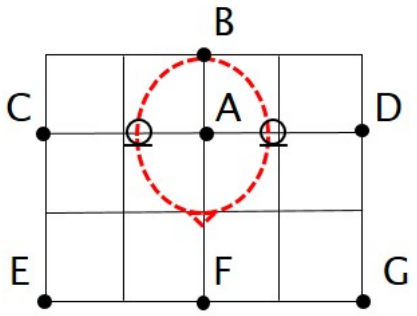

Figure 8.2: Location of the different head positions on the measurement grid.

those on the smooth road, the overall interior noise levels on the rear right seat are more dependent on the vehicle speed rather than the road condition except for a broadband peak in the spectrum at from 70 to 190 Hz. This peak is found in the spectrum at both ears for all four road conditions. Because the car was driven at constant speed and the load on the engine is thus relatively low, structural resonances of the vehicle produced by the interaction between the tyres and road may be more dominant than the engine in this broadband peak. Since this broadband peak is produced at the relatively low frequency range, however, it is expected that this peak could be efficiently controlled with a global active control system using car audio loudspeakers in the doors for example [4, 107]. However, it is necessary to control interior noise above 190 Hz with a local active control system.

To achieve the better attenuation performance with a feedforward active control system, a multiple coherence between the reference signals and the error signals is required. Previous results have shown that the optimal attenuation of the non-causal controller for feedforward active control has an upper limit determined by the multiple coherence function, γ^2, between the reference sensors and the error sensors, as in [4, 14, 55]

$$\text{Att} = 10\log_{10}(1-\gamma^2), \tag{8.1}$$

where γ^2 at a single virtual errror microphone is definded as

$$\gamma^2 = \frac{\mathbf{S}_{xd_e}\mathbf{S}_{xx}^{-1}\mathbf{S}_{xd_e}^{H}}{S_{d_ed_e}}. \tag{8.2}$$

For example, a 10 dB attenuation of the non-causal controller requires $\gamma^2 = 0.9$ and a 7 dB attenuation requires $\gamma^2 = 0.8$. In practice, this estimated attenuation performance can also be affected by diverse factors including the causality of filters, time variance of disturbances and the latency of the control system. The type and position of the reference sensors are still a matter of active investigation in applications of feedforward

(*a*)

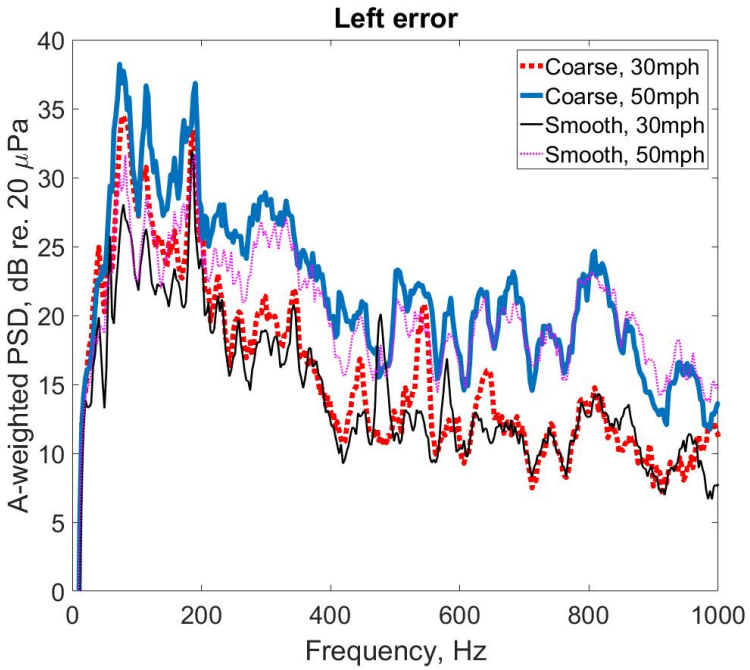

(*b*)

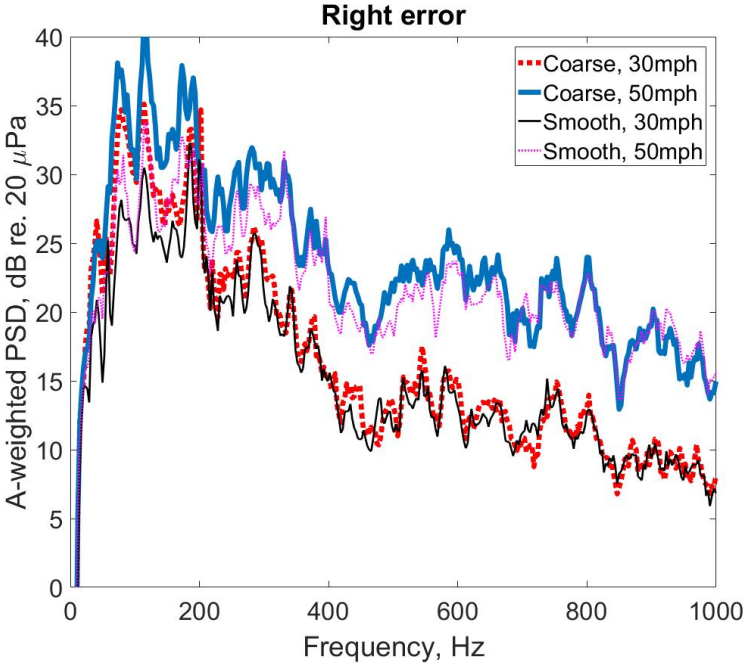

Figure 8.3: A-weighted PSDs of the signals at the left (a) and right (b) error microphones of the dummy head under four different driving conditions: over a rough road at 30 mph (thick dotted lines), over a rough road at 50 mph (thick solid lines), over a smooth road at 30 mph (thin solid lines) and over a smooth road at 50 mph (thin dotted lines).

active control [108] but in this thesis, we have not been concerned with this aspect of the problem since for the test vehicle, the reference signals were supplied by the car manufacturer.

Fig. 8.4 and Fig. 8.5 show the multiple coherences between the eight reference sensors and the two error microphones in the dummy head on the rear right seat under the four different driving conditions. For all four driving conditions, a reasonably large multiple coherence is achieved up to around 200 Hz. The drop-off of the multiple coherence in the frequency range between 400 and 450 Hz is found for the all four driving conditions and this drop-off also corresponds sudden decrease of the A-weighted PSDs in Fig. 8.3, which suggests that nodes of acoustic modes for this frequency range in the vehicle cabin may exist in the positions of the error microphones. The multiple coherence is improved at frequencies above 450 Hz, and under the driving condition over a rough road at constant 50 mph, the multicoherence of around $\gamma^2 = 0.8$ is achieved at frequencies above 600 Hz. To clearly demonstrate effects of the integrated active headrest system at higher frequencies, this driving condition, with the highest levels of noise at the ears of the dummy head on Fig. 8.3, is mainly used in the following analysis.

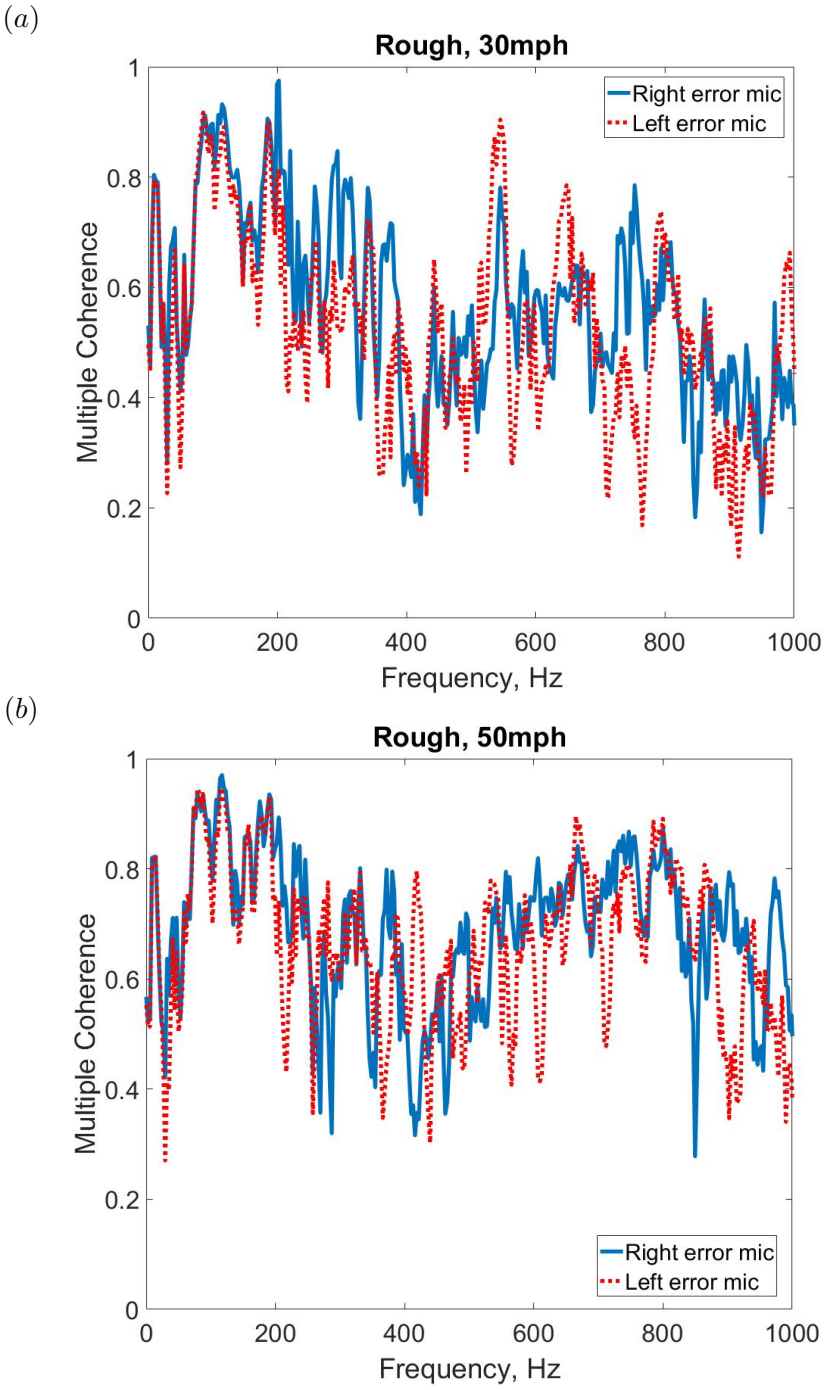

Figure 8.4: The multiple coherence between the eight reference sensors and each of the error microphones in the dummy head, measured when the car was driven either (a) over a rough road at constant 30 mph or (b) over a rough road at constant 50 mph.

(a)

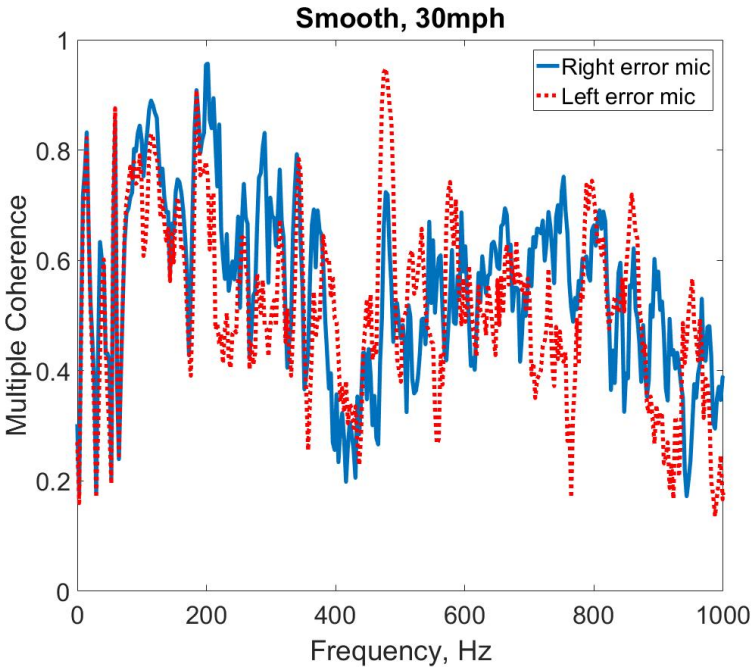

(b)

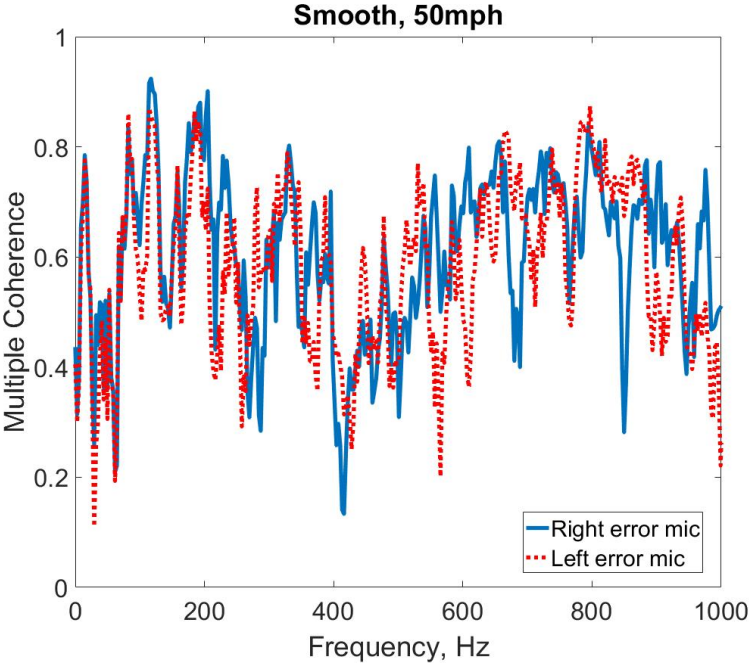

Figure 8.5: The multiple coherence between the eight reference sensors and each of the error microphones in the dummy head, measured when the car was driven either (a) over a smooth road at constant 30 mph or (b) over a smooth road at constant 50 mph.

8.2 Remote microphone technique inside a vehicle

8.2.1 Nearfield estimation of interior noise at desired positions using arrays of monitoring microphones

To conduct the nearfield estimation of interior noise at the ears of the dummy head, the optimal observation filters for the standard and delayed remote microphone techniques were calculated using Eq. (7.14) and Eq. (7.18) using the auto and cross correlation functions calculated from the measured disturbance signals. The normalised mean squared estimation error level at a single virtual error microphone, L_ϵ, can be defined as in Eq. (5.6).

Fig. 8.6, Fig. 8.7 and Fig. 8.8 show examples of the nearfield estimation error when different sets of monitoring microphones are selected from the overall array in Fig. 8.1. The causally constrained optimal observation filters were implemented using FIR filters with $J = 256$ filter coefficients and the dummy head was located in the nominal position 'A', as shown in Fig. 8.2. For the delayed remote microphone technique, a delay of $\Delta = 15$ samples was included, which was considered as a sufficient delay to allow important non-causal components of responses to be included. This delay corresponds to a sound propagation distance of about 1.7 m. To provide a benchmark for the best possible estimation accuracy with this microphone arrangement, the nearfield estimation was also conducted for a non-causal optimal observation filter in the frequency domain, as discussed in Chapter 5. No regularisation factors were required to calculate the observation filters used for the results in Fig. 8.6, Fig. 8.7 and Fig. 8.8, because regularisation was effectively already introduced as a result of the measurement noise and the condition number of inverted terms in the observation filters were already sufficiently small. It can be seen that although the nearfield estimation error is variable, due to the complexity of the acoustic field, the error generally increases as the frequency increases. As expected, the best nearfield estimation is achieved with the non-causal frequency domain filters, which do not enforce any constraints on the causality or the number of filter coefficients, but the causal filters also achieve a similar accuracy to the non-causal filter.

When all the 16 monitoring microphones were selected for the estimation, the result in Fig. 8.6(b) shows that using the remote microphone techniques, the disturbance signals at the right ear can be estimated with less than -10 dB estimation error up to around 800 Hz, except at certain frequencies, but the nearfield estimation error at the left ear in Fig. 8.6(a) is degraded. This is thought to be because sound waves directly propagated from the rear right wheel of the vehicle are dominantly measured at the right ear and the monitoring microphones. Lower correlation between the rear right wheel and the left ear is produced due to the further distance between the rear right wheel and the left ear and the scattering effect of the dummy head. The eight monitoring microphones used for the results in Fig. 8.7 were selected to give the best performance from all 16

(a)

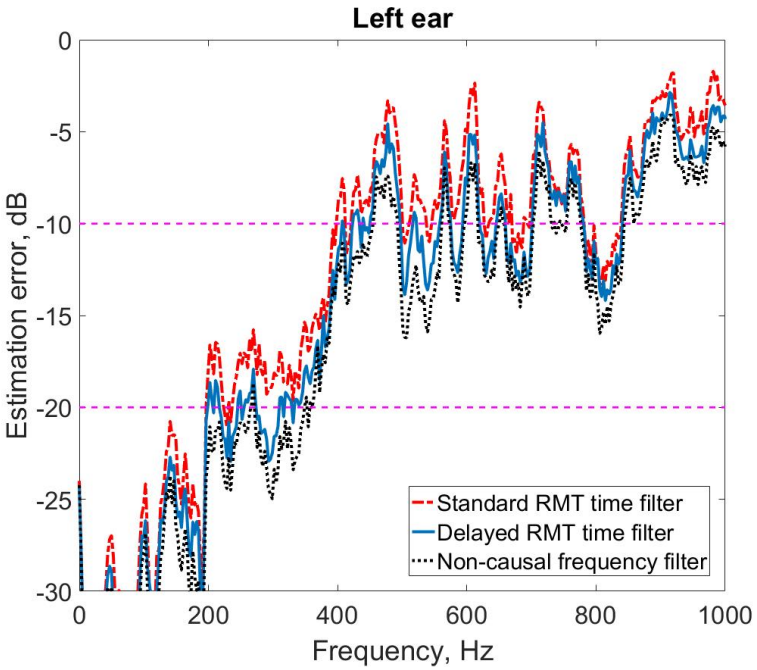

(b)

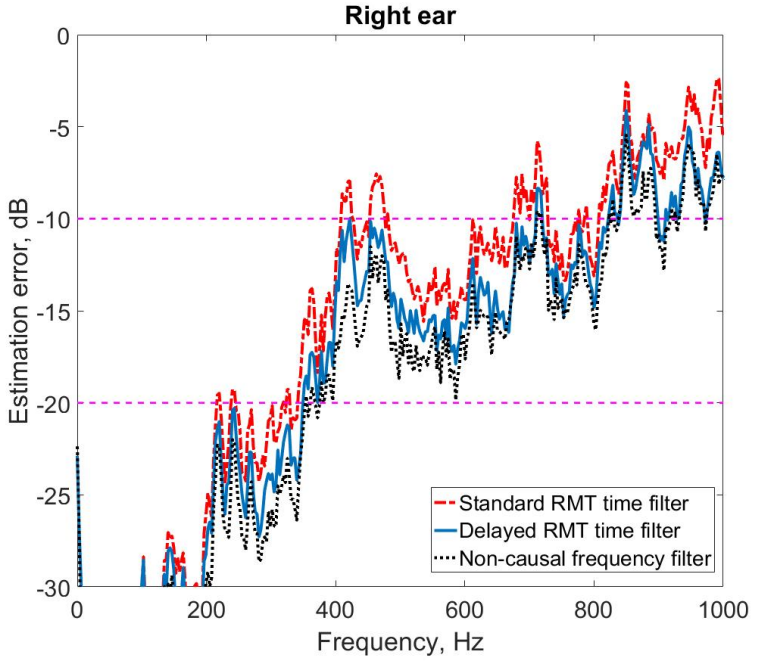

Figure 8.6: The nearfield estimation error of the remote microphone technique (RMT), calculated from data measured on a rough road at 50 mph when all 16 monitoring microphones are selected from the array in Fig. 8.1 to estimate the interior road noise at the ears of the dummy head: the left ear microphone (a) and the right ear microphone (b).

(*a*)

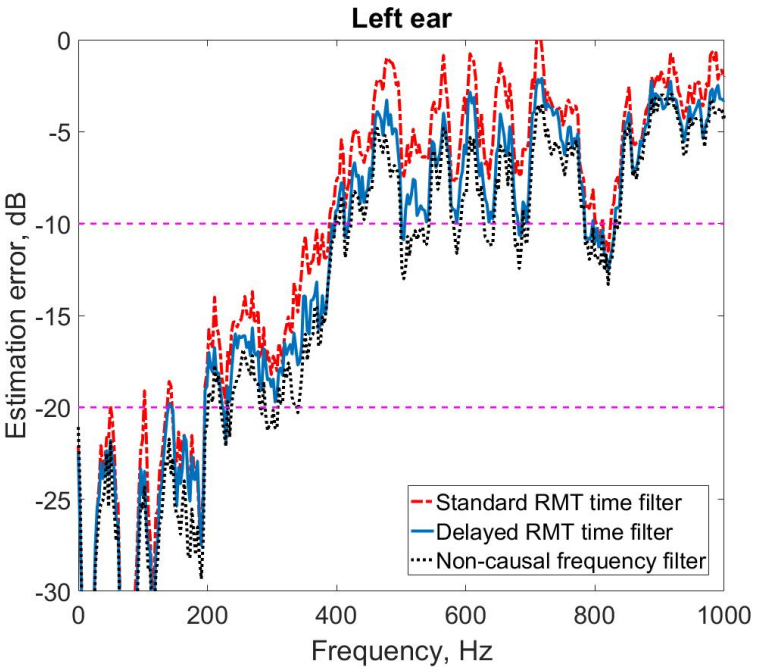

(*b*)

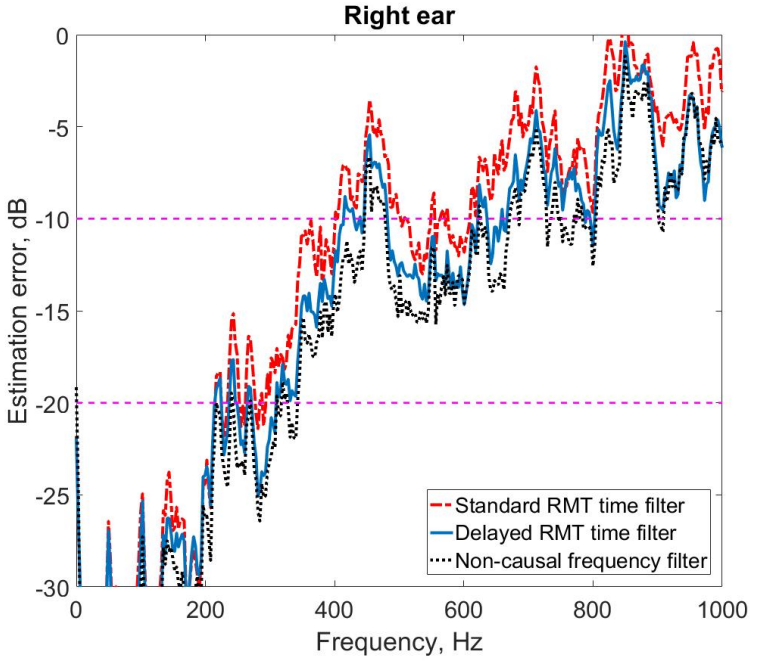

Figure 8.7: The nearfield estimation error of the remote microphone technique (RMT), calculated from data measured on a rough road at 50 mph when 8 monitoring microphones, #1∼#4, #13∼#16 are selected from the array in Fig. 8.1 to estimate the interior road noise at the ears of the dummy head: the left ear microphone (a) and the right ear microphone (b).

(a)

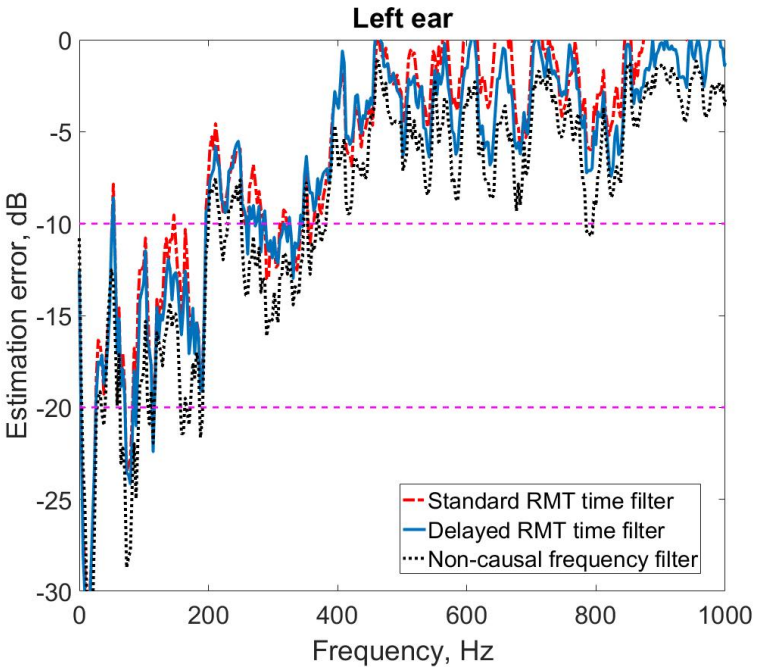

(b)

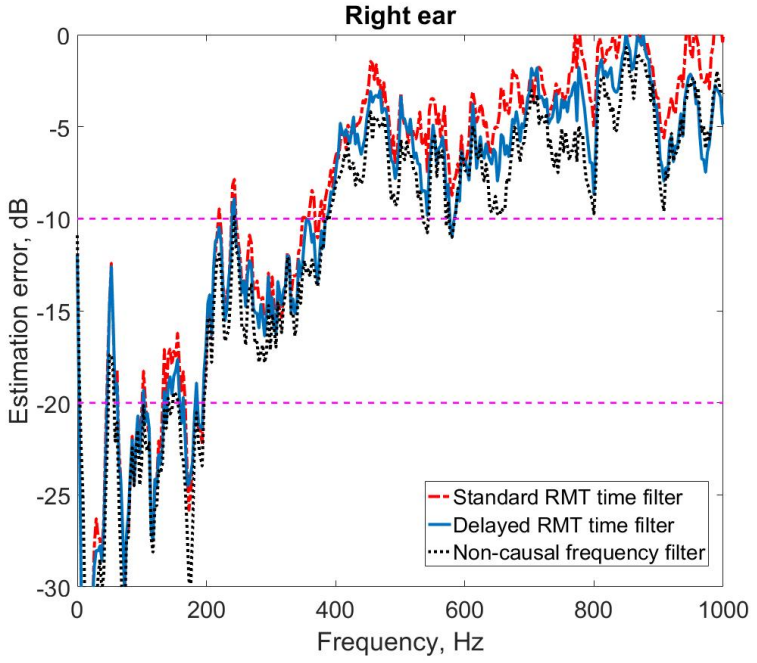

Figure 8.8: The nearfield estimation error of the remote microphone technique (RMT), calculated from data measured on a rough road at 50 mph when 4 monitoring microphones #1, #2, #13, #14 are selected from the array in Fig. 8.1 to estimate the interior road noise at the ears of the dummy head: the left ear microphone (a) and the right ear microphone (b).

monitoring microphones through an exhaustive search and it was found that the best positions were with four microphones (#1∼#4) on and around the headrest and four microphones (#13∼#16) above and both sides of the dummy head. In a similar way, Fig. 8.8 shows the results when only four monitoring microphones were selected using an exhaustive search, with two microphones (#1 and #2) on the headrest and two microphones (#13 and #14) above and in the right of the dummy head. The results in Fig. 8.8 show that although the nearfield estimation error is degraded by the use of a smaller number of monitoring microphones, an estimation error of less than -10 dB can be achieved up to about 400 Hz even with only 4 monitoring microphones. These results suggest that the remote microphone technique for the active headrest system can achieve accurate nearfield estimation for active sound control at low frequencies with a small number of monitoring microphones, but at higher frequencies, larger number of monitoring microphones are necessary to allow good attenuation.

It can also be seen in Fig. 8.6, Fig. 8.7 and Fig. 8.8 that somewhat better nearfield estimation with the delayed remote microphone technique is achieved, compared to the standard remote microphone. This is probably because some non-causal components are present in the vehicle cabin, due to both the complex distribution of primary source excitations and the reverberant nature of the cabin. The effect of the delayed remote microphone technique can also be investigated by comparing the impulse responses of the observation filters with those calculated using the standard method in the frequency domain. These responses are shown in Fig. 8.9 for one of the 32 impulse responses, $\boldsymbol{O}_{11}$, calculated when all 16 potential monitoring microphones are used to estimate the disturbance at the right ear of the dummy head. In Fig. 8.9(a), it can be seen that the impulse response corresponding to the causally constrained time domain filter calculated using the standard remote microphone technique is similar to the causal part of the inverse Fourier transformed optimal observation filter calculated in the frequency domain but the non-causal part of this response is not present in the causally constrained filter. In Fig. 8.9(b), however, it can be seen that by using the delayed remote microphone technique, the important non-causal part of the response is included in the impulse response, which results in the improved nearfield estimation.

When the head position of a listener is changed, pre-calculated optimal observation filters can be updated by position information from an optical head tracking device, as suggested in the previous chapters. Therefore, the availability of the remote microphone technique for different head positions is investigated as the dummy head is located at either position 'E' or 'G' in Fig. 8.2 and the nearfield estimation error with all the 16 monitoring microphones is calculated, as shown in Fig. 8.10 and Fig. 8.11. By comparing Fig. 8.10 and Fig. 8.11 with Fig. 8.6, it can be seen that although the dummy head is moved around 14 cm away from the nominal position, the accuracy of the nearfield estimation can still be maintained with fixed monitoring microphones installed around the dummy head.

(a)

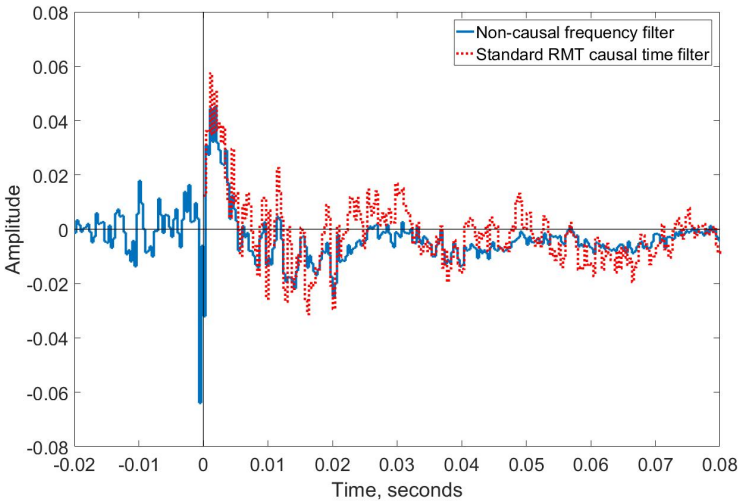

(b)

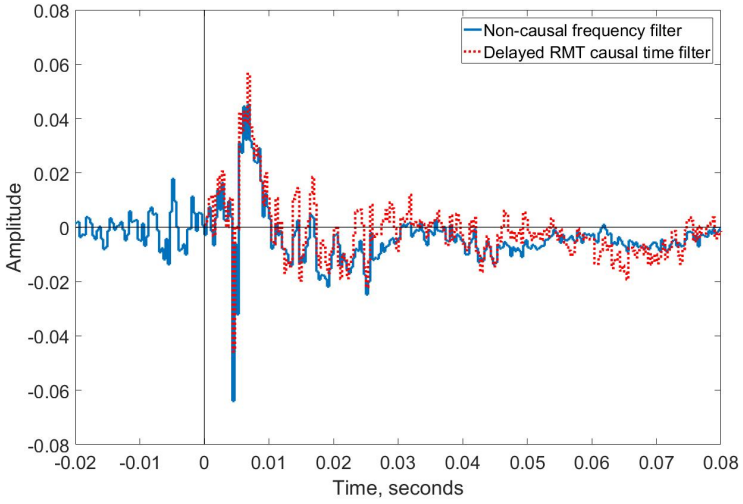

Figure 8.9: Comparison of the impulse response of $\boldsymbol{O}_{11}$ among the FIR filters of the causal constrained time filter with the inverse Fourier transformed $\mathbf{O}_{11}$, which is among responses of the non-causal optimal observation filter in the frequency domain when the 16 monitoring microphones were used to estimate disturbance signals at the right ear of the dummy head when driven at 50 mph on a rough road: (a) the standard remote microphone technique, (b) the delayed remote microphone technique.

(*a*)

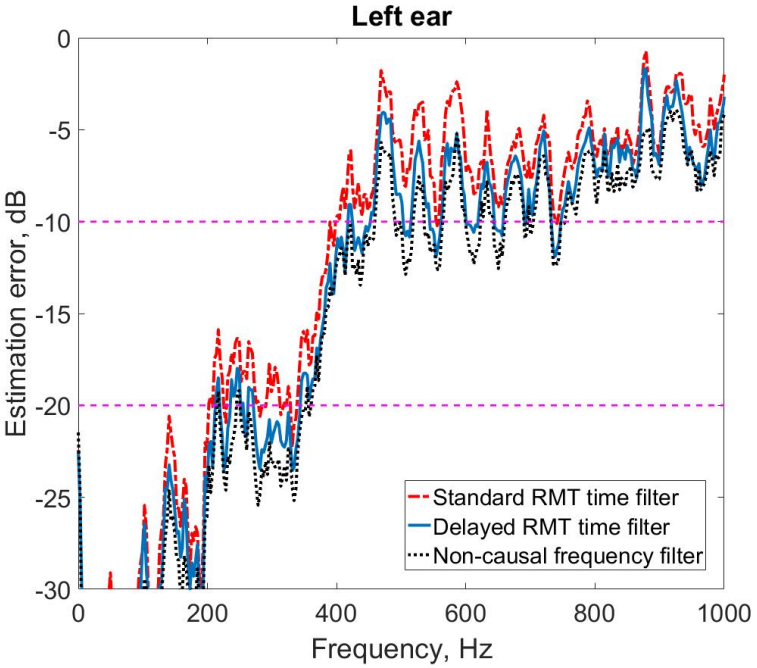

(*b*)

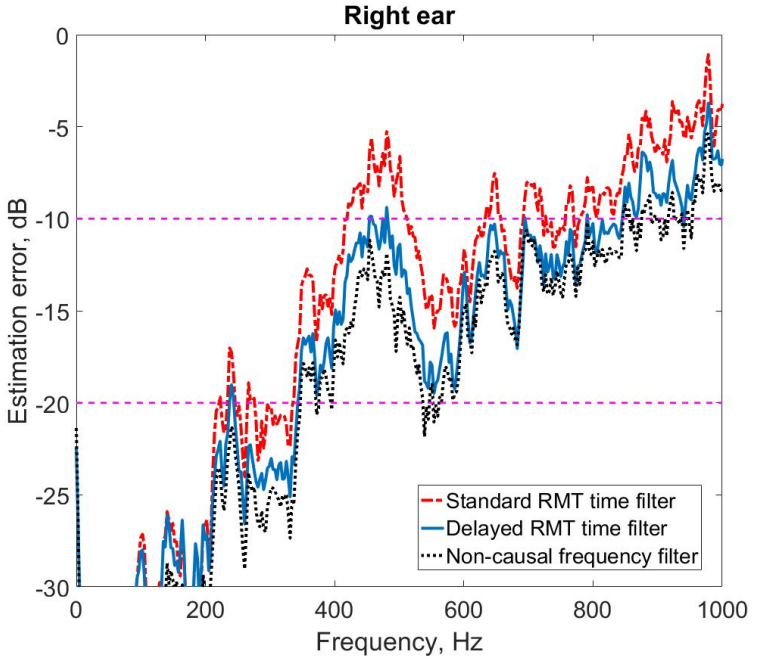

Figure 8.10: The nearfield estimation error for head position 'E' in Fig. 8.2, calculated from data measured on a rough road at 50 mph when 16 monitoring microphones are used to estimate the interior road noise at the ears of the dummy head: the left ear microphone (a) and the right ear microphone (b).

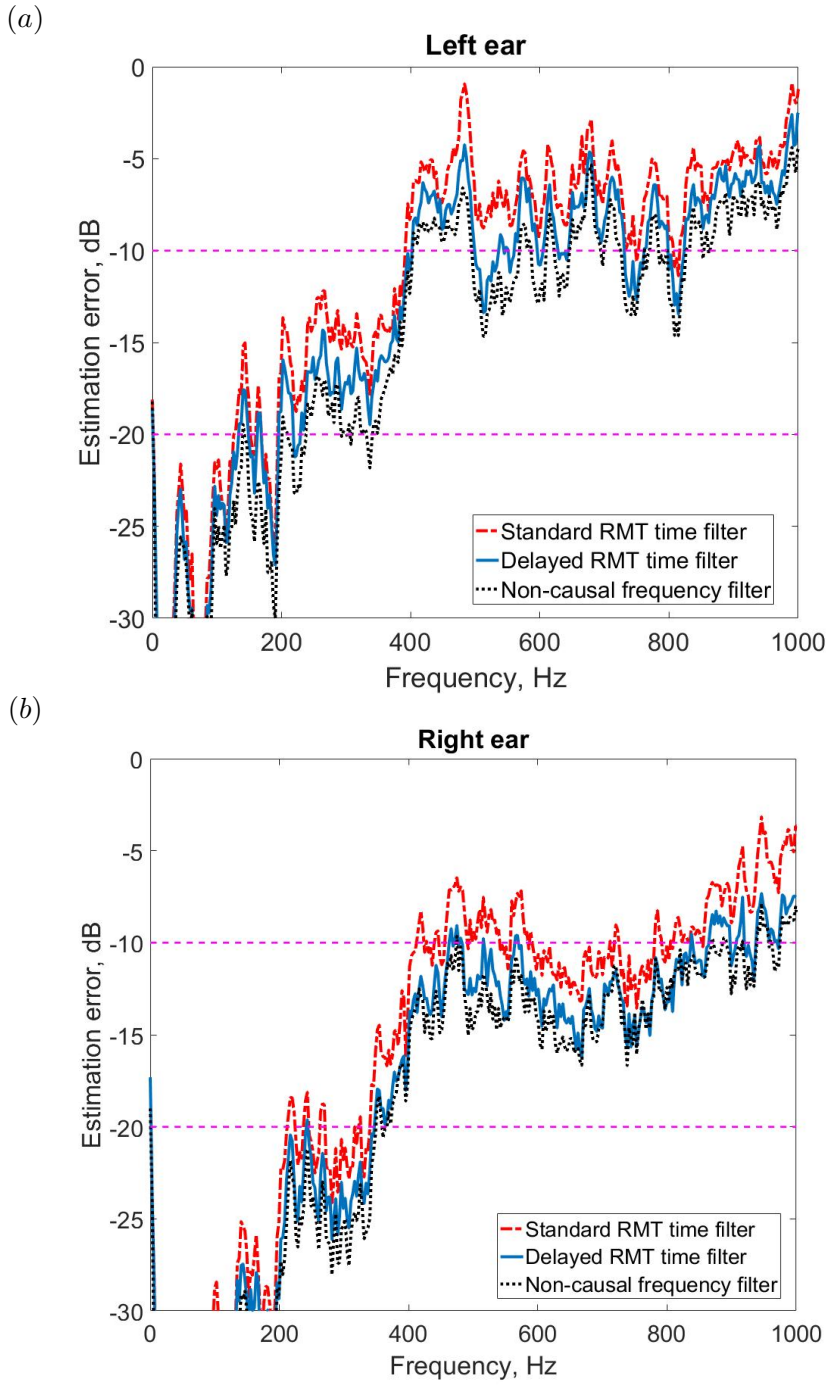

Figure 8.11: The nearfield estimation error for head position 'G'. in Fig. 8.2, calculated from data measured on a rough road at 50 mph when 16 monitoring microphones are used to estimate the interior road noise at the ears of the dummy head: the left ear microphone (a) and the right ear microphone (b).

8.2.2 Robustness of the observation filter to disturbance variation

In the previous section, the observation filter was calculated from premeasured disturbance signals when the car was driven over a rough road at 50 mph. However, because the disturbance signals inside the cabin can vary depending on the driving condition, it is interesting to consider how accurately this pre-defined observation filter can estimate the error signals under different road surface conditions and different speeds.

Fig. 8.12 shows the nearfield estimation error when the observation filter calculated from disturbance signals over the rough road at 50 mph, is used to estimate disturbance signals at the virtual error microphones over the smooth road at 50 mph. The nearfield estimation error with the observation filter calculated from disturbance signals over the smooth road at 50 mph, is also shown in Fig. 8.12, to indicate the best possible estimation accuracy of the causal filter under this driving condition.

From this plot, it can be seen that although the nearfield accuracy with the observation filter calculated for the rough road at 50 mph, is generally lower, the estimation error for these two different observation filters is quite similar to each other, except for significant increases of the estimation error at some particular frequencies. This tendency is also found in Fig. 8.13 and Fig. 8.14 in which disturbance signals at the virtual error microphones over the rough road at 30 mph and over the smooth road at 30 mph are estimated using the observation filter calculated for the rough road at 50 mph respectively. It is interesting that although the interior noise under these two driving conditions is quite different from the interior noise over the rough road at 50 mph, as shown in Fig. 8.3, the degradation of the nearfield accuracy is not excessive. From the results in Fig. 8.12, Fig. 8.13 and Fig. 8.14, it can be concluded that in this installation, the remote microphone technique is reasonably robust to disturbance variations up to 400 Hz and it would also be possible to improve the nearfield accuracy at the higher frequency range by choosing the proper set of observation filters from a limited number of pre-modelled observation filters under different road conditions.

(a)

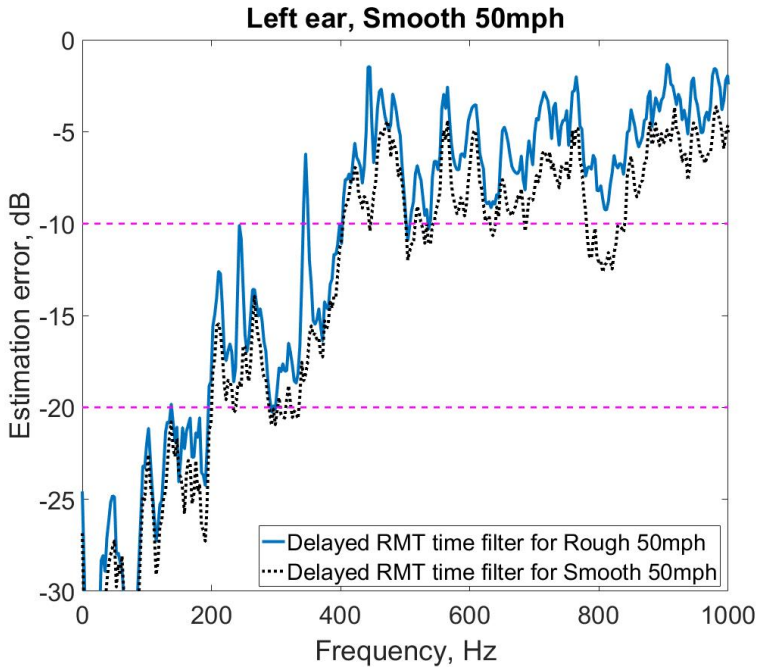

(b)

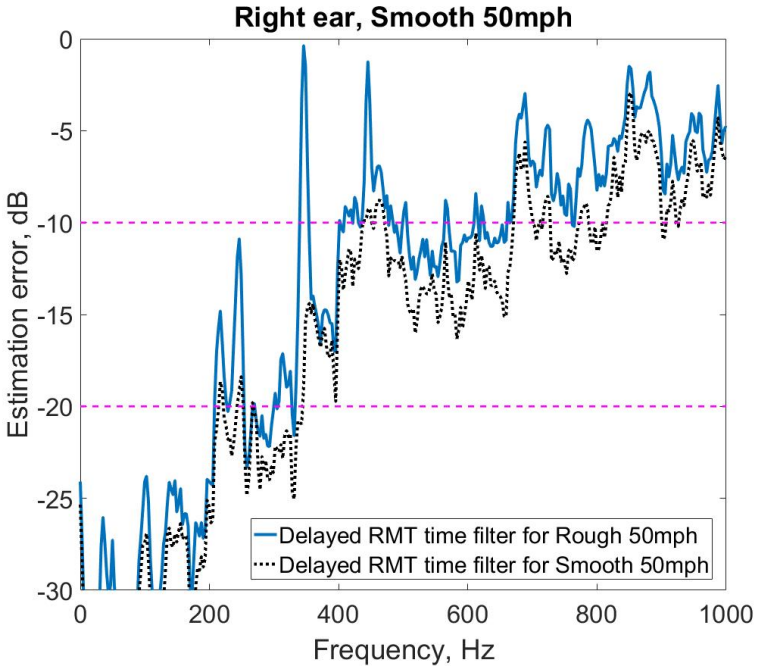

Figure 8.12: The nearfield estimation error of the delayed remote microphone technique (RMT) when the observation filter is calculated from data measured on either a rough road at 50 mph (solid lines) or a smooth road at 50 mph (dotted lines) with the 16 monitoring microphones at the nominal head position 'A' and this observation filter is used to estimate the interior road noise at the ears of the dummy head over a smooth road at 50 mph: the left ear microphone (a) and the right ear microphone (b).

(*a*)

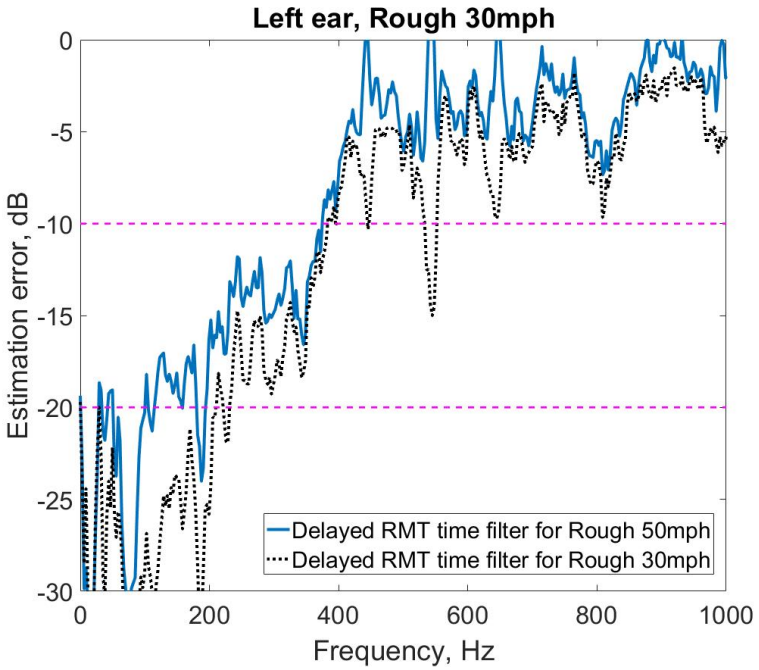

(*b*)

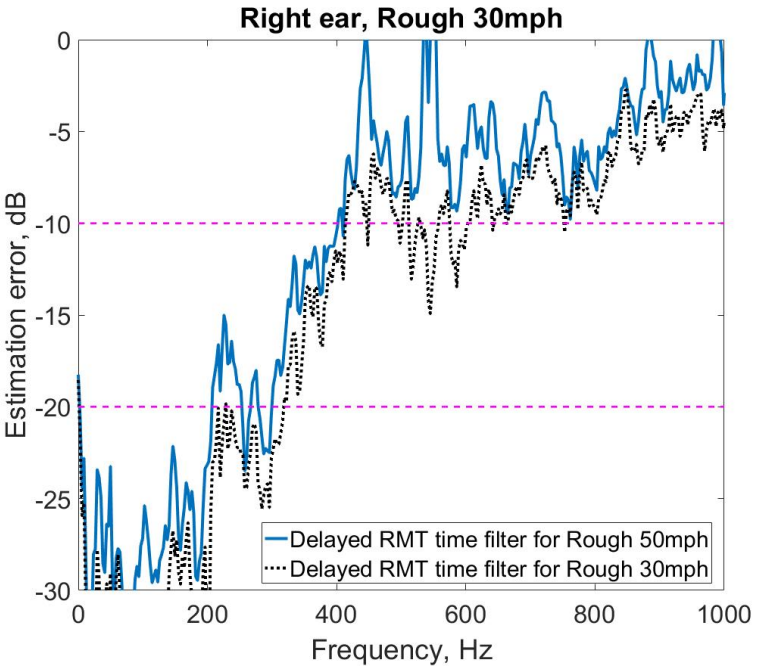

Figure 8.13: The nearfield estimation error of the remote microphone technique (RMT) when the observation filter is calculated from data measured on a rough road at 50 mph with the 16 monitoring microphones at the nominal head position 'A' and this observation filter is used to estimate the interior road noise at the ears of the dummy head on a rough road at 30 mph: the left ear microphone (a) and the right ear microphone (b).

(a)

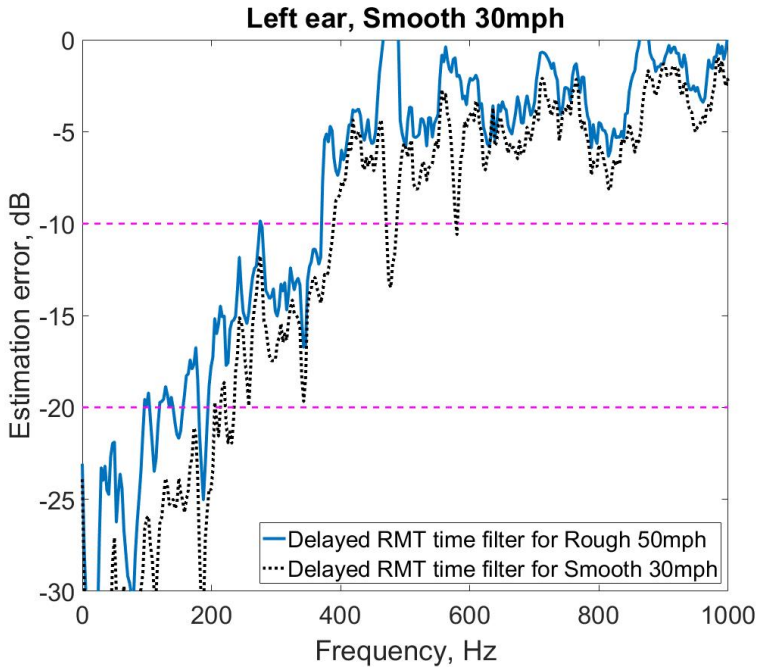

(b)

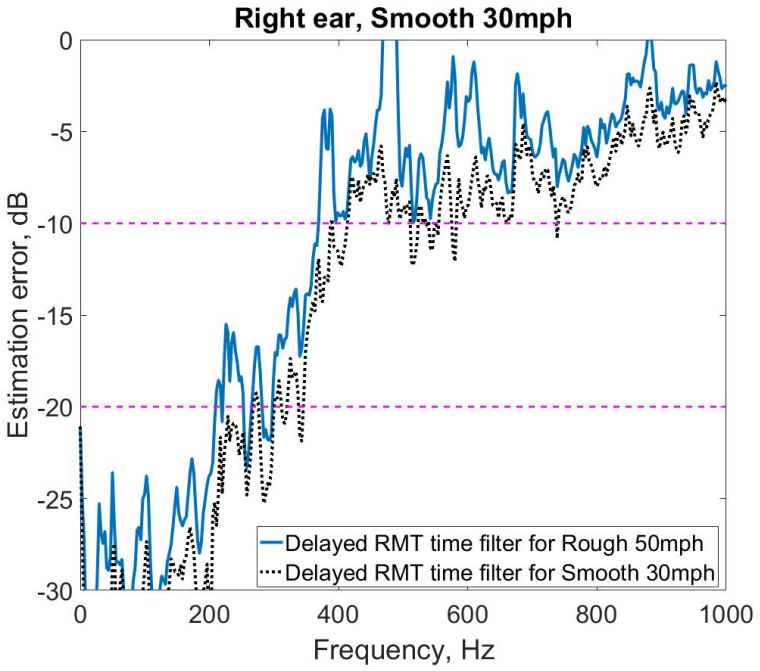

Figure 8.14: The nearfield estimation error of the remote microphone technique (RMT) when the observation filter is calculated from data measured on a rough road at 50 mph with the 16 monitoring microphones at the nominal head position 'A' and this observation filter is used to estimate the interior road noise at the ears of the dummy head on a smooth road at 30 mph: the left ear microphone (a) and the right ear microphone (b).

8.3 Active control of road noise inside a vehicle

8.3.1 Attenuation performance of the multichannel active headrest system

In the previous section, the accuracy of the remote microphone technique (RMT) in the vehicle has been investigated. It is also interesting to predict the potential attenuation performance of the active system in a real vehicle cabin. Therefore, this section presents off-line analysis results of the attenuation performance obtained with the installation described above in a vehicle. The plant responses between two loudspeakers mounted in the active headrest system and the monitoring and error microphones, $\mathbf{G}_e$ and $\mathbf{G}_m$, have been measured and were modelled by $K = 64$th order FIR filters. Fig. 8.15 shows examples of the measured plant responses, $\mathbf{G}_e$ from secondary sources to error microphones in the ears of the dummy head. In Fig. 8.15, $\mathbf{G}_e(1,1)$ is simpler than $\mathbf{G}_e(2,1)$ because the distance from the right secondary loudspeaker to the right error microphone is closer than that to the left error microphone and $\mathbf{G}_e(2,1)$ is more influenced by the scattering effect of the dummy head. It is also found that as the dummy head is moved, the plant response is significantly varied especially at the frequency range above 600 Hz. Plant responses, $\mathbf{G}_m$ in Fig. 8.16, from the secondary loudspeakers to the monitoring microphones, also show that $\mathbf{G}_m(13,1)$ is more variant that $\mathbf{G}_m(1,1)$ due to the further distance from the right secondary source. Changes of $\mathbf{G}_m$ for different dummy head positions are much smaller than those of $\mathbf{G}_e$ but are still significant, since they affect the stability of the feedforward algorithm combined with the remote microphone technique, as discussed in Section 6.1. It can be seen in Fig. 8.15 and Fig. 8.16 that relatively simple responses of $\mathbf{G}_e$ and $\mathbf{G}_m$ are obtained, compared to the disturbance sound fields inside the cabin as shown in Fig. 8.3, because the acoustic responses of $\mathbf{G}_e$ and $\mathbf{G}_m$ are mainly determined by the nearfield of the secondary loudspeaker. Because of the simplicity of the responses and the lack of too many resonances, the plant responses can be efficiently modelled using FIR filters.

For simplicity of calculation, it is assumed that the true plant responses, $\mathbf{G}_m$ and $\mathbf{G}_e$ are identical to the estimated plant responses, $\hat{\mathbf{G}}_e$ and $\hat{\mathbf{G}}_m$, resulting in $\boldsymbol{R}(n) = \boldsymbol{R}_e(n)$ in Eq. (7.17) and $\boldsymbol{R}_{\mathrm{D}}(n) = \boldsymbol{R}_e(n-\Delta)$ in Eq. (7.19). With the pre-calculated optimal observation filters presented in the previous section, the optimal controllers, which were modelled using the $I = 2,048$th order FIR filters, were calculated using Eq. (7.17) and Eq. (7.19). As a benchmark for the best possible performance of the causal controller with this arrangement, a controller was also calculated using disturbance signals from the dummy head microphones directly and using $\boldsymbol{d}_e(n)$ in Eq. (7.17), instead of $\boldsymbol{O}_{\mathrm{opt}}\boldsymbol{d}'_m(n)$.

To find a suitable regularisation factor, ρ in Eq. (7.17) and Eq. (7.19), the averaged attenuation levels up to 1 kHz for different regularisation factors have been calculated from the sums of the power spectral densities (PSDs) of the signals at each physical

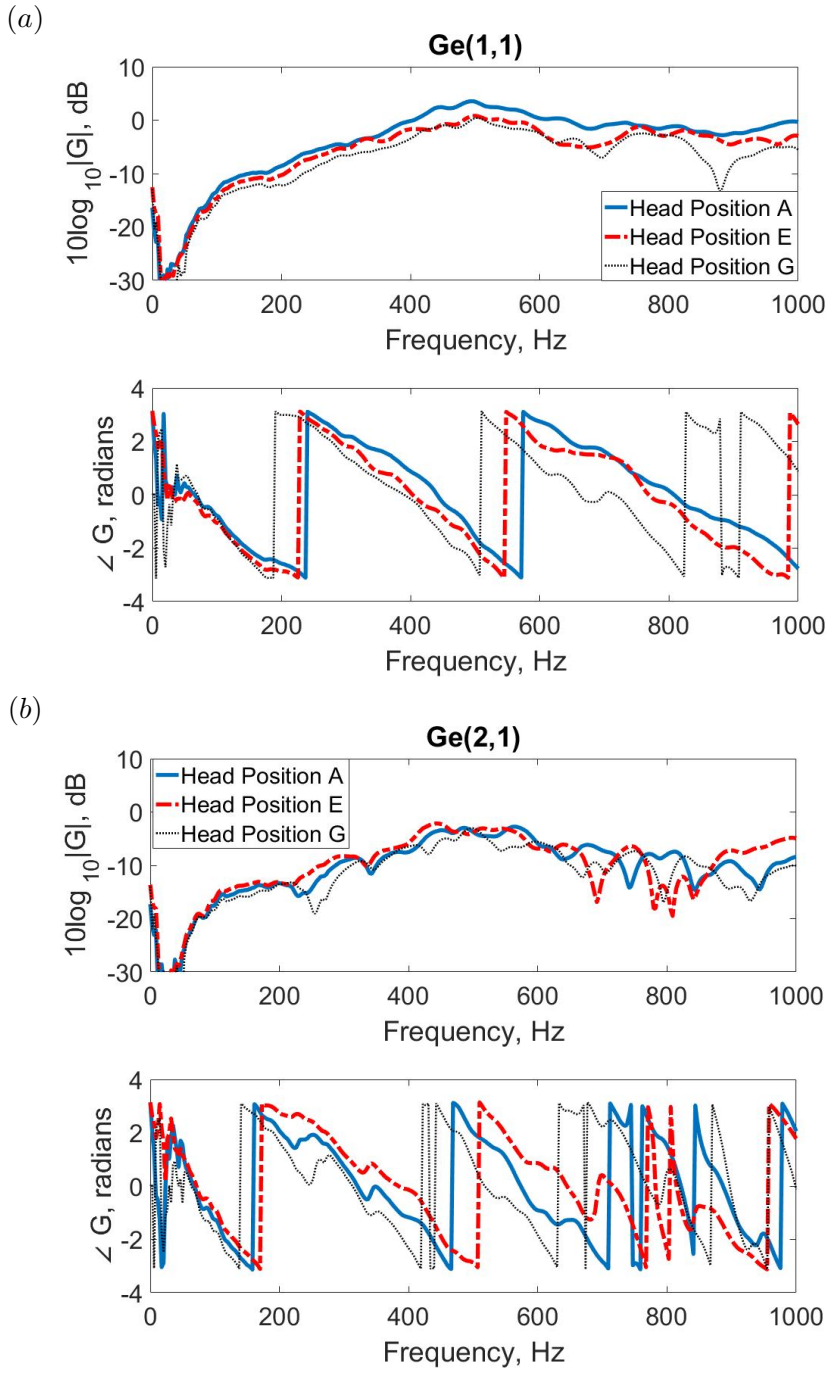

Figure 8.15: Examples of the change in the acoustic transfer response, $\mathbf{G}_e$ for different dummy head positions in Fig. 8.2: (a) $\mathbf{G}_e(1,1)$ and (b) $\mathbf{G}_e(2,1)$ between the right secondary loudspeaker and the right and left error microphones at the dummy head.

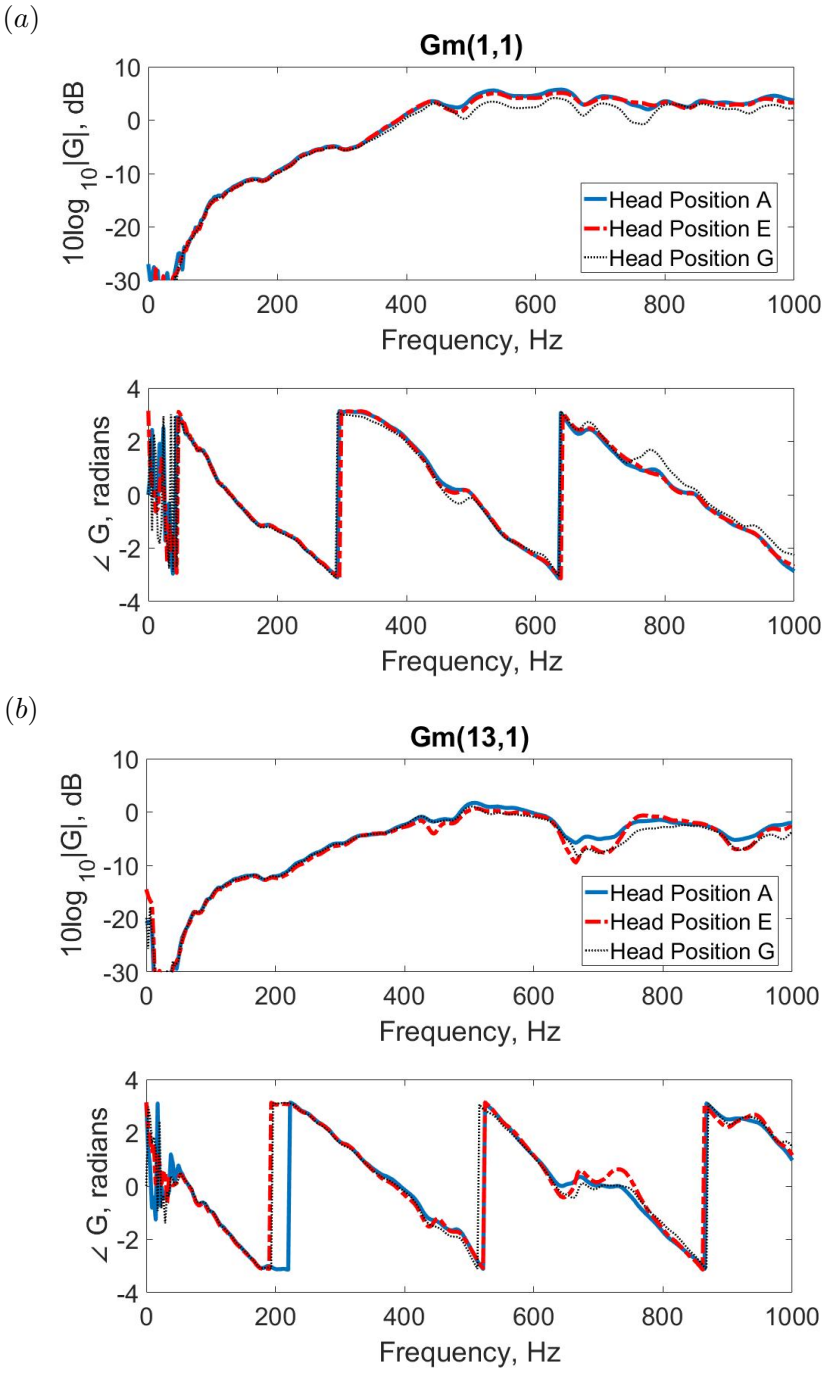

Figure 8.16: Examples of the change in the acoustic transfer responses, $\mathbf{G}_m$ for different dummy head positions in Fig. 8.2: (a) $\mathbf{G}_m(1,1)$ between the right secondary loudspeaker and the monitoring microphone 1 and (b) $\mathbf{G}_m(13,1)$ between the right secondary loudspeaker and the monitoring microphone 13.

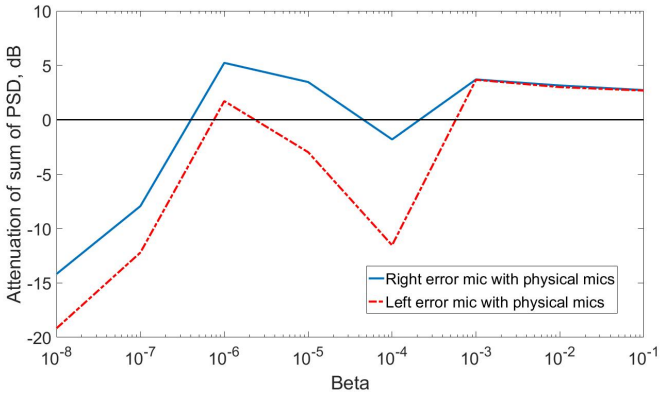

Figure 8.17: Averaged attenuation levels for different regularisation factors, ρ in Eq. (7.17) and Eq. (7.19), obtained from the sums of the PSDs of signals at the physical error microphones when disturbance signals at the dummy head on the position 'A' of the grid and reference signals are measured on a rough road surface at 50 mph and the active headrest system with two secondary loudspeaker is used to reduce noise.

error microphone in the dummy head before and after control, as shown in Fig. 8.17. It can be seen that with smaller regularisation factors, below 10^{-3}, the attenuation level is negative, i.e. an enhancement is predicted, since the inverted term in Eq. (7.17) and Eq. (7.19) is very sensitive to numerical uncertainties, and with larger regularisation factors, above 10^{-3}, the attenuation level is reduced due to the bias in the inverse solution.

With a regularisation factor of $\rho = 10^{-3}$, the optimal performance of the three causal controllers (the controller with direct measurement from the physical error microphones, the controller with the standard RMT and the controller with the delayed RMT) has been calculated. The A-weighted PSDs of error signals at the microphones in the dummy head are shown, with a controller calculated using the interior road noise signals measured at the 16 monitoring microphones and two error microphones, when the car is driven at 50 mph on a rough road surface. In addition, the optimal performance of a non-causal controller using the physical error microphones has been calculated from the frequency responses with the same installation, using the solution given in Chapter 3.

The uncontrolled and controlled disturbances are presented in Fig. 8.18 and in Fig. 8.19. It can be seen in Fig. 8.18 that the causal controller with the physical error microphones can effectively attenuate several peaks of broadband interior noise up to 1 kHz with a maximum reduction at about 750 Hz of 8.6 dB at the right ear and an average reduction of around 3.7 dB, which is similar to that of the non-causal controller, although attenuation levels with these controllers at individual frequencies are different from each other. Fig. 8.19 show that the causal controllers with the RMT can also reduce the broadband interior noise with a similar level of attenuation to that achieved by the controllers with

the physical error microphones, in Fig. 8.18, because the virtual error signals are quite accurately estimated using the observation filters. Although the delayed RMT provides a more accurate nearfield estimation, compared to the standard RMT in Fig. 8.6, the attenuation performance with these two RMT methods are similar to each other, because the performance in this case is limited by the coherence between the reference and disturbance signals, rather than the errors inherent in the RMT estimation. In the previous chapter, however, when the coherence between the reference and disturbance signals is greater, there was a clear difference in the active control performance with the standard and delayed RMT.

(a)

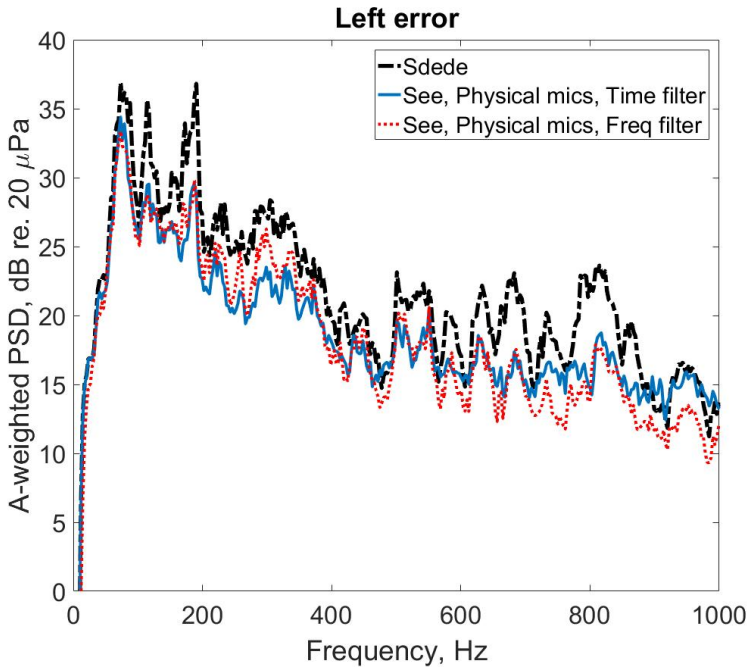

(b)

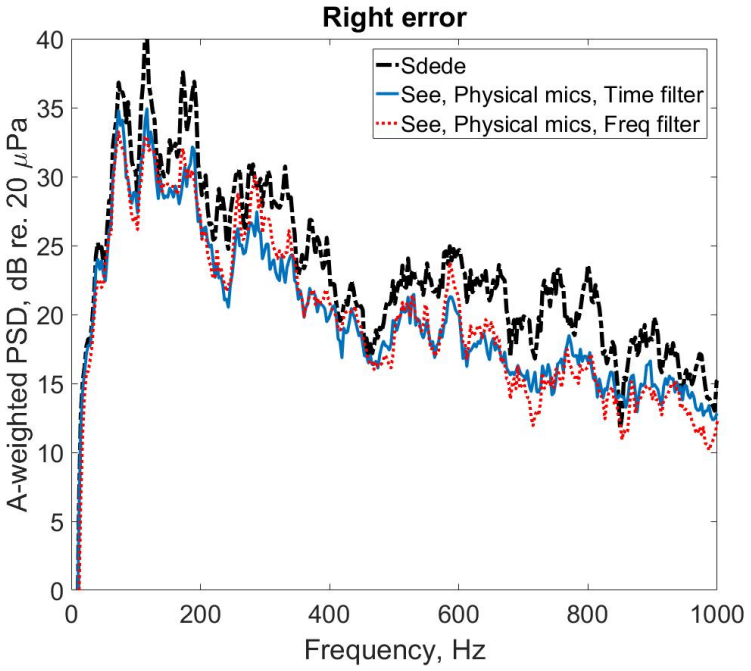

Figure 8.18: A-weighted PSDs of the signals at the left (a) and right (b) error microphones of the dummy head before, $S_{d_e d_e}$, and after control, S_{ee}. Simulations of control have been performed using the plant responses, the interior road noise signals measured at the 16 monitoring microphones and two error microphones, and reference sensor signals when the car is driven at 50 mph on a rough road surface. Predicted performances assuming physical error sensors are used in the ears of the dummy head. The uncontrolled disturbances (dot-dashed lines), the controlled disturbances by the causal time filter with the physical error microphones (solid lines) and the disturbances controlled with the non-causal frequency filter with the physical error microphones (dotted lines).

(*a*)

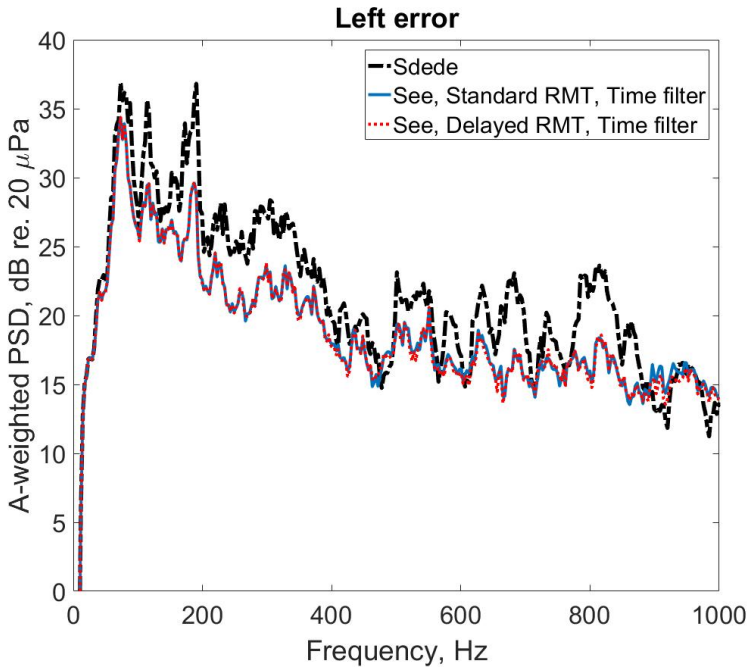

(*b*)

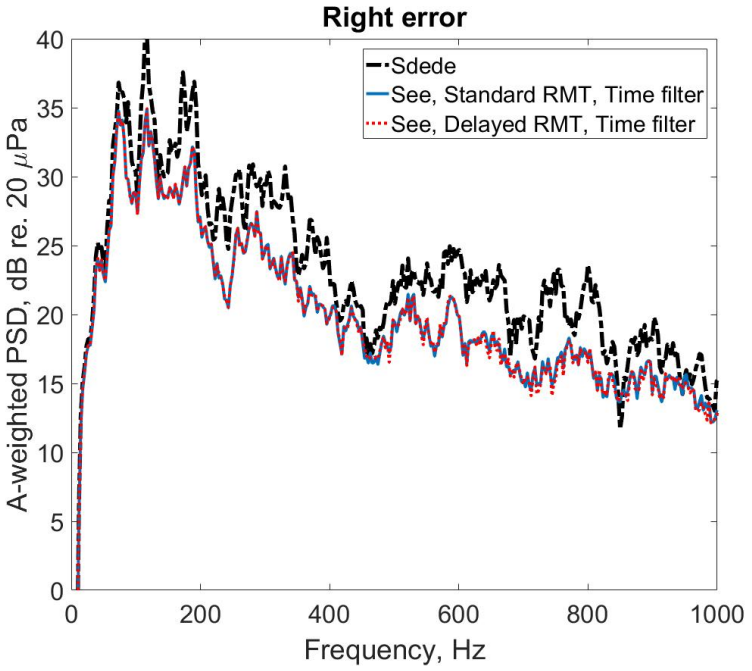

Figure 8.19: A-weighted PSDs of the signals at the left (a) and right (b) error microphones of the dummy head before, $S_{d_e d_e}$, and after control, S_{ee}. Simulations of control have been performed using the plant responses, the interior road noise signals measured at the 16 monitoring microphones and two error microphones, and reference sensor signals when the car is driven at 50 mph on a rough road surface. Predicted performances assuming the causal time filters for the standard and delayed RMT are used. The uncontrolled disturbances (dot-dashed lines), the controlled disturbances by the causal time filter with the standard RMT (solid lines) and the disturbances controlled with the causal time filter with the delayed RMT (dotted lines).

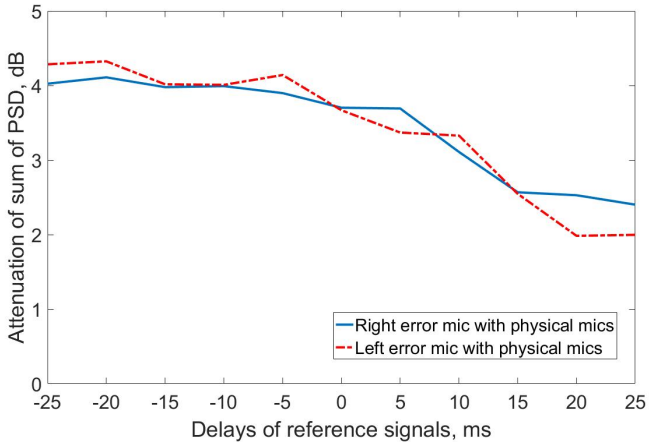

Figure 8.20: Averaged attenuation levels when various delays are applied for the feedforward active headrest system.

8.3.2 Effects of time delays and head movements on performance

For the practical application of the active headrest system, the effect of delays should be considered because although delays from the digital-to-analogue and analogue-to-digital converters (DAC and ADC) and the anti-aliasing and reconstruction filters were already included in the measured signals and transfer responses, in a real-time system additional delays can be generated by the processing time needed to calculate the control signals. Previous research has shown that the attenuation performance can be degraded by these delays [4, 14, 56]. When various delays are applied to the controller, the effect of the delays on the overall reduction of the active headrest system with the physical error microphones is shown in Fig. 8.20. Negative delays, i.e. time advances on the reference signal are also included to illustrate their effects, even though they are clearly unphysical. It can be seen that as the delay is increased, the attenuation performance is progressively degraded and delays of more than 10 ms can decrease the attenuation performance by more than 1 dB. Conversely, if the inherent delays from DAC and ADC and the anti-aliasing and reconstruction filters are reduced, more time-advanced reference signals would be available and the attenuation performance could thus be slightly improved.

When pre-modelled plant responses and observation filters for 16 monitoring microphones are updated for the perturbed head positions, the attenuation performance of the active headrest system is shown in Fig. 8.21. It can be seen that when the dummy head is moved to position 'E' or 'G' in Fig. 8.2, the overall attenuation up to 1 kHz is similar to that achieved at position 'A'. The attenuation with the Delayed RMT is similar to that achieved with the physical error microphones, due to the accurate nearfield estimation, as seen in the previous section. From these results, it is clear that when the head-tracking system updates the pre-modelled observation filters and plant responses,

(*a*)

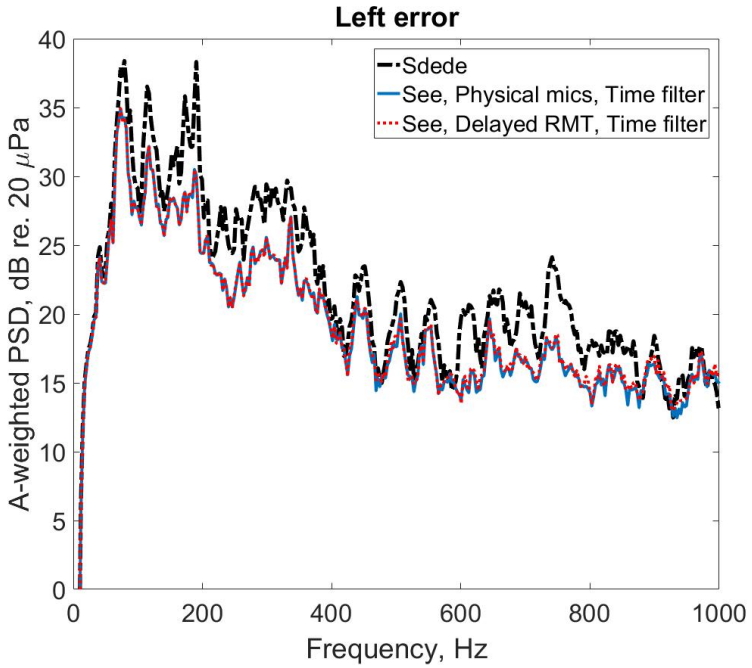

(*b*)

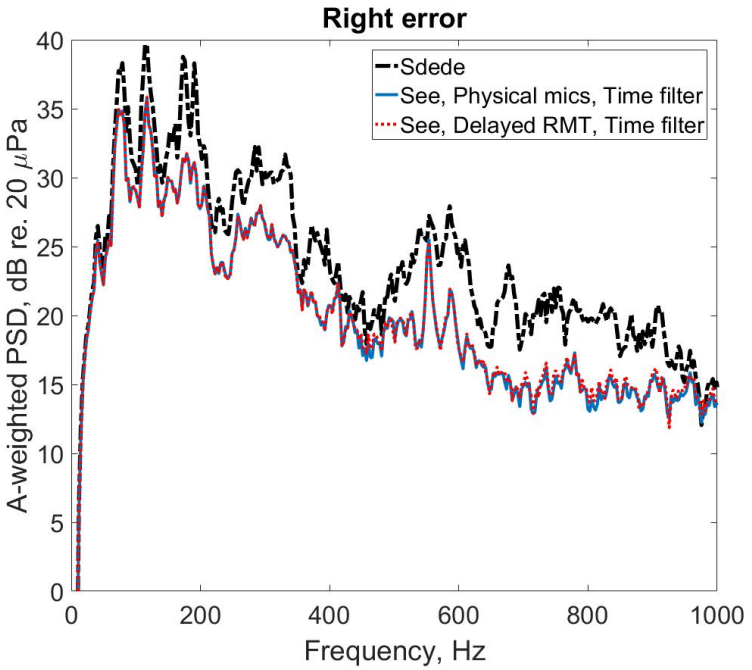

Figure 8.21: The A-weighted PSDs of signals at the left (a) and right (b) error microphones for head position 'E' in Fig. 8.2.

the controlled zones of the active headrest system can move with the ear positions as if the user was wearing active sound control headphones.

(a)

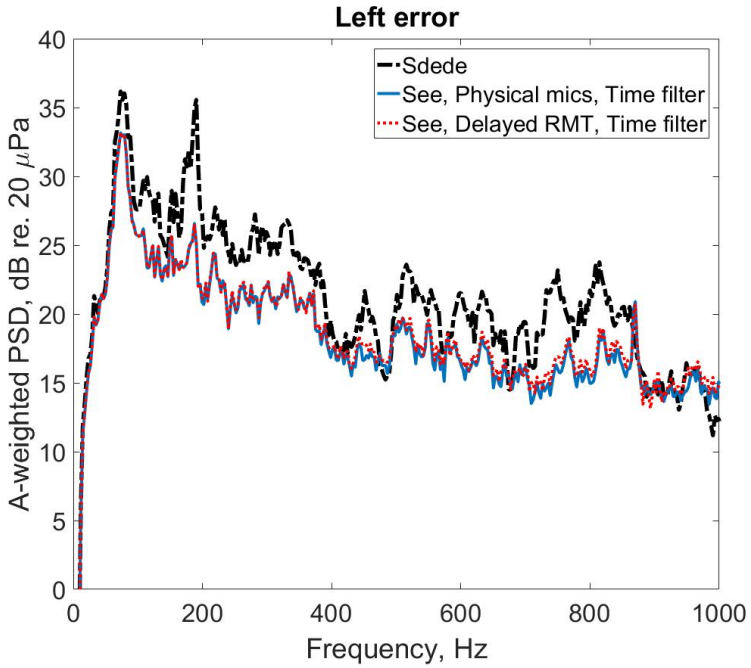

(b)

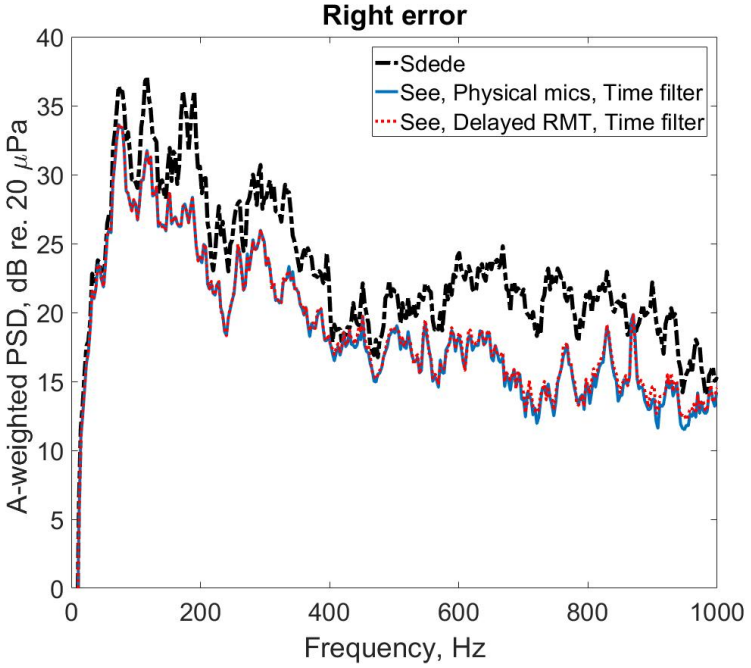

Figure 8.22: The A-weighted PSDs of signals at the left (a) and right (b) error microphones for head position 'G' in Fig. 8.2.

8.4 Summary

Local active sound control with an active headrest system may be an effective method to reduce broadband random road noise in a vehicle cabin at frequencies higher than can be controlled with a global active control system, using more distributed loudspeakers and microphones. Since the direct measurement of the error signals at the ears of a listener is not practical, we have investigated the potential accuracy of the remote microphone technique in this application, to estimate the error signals at the ear positions. The potential performance of the active headrest system in controlling random road noise has also been investigated, using the remote microphone technique. The optimal observation filter for the remote microphone technique, and the corresponding optimal controller with a causality constraint, have been formulated in the time domain, to sense and control broadband random disturbances. To improve the causality of the remote microphone technique, a formulation for the 'delayed' remote microphone technique has also been used to estimate delayed signals at the virtual error microphones and the optimal controller with this technique has also been formulated.

The performance of the remote microphone technique in the vehicle cabin has been investigated by processing the disturbance signals measured at 16 monitoring microphones around the cabin and two error microphones at the ears of a dummy head, when the car was driven over a rough road at 50 mph. The calculated nearfield estimation error between actual and estimated disturbances at the error microphones has shown that with all 16 monitoring microphones, an estimation error of less than -10 dB is achieved up to 800 Hz at the right ear whereas with only four monitoring microphones, this estimation error is only achieved up to 400 Hz. When the dummy head is moved to different positions, the results demonstrate that if a pre-modelled observation filter is updated using position information, from a head tracking device for example, the signals at the perturbed virtual error sensors can still be estimated using fixed monitoring sensors.

The performance of a multichannel feedforward active headrest system combined with the remote microphone technique has been predicted off-line using disturbance signals at the monitoring and error microphones, plant responses and reference signals measured in the car. The causal controller achieves a broadband average reduction of around 3.7 dB up to 1 kHz and a maximum reduction of 8.6 dB is achieved at about 750 Hz at the right ear. The attenuation performance with the remote microphone technique using 16 monitoring microphones is similar to that obtained if the pressure at the ears of the dummy head used in these experiments were directly controlled, illustrating the potential for using remote monitoring microphones. It may be worth to mentioning that the test vehicle is now on the market and various sound absorbing materials have thus been already applied. If the local active control system is considered at the early developing stage of vehicles, less sound absorbing materials would be required for passive control of mid- and high frequency noise sources. When the dummy head is moved to

different positions, the simulation results show that good attenuation at the ears can still be achieved by updating pre-modelled plant responses and observation filters, if the position of the head is always known.

Chapter 9

Conclusions and suggestions for further work

The active headrest system has been shown to be a practical configuration of local active sound control, which produces localised zones of quiet around desired locations. This system has been considered as a potential solution to actively controlling the broadband and random road noise inside automobile cabins. This thesis describes the development of an improved active headrest system for effectively reducing road noise around occupants. In particular, work has mainly focused on the application of the remote microphone technique and the head-tracking to the active headrest system, in order to improve the attenuation performance and the stability of active noise control. This chapter summarises a number of research outcomes generated from the investigations in the thesis. The chapter concludes with suggestions for potential further work, which could be done to improve the performance of the active control system.

9.1 Conclusions

The initial work focused on the effects of various factors including the spatial properties of the primary sound field and the local geometry of the active headrest system on the performance. A general formulation for calculating the optimal performance of feedforward local active sound control systems has been used to illustrate the effects of these factors. Using numerical simulations with a two channel headrest, it has been shown that in a free field, the performance of the controller is generally better for primary source locations behind the secondary source than it is in front, since in this case its phase more closely matches that of the secondary field. This result has been also found in more reverberant field simulations, which were modelled by the summation of a series of acoustic modes to provide a more realistic in-vehicle acoustic environment. These

initial numerical investigations were used to investigate the fundamental characteristics of conventional local active control in enclosures.

The stability of adaptive feedforward active control has then been investigated, in terms of the uncertainties in the plant response. Since excessive phase differences between the pre-modelled and physical plant responses would produce the instability of the active control system, the changes in the plant responses of the active headrest system have been measured as the error sensors in a dummy head were moved to different positions. By analysing the real part of the appropriate eigenvalues, it has been found that instability in both the SISO and MIMO control systems would be produced by ordinary head movements. To avoid this instability, a commercial head tracker, the Microsoft Kinect, was used to detect the head movements and thus allowed the active headrest system to use an appropriate plant response, selected from a look-up table of premeasured plant responses. The test results with a human listener moving their head 10 cm have shown that when for a primary source at 650 Hz, a diverging adaptive active system can become stable again, as the head-tracker is turned on.

The potential for using the remote microphone technique in an active headrest system, to avoid the installation of physical error sensors at the ears of a listener, was then investigated. To estimate the signals at the virtual error microphones from the physical monitoring microphones, a least squares formulation was used for the optimal observation filter, including a regularisation factor. This was chosen using the trade-off between the accuracy of the nearfield estimation and the conditioning of the inversion. The formulation has been used to assess the accuracy of the nearfield estimation, in both numerical and experimental investigations. Simulations in either a diffuse field or a free field with a line array of six uncorrelated primary sources have shown that the estimation accuracy depends on the relative geometry of the monitoring microphone array and the primary source locations. Examples showed better estimation with a circular array of four monitoring microphones in the diffuse field and with a line array of four monitoring microphones in the free field. The performance of the remote microphone technique has been predicted with the active headrest, in both an anechoic chamber and a demo room at ISVR. It has been shown that the choice of the monitoring microphone positions should again consider both the spatial correlation of the primary field and the condition number of the inverted term of the observation filter.

The integration of both the remote microphone technique and head-tracking into a feedforward active headrest system has then been investigated. For tonal noise control, equations for the optimal attenuation performance and for the stability of an adaptive control system have been derived in the frequency domain. It has been shown that the optimal performance and the stability would be degraded by differences respectively between pre-modelled plant responses and physical plant responses, and head movements can produce significant differences between these acoustic responses. The integration of the remote microphone technique and head-tracking have been verified through real-time

experiments, controlling tonal noise in either the anechoic chamber or the demo room. In the anechoic chamber, the estimation error was less than -15 dB and greater than 15 dB attenuation were achieved by the integrated active headrest system for frequencies up to 700 Hz. The good attenuation can be maintained by the head-tracking, when the location of the head was changed. The performance was not so great in the demo room, but an attenuation of 10 dB has still been achieved.

The attenuation performance of the integrated active headrest system was then investigated for the reduction of broadband random disturbances. The optimal observation filter and the control filter for active control, with a causality constraint, have been formulated in the time domain. When the primary source behind the headrest produced broadband random noise in the anechoic chamber, real-time control with the remote microphone technique have demonstrated that disturbance signals at the error microphones in a dummy head were reduced to $20-30$ dB up to about 1 kHz. In addition, with head tracking, good cancellation has been maintained even during head motion. When the primary source was in front of the active headrest system, the delayed remote microphone technique was used, to overcome the non-causal response due to the relative geometry of the microphones and the primary source. With a modelling delay, the accuracy of the nearfield estimation and the attenuation performance was significantly improved.

Finally, the estimation accuracy of the remote microphone technique and the attenuation performance of the active headrest system have been investigated in a vehicle. It has shown that by processing the disturbance signals measured at 16 monitoring microphones around the cabin and two error microphones at the ears of a dummy head, when the car was driven over a rough road at 50 mph, the estimation error is less than -10 dB up to 800 Hz at the right ear. The causal feedforward active headrest system is also predicted to achieve a broadband average reduction of around 3.7 dB up to 1 kHz, with a maximum reduction of 8.6 dB is achieved at 747 Hz at the right ear. The attenuation performance with the remote microphone technique was similar to that obtained if the pressure at the ears of the dummy head used in these experiments were directly controlled, illustrating the potential for using remote monitoring microphones. When the dummy head was moved to different positions, the simulation results have shown that good attenuation and nearfield estimation at the ears can still be achieved if a pre-modelled plant responses and observation filters are updated using position information, from a head tracking device for example.

9.2 Suggestions for further work

The investigations presented in this thesis have shown that it is possible to control broadband random noise with an integrated active headrest system. To improve the

performance of the system, the following areas are suggested for potential future work.

Further investigations on the control algorithms for the integrated active headrest system

In this thesis, the FIR filter based filtered-reference LMS algorithm has been used for adaptive feedforward active control of the integrated system. The laboratory results in Chapter 7 have demonstrated that the adpative integrated system can improve the attenuation performance, stability and controllable frequency range for *stationary* broadband. However, other adaptive algorithms could also be applied to the integrated active headrest system for better performance in more realistic, non-stationary environments. Although the FIR filter based filtered-reference LMS algorithm has been widely investigated here, due to the simple interpretation of the optimal controller and its robustness, the slow convergence speed of the filtered-reference LMS algorithm can be a limitation to adaptive control. For example, if nonstationary disturbances are produced by sudden changes in vehicle driving conditions and head positions, the performance of the filtered-reference LMS algorithm with long FIR filters may be degraded. In order to improve the speed of convergence, a number of algorithms could be considered, such as: frequency domain adaptation [109–111], recursive least-squares (RLS) algorithm [112, 113], the delayless subband adaptive filtering [114–116]. In addition, because a greater number of reference sensors are generally used than error sensors for broadband local active control in vehicles, the filtered-error LMS algorithm can reduce the computational demand [55] and some modified filtered-error LMS algorithms have been proposed to improve the convergence speed [117, 118].

The integrated active headrest system with head-tracking has been shown to improve the stability of convergence when the physical plant response varies from the pre-modelled plant response. However, the leaky filtered-reference LMS algorithm can be employed to improve the robust stability of the algorithm by adding a positive value to the eigenvalues in Eq. (4.18) and Eq. (6.13), although the attenuation performance may then be degraded. Therefore, the effects of the leakage term on the integrated system could be investigated to find methods of balancing the attenuation performance and the stability of convergence. The use of a more robust control algorithm may allow the use of a coarser resolution on the head tracking. It might also be advantageous to interpolate between the desirable estimations of the plant and observation filter, instead of just switching from one to another.

This work may initially consider the integration of both the remote microphone technique and the head-tracking into the feedforward active headrest system and it would also be interesting to extend this investigation to consider both feedback and combined feedforward-feedback control. Since both these control strategies have widely investigated for both active headrest systems and the active headsets [17, 61, 63, 78, 119–121], the integration of both the remote microphone technique and the head-tracking could

be applied in the future to improve the performance with this combined strategy.

Practical appplications of the active headrest system in vehicles

The effects of implementing the integrated active headrest system in the car cabin for road noise control have been investigated through off-line simulations with measured data and it has been shown that the optimal active headrest system with the monitoring microphones effectively reduces interior noise up to 1 kHz. However, an adaptive active control system was not implemented in this thesis, since this was not achievable using the available dSPACE-based hardware. Since the interior noise can change under different driving conditions, future work could focus on the development of real-time adaptive active headrest systems in vehicles, for practical demonstration.

Feedforward active control systems have been studied in this thesis, and the choice of the reference sensors is one of the most crucial factors in determining their performance. It has been assumed that reference sensor signals can be directly accessed from the primary source, for the experiments in the anechoic chamber and the demo room. In addition, for the vehicle test, the reference sensor signals have been provided by JLR, since research on the reference sensors was beyond the scope of this thesis. Therefore, future work could investigate the type and position of the reference sensors, which should be carefully located on the vehicle for better correlation and causality.

Optimal sensor placement for the remote microphone technique

Experimental results with the 24 monitoring microphones around the dummy head in Chapter 5 have led to the conclusion that the selection of the monitoring microphone positions needs to be considered with regard to both the spatial correlation of the primary field and the condition number of the inverted term of the observation filter. The combination of monitoring microphones for the best nearfield estimation was found through an exhaustive search of all sets of four monitoring microphones. However, to reduce the computational demand and extend the capability of microphones, a number of methods of selecting optimal sensor positions have been suggested [101, 122, 123]. Therefore, these methods could be investigated in more detail.

Further investigations on the head-tracking

When a listener's head position is changed during adaptive control with head tracking it has been shown that the zones of quiet move with the ear locations and good cancellation and stability are maintained. In thesis, we have only tracked the translational motion of the head, in two directions, 'forward and backward' and 'right and left', due to experimental limitations. In fact, the Kinect system can detect not only translational movement in three dimensional movements, but also rotational movements of the head and although initial experiment for detecting these movements was implemented as part

of this project, there was not time to incorporate this into the active headrest. Therefore, future work is necessary to understand the effects of rotational movements of the head on local active control, and to incorporate rotational movements of the head into the integrated control algorithm.

Appendix A

Detailed derivations of formulations

A.1 The optimal control filter in the frequency domain

To minimise the cost function J_1 in Chapter 3, which is written again as

$$J_1 = \text{trace}\Big\{ E\left[(\mathbf{d}+\mathbf{GWx})(\mathbf{d}+\mathbf{GWx})^{\text{H}}\right] \Big\} \tag{A.1a}$$

$$= \text{trace}\Big\{ \mathbf{S}_{dd} + \mathbf{GWS}_{xd}^{\text{H}} + \mathbf{S}_{xd}\mathbf{W}^{\text{H}}\mathbf{G}^{\text{H}} + \mathbf{GWS}_{xx}\mathbf{W}^{\text{H}}\mathbf{G}^{\text{H}} \Big\}, \tag{A.1b}$$

the optimum matrix of control filters, $\mathbf{W}_{\text{opt}}$ can be calculated using the derivatives of the trace of a complex matrix. The derivative of Eq. (A.1) with respect to the real and imaginary parts of $\mathbf{W}$ can be obtained using the properties of the trace of a matrix, described in Ref. [55] as

$$\frac{\partial J_1}{\partial \mathbf{W}_{\text{R}}} + j\frac{\partial J_1}{\partial \mathbf{W}_{\text{I}}} = 2\mathbf{G}^{\text{H}}\mathbf{S}_{xd} + 2\mathbf{G}^{\text{H}}\mathbf{GWS}_{xx}. \tag{A.2}$$

Provided $\mathbf{G}^{\text{H}}\mathbf{G}$ and $\mathbf{S}_{xx}$ are non-singular matrices, Eq. (A.2) can be set to zero and the optimal control filter, $\mathbf{W}_{\text{opt}}$, can be obtained as Eq. (3.3).

A.2 The optimal observation filter in the frequency domain

To minimise the cost function J_2 in Chapter 5, which is written again as

$$J_2 = \text{trace}\Big\{ E\left[(\mathbf{d}_e - \mathbf{O}\mathbf{d}_m)(\mathbf{d}_e - \mathbf{O}\mathbf{d}_m)^{\text{H}} + \beta\ \mathbf{O}\mathbf{O}^{\text{H}}\right] \Big\} \tag{A.3a}$$

$$= \text{trace}\Big\{ \mathbf{S}_{d_e d_e} - \mathbf{S}_{d_m d_e}\mathbf{O}^{\text{H}} - \mathbf{O}\mathbf{S}_{d_m d_e}^{\text{H}} + \mathbf{O}(\mathbf{S}_{d_m d_m} + \beta\mathbf{I})\mathbf{O}^{\text{H}} \Big\}, \tag{A.3b}$$

the optimum matrix of observation filters, $\mathbf{O}_{\text{opt}}$ can be calculated using the derivatives of the trace of a complex matrix. The derivative of Eq. (A.3) with respect to the real and imaginary parts of $\mathbf{O}$ can be obtained using the properties of the trace of a matrix, described in Ref. [55] as

$$\frac{\partial J_2}{\partial \mathbf{O}_{\text{R}}} + j\frac{\partial J_2}{\partial \mathbf{O}_{\text{I}}} = 2\mathbf{O}(\mathbf{S}_{d_m d_m} + \beta\mathbf{I}) - 2\mathbf{S}_{d_m d_e}. \tag{A.4}$$

Because $\mathbf{S}_{d_m d_m} + \beta\mathbf{I}$ is a non-singular matrix, Eq. (A.4) can be set to zero and the optimal observation filter, $\mathbf{O}_{\text{opt}}$, can be obtained as Eq. (5.5).

A.3 The optimal controller combined with the remote microphone technique for tonal disturbances in the frequency domain

To minimise the cost function J_3 in Chapter 6, which is written again as

$$J_3 = \text{trace}\Big\{ E\left[(\hat{\mathbf{O}}_{\text{opt}}\mathbf{d}_m + \mathbf{G}\mathbf{u})(\hat{\mathbf{O}}_{\text{opt}}\mathbf{d}_m + \mathbf{G}\mathbf{u})^{\text{H}}\right] \Big\} \tag{A.5a}$$

$$= \text{trace}\Big\{ \hat{\mathbf{O}}_{\text{opt}}\mathbf{S}_{d_m d_m}\hat{\mathbf{O}}_{\text{opt}}^{\text{H}} + \mathbf{G}\mathbf{S}_{d_m u}\hat{\mathbf{O}}_{\text{opt}}^{\text{H}} + \hat{\mathbf{O}}_{\text{opt}}\mathbf{S}_{d_m u}^{\text{H}}\mathbf{G}^{\text{H}} + \mathbf{G}\mathbf{S}_{uu}\mathbf{G}^{\text{H}} \Big\}, \tag{A.5b}$$

the optimal control signals, $\mathbf{u}_{\text{opt}}$ can be calculated using the derivatives of the trace of a complex matrix. The derivative of Eq. (A.5) with respect to the real and imaginary parts of $\mathbf{u}$ can be obtained using the properties of the trace of a matrix, described in Ref. [55] as

$$\frac{\partial J_3}{\partial \mathbf{u}_{\text{R}}} + j\frac{\partial J_3}{\partial \mathbf{u}_{\text{I}}} = 2\mathbf{G}^{\text{H}}\mathbf{G}\mathbf{u} + 2\mathbf{G}^{\text{H}}\hat{\mathbf{O}}_{\text{opt}}\mathbf{d}_m. \tag{A.6}$$

Provided $\mathbf{G}^{\text{H}}\mathbf{G}$ is a non-singular matrix, Eq. (A.6) can be set to zero and the optimal control signals, $\mathbf{u}_{\text{opt}}$, can be obtained as Eq. (6.5).

A.4 The optimal observation filter in the time domain

To minimise the cost function J_4, which is defined as

$$J_4 = \text{trace}\Big\{ E\left[(\boldsymbol{d}_e(n) - \boldsymbol{O}\boldsymbol{d}_m^{'}(n))(\boldsymbol{d}_e(n) - \boldsymbol{O}\boldsymbol{d}_m^{'}(n))^{\mathrm{T}} + \beta\ \boldsymbol{O}\boldsymbol{O}^{\mathrm{T}}\right]\Big\} \tag{A.7a}$$

$$= \text{trace}\Big\{ \boldsymbol{R}_{d_e d_e} - \boldsymbol{R}_{d_m d_e}\boldsymbol{O}^{\mathrm{T}} - \boldsymbol{O}\boldsymbol{R}_{d_m d_e}^{\mathrm{T}} + \boldsymbol{O}(\boldsymbol{R}_{d_m d_m} + \beta\mathbf{I}^{'})\boldsymbol{O}^{\mathrm{T}}\Big\}, \tag{A.7b}$$

where $\boldsymbol{R}_{d_e d_e} = E\left[\boldsymbol{d}_e(n)\boldsymbol{d}_e^{\mathrm{T}}(n)\right]$, $\boldsymbol{R}_{d_m d_e} = E\left[\boldsymbol{d}_e(n)\boldsymbol{d}_m^{'\mathrm{T}}(n)\right]$ and $\boldsymbol{R}_{d_m d_m} = E\left[\boldsymbol{d}_m^{'}(n)\boldsymbol{d}_m^{'\mathrm{T}}(n)\right]$, the optimal observation filters, $\boldsymbol{O}_{\text{opt}}$ can be calculated using the derivatives of the trace of a matrix.

The derivative of Eq. (A.7) with respect to the elements of $\boldsymbol{O}$ can be obtained using the properties of the trace of a matrix, described in Ref. [55] as

$$\frac{\partial J_4}{\partial \boldsymbol{O}} = 2\boldsymbol{O}(\boldsymbol{R}_{d_m d_m} + \beta\mathbf{I}^{'}) - 2\mathbf{R}_{d_m d_e}. \tag{A.8}$$

Because $\boldsymbol{R}_{d_m d_m} + \beta\mathbf{I}^{'}$ is a non-singular matrix, Eq. (A.8) can be set to zero and the optimal observation filter, $\boldsymbol{O}_{\text{opt}}$, can be obtained as Eq. (7.14) in Chapter 7.

A.5 The optimal controller combined with the remote microphone technique in the time domain

To minimise the cost function J_5 in Chapter 7, which is written again as

$$J_5 = \text{trace}\Big\{ E\left[\hat{\boldsymbol{e}}(n)\ \hat{\boldsymbol{e}}^{\mathrm{T}}(n) + \rho\ \boldsymbol{w}\boldsymbol{w}^{\mathrm{T}}\right]\Big\} \tag{A.9a}$$

$$= \text{trace}\Big\{ E\left[(\hat{\boldsymbol{O}}_{\text{opt}}\boldsymbol{d}_m^{'}(n) + \boldsymbol{R}(n)\boldsymbol{w})(\hat{\boldsymbol{O}}_{\text{opt}}\boldsymbol{d}_m^{'}(n) + \boldsymbol{R}(n)\boldsymbol{w})^{\mathrm{T}} + \rho\ \boldsymbol{w}\boldsymbol{w}^{\mathrm{T}}\right]\Big\} \tag{A.9b}$$

$$= \text{trace}\Big\{ \hat{\boldsymbol{O}}_{\text{opt}}\boldsymbol{R}_{d_m d_m}\hat{\boldsymbol{O}}_{\text{opt}}^{\mathrm{T}} + E\left[\hat{\boldsymbol{O}}_{\text{opt}}\boldsymbol{d}_m^{'}(n)\boldsymbol{w}^{\mathrm{T}}\boldsymbol{R}(n)^{\mathrm{T}} + \boldsymbol{R}(n)\boldsymbol{w}\boldsymbol{d}_m^{'\mathrm{T}}(n)\hat{\boldsymbol{O}}_{\text{opt}}^{\mathrm{T}}\right]$$

$$+ \left(E\left[\boldsymbol{R}(n)\boldsymbol{w}\boldsymbol{w}^{\mathrm{T}}\boldsymbol{R}(n)^{\mathrm{T}} + \rho\boldsymbol{w}\boldsymbol{w}^{\mathrm{T}}\right]\right)\Big\}, \tag{A.9c}$$

the optimal control filters, $\boldsymbol{w}_{\text{opt}}$ can be calculated using the derivatives of the trace of a matrix.

The derivative of Eq. (A.9) with respect to the elements of $\boldsymbol{w}$ can be obtained using the properties of the trace of a matrix, described in Ref. [55] as

$$\frac{\partial J_5}{\partial \boldsymbol{w}} = 2E\left[\boldsymbol{R}(n)^{\mathrm{T}}\boldsymbol{R}(n) + \rho\mathbf{I}\right]\boldsymbol{w} + 2E\left[\boldsymbol{R}(n)^{\mathrm{T}}\hat{\boldsymbol{O}}_{\mathrm{opt}}\boldsymbol{d}_m'(n)\right]. \tag{A.10}$$

Because $E\left[\boldsymbol{R}(n)^{\mathrm{T}}\boldsymbol{R}(n) + \rho\mathbf{I}\right]$ is a non-singular matrix, Eq. (A.10) can be set to zero and the optimal observation filter, $\boldsymbol{w}_{\mathrm{opt}}$, can be obtained as Eq. (7.17).

Appendix B

Further investigation on the nearfield estimation

In Chapter 5, contour plots of the estimation error area for different positions of the virtual error microphone on a $\pm 5L$ grid were obtained by the optimal observation filters with the properly chosen regularisation factors. To select an appropriate regularisation factor, it is necessary to consider the trade-off between the estimation accuracy and the robustness to uncertainties. In this chapter, the details of this process are discussed and the responses of the observation filters with/without the regularisation factors are investigated for different acoustic fields and different microphone arrays.

B.1 Trade-off between the estimation accuracy and the robustness to uncertainties in a diffuse field

In Section 5.2.1, when the line array of four monitoring microphones is used to estimate disturbance signals at a virtual error microphone at $x = 0$, $y = -2L$ at $kL = 0.25$ in a single frequency diffuse field, the appropriate regularisation factor is determined via the process illustrated in Fig. 5.5. Fig. B.1 shows similar process at $kL = 0.5$ and $kL = 1$, respectively. At $kL = 2$ the regularisation factor is not required due to sufficiently small conditioning number.

When the circular array of four monitoring microphones was used to estimate disturbance signals at a virtual error microphone at $x = 0$, $y = -2L$ at $kL = 0.25$ in a diffuse field, the appropriate regularisation factor is chosen via the process as shown in Fig. B.2. At higher frequencies, the regularisation factor is not required.

As mentioned in Chapter 5, with regularisation, the amplitudes of the observation filter responses are significantly reduced, and also the amplitude and phase of the responses change less with the position of the virtual microphone.

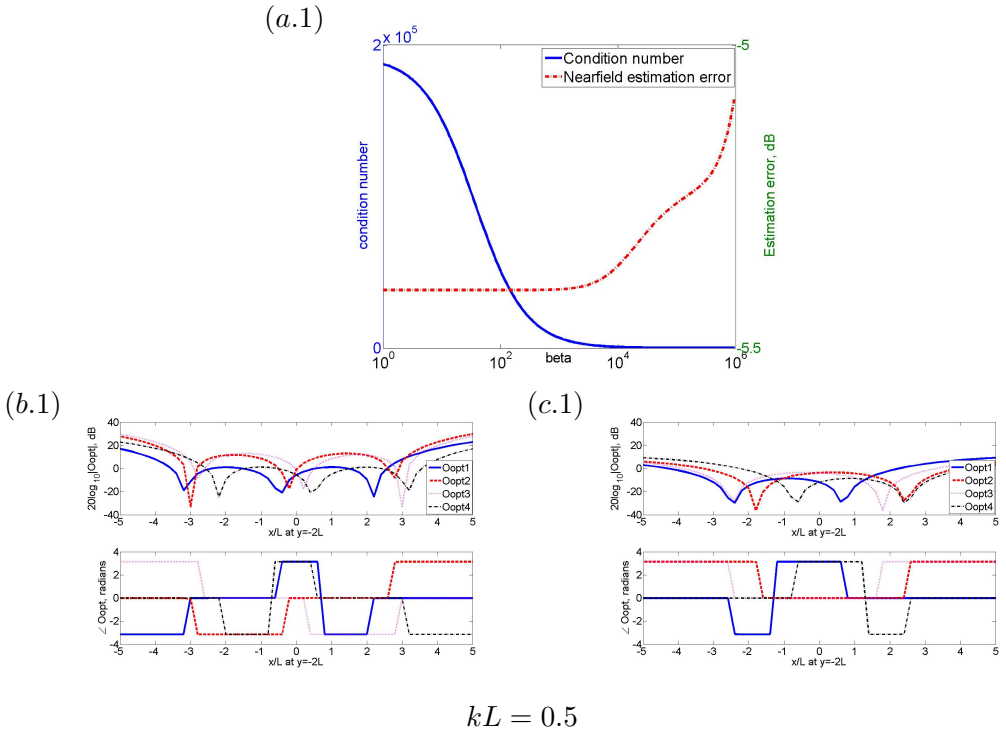

$kL = 0.5$

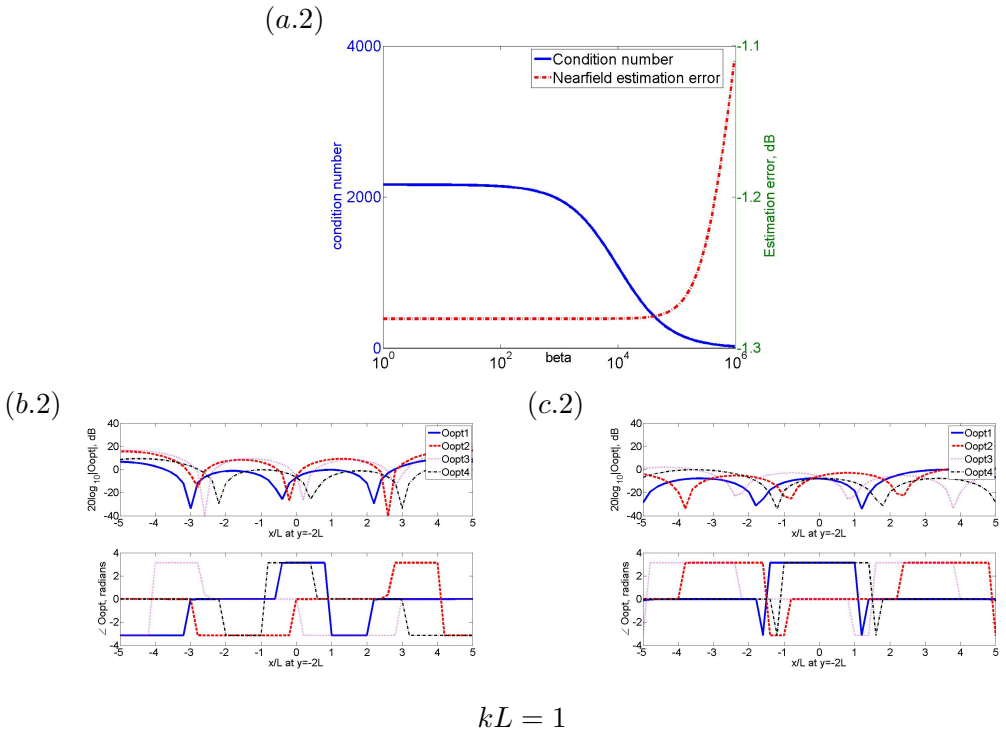

$kL = 1$

Figure B.1: (a) Condition number of the inverse term in Eq. (5.5) (Solid line) and the nearfield estimation error (Dash-dot line), at a frequency such that either $kL = 0.5$ or $kL = 1.0$, with different regularisation factors in the observation filter when the **line** array of four monitoring microphones at $y = 0$ are used to estimate the disturbance at a virtual error microphone at $x = 0$, $y = -2L$ in a single frequency ***diffuse*** field. The responses of the observation filter matrix, as the location of the single virtual error microphone is varied along x-axis, is also shown (b) without and (c) with the regularisation factor ($\beta = 6.6 \times 10^3$ for $kL = 0.5$, $\beta = 6.6 \times 10^4$ for $kL = 1.0$).

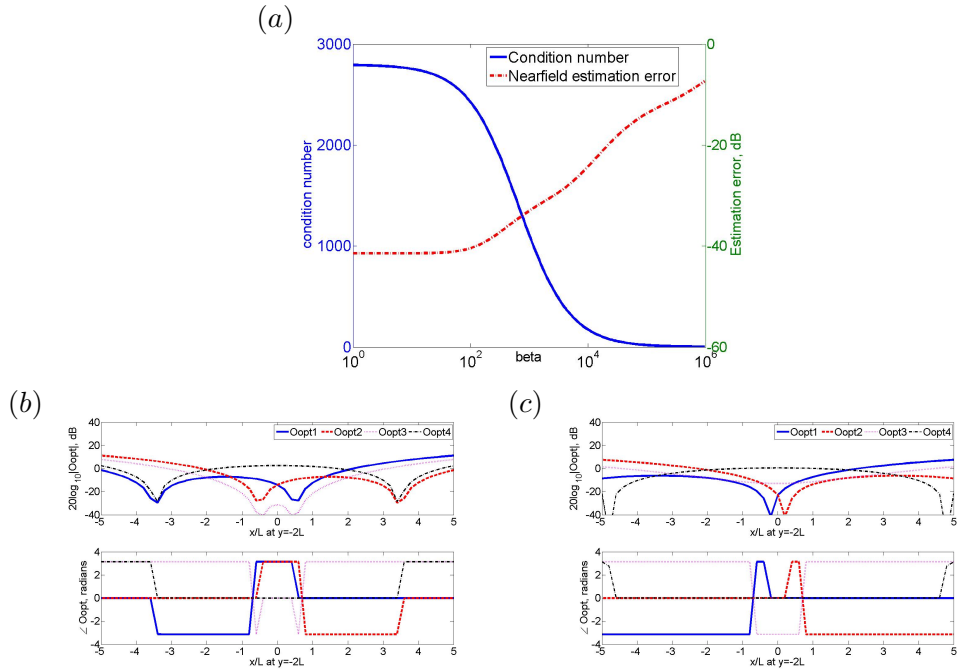

Figure B.2: (a) Condition number of the inverse term in Eq. (5.5) (Solid line) and the nearfield estimation error (Dash-dot line), at a frequency such that $kL = 0.25$, with different regularisation factors in the observation filter when the **circular** array of four monitoring microphones, which has a diameter of $3L$, are used to estimate the disturbance at a virtual error microphone at $x = 0$, $y = -2L$ in a single frequency ***diffuse*** field. The responses of the observation filter matrix, as the location of the single virtual error microphone is varied along x-axis, is also shown (b) without and (c) with the regularisation factor ($\beta = 10^3$).

B.2 Trade-off between the estimation accuracy and the robustness to uncertainties with the primary sources located on one side of the monitoring microphones in the free field

When the line array of four monitoring microphones is used to estimate disturbance signals at a virtual error microphone at $x = 0$, $y = -2L$ at $kL = 0.25$ with 6 primary sources separated by $8L$ at $y = 30L$, behind the microphone array in Fig. 5.4, producing disturbances in the free field, the appropriate regularisation factor is determined via the process shown in Fig. B.3. Fig. B.4 shows similar process at $kL = 0.5$ and $kL = 1.0$, respectively. At $kL = 2$ the regularisation factor is not required.

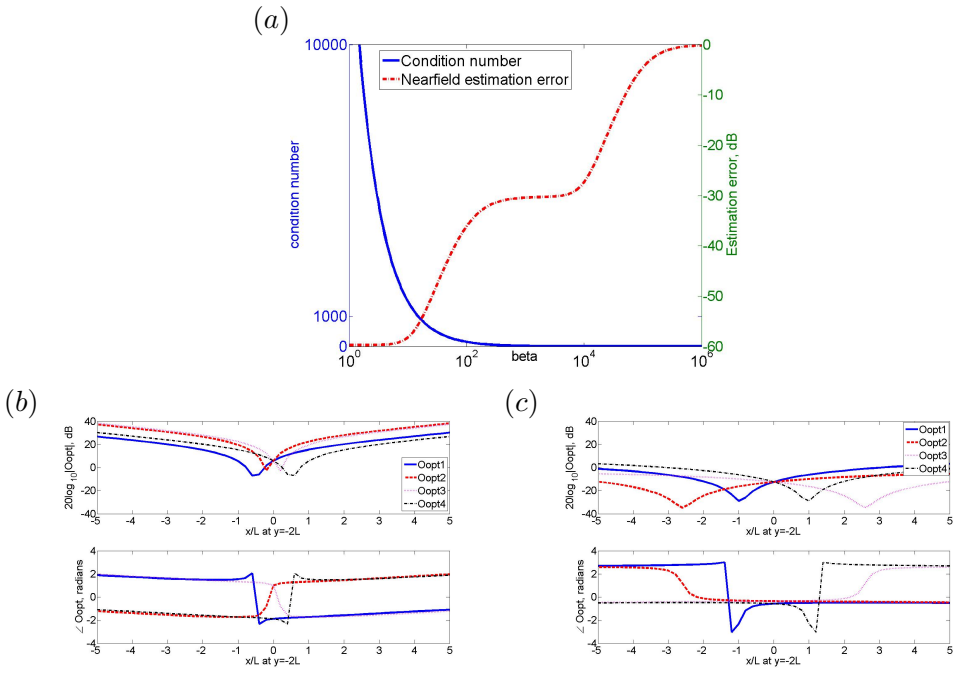

Figure B.3: (a) Condition number of the inverse term in Eq. (5.5) (Solid line) and the nearfield estimation error (Dash-dot line), for the arrangement shown in Fig. 5.4 at a frequency such that $kL = 0.25$, with different regularisation factors in the observation filter used to estimate disturbance signals of a virtual error microphone at $x = 0$, $y = -2L$ from the **line** of four monitoring microphones, with 6 primary sources separated by $8L$ at $y = 30L$, **behind** the microphone array in Fig. 5.4, producing disturbances in the free field. The responses of the observation filter matrix, as the location of the single virtual error microphone is varied along x-axis, is also shown (b) without and (c) with the regularisation factor ($\beta = 15$ for $kL = 0.25$).

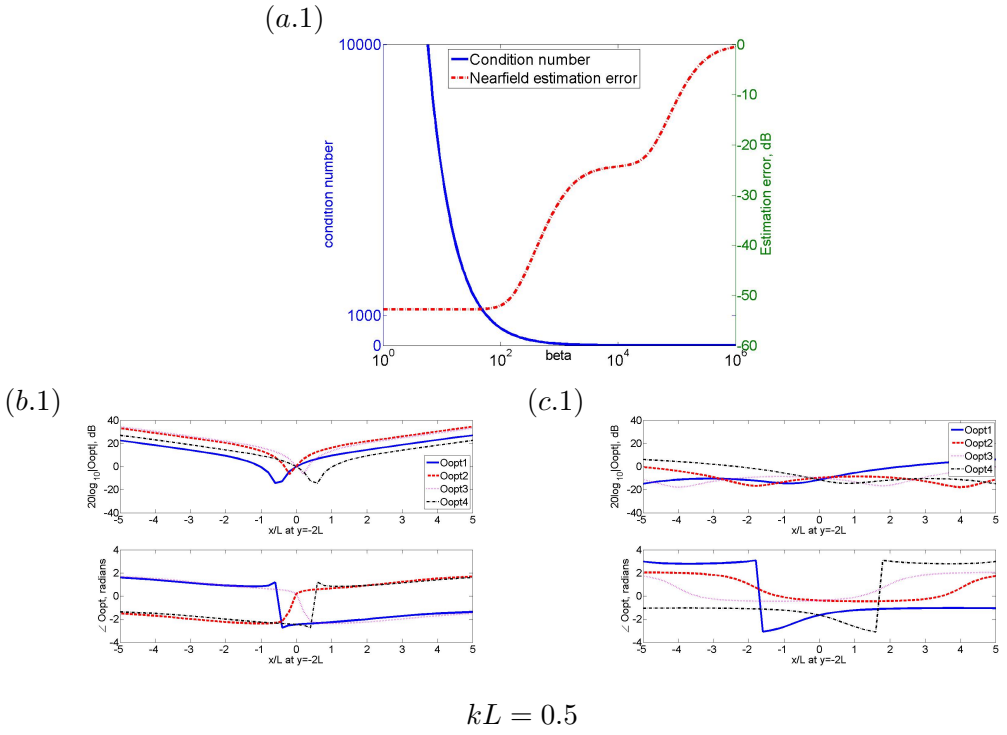

$kL = 0.5$

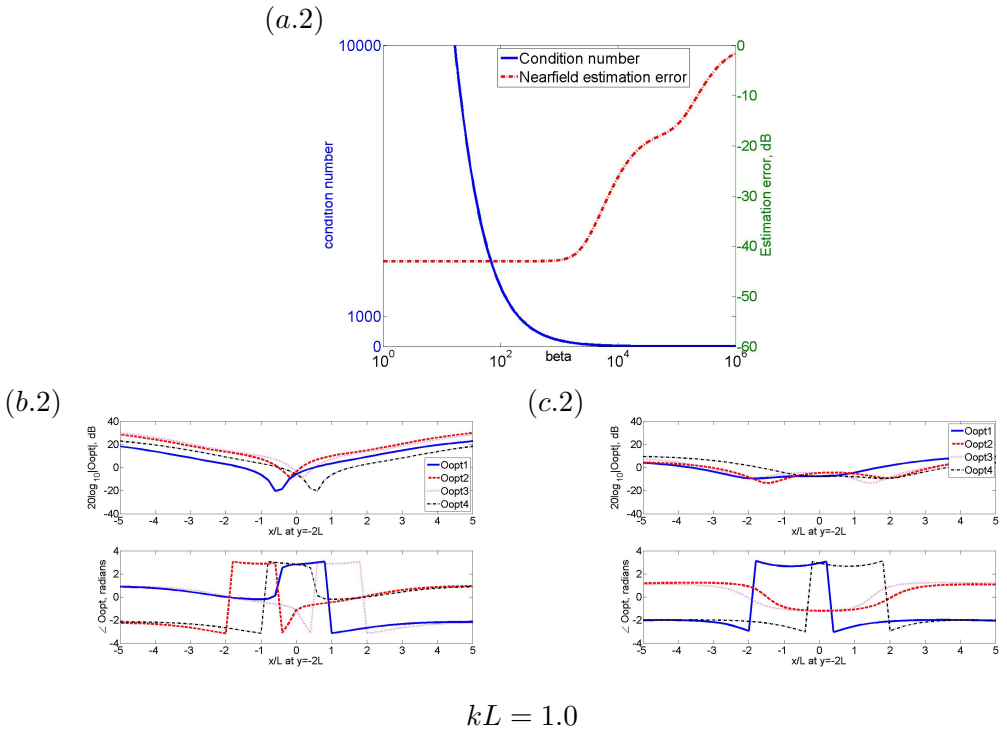

$kL = 1.0$

Figure B.4: (a) Condition number of the inverse term in Eq. (5.5) (Solid line) and the nearfield estimation error (Dash-dot line), for the arrangement shown in Fig. 5.4 at a frequency such that either $kL = 0.5$ or $kL = 1.0$, with different regularisation factors in the observation filter used to estimate disturbance signals of a virtual error microphone at $x = 0$, $y = -2L$ from the **line** of four monitoring microphones, with 6 primary sources separated by $8L$ at $y = 30L$, **behind** the microphone array in Fig. 5.4, producing disturbances in the free field. The responses of the observation filter matrix, as the location of the single virtual error microphone is varied along x-axis, is also shown (b) without and (c) with the regularisation factor ($\beta = 60$ for $kL = 0.5$, $\beta = 200$ for $kL = 1.0$).

Appendix C

Further investigation of the integrated active headrest system in a more reverberant room

In Chapter 5, the nearfield estimation with the remote microphone technique has been studied in an anechoic chamber and in Chapter 6, the stability and the optimal performance of the integrated active headrest system have been investigated off-line from transfer responses measured in the anechoic chamber. In addition, in Chapter 6 and Chapter 7, the real-time implementation of the nearfield estimation and integrated active headrest system for controlling both tonal and broadband sounds have been investigated also in the anechoic chamber. To investigate effects of this research in a more reverberant room, similar experiments have been conducted in a demonstration room for active noise control at ISVR. This demo room was built to simulate active noise control inside an aircraft cabin, and is about 4.9 m×2.2 m×2.1 m with a carpet and all four walls covered in 5.5 cm open-cell foam in a hessian covering.

In Section C.1, the performance of the remote microphone technique is investigated via experiments in the demo room, using multiple loudspeakers and the microphone array which were described in Chapter 5. In Section C.2, the stability and the optimal performance of the integrated active headrest system are investigated off-line with measured transfer responses. Section C.3 describes the real-time implementation of the nearfield estimation and the integrated active headrest system for controlling tonal sounds in the demo room. In Section C.4, the integrated active headrest system with either the standard or the delayed remote microphone technique is used to adaptively control broadband noise in the demo room. Finally, Section C.5 presents a summary of these results.

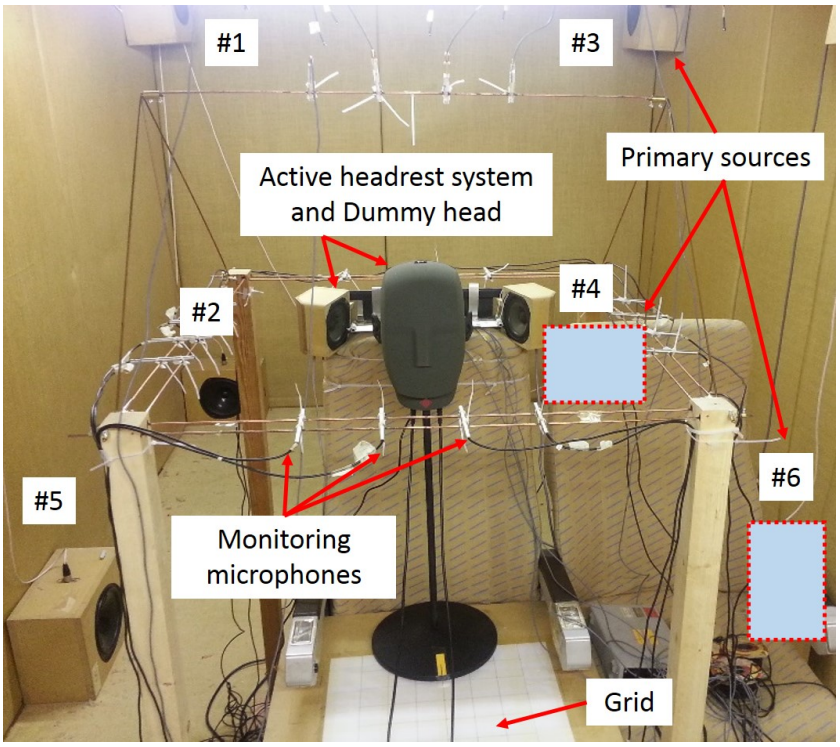

Figure C.1: The overall installation for the nearfield estimation experiments when six primary sources produce uncorrelated random disturbance signals and with monitoring microphones installed around an active headrest system to estimate the disturbance signals at two error microphones in the ears of a dummy head in a demo room at ISVR as a more reverberant acoustic field.

C.1 Experimental study for nearfield estimation using the remote microphone technique in a more reverberant room

C.1.1 Test installation in a more reverberant room

To estimate the accuracy of the remote microphone technique in a more reverberant room, the same array was used as in Chapter 5, with 24 monitoring microphones and the two error microphones in the dummy head used in Fig. 5.13, which was installed in a demo room, as shown in Fig. C.1. However, in Fig. C.1, six loudspeakers acting as primary sources were also installed at different locations in the demo room. The same grid used above, as in Fig. 5.13, was installed on the seat in the demo room and various acoustic transfer responses were measured and used to calculate optimum observation filters for the various combinations of monitoring microphones and the different head positions, using Eq. (5.5). The potential accuracy of the remote microphone technique was then estimated.

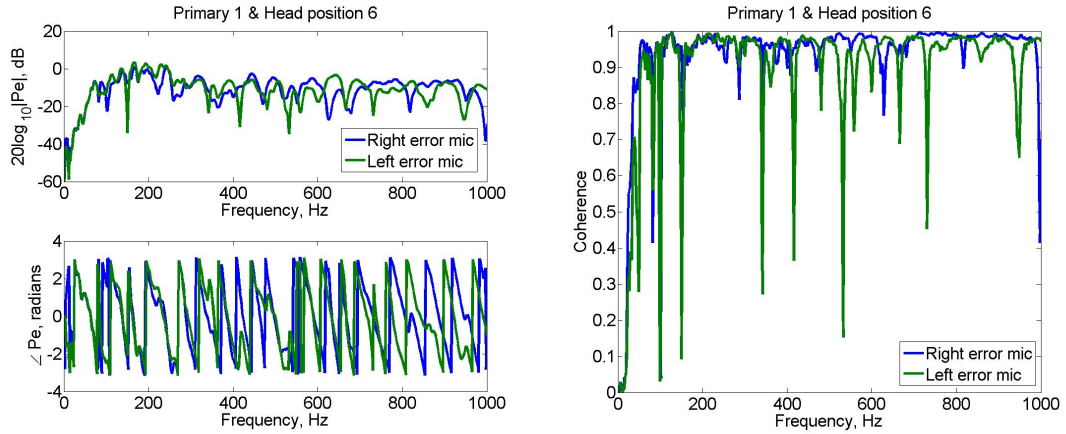

Figure C.2: The transfer response, $\mathbf{P}_e$ (left) and coherence (right) between the primary source #1, operating alone, and the left and right error microphones at head position #6.

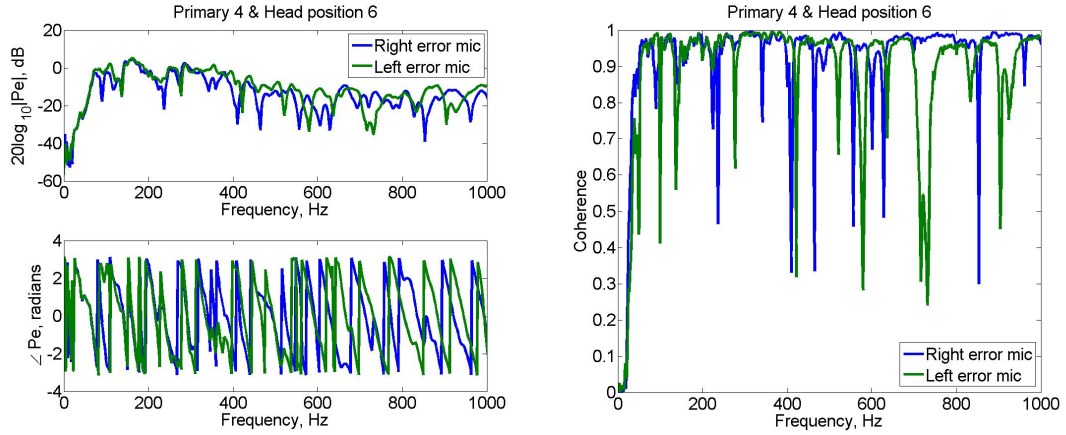

Figure C.3: The transfer response, $\mathbf{P}_e$ (left) and coherence (right) between the primary source #4, operating alone, and the left and right error microphones at head position #6.

C.1.2 Measurement of the acoustic transfer response and coherence

When the primary source #1 and #4, as numbered in Fig. C.1, are separately driven, the acoustic transfer responses, $\mathbf{P}_e$ and $\mathbf{P}_m$ at the error microphones and the monitoring microphones #21, #22, #23 and #24, as numbered in Fig. 5.13(c), are shown in Fig. C.2, Fig. C.3, Fig. C.4 and Fig. C.5. The transfer responses in the more reverberant enclosure have a greater variation with frequency than in the anechoic chamber. This is because resonances and anti-resonances of acoustic modes induce a number of peaks and dips in the frequency responses and the dips also lead to poor coherences. It is expected that these more complicated responses and the poorer coherences will lead to a worse nearfield estimation in the more reverberant field.

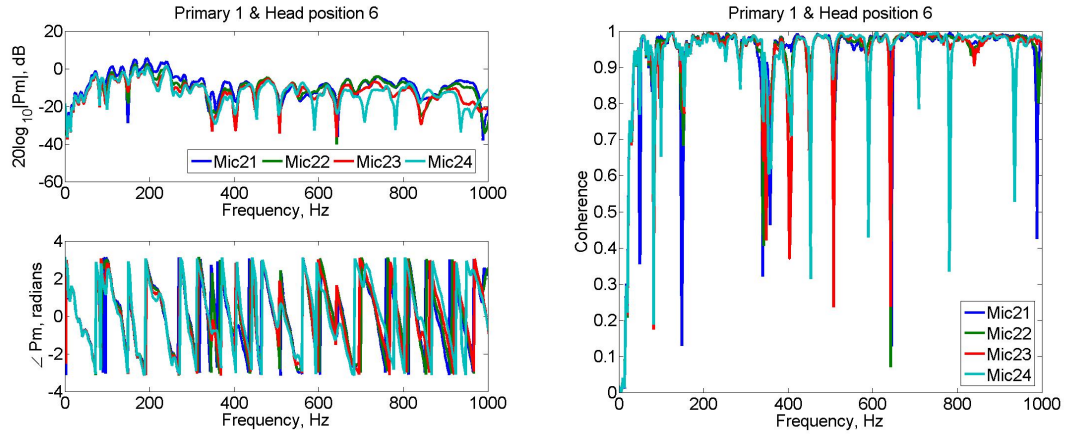

Figure C.4: The transfer response, $\mathbf{P}_m$ (left) and coherence (right) between the primary source #1, operating alone, and the monitoring microphones #21, #22, #23 and #24 at head position #6.

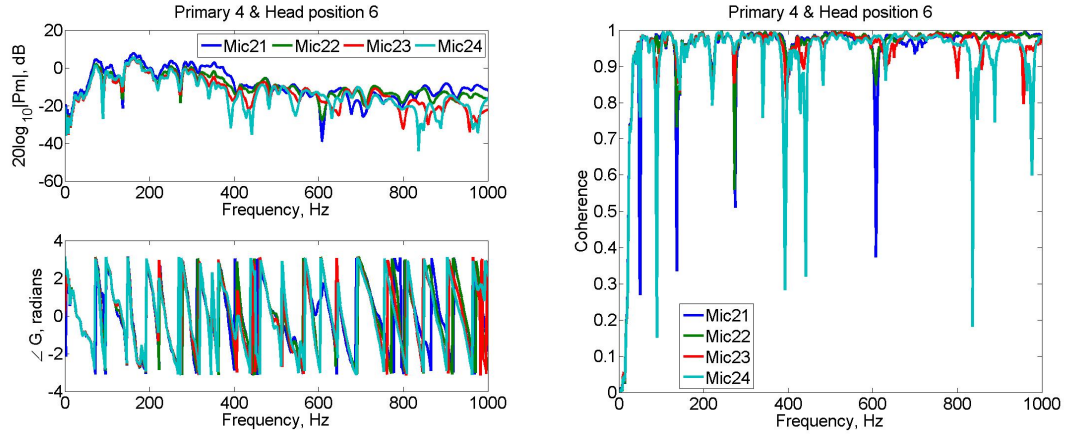

Figure C.5: The transfer response, $\mathbf{P}_m$ (left) and coherence (right) between the primary source #4, operating alone, and the monitoring microphones #21, #22, #23 and #24 at head position #6.

C.1.3 Nearfield estimation for different monitoring microphones array and different head positions in a more reverberant room

Measurements of the various acoustic transfer responses in section C.1.2 were used to calculate optimum observation filters for the various combinations of monitoring microphones, using Eq. (5.5). The potential accuracy of the remote microphone technique has also been estimated. Regularisation factors for different combinations of monitoring microphones were obtained by a consideration of the trade-off between the estimation accuracy and the robustness, as in Chapter 5. The dummy head is initially located in the nominal head position #6.

Fig. C.6 shows the estimation error at the two ears of the dummy head, calculated with regularisation, and the condition numbers of the inverted term in Eq. (5.5) with and without regularisation, as a function of frequency, when using monitoring microphones #21, #22, #23 and #24, which are located on the headrest. This estimation error may be compared with the result with the same monitoring microphones in the anechoic chamber in Fig. 5.19. The results here are similar to those in Fig. 5.19 up to about 200 Hz but the estimation error is then larger than that in the anechoic chamber, due to the complexity of the acoustic transfer responses.

When monitoring microphones #3, #7, #10, #14 were selected, which form a ring around the headrest, the results are shown in Fig. C.7. It can be seen that the estimation error with these monitoring microphones, at frequencies below 400 Hz, is better than those in Fig. C.6 but the estimation error in the frequency range from 400 to 700 Hz is similar to each other and the estimation error in the frequency range above 700 Hz is worse than the result in Fig. C.6. When the results in Fig. C.7 are compared to those in Fig. 5.20, it is found that the estimation error up to around 400 Hz in the demo room is similar to that in the anechoic chamber but at higher frequencies, the estimation error in the demo room is degraded, compared to those in Fig. 5.20.

As in Chapter 5, the best nearfield estimation is achieved with monitoring microphones #13, #22, #23, #16, i.e. with two microphones on the headrest and two on the rear supporting structure, as shown in Fig. C.8, which can be compared with Fig. 5.21 in the anechoic chamber. From the results in this section and in Chapter 5, it is verified that when both the spatial correlation of the primary field and the condition number of the inverted term in Eq. (5.5) are considered for the selection of the monitoring microphone positions, the better estimation error can be achieved. The general trend in terms of the condition numbers in Fig. C.6, Fig. C.7 and Fig. C.8 for the more reverberant enclosure still corresponds with the results in Chapter 5. For instance, in Fig. C.6, because of the small distance between the monitoring microphones, the large condition number is produced. Conversely, in Fig. C.7, the condition number is much lower due to the larger spacing between the microphones. Finally, the monitoring microphone array in Fig. C.8 achieves a good trade-off between spatial matching of the acoustic field and the condition number associated with the inversion.

Fig. C.9 shows the estimation error at the left and right error microphones when the dummy head is located at 3 different positions on the grid shown in Fig. 5.14(a): position #6 (the nominal position), position #2 (5 cm backward from the nominal position) and position #16 (10 cm forward from the nominal position). A general trend of the results in Fig. C.9 for the demo room also corresponds to the results in Fig. 5.22 for the anechoic chamber: That is, as the distance from the monitoring microphones to the error microphones increases, the estimation performance between about 200 Hz and 800 Hz is degraded.

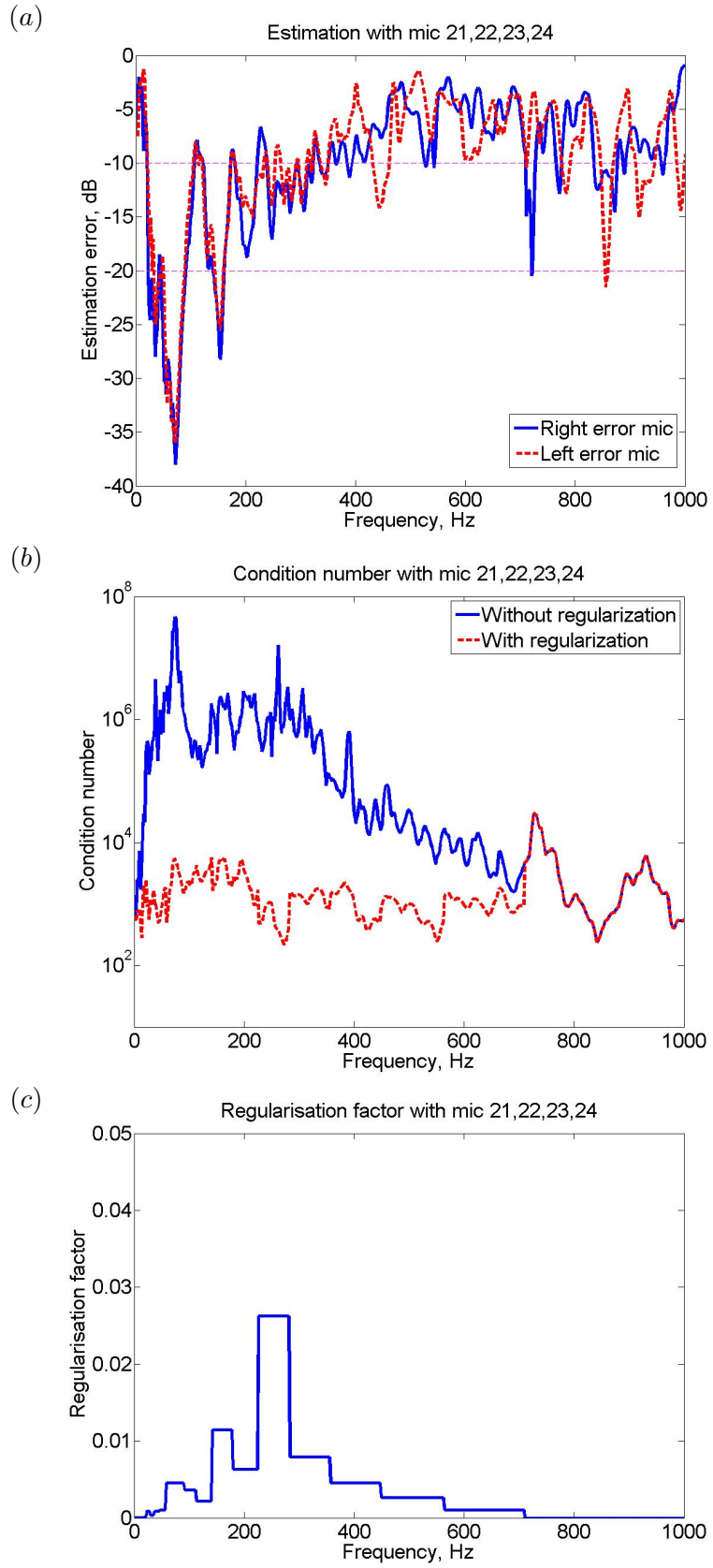

Figure C.6: The nearfield estimation error (a), condition number (b) and regularisation factor (c) calculated from the measured data when four monitoring microphones, #21, #22, #23, #24, are selected from the monitoring array in Fig. 5.13 to estimate the disturbance signals at the ears of the dummy head when 6 primary sources located at the rear of the headrest are driven with uncorrelated white noise in a more reverberant enclosure.

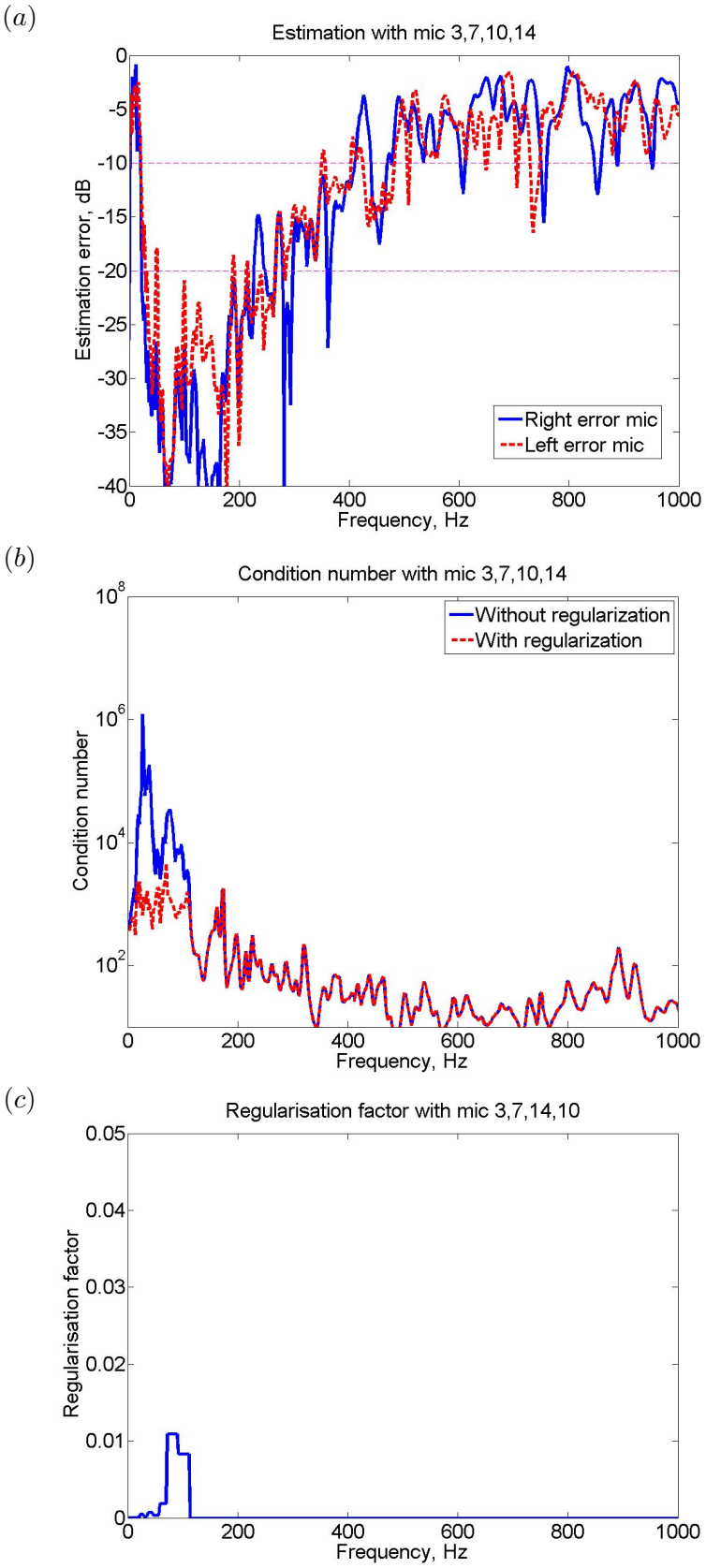

Figure C.7: The nearfield estimation error (a), condition number (b) and regularisation factor (c) calculated from the measured data when four monitoring microphones, #3, #7, #10, #14, are selected from the monitoring array in Fig. 5.13 to estimate the disturbance signals at the ears of the dummy head when 6 primary sources located at the rear of the headrest are driven with uncorrelated white noise in a more reverberant enclosure.

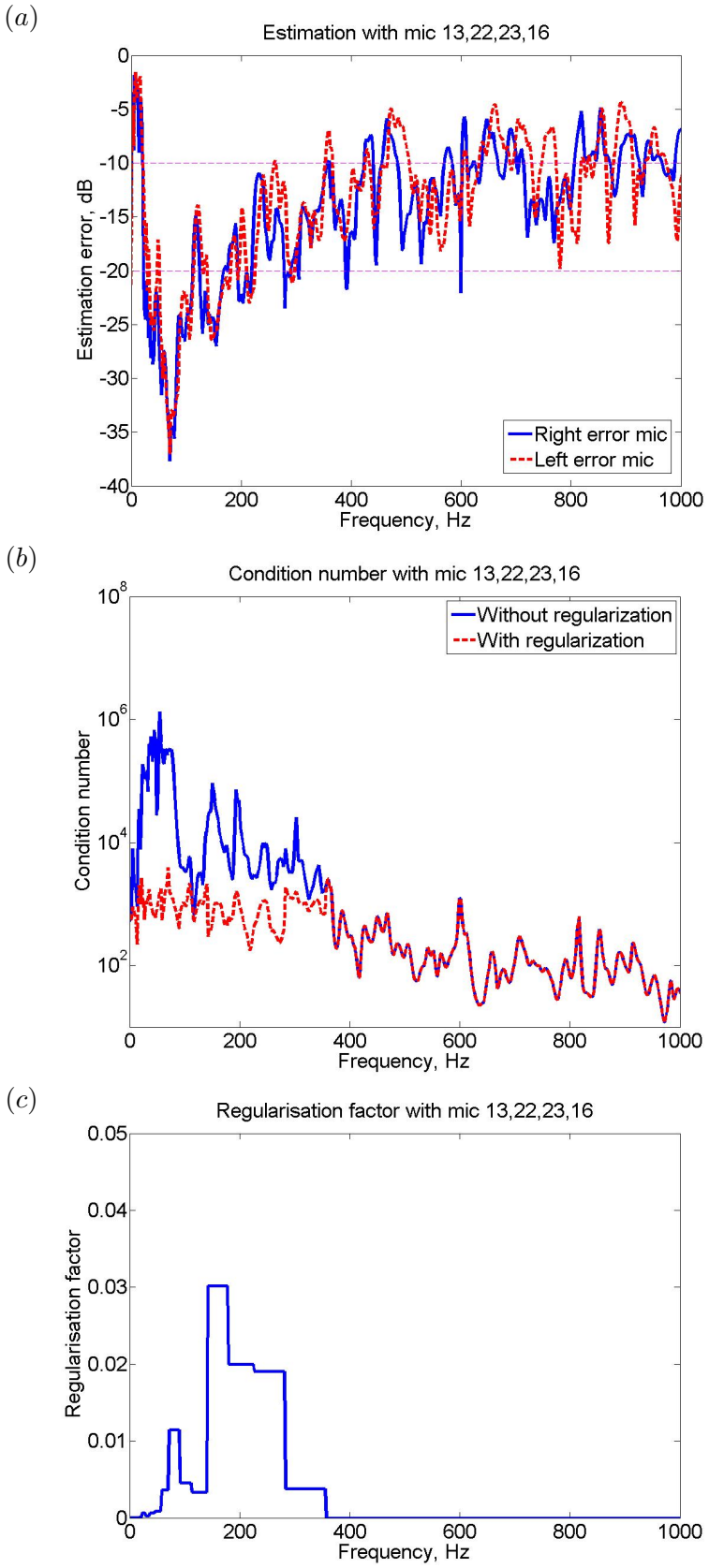

Figure C.8: The nearfield estimation error (a), condition number (b) and regularisation factor (c) calculated from the measured data when four monitoring microphones, #13, #22, #23, #16, are selected from the monitoring array in Fig. 5.13 to estimate the disturbance signals at the ears of the dummy head when 6 primary sources located at the rear of the headrest are driven with uncorrelated white noise in a more reverberant enclosure.

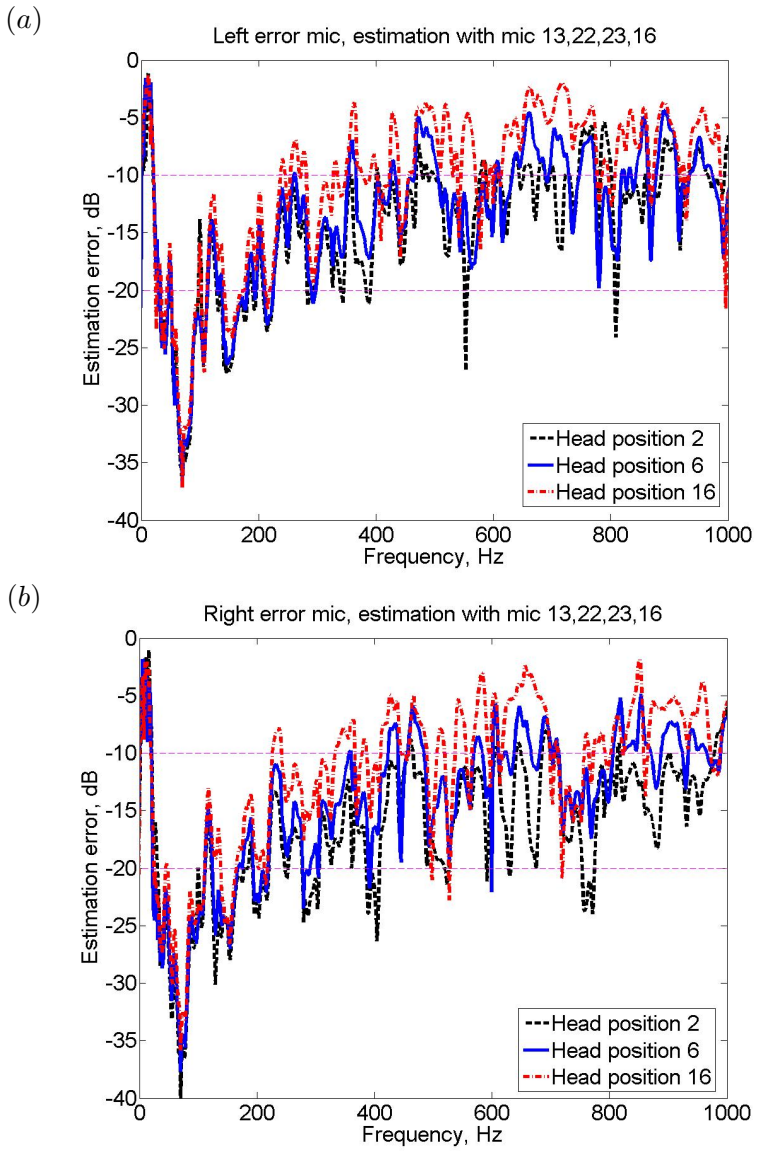

Figure C.9: The comparison of the nearfield estimation error for the different head positions with the monitoring microphones, #13, #22, #23, #16 when 6 uncorrelated random primary sources are behind the active headrest system in a more reverberant enclosure : (a) the left error microphone, (b) the right error microphone.

C.1.4 The response of the observation filter in the frequency and time domain

In the more reverberant enclosure, the response of the observation filter, $\mathbf{O}_{\text{opt}}$ was also investigated, when the disturbance signals at the error microphones from the 6 primary sources in the rear are estimated using the monitoring microphones #13, #22, #23, #16, as used in Fig. C.7. Under this condition, the frequency responses of $\mathbf{O}_{\text{opt}}$ used to estimate the signals at the left error microphone, are calculated and shown in Fig. C.10 and Fig. C.11, which should be compared with Fig. 5.23 for the anechoic case. The frequency responses of $\mathbf{O}_{\text{opt}}$ for the right error microphone are shown in Fig. C.12 and Fig. C.13, which can be compared with Fig. 5.24.

It is found that the frequency responses of $\mathbf{O}_{\text{opt}}$ in the more reverberant enclosure are more complicated than the responses in the anechoic chamber, due to the complex acoustic transfer response. Each disturbance signal at the monitoring microphones are differently weighted by the observation filter to estimate signals at the error microphones and the magnitude of weighting is decided by the distance of the monitoring microphones to the virtual error microphones. Because the monitoring microphones #22, #23 are closer to the error microphones than the monitoring microphones #13, #16, the magnitude of $\mathbf{O}_{\text{opt}}$ for the monitoring microphones #22, #23 is larger.

If the causality constraint is relaxed, the time domain response of the observation filter can be obtained from the inverse Fourier transform of the frequency responses in $\mathbf{O}_{\text{opt}}$. The impulse responses of the observation filter for the left-hand ear from the monitoring microphones #13, #22, #23 and #16 are shown in Fig. C.14 which can be compared with Fig. 5.25 for the anechoic case. Fig. C.14 shows that the monitoring microphones #22 and #23 are again more weighted than the other monitoring microphones. In addition, by comparing the results in Fig. 5.25 for the anechoic chamber with the results in Fig. C.14 for the demo room, it is found that the observation filters for the more reverberant chamber have similar non-causal components.

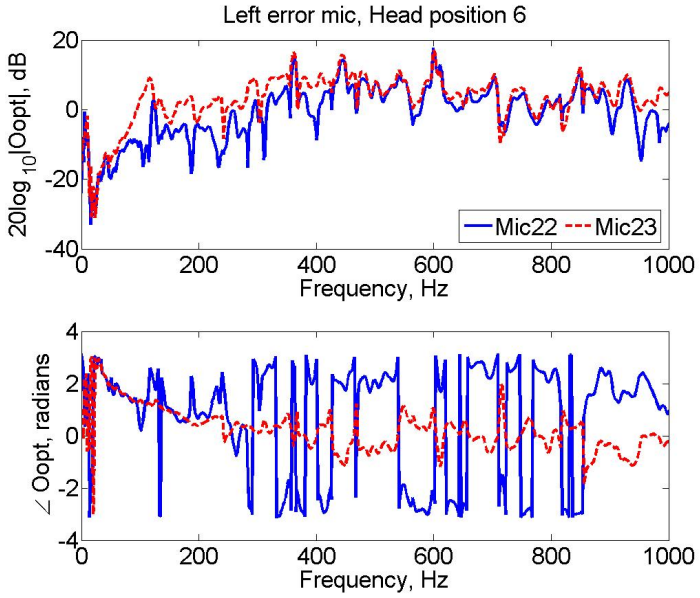

Figure C.10: The frequency response of $\mathbf{O}_{\text{opt}}$ for the monitoring microphones #22, #23 to estimate the signals of the ***left*** error microphone at the head position #6 by the monitoring microphones #13, #22, #23, #16 when 6 uncorrelated primary sources are driven in rear in a more reverberant enclosure.

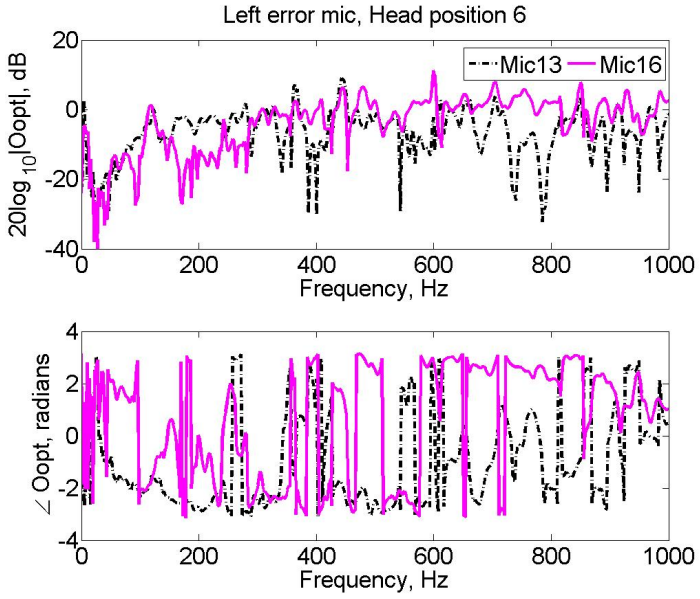

Figure C.11: The frequency response of $\mathbf{O}_{\text{opt}}$ for the monitoring microphones #13, #16 to estimate the signals of the ***left*** error microphone at the head position #6 by the monitoring microphones #13, #22, #23, #16 when 6 uncorrelated primary sources are driven in rear in a more reverberant enclosure.

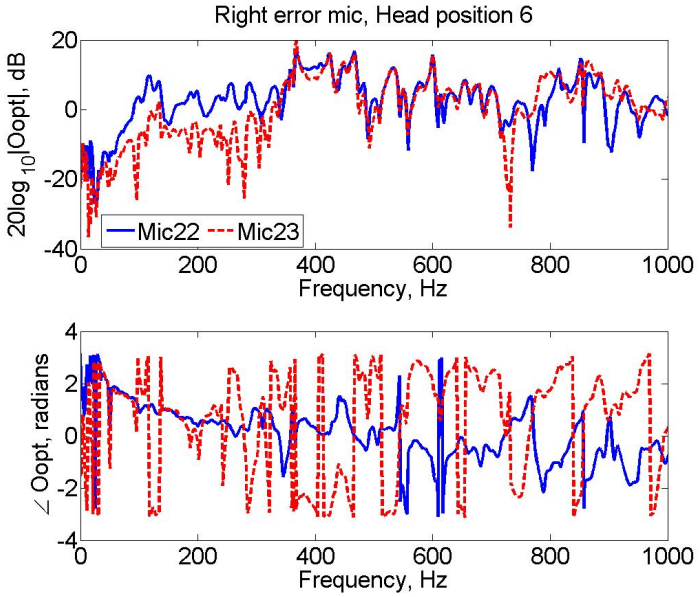

Figure C.12: The frequency response of $\mathbf{O}_{\text{opt}}$ for the monitoring microphones #22, #23 to estimate the signals of the ***right*** error microphone at the head position #6 by the monitoring microphones #13, #22, #23, #16 when 6 uncorrelated primary sources are driven in rear in rear in a more reverberant enclosure.

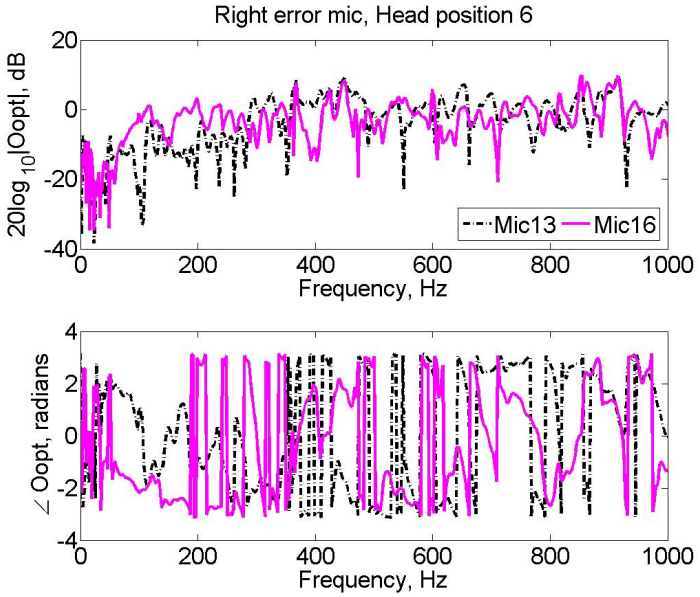

Figure C.13: The frequency response of $\mathbf{O}_{\text{opt}}$ for the monitoring microphones #13, #16 to estimate the signals of the ***right*** error microphone at the head position #6 by the monitoring microphones #13, #22, #23, #16 when 6 uncorrelated primary sources are driven in rear in rear in a more reverberant enclosure..

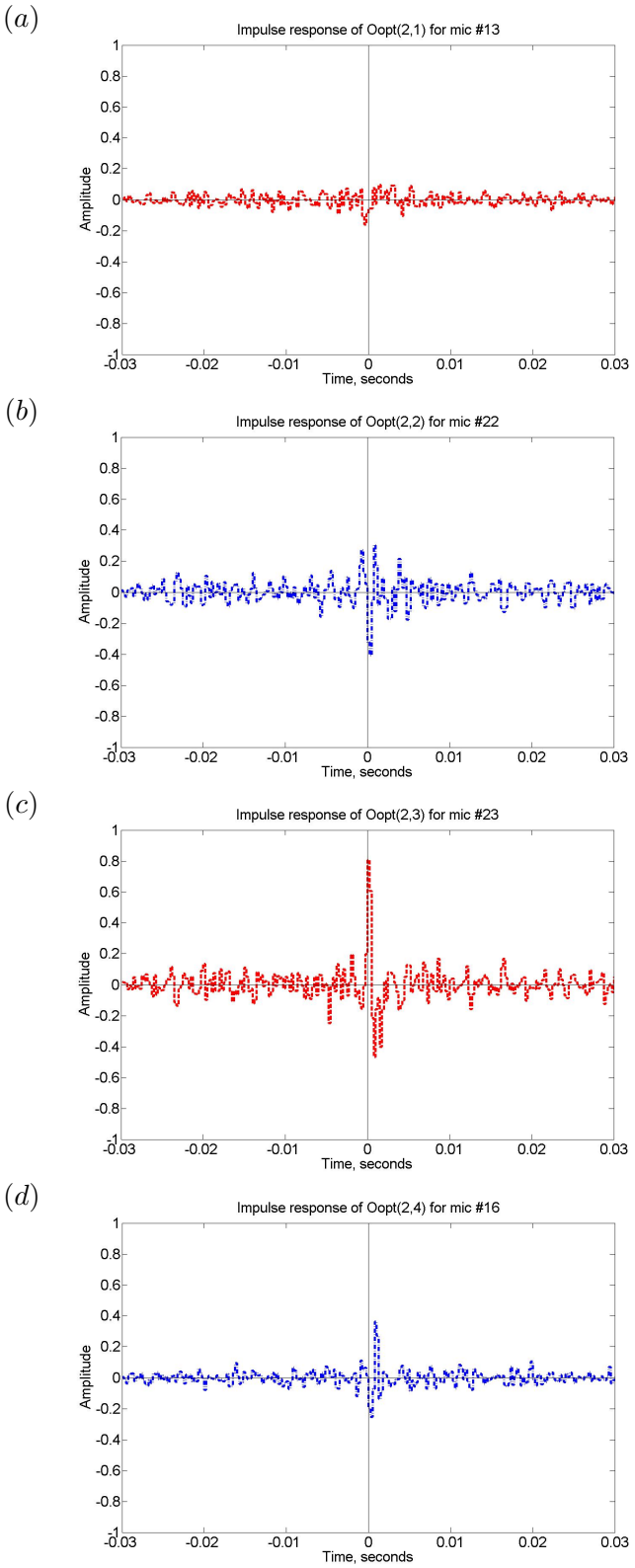

Figure C.14: The impulse response of the observation filter to estimate the signals of the left error microphone at the head position #6 by the monitoring microphones #13, #22, #23 and #16, when six uncorrelated primary sources are driven behind the active headrest system: (a) the observation filter, $\mathbf{O}_{\text{opt}}(2,1)$ for the monitoring microphone #13, (b) the observation filter, $\mathbf{O}_{\text{opt}}(2,2)$ for the monitoring microphone #22, (c) the observation filter, $\mathbf{O}_{\text{opt}}(2,3)$ for the monitoring microphone #23, (d) the observation filter, $\mathbf{O}_{\text{opt}}(2,4)$ for the monitoring microphone #16.

C.2 Off-line investigation of the stability and performance of the integrated system in a more reverberant room

The effects of the integrated active headrest system is also investigated off-line using the acoustic transfer responses measured from the installation in the demo room, as shown in Fig. C.1. The theory in Chapter 6 is again used.

The plant response matrix between the virtual error microphones at the dummy head and the right secondary source, $\mathbf{G}_e$ was obtained at head position #6, as shown in Fig. C.15. The comparison between Fig. 6.3(a) and Fig. C.15 shows that two plant responses have similar responses but the plant responses in the more reverberant enclosure has more variation due to the effect of the acoustic modes. The plant response between the monitoring microphones #13, #22, #23, #16 and the right secondary source, $\mathbf{G}_m$ is also shown in Fig. C.16. The responses of Fig. C.16 also seem to be similar with the results of Fig. 6.3(b), although the plant responses at the more reverberant room have more fluctuating structure. The coherence is almost unity except the low frequency range.

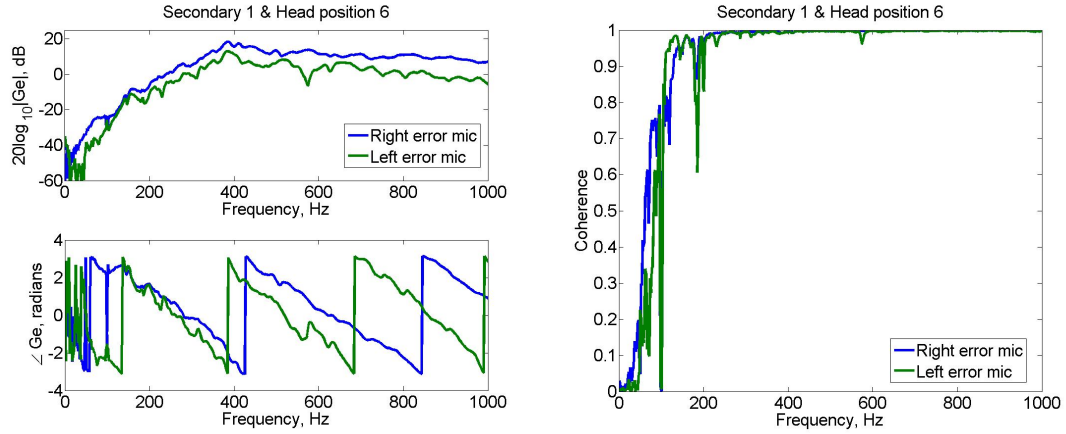

Figure C.15: The plant response, $\mathbf{G}_e$ (left) and coherence (right) between the secondary source 1(the right secondary loudspeaker) and the physical error microphones in the dummy head at head position #6.

The attenuation performance and stability were investigated when the active headrest system is combined with the monitoring microphones, #13, #22, #23 and #16. It was assumed that the six primary sources are driven by uncorrelated white noise sources. To show the effect of the head-tracking, it was assumed that the dummy head is moved from position 'A' to position 'B' in Fig. 6.2 with and without the head-tracking device. The head-tracking device was simulated by updating the filters, $\hat{\mathbf{G}}_m$, $\hat{\mathbf{G}}_e$ and $\hat{\mathbf{O}}_{\text{opt}}$ for position 'B'. From Eq. (6.5) and Eq. (6.6), the optimal attenuation performance of the active headrest system with and without the headtracker is calculated and shown in Fig. C.17. It is found that the application of the headtracker can improve the performance of the

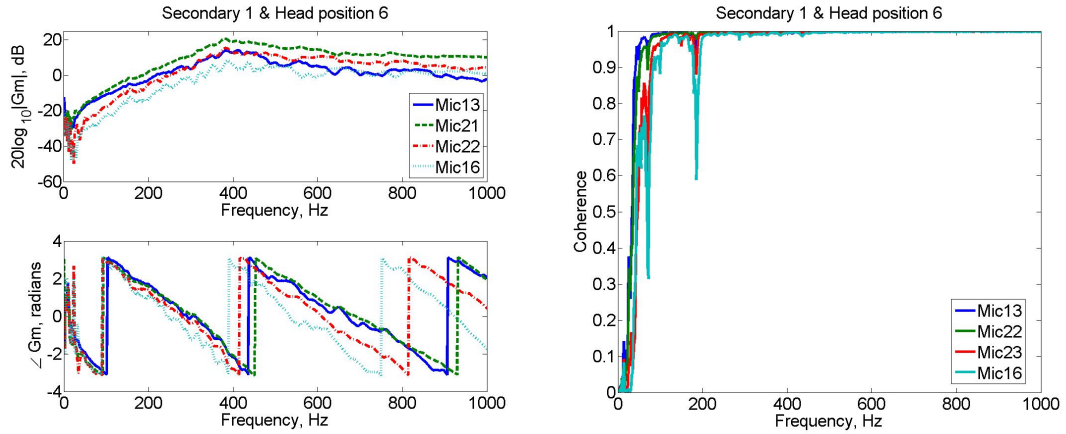

Figure C.16: The plant response, $\mathbf{G}_m$ (left) and coherence (right) between the secondary source 1(the right secondary loudspeaker) and the monitoring microphones #13, #22, #23 and #16 at head position #6.

active headrest system in the more reverberant room. Compared with the results of Fig. 6.4 the attenuation performance is decreased, particularly at higher frequencies, and thus the effect of the head-tracker seems to be smaller in the more reverberant room. Although the extent of the improvement in the more reverberant room is less than the result of the anechoic chamber, the head tracker can still significantly improve the attenuation performance and prevent drastic noise enhancement.

To investigate the stability of the adaptive active headrest system at the more reverberant room, changes in the eigenvalues due to head movements both with and without the headtracker are compared using Eq. (6.13), as shown in Fig. C.18. In Fig. C.18(a), when the headtracker is not applied, although most eigenvalues are positive, several eigenvalues at around 900 Hz have small negative values. This suggests that the active control system will be unstable when the disturbance signals are driven at these frequencies. However, with the headtracker, the stability can be improved, as the eigenvalues are always positive, .

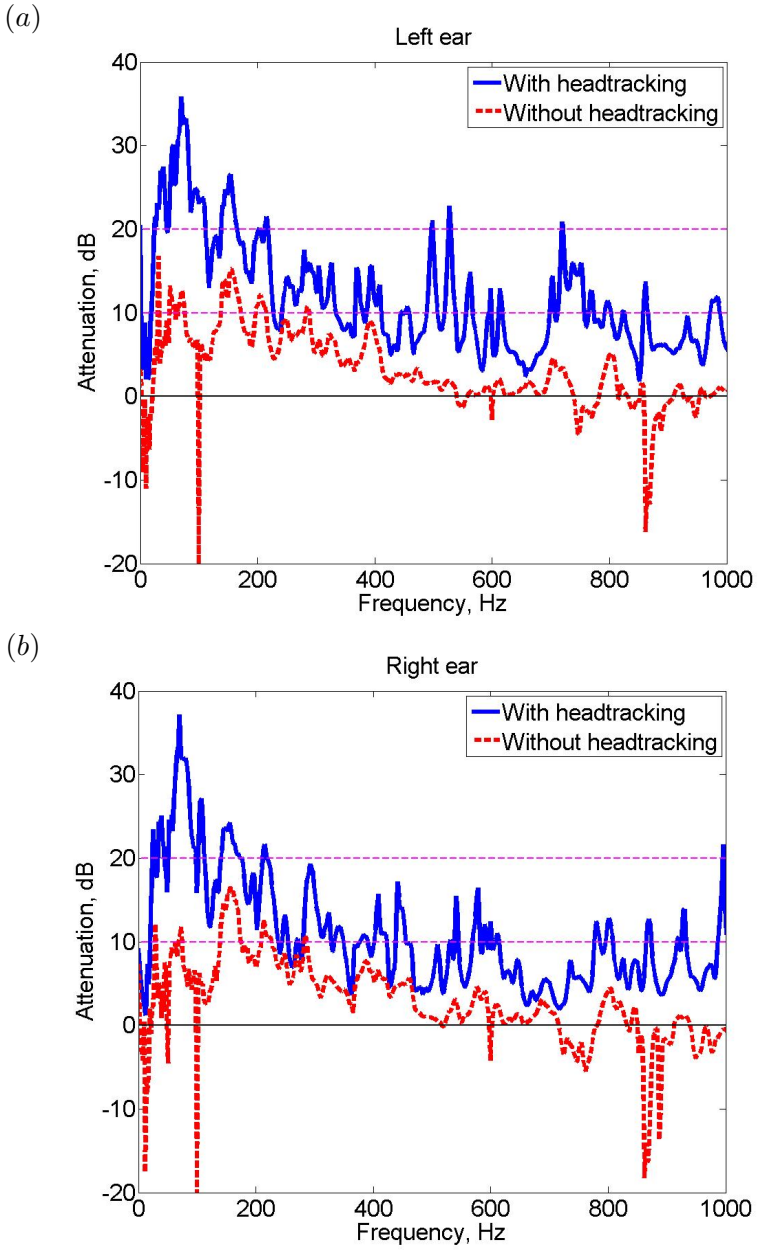

Figure C.17: The optimal attenuation performance of the integrated active headrest system simulated with and without the headtracker when the head is moved from position 'A' to position 'B' in the anechoic chamber: at the left ear(a) and at the right ear(b).

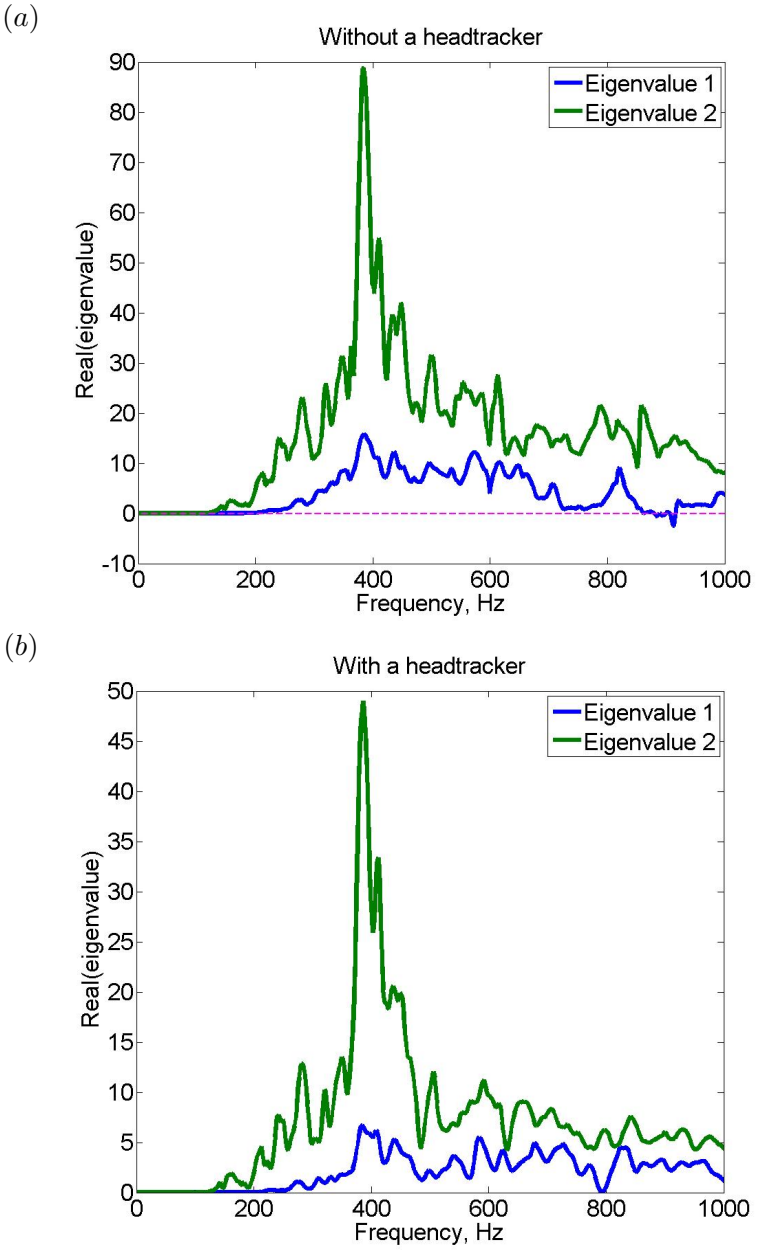

Figure C.18: The real parts of the eigenvalues of $\hat{\mathbf{G}}^{\mathrm{H}}\mathbf{G}$ in Eq. (6.13) when the head is moved from position A' to position B': (a) without the headtracker and (b) with the headtracker.

C.3 Real-time implementation for active control of tonal disturbances in a more reverberant room

Fig. C.19 shows the experimental installation used for the real-time implementation and testing in a demo room at ISVR as a more reverberant field. Four monitoring microphones were located at the same positions of monitoring microphones, #13, #22, #23 and #16 in Fig. 5.13 and the active headrest using the two loudspekers on the headrest was also installed. A single loudspeaker was installed behind the active headrest system to act as the primary source, driven by a single frequency signal. The Microsoft Kinect was installed in front of the dummy head and used to track the head position. The overall installation is almost similar to that in Fig. 6.6 in Chapter 6 and details about the experiment arrangement presented in Section 6.3.1 are also applied to the experiment in this chapter.

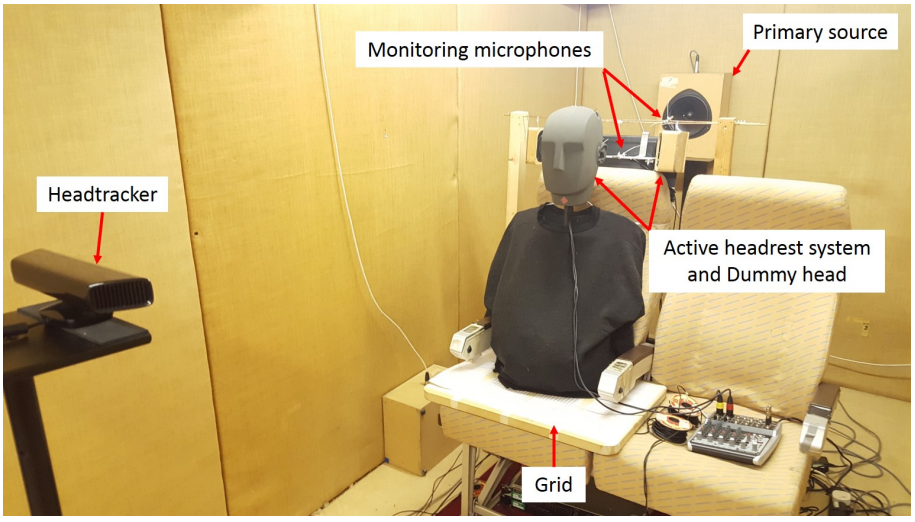

Figure C.19: The overall installation for the real-time operation of both the nearfield estimation and the integrated active headrest system for controlling tonal disturbance signals in a demo room.

An appropriate regularization factor for the real-time nearfield estimation is determine as $\beta = 10^{-2}$ through the trade-off between the robustness to uncertainties and the estimation accuracy, and the estimation accuracy is calculated off-line with different acoustical uncertainties, Δ_{d_m} defined as in Eq. (6.15), and results are shown in Fig. C.20 which can be compared with Fig. 6.8 for the anechoic case. From the results in Fig. C.20, it can be seen that with $\beta = 10^{-2}$ the variation in the estimation error for different levels of uncertainty is less than 1 dB and the estimation error of less than -10 dB is generally achieved apart from narrow bands at specific frequency ranges.

When tonal disturbance signals at the dummy head error microphones at different frequencies are measured and compared with those estimated from the monitoring microphones in real-time, with the pre-calculated observation filter using a regularisation

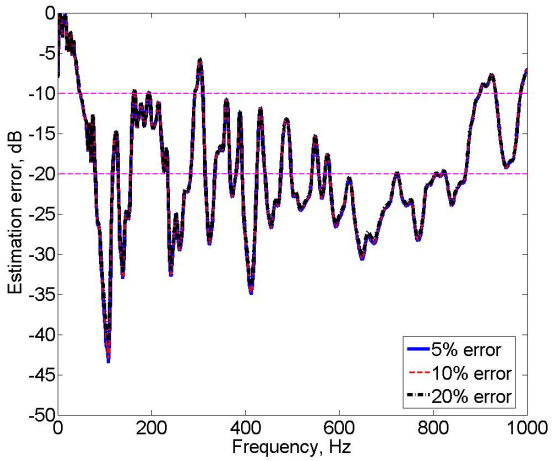

Figure C.20: Changes in the nearfield estimation error for different acoustic uncertainties in the analysis of the monitoring microphones when the observation filter with $\beta = 10^{-2}$ is applied.

Table C.1: Comparisons of the nearfield estimation error between the off-line and real-time test when tonal disturbance signals at the right error microphone of the dummy head are estimated by the 4 monitoring microphones around the headrest with the pre-calculated observation filter in the more reverberant room.

Frequencies	Off-line estimation error (dB)	Real-time estimation error Magnitude (dB), Phase (radians)
300 Hz	-7.3	-6.9, 0.02π
400 Hz	-28.5	-20.7, -0.02π
500 Hz	-22.3	-17.3, 0.04π
600 Hz	-25.6	-17.8, 0.01π
700 Hz	-24.3	-17.0, -0.01π

of $\beta = 10^{-2}$, the results, in Table C.1, show that less than -15 dB estimation error is achieved at frequencies between 400 and 700 Hz. Table 6.1 also shows that the off-line results, which are predicted from the measured acoustic responses, give a reasonable indication of the real-time performance. At 300 Hz, however, an estimation error of more than -10 dB is produced due to limited linear association between the monitoring and virtual error microphones.

With this nearfield estimation, when the dummy head was located in the nominal position 'A' in Fig. 6.9, the attenuation performance was measured, as summarised in Table C.2. The "predicted" attenuation, which is defined as the attenuation of the estimated error signals inside the control system, i.e. $\hat{\mathbf{e}}(n)$ in Eq. (6.8), is almost perfect for the adaptive controller. The attenuation actually achieved at the microphones in the dummy head is more than 10 dB attenuation at the frequencies between 400 and 700 Hz. At 300 Hz, the attenuation performance is limited by the nearfield estimation error.

Table C.2: Predicted and achieved attenuation performance of the integrated active headrest system for tonal disturbances at different frequencies in the ANC demo room when the dummy head is located in position 'A'.

Frequencies	Predicted attenuation right / left ear, (dB)	Achieved attenuation right / left ear, (dB)
300 Hz	57.3 / 59.1	7.1 / 6.8
400 Hz	77.4 / 77.8	16.7 / 19.3
500 Hz	94.6 / 88.5	12.8 / 16.2
600 Hz	72.1 / 70.2	17.2 / 14.3
700 Hz	73.8 / 68.2	11.0 / 20.9

The effect of the head-tracking device on the integrated active control system was then investigated by moving the dummy head from position 'A' to position 'B' indicated in Fig. 6.9. In Table C.3, attenuation results for the active headrest system with and without the headtracker in operation are compared for position 'B' and it is verified that the improvement of the attenuation performance in the more reverberant room is achieved by the head-tracking.

Table C.3: Comparison between the actual attenuation performance of the integrated active headrest system with and without the head-tracking system when the dummy head is moved to position 'B' and a single loudspeaker produces a tonal disturbance at different frequencies in the ANC demo room.

Frequencies	Position 'B', Actual attenuation, right/left ear (dB)	
	without head-tracking	with head-tracking
300 Hz	3.3 / 5.1	8.0 / 7.0
400 Hz	2.8 / 1.6	13.1 / 19.2
500 Hz	1.3 / 2.7	10.5 / 20.5
600 Hz	9.6 / 5.8	17.6 / 13.8
700 Hz	4.9 / 15.0	19.4 / 10.9

Fig. C.21 shows the time history of the signal measured by the microphone in the dummy head as it is moved from position 'A' to 'B' for a disturbance frequency of either 600 Hz or 700 Hz and can be compared with Fig. 6.12 for the anechoic case. It is found that when the head tracker is in operation, during the third time interval, the attenuation performance is significantly improved at both frequencies.

In this chapter, the feasibility of the integrated active headrest system was tested in the more reverberant room and it is verified that a general trend of the results is similar with the results of the anechoic chamber in Chapter 6.

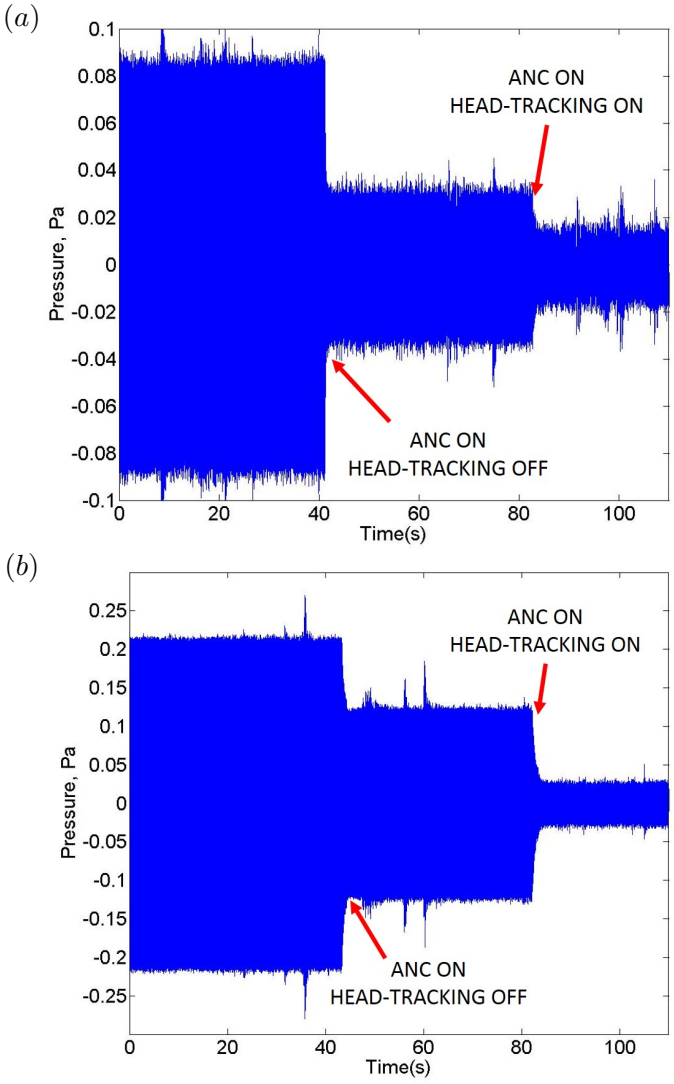

Figure C.21: Measured signals at the right error microphone of the dummy head at position 'B' when the integrated active headrest system with the remote microphone technique and the head tracker reduces the tonal disturbance signals from a single primary source in the ANC demo room: (a) 600 Hz, (b) 700 Hz

C.4 Real-time implementation for active control of broadband random disturbances in a more reverberant room

A similar experimental arrangement to that for the active control of tonal noise in Fig. C.19 has been used to reduce broadband random disturbances in the demo room. In addition, details about the experiment arrangement presented in Section 7.2.1 are used to the following demonstration.

C.4.1 Real-time adaptive control with the standard remote microphone technique and head-tracking

The loudspeaker acting as the primary source was initially located behind the headrest, as in Fig. C.19, and driven by band-limited Gaussian white noise between 200 and 1,000 Hz. The dummy head was in the nominal position, 'A' in Fig. 6.9. The optimal observation filter with the causality constraint was obtained from Eq. (7.14) with $\beta = 10^{-3}$, which was chosen based on the trade-off between the accuracy of the nearfield estimation and the robustness to any uncertainties, as studied in Chapter 5. The impulse responses of $\hat{\boldsymbol{O}}_{11}$ and $\hat{\boldsymbol{O}}_{12}$ chosen from the 8 FIR filters in the matrix of $\hat{\boldsymbol{O}}_{opt}$ are shown in Fig. C.22, which can be compared with Fig. 7.3 for the anechoic case. The optimised observation filters in the frequency domain without the causality constraint are also transformed by inverse Fourier transform and compared with the impulse responses of $\hat{\boldsymbol{O}}_{11}$ and $\hat{\boldsymbol{O}}_{12}$ in Fig. C.22. The causally constrained observation filters in the more reverberant room in Fig. C.22 is less similar to the non-causal filters, compared to those of Fig. 7.3. This is because in the more reverberant room, larger noncausal components of $\hat{\mathbf{O}}_{11}$ and $\hat{\mathbf{O}}_{12}$ are generated and these are excluded from the the impulse response of $\hat{\boldsymbol{O}}_{11}$ and $\hat{\boldsymbol{O}}_{12}$. Therefore, Fig. C.23 shows that when the accuracy of the nearfield estimation of the causally constrained observation filter is compared with that of the non-causal filter, the nearfield estimation error is increased compared to that of the non-causal filter. The extent of increase in the nearfield estimation error in Fig. C.23 is significantly greater than Fig. 7.4.

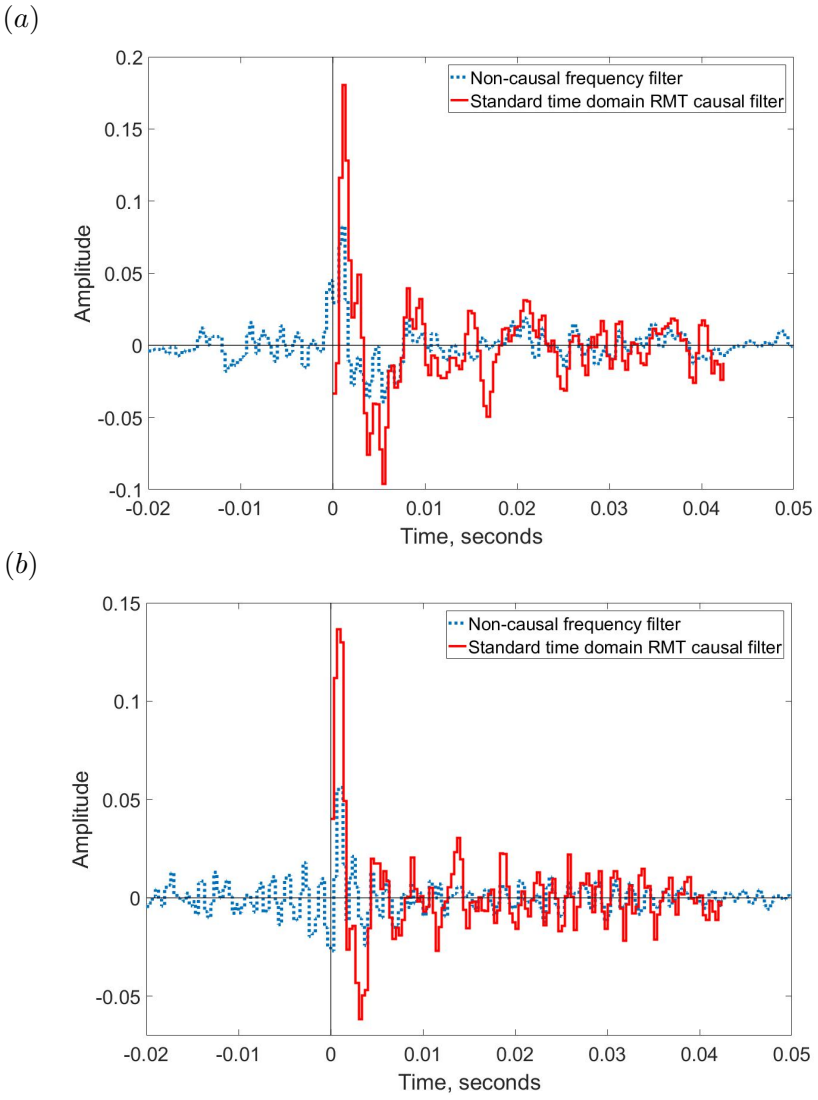

Figure C.22: The impulse responses (solid line) of $\hat{\boldsymbol{O}}_{11}$ (a) and $\hat{\boldsymbol{O}}_{12}$ (b) chosen from the 8 FIR filters of the causal constrained $\hat{\boldsymbol{O}}_{opt}$. Also shown are the inverse Fourier transformed $\hat{\mathbf{O}}_{11}$ and $\hat{\mathbf{O}}_{12}$ (dashed line) for $\hat{\mathbf{O}}_{opt}$ calculated in the frequency domain, without the causal constraint.

(a)

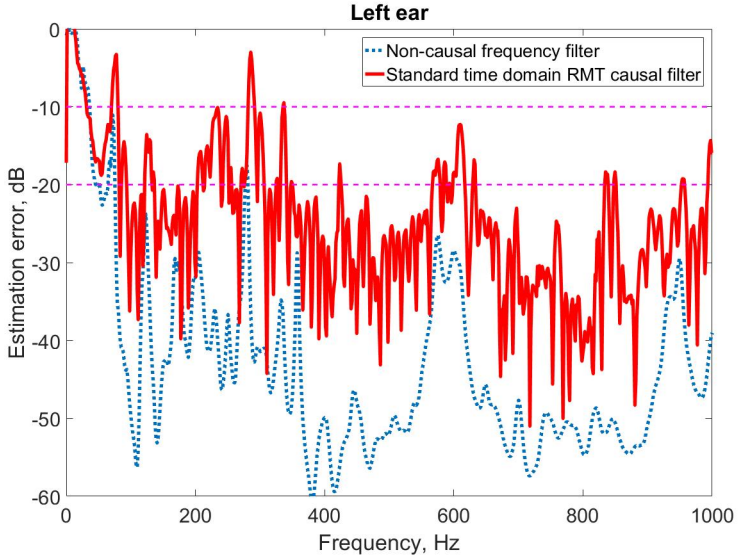

(b)

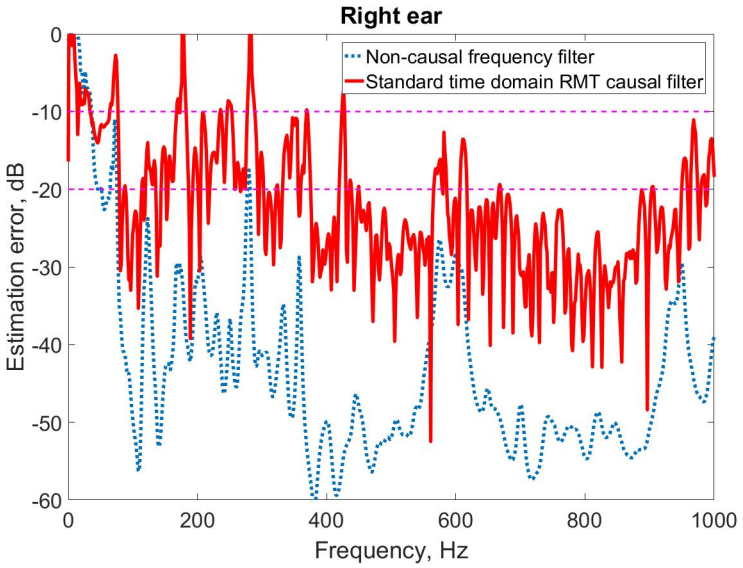

Figure C.23: Comparison of the nearfield estimation of the standard remote microphone technique, RMT with the causality constraint (solid line) to that with the non-causal frequency filter (dashed line).

The attenuation performance of the causally constrained controller is also investigated. The power spectral density of the pressure signals from the microphones in the left and right-hand ear positions of the dummy head was measured, as shown by the solid lines in Fig. C.24. The dummy head was located at the nominal position, 'A' in Fig. 6.9. As a benchmark for the best possible performance with this arrangement, control was also implemented using the signals from the microphones mounted in the dummy head directly as error signals, with the results also shown by the dot-dashed lines in Fig. C.24. Reductions in pressure of about 20 dB are observed at the error microphones on both sides of the dummy head after active control, from about 300 Hz to about 1 kHz. The results obtained using the monitoring microphones and remote microphone technique, as shown by the dashed lines in Fig. C.24, are degraded in the frequency range above 600 Hz because the nearfield estimation error is increased. However, more than 10 dB attenuation is still achieved between 300 Hz and 1000 Hz except specific frequency ranges. Although the results with the dummy head microphones are similar to those obtained for the anechoic case, as shown in Fig. 7.5, the results with the remote microphone technique are not quite as good in the demo room as in the anechoic chamber, probably because of the poorer performance of the observation filter here.

The head tracking performance was then tested by moving the dummy head from the nominal position to other head positions. Figure C.25 shows the time history of the signal from the right-hand ear of the dummy head after it had been moved to position 'E' on the grid shown in Fig. 6.9, which is about 14 cm from the nominal head position, 'A'. During the second interval shown in Fig. C.25(a), from 30 to 60 seconds, the control system is switched on but with the observation filter and plant responses appropriate to the head position still being in the nominal head position, 'A'. The results shows that the control system rarely reduces broadband random disturbances without the head-tracking. When the head tracker was switched on, after 60 seconds and the correct head position is acquired, the attenuation performance of more than 10 dB is achieved. The spectrum of the pressure at the right-hand ear of the dummy head in Fig. C.25(b) confirms these results, although are not clearly as for the anechoic case in Fig. 7.6.

Experiments have also been performed moving the dummy head to other locations. For instance, when the dummy is in position 'G' , the results in Fig. C.26 show the effect of the head-tracking more dramatically. That is, the active control became unstable without the headtracking but by applying the head-tracking, the active control remains stable and has better attenuation performance.

(a)

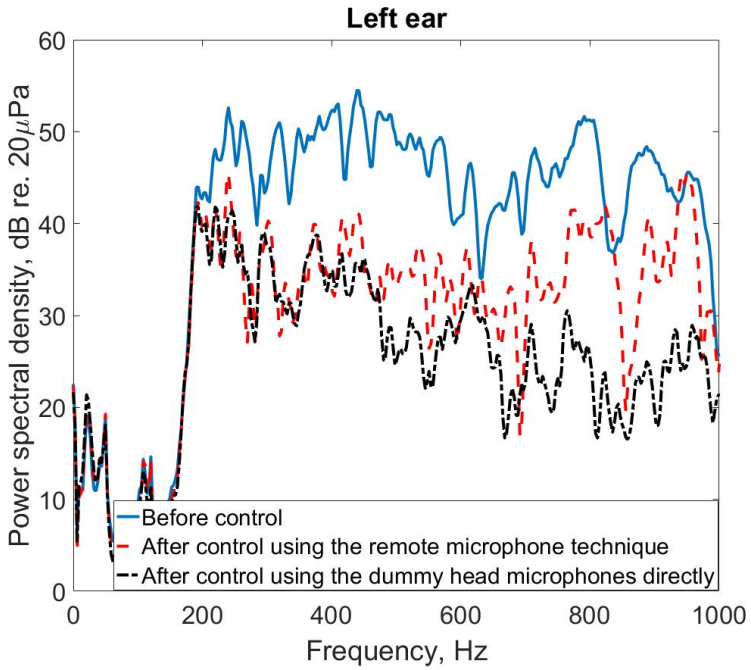

(b)

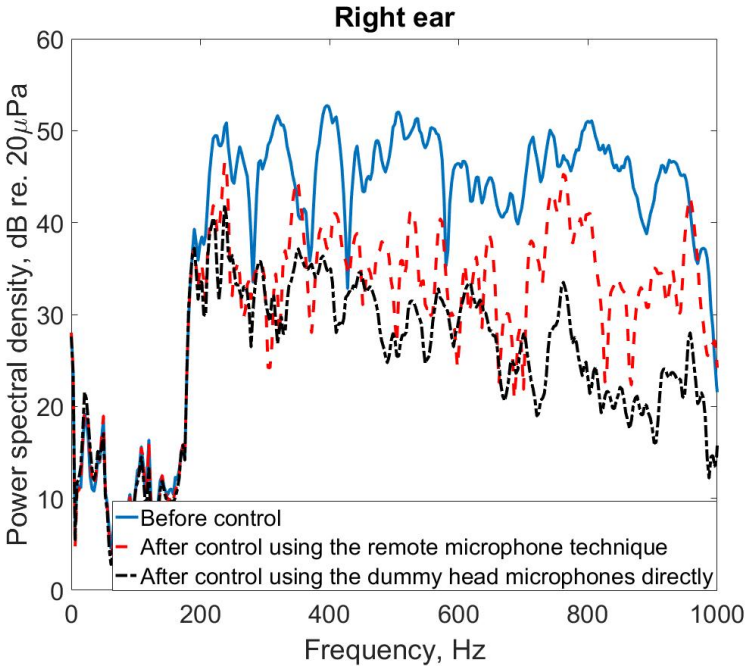

Figure C.24: Power spectral density of the signal measured at the microphones in the left and right hand side of the dummy head when it was in the nominal position and the primary source was behind the headrest before control, solid line, after control using the monitoring microphones and observation filter to estimate the signal at the ear position using the remote microphone technique, dashed line, and, for reference, when the microphones in the dummy head themselves were used as the error signals in the control algorithm, dot-dashed line.

(*a*)

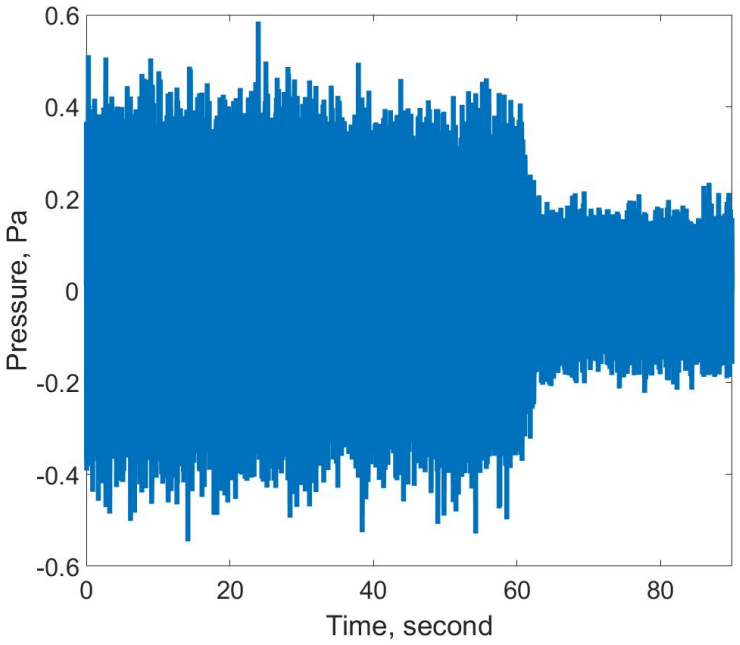

(*b*)

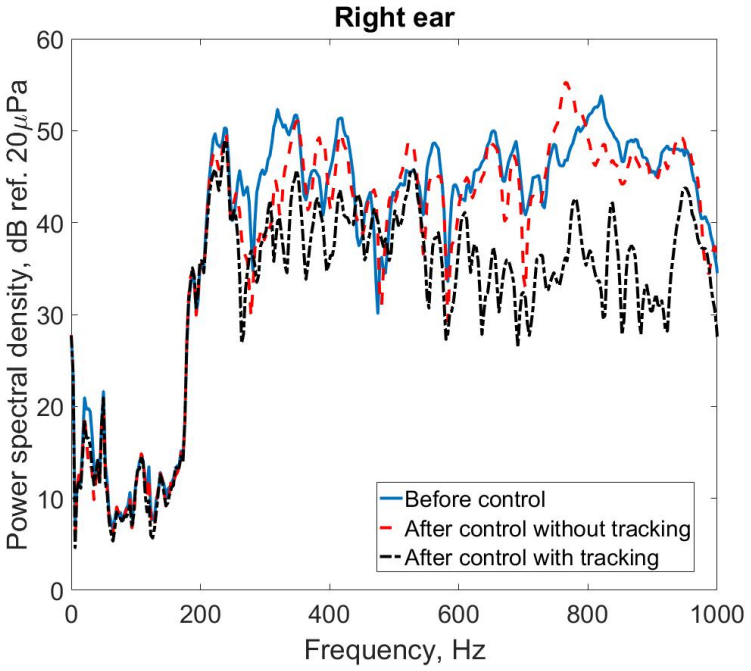

Figure C.25: Time history of the pressure signal measured in the right-hand ear of the dummy head, (a), when in position 'E' before control, up to 30 seconds, when control is implemented with the observation filter and plant responses appropriate for the nominal head position, from 30 to 60 seconds, and when the head tracker is enabled so that the correct head position is identified, after 60 seconds. The power spectral density of the signal at this microphone is also shown, (b), before control, after control but without head tracking and after control with the head tracker enabled.

(*a*)

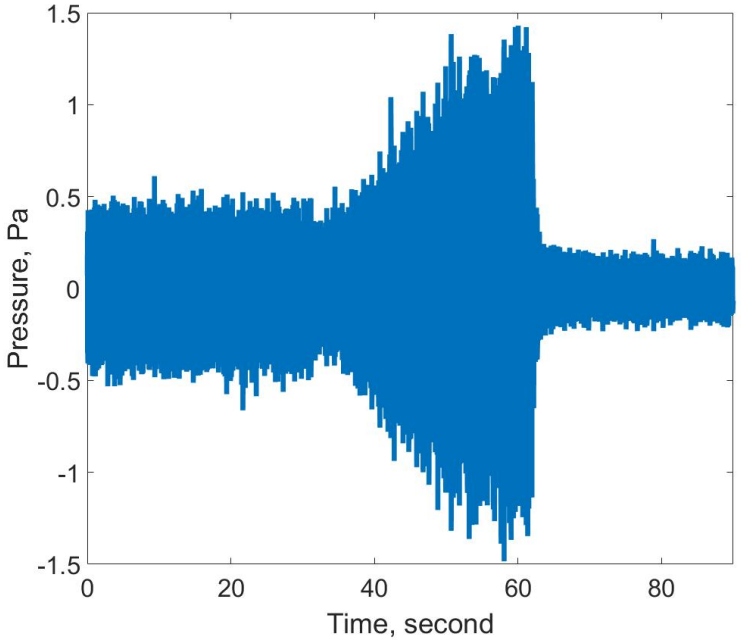

(*b*)

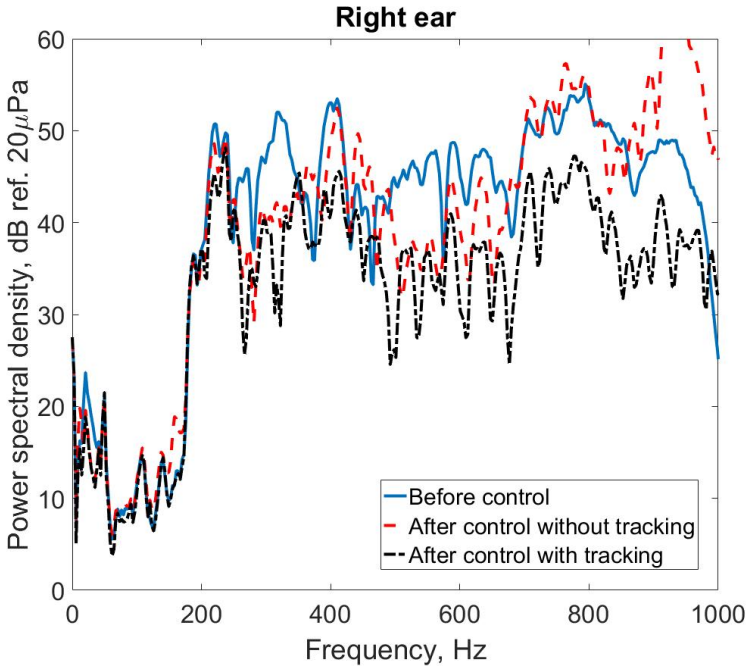

Figure C.26: Time history of the pressure signal measured in the right-hand ear of the dummy head, (a), when in position 'G' before control, up to 30 seconds, when control is implemented with the observation filter and plant responses appropriate for the nominal head position, from 30 to 60 seconds, and when the head tracker is enabled so that the correct head position is identified, after 60 seconds. The power spectral density of the signal at this microphone is also shown, (b), before control, after control but without head tracking and after control with the head tracker enabled.

C.4.2 Real-time adaptive control with the delayed remote microphone technique for the front primary source

When the primary source is in front of the active headrest system, as shown in Fig. C.27, the causality between the error and monitoring microphones can be degraded and therefore the 'delayed' remote microphone technique was used for active control of broadband random noise.

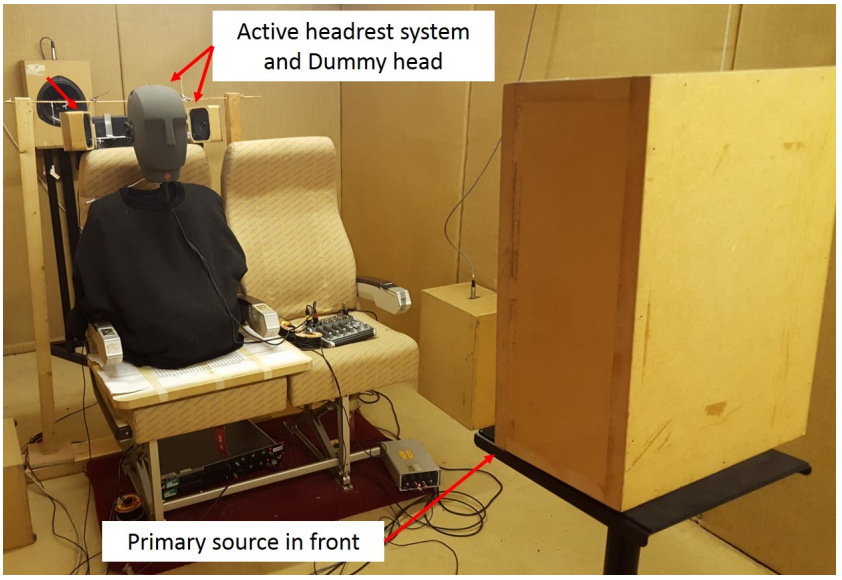

Figure C.27: Experimental arrangement for local active control of broadband random noise driven from a single primary source in front.

To investigate the effect of the delayed remote microphone technique, the impulse responses of the causally constrained observation filters are compared with those of the non-causal observation filters calculated using the standard method in the frequency domain. The dummy head was located at the nominal position 'A' and a modelling delay of about 0.7 ms corresponding to 2 samples, is applied since the average distance from the dummy head to the monitoring microphones is around 225 mm. Fig. C.28 shows the responses of $\hat{\boldsymbol{O}}_{12}$ in this case. It can be seen that the impulse response corresponding to the causally constrained time domain filter calculated using the standard remote microphone technique is now significantly different from the causal part of the inverse Fourier transformed optimal observation filter calculated in the frequency domain since important non-causal components of this response are not present in the causally constrained filter. In Fig. C.28(b), however, it can be seen that by using the delayed remote microphone technique, the important non-causal components of the response are included in the impulse response, which results in the improved nearfield estimation. By comparing the results of Fig. C.28 to those in Fig. 7.10, it can be seen that the effect of the delayed remote microphone technique in the more reverberant room is degraded in

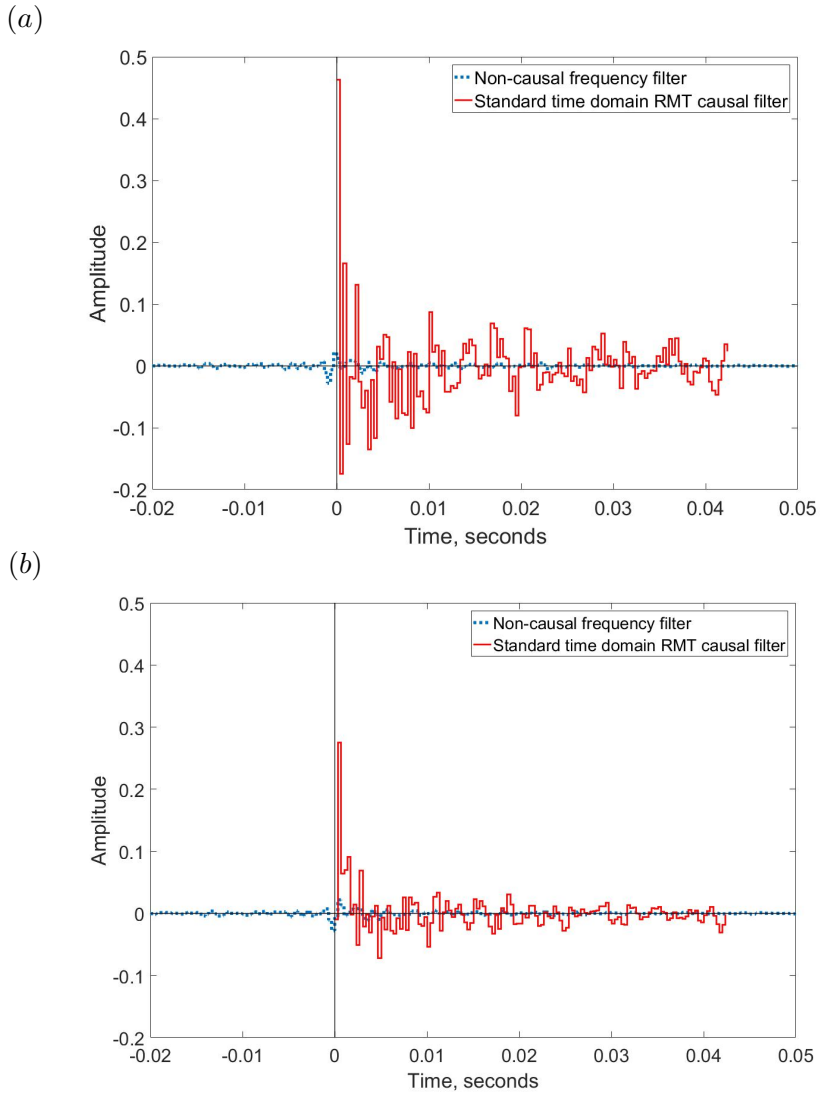

Figure C.28: Comparison of the impulse response of $\hat{\boldsymbol{O}}_{12}$ among the FIR filters of the causal constrained time filter with the inverse Fourier transformed $\hat{\mathbf{O}}_{12}$, which is among responses of the non-causal optimal observation filter in the frequency domain when broadband random disturbances are driven from a single primary source in front: (a) the standard remote microphone technique, (b) the delayed remote microphone technique.

terms of the modelling accuracy. This might be important by increasing the modelling delay on using a longer observation filter, although this was not investigated here.

The results of real-time active control are shown in Fig. C.29 when the standard and the delayed remote microphone technique are used. When the standard remote microphone technique, with no modelling delays, is used, as can be seen from the dashed lines in Fig. C.29, then the attenuation is limited and noise enhancement is induced at frequencies above about 900 Hz. However, with the delayed remote microphone technique as shown by the dot-dashed lines in Fig. C.29, reductions in pressure of about 10 dB are

observed at the error microphones on both sides of the dummy head after active control, from about 300 Hz up to about 1 kHz.

(a)

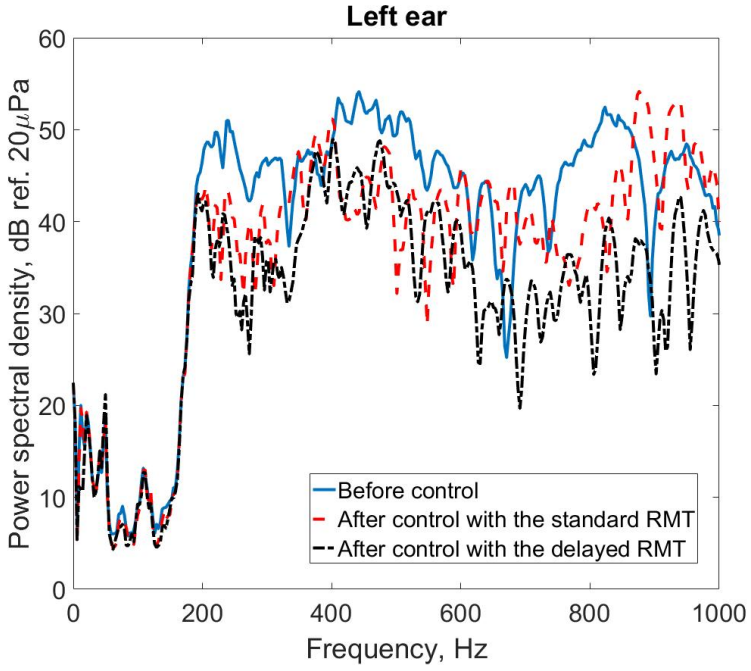

(b)

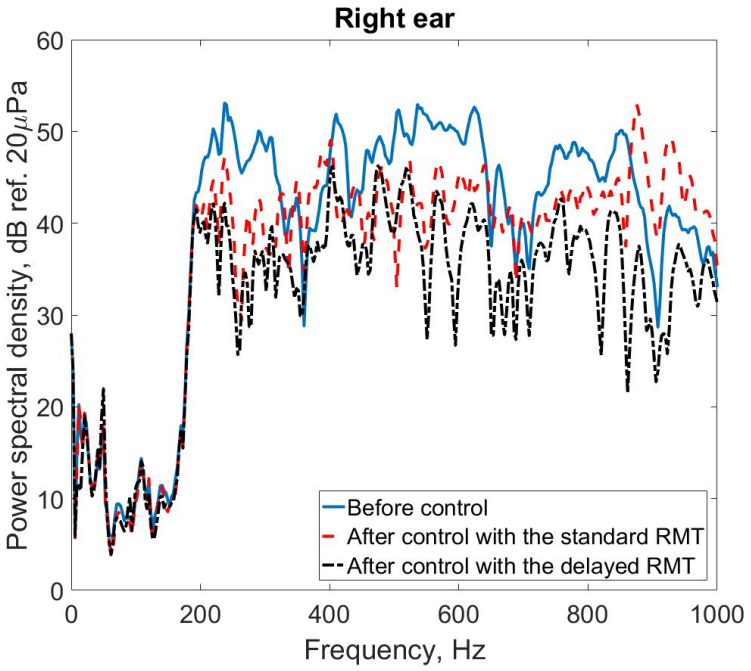

Figure C.29: Power spectral density of the signal measured at the microphones in the left and right hand side of the dummy head when it was in the nominal position and the primary source was positioned in front of the headrest before control, solid line, after control using the standard remote microphone technique, RMT, dashed line, and after control using the delayed RMT, when it includes a modelling delay of 0.7 ms, dot-dashed line.

C.5 Summary

In this chapter, the nearfield estimation of the remote microphone technique and the performance of the integrated active headrest system have been investigated in the ANC demo room at the ISVR, as an example of a more reverberant acoustic field.

When six primary sources in rear produced uncorrelated random noise, four monitoring microphones among 24 monitoring microphones were selected to estimate disturbance signals at virtual error microphones in each ear of a dummy head in the demo room. It has been found that the acoustical responses have more variation than those of the anechoic chamber due to resonances and reflections. The nearfield estimation at the more reverberant chamber has been degraded from the results of the anechoic chamber, which indicates that the relation between the monitoring and error microphones in the more reverberant room is more complicated. Results of the three different monitoring microphone arrays have shown a similar tendency with those of the anechoic chamber. Therefore, the formation of the monitoring microphones have also considered the trade-off between the spatial distribution of the acoustic field and the conditioning number for the inversion. Responses in the time domain have also shown that non-causal components were generated in the more reverberant room due to the sound reflection.

Effects of the integrated active headrest system with the remote microphone technique and the head-tracking have been verified off-line by measured acoustic responses in the demo room. Results in the demo room are comparable with those in the anechoic chamber in Chapter 6. That is, with the head-tracking, the optimal attenuation performance has been significantly improved at the more reverberant room but without the head-tracking, noise enhancements have been generated at several frequencies. In addition, negative eigenvalues were found at around 900 Hz without the head-tracking, whereas with the head-tracking, the real parts of the eigenvalues always remained positive, which indicated an improvement in the stability

The real-time performance of the combined adaptive active control system has also been tested in the demo room when a tonal primary source was applied. It has been found that nearfield estimation errors in the demo room were larger than those in the anechoic chamber in Chapter 6. However, more than 10 dB attenuation at targeted frequencies except 300 Hz has still been achieved in the more reverberant room. When the dummy head was moved 10cm forward, the attenuation performance has again been significantly improved by the head-tracking.

The attenuation performance of an active headrest system integrated with the remote microphone technique and head-tracking has been investigated to reduce broadband random disturbances in the more reverberant room. When the primary sources in rear of the active headrest system produced broadband random noise, the causally constrained observation filter has achieved less than -10 dB estimation error and real-time control

has reduced disturbances by up to 20 dB attenuation between 300 Hz and 1 kHz, even though the estimation error and the attenuation performance in the demo room were degraded from those in the anechoic chamber. The application of the head-tracking has improved the attenuation performance and convergence stability when the dummy head was moved to different positions from the nominal position. When the primary source was in front of the active headrest system at the demo room, the delayed remote microphone technique was also applied. In this case, active control with the delayed remote microphone still achieved more than 10 dB attenuation, while active control with the standard remote microphone was significantly degraded and noise enhancement was observed above 900 Hz.

The results in this chapter can be compared with those in the anechoic chamber in the previous chapters. Although the nearfield estimation error and the attenuation levels have more variation due to the complex acoustic fields in the demo room, the general trends support with the results in the anechoic chamber.

Appendix D

List of equipment

D.1 Plant response measurement and real-time active control with a headtracker in Chapter 4

- Laptop PC running Matlab/Simulink 2010a and DSpace control desk 3.6.
- DSpace DS1103 system and break-out board.
- Laptop PC running Cycling '74 Max 7.
- 2 Panasonic WM-063T electret condenser microphones in a dummy head.
- 2 Panasonic WM-063T electret condenser microphones for a subject.
- 2 electret microphone pre-amplifiers (custom built).
- 1/4 Microphone calibrator.
- 2 Behringer iNuke1000 Audio power amplifiers (3 channels).
- 2×KEMO VBF8MK4 2-channel low-pass filter boxes.
- 2 loudspeakers, constructed using AUDAX AT100M0 drivers (custom built enclosure) for secondary loudspeakers mounted on a seat.
- 1 KEF B200-G loudspeaker mounted in 0.01 m^3 closed-back enclosure.
- Microsoft Kinect 1.0 for Windows.
- Wooden panel grid (custom built).

D.2 Acoustic response measurement for the remote microphone technique in Chapter 5

- Desktop PC running Matlab/Simulink 2014a and DSpace control desk 4.2.
- DSpace Autobox, DS2002 multi-channel A/D board and DS2103 multi-channel D/A board.
- Neumann KU100 dummy head.
- Behringer Xenyx 802 analog mixer.
- 24 Panasonic WM-063T electret condenser microphones.
- 24 electret microphone pre-amplifiers (custom built).
- 1/4 Microphone calibrator.
- 2 Behringer iNuke1000 Audio power amplifiers (3 channels).
- 2×KEMO VBF8 2-channel low-pass filter boxes.
- 2 loudspeakers, constructed using AUDAX AT100M0 drivers (custom built enclosure) for secondary loudspeakers mounted on a seat.
- 5 KEF B200-G loudspeaker mounted in 0.01 m^3 closed-back enclosure.
- 1 KEF B300-B loudspeaker mounted in 0.026 m^3 closed-back enclosures.
- Structure to mount the microphones (custom built).
- Wooden panel grid (custom built).

D.3 Real-time active sound control of the integrated active headrest system in Chapter 6 and Chapter 7

- Desktop PC running Matlab/Simulink 2014a and DSpace control desk 4.2.
- DSpace Autobox, DS2002 multi-channel A/D board and DS2103 multi-channel D/A board.
- Laptop PC running Cycling ‘74 Max 7.
- Neumann KU100 dummy head.
- Behringer Xenyx 802 analog mixer.
- 6 Panasonic WM-063T electret condenser microphones.

- 6 electret microphone pre-amplifiers (custom built).
- 1/4 Microphone calibrator.
- 2 Behringer iNuke1000 Audio power amplifiers (3 channels).
- 1×KEMO VBF8 2-channel low-pass filter boxes.
- 2×KEMO VBF22 1-channel low-pass filters.
- 2 loudspeakers, constructed using AUDAX AT100M0 drivers (custom built enclosure) for secondary loudspeakers mounted on a seat for tonal noise control.
- 2 loudspeakers, constructed using VISATON R10S drivers (custom built enclosure) for secondary loudspeakers mounted on a seat for broadband control.
- 2 KEF B200-G loudspeaker mounted in 0.01 m^3 closed-back enclosure.
- Microsoft Kinect 1.0 for Windows.
- Structure to mount the microphones (custom built).
- Wooden panel grid (custom built).

D.4 Acoustic response measurement inside a vehicle in Chapter 8

- Labtop PC running Matlab/Simulink 2014a and DSpace control desk 4.2.
- DSpace Autobox, DS2002 multi-channel A/D board and DS2103 multi-channel D/A board.
- Neumann KU100 dummy head.
- Behringer Xenyx 802 analog mixer.
- 16 Panasonic WM-063T electret condenser microphones.
- 16 electret microphone pre-amplifiers (custom built).
- 1/4 Microphone calibrator.
- 1 Behringer iNuke1000 Audio power amplifier (2 channels).
- 26×KEMO 1600 series filter modules.
- 2 loudspeakers, constructed using VISATON R10S drivers (custom built enclosure) for secondary loudspeakers mounted on a seat.
- Mercury DC to AC 1000 W pure sine wave inverter.
- Steel panel grid (custom built).

D.5 Equipment Specifications

D.5.1 PanasonicWM-063T Electret Condenser Microphones

- Dimensions: 6.0×5.0 mm
- Frequency range: 20 Hz 20 kHz
- Sensitivity: -64 dB ± 3 dB re. 1V/Pa.
- Omnidirectional

D.5.2 AUDAX AT100M0 loudspeaker data sheet

JAN. 94

AUDAX

LA PASSION DU HAUT-PARLEUR

AT100M0

BASS MIDRANGE

100859W

4" - SHIELDED PAPER CONE DRIVER - 100 mm

CLASSIC SERIES

Shielded magnet for audio/video
Extended bass response (Fs : 64 Hz)
Paper cone
Foam suspension
Long excursion
High temperature voice coil
Stamped steel chassis

Anti-magnétique pour audio/vidéo
Réponse étendue dans le grave (Fs : 64 Hz)
Cône papier
Suspension mousse
Grande excursion
Bobine haute température
Châssis acier embouti

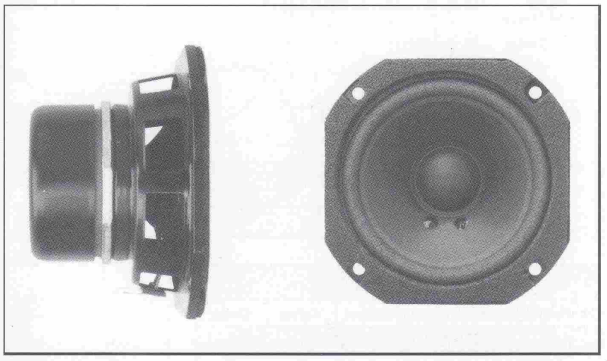

The low free air resonance and compact paper cone of this 4" bass midrange driver make it ideally suited for mini-enclosures. The high temperature 1" voice coil ensures good power handling. The magnet structure is fully shielded (compensation magnet + shield) for audio/video application. The "Suggested applications" charts indicate various driver loads. The response curves shown on the diagram indicate the predicted low end response of the driver in the suggested box volume (Vb) with suggested port (Dp-Lp).

Ce haut-parleur très compact, 100 mm, combine une bande passante étendue à de réelles possibilités de longues excursions. La résonance basse pour sa taille le destine plus particulièrement à de petites enceintes, satellites triphonique, ... La bobine haute température sur support aluminium autorise une puissance admissible importante. Il est doté d'une contre-ferrite et d'un capot anti-magnétique (application audio/vidéo). Le tableau "Suggested applications" indique différents types de charge. Les courbes publiées correspondent à la réponse dans le grave pour un volume (Vb) et une dimension d'évent donnée (Vp-Lp).

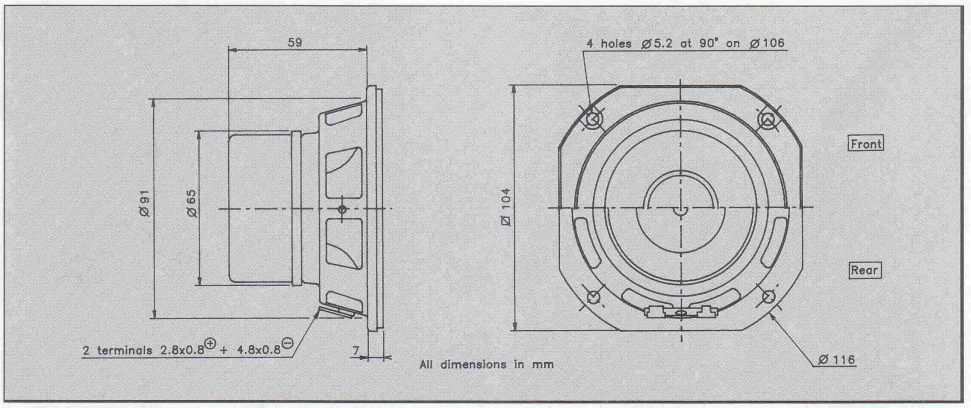

AT100M0 W08PML2511

100881R

D.5.3 VISATON R10S loudspeaker data sheet

GERMANY
VISATON®

R 10 S

Art. No. 2036 – 4 Ω
Art. No. 2037 – 8 Ω


Art. No. 4642 *)


Art. No. 4670 *)


Art. No. 4640 *)


Art. No. 4744 *)

10 cm (4") Breitbandlautsprecher mit hohem Wirkungsgrad und ausgeglichenem Frequenzgang mit Hochtonanstieg. Dadurch sehr gute Sprachverständlichkeit. Besonders geeignet als Einbaulautsprecher für elektronische Geräte und Beschallungsanlagen. Entspricht dem Modell R 10 S TE, jedoch mit Anschlussfahnen 5,2 x 0,5 mm (+) und 2,8 x 0,5 mm (–).

Anwendungsmöglichkeiten: Kontroll-Lautsprecher für elektronische Geräte, Deckenlautsprecher in Schienenfahrzeugen und Bussen, Modellbau

Zubehör: Schutzgitter (Art. No. 4640, 4642, 4670, 4744)

***10 cm (4") fullrange speaker** with high efficiency and balanced frequency response. Especially suitable as control speaker for electronic devices. Equivalent to model R 10 S TE, but with connectors 5.2 x 0.5 mm (+) und 2.8 x 0.5 mm (–).*

***Typical applications:** Control speakers for electronic devices, Ceiling-mounted speakers in railway carriages and busses, Model construction*

***Accessories:** Protective grilles (Art. No. 4640, 4642, 4670, 4744)*

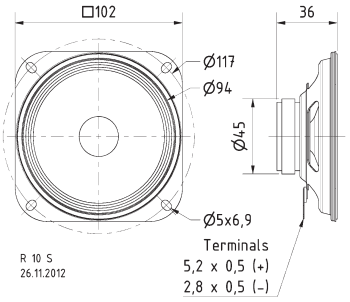

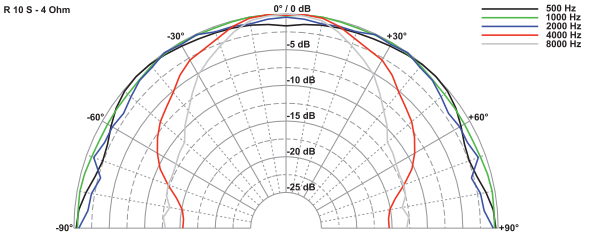

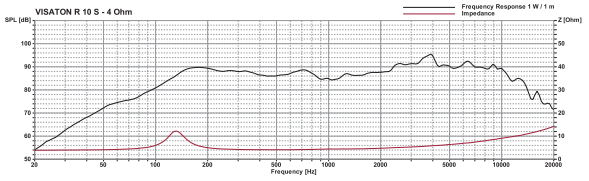

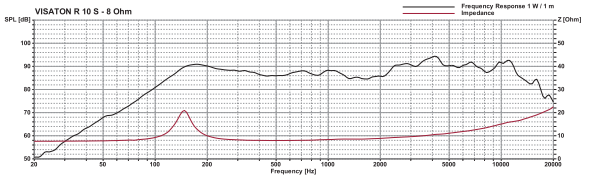

Technische Daten / *Technical Data*	
Nennbelastbarkeit *Rated power*	20 W
Musikbelastbarkeit *Maximum power*	30 W
Impedanz *Impedance*	4 Ω / 8 Ω
Übertragungsbereich (–10 dB) *Frequency response (–10 dB)*	100–13000 Hz
Mittlerer Schalldruckpegel *Mean sound pressure level*	90 dB (1 W/1 m)
Grenzauslenkung x_{mech} *Excursion limit* x_{mech}	± 1,5 mm
Resonanzfrequenz *Resonant frequency*	160 Hz
Obere Polplattenhöhe *Height of front pole-plate*	3 mm
Schwingspulendurchmesser *Voice coil diameter*	15 mm Ø
Wickelhöhe *Height of winding*	4 mm
Schallwandöffnung *Cut-out diameter*	93 mm Ø
Gewicht netto *Net weight*	0,16 kg

***) Details und Zeichnungen siehe Seite 267–271 /**
Details and drawings see page 267–271

Weitere Daten Seiten / *for further data see pages 274–275*

D.5.4 KEF B200-G loudspeaker data sheet

KEF **DATA SHEET**

B200·G

Specification Number SP1075

Low/mid range unit with visco-elastic damped Bextrene diaphragm and high temperature coil assembly, suitable for use where low distortion and high power handling are required.

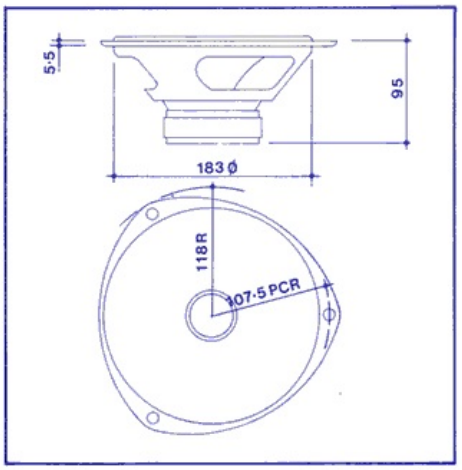

Net weight: 1.35 kg

Nominal impedance: 5 ohms

Nominal frequency range: 25-3,500 Hz

Typical enclosure volumes: Totally enclosed box 20-25 litres

Power handling:
Continuous sine wave 28 V RMS (see note 1)
Programme 150 W (see note 2)

Magnet:
Flux density 1.1 T (11,000 gauss)
Total flux 7.15 x 10^{-4}Wb (71,500 Maxwells)

Voice coil:
Diameter 32.6 mm
Inductance
Max continuous service temperature (30 min) 250°C
Max intermittent temperature (5 sec) 340°C
Nominal DC Resistance, R_{DC} 4.7 ohms (tolerance ± 5%)
Minimum impedance (in nominal frequence range) 5.3 ohms at 160 Hz

Diaphragm:
Effective area, S_D 246 cm²
Effective moving mass, M_D 24.3 g
Max linear excursion, X_D 6 mm peak-peak
Max damage limited excursion 20 mm peak-peak

Free air resonance frequency, f_s:
Nominal 27 Hz

Total mechanical resistance of suspension, R_{MS}:
1.38 mech ohms

Suspension compliance, C_{MS}: 1.4 x 10^{-3} m/N

Force factor, Bl: 6.82 N/A

Damping:
Mechanical Q_M: 3.03
Electrical Q_E: 0.42
Total Q_T: 0.37 (see note 3)

Notes

1 Continuous Power Rating (Pc).

$$Pc = \frac{V^2}{R}$$

V is the RMS voltage which can be applied to the unit continuously without thermal overload of the voice coil. At low frequencies the continuous power rating of the speaker may be reduced because of limitations imposed on diaphragm excursion by the acoustic loading.

2 The programme rating of a unit is equal to the maximum programme rating of any system with which the unit may be safely used in conjunction with the recommended dividing network and enclosure.
The programme rating of any system is the undistorted power output of an amplifier with which the system may be satisfactorily operated on normal programme over an extended period of time.

3 $$Q_M = \frac{2\pi f_S M_D}{R_{MS}} \qquad Q_E = \frac{2\pi f_S M_D}{(Bl)^2/R_{DC}} \qquad \frac{1}{Q_T} = \frac{1}{Q_M} + \frac{1}{Q_E}$$

KEF Electronics Limited Tovil Maidstone ME15 6QP England ☎ 0622 672261

KEF reserve the right to incorporate developments and amend the specification without prior notice, in line with continuous research and product improvement.

PL348 EN01

D.5.5 KEF B300-B loudspeaker data sheet

KEF **DATA SHEET**

B300·B

Specification Number SP1071

Low frequency unit with visco-elastic damped Bextrene diaphragm and high temperature coil assembly, suitable for use where low distortion and high power handling are required.

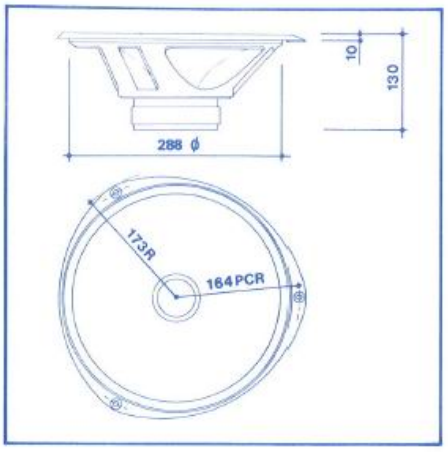

Net weight: 3.75 kg (8 lb 4 oz)

Nominal impedance: 8 ohms

Nominal frequency range: 25-2,000 Hz

Typical enclosure volumes:
Totally enclosed box 65-75 litres
Reflex 90-180 litres

Power handling:
Continuous sine wave 35 V RMS (see note 1)
Programme 200 W (see note 2)

Magnet:
Flux density 1.02 T (10,200 gauss)
Total flux 1.3 mWb (130 k Maxwells)

Voice coil:
Nominal diameter 52 mm
Nominal DC resistance, R_{DC} 6.9 ohms (tolerance ± 5%)
Minimum impedance 7.8 ohms at 120 Hz (in nominal frequency range)
Max continuous service temperature (30 min) 250°C
Max intermittent temperature (5 sec) 340°C

Diaphragm:
Effective area, S_D 520 cm²
Effective moving mass, M_D 73 gm
Max linear excursion, X_D 12 mm peak-peak
Max damage-limited excursion 25 mm peak-peak

Free air resonane frequency, f_s:
Nominal 23 Hz (tolerance ± 5 Hz)

Total mechanical resistance of suspension, R_{MS}:
2.0 mech ohms

Suspension compliance, C_{MS}: 6.6 x 10^{-4} m/N
Equivalent volume of compliance, V_{AS}: 250 litres
Force factor, Bl: 12 N/A

Damping:
Mechanical Q_M 5.3
Electrical Q_E 0.50
Total Q_T 0.46 (see note 3)

Notes

1 Continuous Power Rating (Pc).

$$Pc = \frac{V^2}{R}$$

V is the RMS voltage which can be applied to the unit continuously without thermal overload of the voice coil. At low frequencies the continuous power rating of the speaker may be reduced because of limitations imposed on diaphragm excursion by the acoustic loading.

2 The programme rating of a unit is equal to the maximum programme rating of any system with which the unit may be safely used in conjunction with the recommended dividing network and enclosure.
The programme rating of any system is the undistorted power output of an amplifier with which the system may be satisfactorily operated on normal programme over an extended period of time.

3 $$Q_M = \frac{2\pi f_s M_D}{R_{MS}} \qquad Q_E = \frac{2\pi f_s M_D}{(Bl)^2/R_{DC}} \qquad \frac{1}{Q_T} = \frac{1}{Q_M} + \frac{1}{Q_E}$$

Appendix E

Implementation of Simulink active controller and Max headtracker

In Chapter 6 the design and performance of the feedforward active control system combined with both the remote microphone technique and the head-tracker have been presented to reduce tonal disturbances in real-time. This appendix provides additional details of the controller, implemented in MATLAB Simulink, and the head-tracker, implemented in Cycling '74 MAX.

E.1 Real-time controller of the integrated active headrest system for tonal noise control

Fig. E.1 shows the main block diagram of the feedforward controller implemented in Simulink. To obtain the estimated error signals, $\hat{\mathbf{e}}$, controlled signals at the monitoring microphones, $\mathbf{m}$, are measured from the blocks labelled $DS2003\_B1$ at the top left hand side of the block diagram. In addition, Another input to the controller, which is the block labelled $DS1005SER$ at the bottom left hand side of the block diagram, is related to head position data obtained from MAX connecting with Microsoft Kinect 1.0. The contents of MAX are shown in more detail in Fig. E.5. To drive a single loudspeaker as a primary source, a specific frequency value is used to the cosine function. To drive two secondary loudspeakers, the real values of control signals from the controller are also obtained. These three output signals are sent to each loudspeaker through the block labelled $DS2103\_B1$ on the right-hand side.

The measured signals at the monitoring microphones are connected to the block labelled *Remote_microphone_technique*, which calculates real values of the estimated error signals, $\hat{\mathbf{e}}$ which are used to adapt coefficients of the control filters in the block labelled *LMS_adaptation*. The detailed contents of the block labelled *Remote_microphone_technique* for the remote microphone technique is shown in Fig. E.2 and discussed in Section E.2. The head position data is also sented to the *Remote_microphone_technique* block to update $\hat{\mathbf{G}}_e$, $\hat{\mathbf{G}}_m$ and $\hat{\mathbf{O}}_{\text{opt}}$. The block labelled *alpha* is used to adjust the convergence coefficent of the filtered-reference LMS algorithm at the DSpace control desk. Filtered-reference signals are generated from the block labelled $Filtered - reference$ and the detailed contents of this block are provided in Fig. E.3. The filtered-reference signals and the estimated error signals are sent to the *LMS_adaptation* block, which implements the adaptive LMS algorithm. The details of this block is shown in Fig. E.4. The $Filtered - reference$ and *LMS_adaptation* blocks for the filtered-reference LMS algorithm are discussed in Section E.3.

E.2 Remote microphone technique in real-time

The remote microphone technique block is presented in Fig. E.2. This block receives the controlled signals from the monitoring microphones. In addition, the data about the head movements is received to update $\hat{\mathbf{G}}_e$, $\hat{\mathbf{G}}_m$ and $\hat{\mathbf{O}}_{\text{opt}}$. The in-phase and quadrature control signals from the controller are also received to calculate both disturbance signals at the monitoring microphones and controlled signals at the virtual error microphones. At the first five blocks on the left of the block diagram, in-phase components of the signals from the controller at the monitoring microphones are calculated and these in-phase signals are subtracted from in-phase signals at the monitoring microphones, which produces an estimate of in-phase disturbance signals at the monitoring microphones, $\text{Re}(\hat{\mathbf{d}}_m)$. To obtain an estimate of quadrature disturbance signals at the monitoring microphones, a pre-modelled FIR filter for the narrowband Hilbert transform is used. The amplitude and phase of the Hilbert transform filter, $H(\omega)$ are given by [87]

$$|H(\omega)| = 1 \tag{E.1a}$$

$$\arg\, H(\omega) = -\pi/2. \tag{E.1b}$$

The Hilbert transform is often referred to as a 90° phase shifter and quadrature signals of sinusoidal signals can thus be calculated by this transform. However, since the broadband Hilbert transform is a non-causal filter with a singularity at $t = 0$, this filter may be not practicable for broadband signals. In the next four blocks, as the in-phase and quadrature signals of $\text{Re}(\hat{\mathbf{d}}_m)$ are multiplied by real and imaginary values of the pre-calculated $\hat{\mathbf{O}}_{\text{opt}}$, $\text{Re}(\hat{\mathbf{d}}_e)$ is calculated. To calculate in-phase signals of $\hat{\mathbf{e}}$ it is necessary

to calculate in-phase signals of the control signals from the controller to the virtual error microphones and add these in-phase signals with $\mathrm{Re}(\hat{\mathbf{d}}_e)$. This calculation is performed by the remaining blocks in the right of the block diagram.

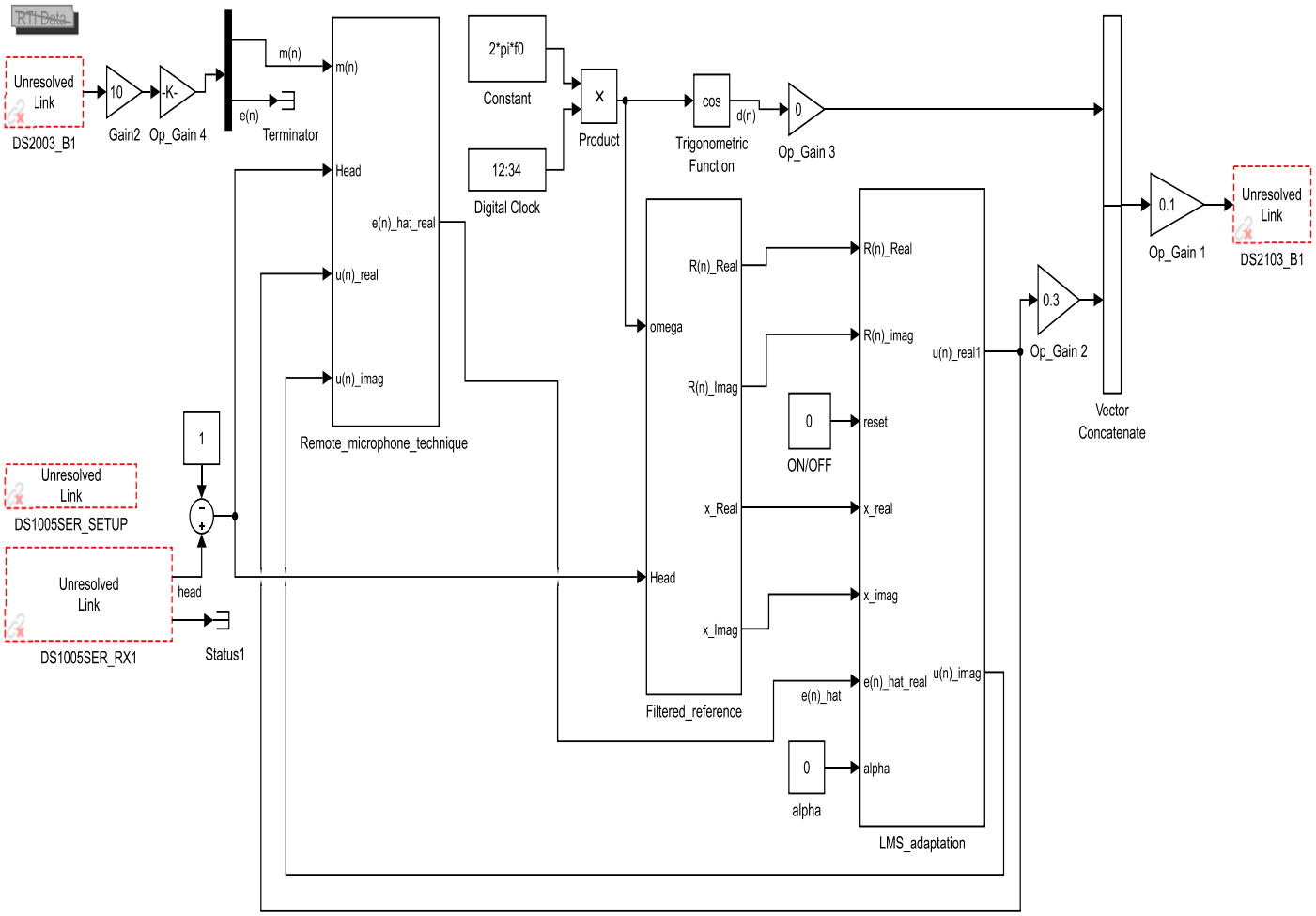

Figure E.1: The implementation of the integrated feedforward active controller with the remote microphone technique and the head-tracking for tonal noise control in Simulink.

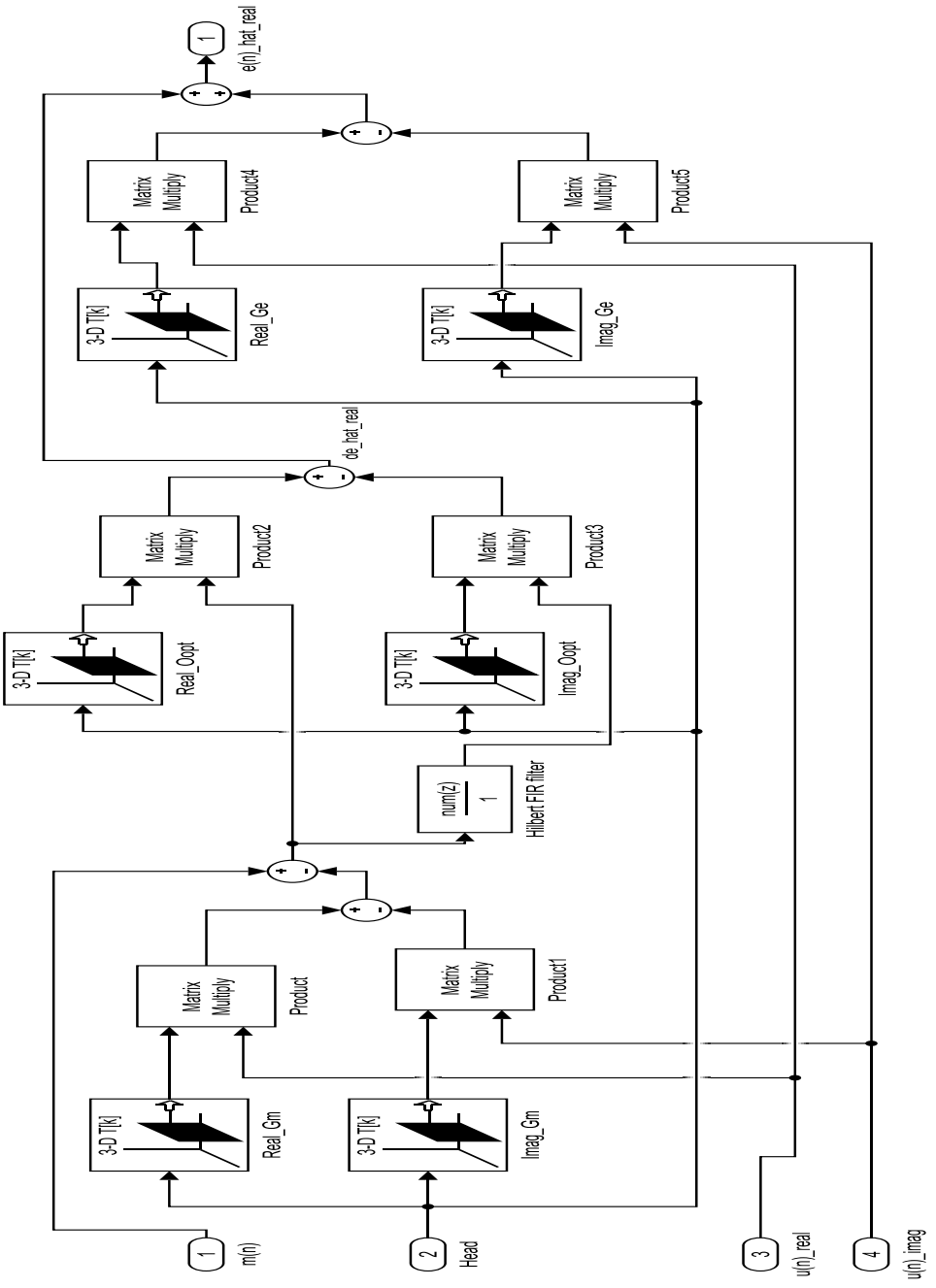

Figure E.2: The implementation of the remote microphone technique for tonal noise control in Simulink.

E.3 Filtered-reference LMS algorithm

The reference signal filtering block is presented in Fig. E.3. The first input to this block is an angular frequency, ω, which is used to drive the primary source. The in-phase and quadrature reference signals are generated by the cosine and sine function, respectively. The other input is head position data to update $\hat{\mathbf{G}}_e$ of the look-up table as the head position is changed. The in-phase and quadrature reference signals are filtered by real and imaginary values of the updated plant responses to produce matrices of in-phase and quadrature values of the filtered-reference signals. The output of the $Filtered-reference$ block is provided to the $LMS\_adaptation$ block presented in Fig. E.4. To implement the LMS adaptive algorithm in Eq. (6.7), Re($\hat{\mathbf{e}}$) from the $Remote\_microphone\_technique$ block, the in-phase and quadrature signals of the filtered-reference signals from the $Filtered-reference$ block are used as the inputs to the $LMS\_adaptation$ block. Another input is the convergence coefficient, α, which will be adjusted at the DSpace control desk. These three inputs are multiplied by each other and subtracted from a matrix of filter coefficients of the controller at the previous iteration number. In this block, the in-phase and quadrature parts of the controller are separately adjusted [124–126] and each part of the controller is multiplied by the in-phase and quadrature reference signal, respectively, and finally the two output signals from the multiplication are added together to calculate the in-phase control signals. The quadrature control signals are calculated by the Hilbert transform.

E.4 Head-tracking implementation in MAX

The head-tracker processing in Cycling '74 MAX is presented in Fig. E.5. In particular, Fig. E.5(b) shows the overall process of the head-tracking. First, before the active control, three dimensional coordinates of a nominal head position from the Kinect is measured and in this experiment, two dimensional coordinates, which only have the two directions, 'forward and backward' and 'right and left'. These coordinates of the nominal head position are saved. During active sound control, when the head is moved, the headtracker detects coordinates of moved head positions and these coordinates are subtracted from the saved coordinates of the nominal head position. These relative coordinates of the moved head position is compared to pre-selected positions on a grid such as the grid in Fig. 6.9, so that the closest pre-calculated head position is identified. The number of the selected head position is sent to the DSpace Autobox controller through the serial communication.

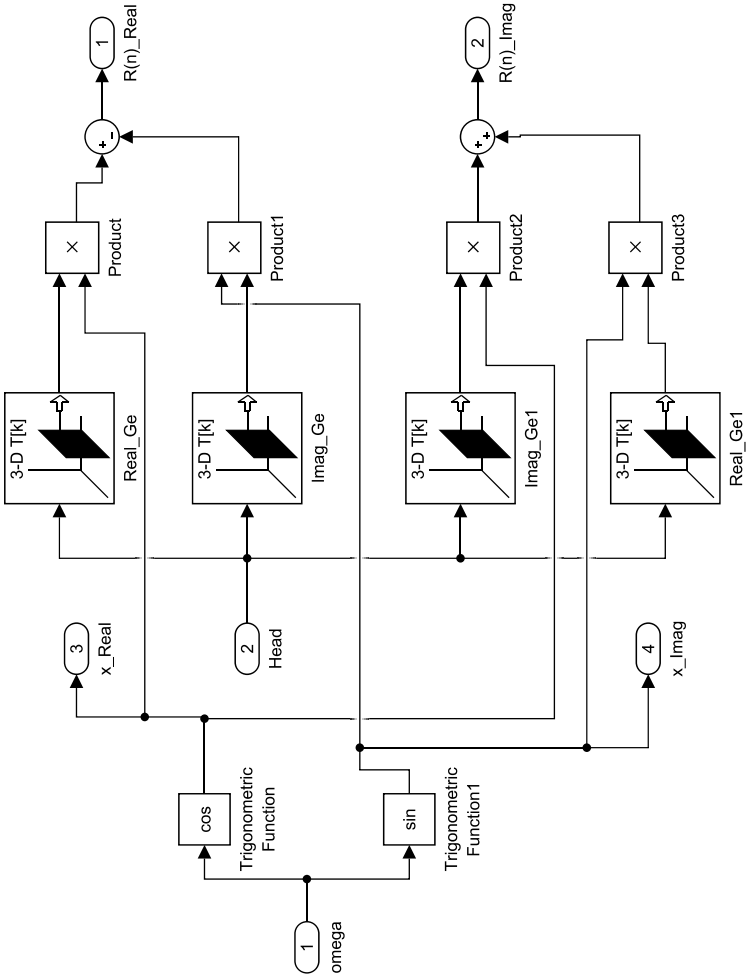

Figure E.3: The implementation of the reference signal filtering for tonal noise control in Simulink.

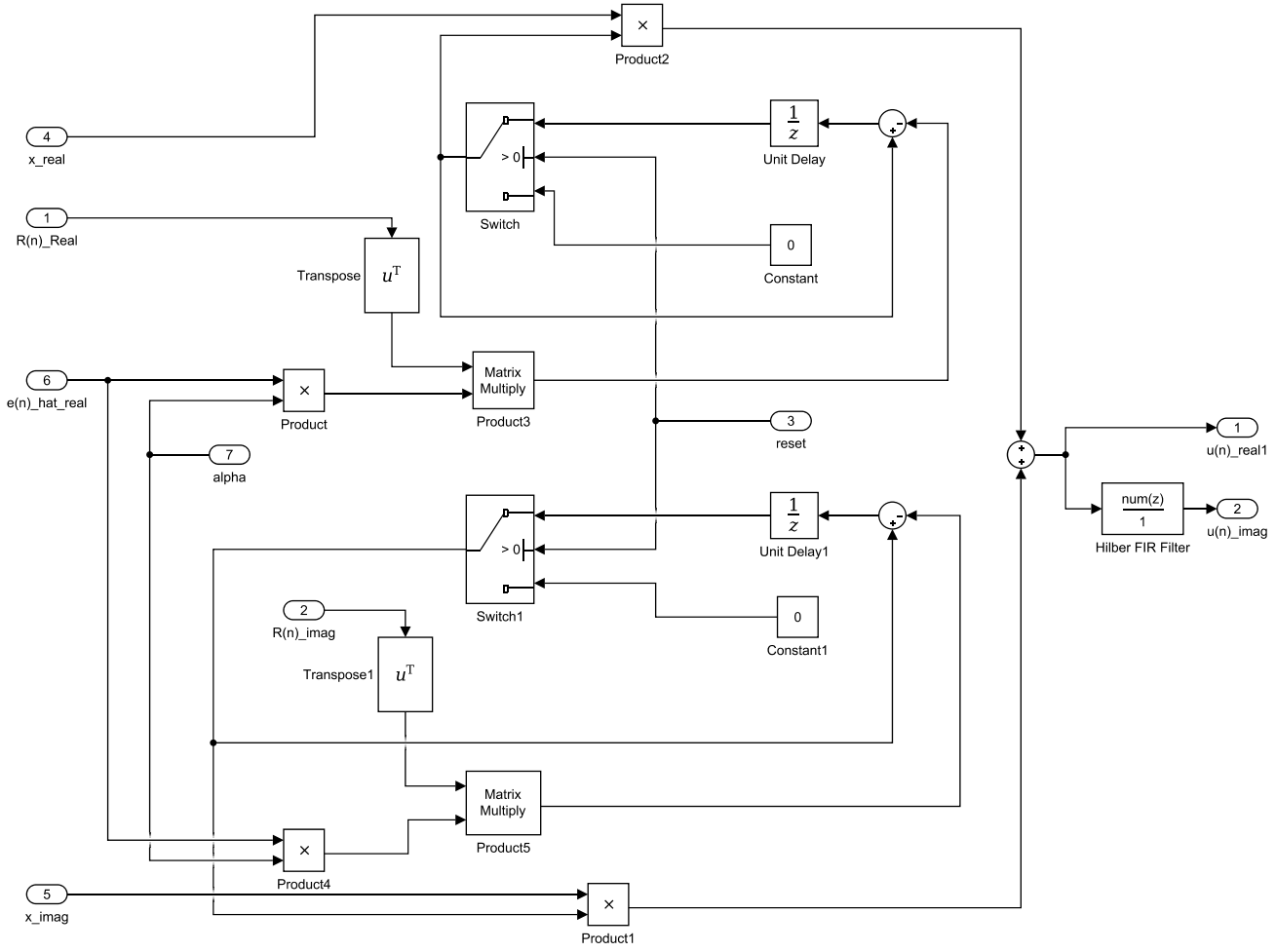

Figure E.4: The implementation of the least mean squares adaptation algorithm for tonal noise control in Simulink.

(*a*)

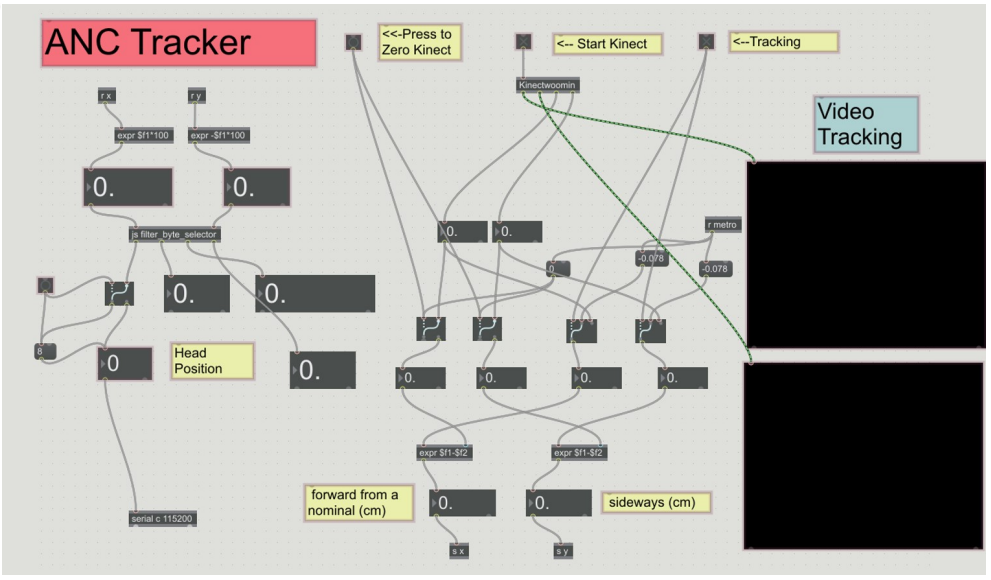

(*b*)

Step 1: A headtracker detects 3 dimensional coordinates of a nominal head position from the headtracker. These coordinates are saved at the program.

Step 2: The headtracker detects moved head positions and coordinates of the moved positions are subtracted from the saved coordinates of the nominal head position.

Step 3: The relative coordinates from the nominal position is filtered to obtain a corresponding position on the grid. The position data is sent to DSpace controller through the serial communication.

Figure E.5: Head-tracking implementation in MAX. The details of the block diagram for head-tracking in Cycling '74 MAX (a) and the overall process of the headtracking (b).

Appendix F

Head movement measurements using a head-tracking device inside a car cabin

In the above chapters, the integration of the head-tracking into an active headrest system has been investigated through laboratory based experiments. To investigate the availability of the head-tracking under practical conditions, an occupant's head movements inside a car cabin were measured using the Kinect, which was installed on the dashboard in front of the front passenger seat, as shown in Fig. F.1.

Figure F.1: The installation of a head tracking device, the Kinect on the dashboard inside a vehicle cabin for measuring head movements of an occupant.

When the car was driven under the normal driving condition over a city road, the time history of the relative displacements of the occupant's head movements from the nominal head position in Cartesian coordinates is shown in Fig. F.2. The time taken for the Kinect to acquire a new position is about 1/30 second [88]. In Fig. F.2, the

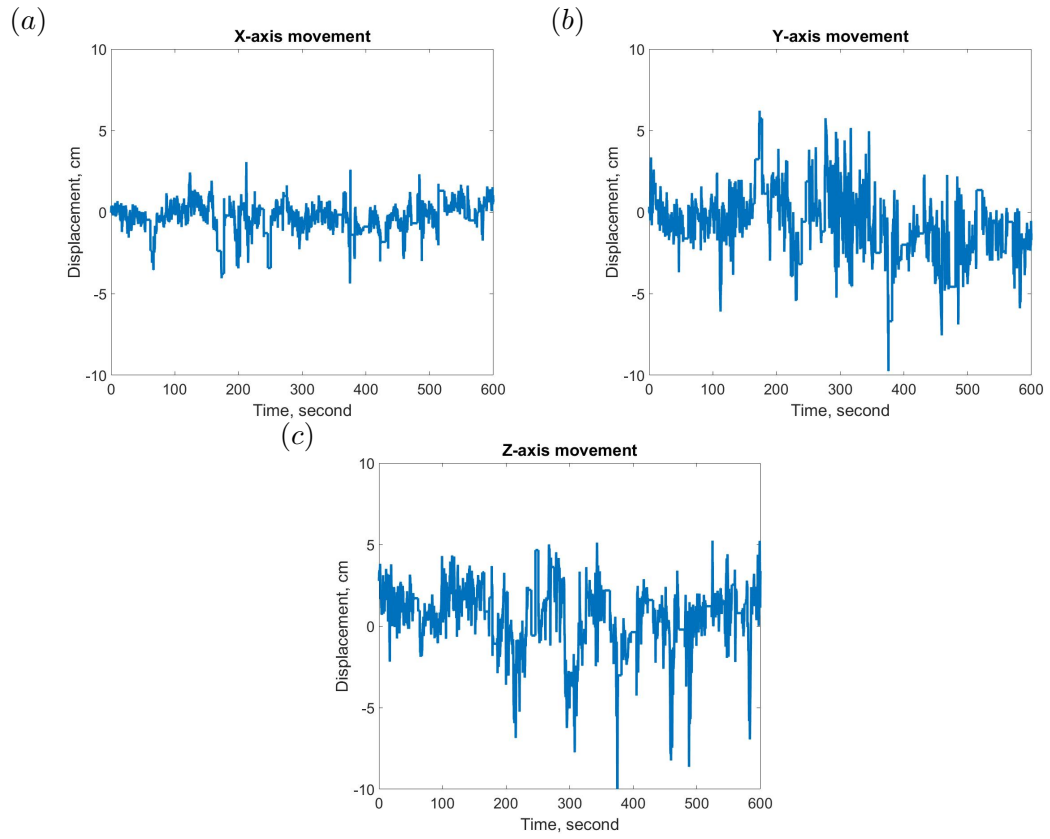

Figure F.2: Time history of the relative displacements of the occupant's head movements from the nominal position in Cartesian coordinates in Fig. F.1 under the normal driving condition over a city road: x-axis(a), y-axis(b) and z-axis(c).

displacements in the y-axis and the z-axis are generally larger than those in the x-axis. Since the displacements in the three directions are within ±10 cm, the grids in Fig. 4.3 and Fig. 5.14 have reasonable dimensions to investigate the effects of head movements.

Power spectral densities of the relative displacements of the occupant's head movements from the nominal position are shown in Fig. F.3. It can be seen that in all the three directions, most head movements are generated below about 1 Hz, which is significantly smaller than a sample frequency of adaptation filters for active noise control. Therefore, an active headrest system with a head-tracking device appears to be practicable to reduce interior noise inside a vehicle during normal operating conditions.

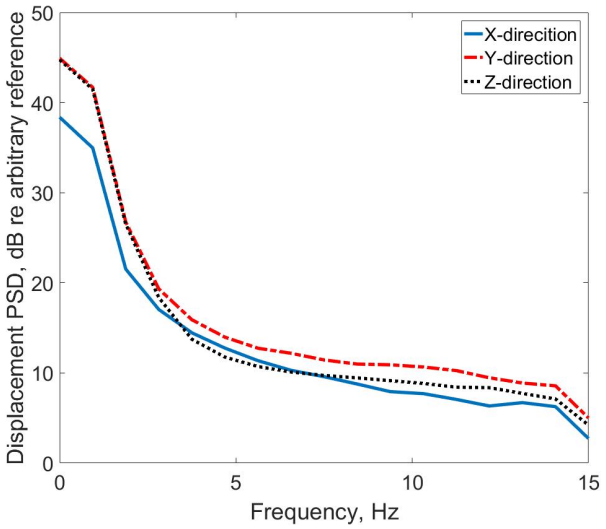

Figure F.3: PSDs of the relative displacements of the occupant's head movements from the nominal position in Cartesian coordinates under the normal driving condition over a city road.

References

1. Sano, H., Inoue, T., Takahashi, A., Terai, K. & Nakamura, Y. Active control system for low-frequency road noise combined with an audio system. *IEEE Transactions on speech and audio processing* **9,** 755–763 (2001).
2. Schirmacher, R., Kunkel, R. & Burghardt, M. *Active noise control for the 4.0 TFSI with cylinder on demand technology in Audi's S-series* tech. rep. No. 2012-01-1533 (SAE Technical Paper, 2012).
3. Kajikawa, Y., Gan, W. & Kuo, S. M. *Recent applications and challenges on active noise control* in *Image and Signal Processing and Analysis (ISPA), 2013 8th International Symposium on* (2013), 661–666.
4. Cheer, J. & Elliott, S. J. Multichannel control systems for the attenuation of interior road noise in vehicles. *Mechanical Systems and Signal Processing* **60,** 753–769 (2015).
5. Honda, N. Z. *Active Noise Cancellation (ANC)* Last accessed 13 March 2018. https://www.honda.co.nz/technology/driving/anc.
6. Bose. *Bose active sound management technology* Last accessed 13 March 2018. http://boseautomotive.com/technologies.
7. HARMAN. *HALOsonic active noise cancellation* Last accessed 13 March 2018. http://www.halosonic.co.uk.
8. Schirmacher, R. Current Status and Future Development of ANC Systems. *SOUND & VIBRATION,* 17 (2016).
9. Nelson, P. A. & Elliott, S. J. *Active control of sound* ISBN: 9780125154260 (Academic press, Cambridge, USA, 1991).
10. Elliott, S. J. in *Vehicle Noise and Vibration Refinement* (ed Wang, X.) 235–251 (Elsevier, Amsterdam, 2010).
11. Cheer, J. *Active control of the acoustic environment in an automobile cabin* PhD thesis (University of Southampton, Southampton, UK, 2012).
12. Samarasinghe, P. N., Zhang, W. & Abhayapala, T. D. Recent advances in active noise control inside automobile cabins: Toward quieter cars. *IEEE Signal Processing Magazine* **33,** 61–73 (2016).

13. Inoue, T., Takahashi, A., Sano, H., Onishi, M. & Nakamura, Y. *NV countermeasure technology for a cylinder-on-demand engine-development of active booming noise control system applying adaptive notch filter* tech. rep. No. 2004-01-0411 (SAE Technical Paper, 2004).

14. Sutton, T. J., Elliott, S. J., McDonald, A. M. & Saunders, T. J. Active control of road noise inside vehicles. *Noise Control Engineering Journal* **42,** 137–146 (1994).

15. Oh, S., Kim, H. & Park, Y. Active control of road booming noise in automotive interiors. *The Journal of the Acoustical Society of America* **111,** 180–188 (2002).

16. Olson, H. F. & May, E. G. Electronic sound absorber. *Journal of the Acoustical Society of America* **25,** 1130–1136 (1953).

17. Rafaely, B., Elliott, S. J. & Garcia-Bonito, J. Broadband performance of an active headrest. *Journal of the Acoustical Society of America* **106,** 787–793 (1999).

18. Pawelczyk, M. Adaptive noise control algorithms for active headrest system. *Control Engineering Practice* **12,** 1101–1112 (2004).

19. Booij, P. & Berkhoff, A. P. *Virtual sensors for local, three dimensional, broadband multiple-channel active noise control and the effects on the quiet zones* in *24th International Conference on Noise and Vibration Engineering, ISMA 2010* (2010), 151–166.

20. Jung, W., Elliott, S. J. & Cheer, J. Combining the remote microphone technique with head-tracking for local active sound control. *The Journal of the Acoustical Society of America* **142,** 298–307 (2017).

21. Elliott, S. J., Jung, W. & Cheer, J. Head tracking extends local active control of broadband sound to higher frequencies. *Scientific Reports* **8,** 5403 (2018).

22. Jung, W., Elliott, S. J. & Cheer, J. Estimation of the pressure at a listener's ears in an active headrest system using the remote microphone technique. *The Journal of the Acoustical Society of America* **143,** 2858–2869 (2018).

23. Jung, W., Elliott, S. J. & Cheer, J. *Local active sound control using the remote microphone technique and head-tracking for tonal and broadband noise sources* in *24th Int. Congress on Sound & Vibration Proceedings* (2017).

24. Jung, W., Elliott, S. J. & Cheer, J. *Identifying of interior noise sources in a vehicle cabin using the inverse method* in *Proceedings of the 23rd International Congress of Sound and Vibration* (2016).

25. Jung, W., Elliott, S. J. & Cheer, J. *The effect of remote microphone technique and head-tracking on local active sound control* in *Proceedings of the 23rd International Congress of Sound and Vibration* (2016).

26. Elliott, S. J., Simon, M., Cheer, J. & Jung, W. *Head tracking for local active noise control* in *12th Western Pacific Acoustics Conference* (2015).

27. Cheer, J., Elliott, S. J. & Woomin, J. *Sound field control in the automotive environment* in *Proceedings of the 3rd International ATZ Automotive Acoustics Conference* (2015).

28. Elliott, S. J., Jung, W. & Cheer, J. *The spatial properties and local active control of road noise* in *Proc. of Euro-noise* (2015), 2189–2194.

29. Wang, X. *Vehicle Noise and Vibration Refinement* ISBN: 9781845698041 (Elsevier, Amsterdam, 2010).

30. Cerrato, G. Automotive sound quality–powertrain, road and wind noise. *Sound & vibration* **43,** 16–24 (2009).

31. Harrison, M. *Vehicle Refinement: Controlling Noise and Vibration in Road Vehicles* ISBN: 9780750661294 (Elsevier, Amsterdam, 2004).

32. Thompson, D. J. & Dixon, J. in *Advanced applications in acoustics, noise and vibration* (ed Fahy, F.) 236–291 (CRC Press, Florida, USA, 2004).

33. Lalor, N. & Priebsch, H. H. *The prediction of low-and mid-frequency internal road vehicle noise: a literature survey* in *Proceedings of the Institution of Mechanical Engineers, Part D: Journal of Automobile Engineering* **221** (2007), 245–269.

34. Lalor, N. & Bharj, T. *The application of SEA to the reduction of passenger car interior noise* in *proceedings of the 27th ISATA Conference* (1994).

35. Joseph, P. *Lecture notes in Vehicle powertrain, noise and vibration* June 2015.

36. Sandberg, U. *Tyre/road noise: myths and realities* (Swedish National Road and Transport Research Institute, 2001).

37. Reff, B. in *Vehicle Noise and Vibration Refinement* (ed Wang, X.) 318–350 (Elsevier, Amsterdam, 2010).

38. Hansen, C., Snyder, S., Qiu, X., Brooks, L. & Moreau, D. *Active control of noise and vibration* (CRC press, Florida, USA, 2012).

39. Elliott, S. J. & Nelson, P. A. Active noise control. *IEEE signal processing magazine* **10,** 12–35 (1993).

40. Sakamoto, K. & Inoue, T. Development of feedback-based active road noise control technology for noise in multiple narrow-frequency bands and integration with booming noise active noise control system. *SAE International Journal of Passenger Cars-Mechanical Systems* **8,** 1–7 (2015).

41. Stanef, D. A., Hansen, C. H. & Morgans, R. C. Active control analysis of mining vehicle cabin noise using finite element modelling. *Journal of Sound and Vibration* **277,** 277–297 (2004).

42. Schroeder, M. R. Frequency-Correlation Functions of Frequency Responses in Rooms. *The Journal of the Acoustical Society of America* **34,** 1819–1823 (1962).

43. Elliott, S. J., Joseph, P., Bullmore, A. J. & Nelson, P. A. Active cancellation at a point in a pure tone diffuse sound field. *Journal of sound and vibration* **120,** 183–189 (1988).

44. Joseph, P., Elliott, S. J. & Nelson, P. A. Near field zones of quiet. *Journal of sound and vibration* **172,** 605–627 (1994).

45. Garcia-Bonito, J. & Elliott, S. J. Local active control of diffracted diffuse sound fields. *The Journal of the Acoustical Society of America* **98,** 1017–1024 (1995).

46. Elliott, S. J. & Cheer, J. Modeling local active sound control with remote sensors in spatially random pressure fields. *The journal of the Acoustical Society of America* **137,** 1936–1946 (2015).

47. Gonzalez, A., Ferrer, M., De Diego, M., Pinero, G. & Garcia-Bonito, J. J. Sound quality of low-frequency and car engine noises after active noise control. *Journal of Sound and Vibration* **265,** 663–679 (2003).

48. Rafaely, B. Spherical loudspeaker array for local active control of sound. *The Journal of the Acoustical Society of America* **125,** 3006–3017 (2009).

49. Tanaka, N. & Tanaka, M. Active noise control using a steerable parametric array loudspeaker. *The Journal of the Acoustical Society of America* **127,** 3526–3537 (2010).

50. Tanaka, K., Shi, C. & Kajikawa, Y. *Multi-channel active noise control using parametric array loudspeakers* in *Signal and Information Processing Association Annual Summit and Conference (APSIPA), 2014 Asia-Pacific* (2014), 1–6.

51. Tanaka, K., Shi, C. & Kajikawa, Y. Binaural active noise control using parametric array loudspeakers. *Applied Acoustics* **116,** 170–176 (2017).

52. Howard, C. Q., Hansen, C. H. & Zander, A. C. A review of current ultrasound exposure limits. *The Journal of Occupational Health and Safety of Australia and New Zealand* **21,** 253–257 (2005).

53. Leighton, T. Comment on 'Are some people suffering as a result of increasing mass exposure of the public to ultrasound in air'. *Proc. R. Soc. A* **473,** 20160828 (2017).

54. Diaz, J., Egana, J. & Vinolas, J. A local active noise control system based on a virtual-microphone technique for railway sleeping vehicle applications. *Mechanical systems and signal processing* **20,** 2259–2276 (2006).

55. Elliott, S. J. *Signal processing for active control* ISBN: 9780080517131 (Academic press, Cambridge, USA, 2000).

56. Elliott, S. J. & Sutton, T. J. Performance of feedforward and feedback systems for active control. *IEEE Transactions on Speech and Audio Processing* **4,** 214–223 (1996).

57. Kuo, S. M. & Morgan, D. R. Active noise control: a tutorial review. *Proceedings of the IEEE* **87,** 943–973 (1999).

58. David, A. & Elliott, S. Numerical studies of actively generated quiet zones. *Applied Acoustics* **41,** 63–79 (1994).

59. Elliott, S. J. *et al. The active control of engine noise inside cars* in *INTER-NOISE and NOISE-CON Congress and Conference Proceedings* **1988** (1988), 987–990.

60. Cheer, J. & Elliott, S. J. The design and performance of feedback controllers for the attenuation of road noise in vehicles. *International Journal of Acoustics and Vibration* **19,** 155–164 (2014).

61. Pawelczyk, M. Multiple input–multiple output adaptive feedback control strategies for the active headrest system: design and real-time implementation. *International Journal of Adaptive Control and Signal Processing* **17,** 785–800 (2003).

62. Cheer, J. & Elliott, S. *Mutlichannel feedback control of interior road noise* in *Proceedings of Meetings on Acoustics ICA2013* **19** (2013), 030118.

63. Duan, J. *et al.* Combined feedforward–feedback active control of road noise inside a vehicle cabin. *Journal of Vibration and Acoustics* **136,** 041020 (2014).

64. Akhtar, M. T. & Mitsuhashi, W. Improving performance of hybrid active noise control systems for uncorrelated narrowband disturbances. *IEEE transactions on audio, speech, and language processing* **19,** 2058–2066 (2011).

65. Wu, L., Qiu, X., Burnett, I. S. & Guo, Y. Decoupling feedforward and feedback structures in hybrid active noise control systems for uncorrelated narrowband disturbances. *Journal of Sound and Vibration* **350,** 1–10 (2015).

66. Cheer, J. & Elliott, S. J. Active noise control of a diesel generator in a luxury yacht. *Applied Acoustics* **105,** 209–214 (2016).

67. De Oliveira, L. P. *et al.* Active sound quality control of engine induced cavity noise. *Mechanical systems and signal processing* **23,** 476–488 (2009).

68. Sahib, M. A. & Streif, S. *Design of an active noise controller for reduction of tire/road interaction noise in environmentally friendly vehicles* in *Signal Processing: Algorithms, Architectures, Arrangements, and Applications (SPA), 2017* (2017), 59–62.

69. Duan, J. *Active control of vehicle powertrain and road noise* PhD thesis (University of Cincinnati, Cincinnati, USA, 2011).

70. Guo, J., Pan, J. & Bao, C. Actively created quiet zones by multiple control sources in free space. *The Journal of the Acoustical Society of America* **101,** 1492–1501 (1997).

71. Booij, P. S. & Berkhoff, A. P. *Application of virtual sensors in three-dimensional broadband active noise control and the effects on the quiet zones* in *18th International Confgress on Sound and Vibration Control, ICSV 2011* (2011).

72. Garcia-Bonito, J., Elliott, S. J. & Boucher, C. C. Generation of zones of quiet using a virtual microphone arrangement. *The journal of the Acoustical Society of America* **101,** 3498–3516 (1997).

73. Fahy, F. & Walker, J. *Advanced Applications in Acoustics, Noise and Vibration* ISBN: 9780203645130 (CRC Press, Florida, USA, 2004).

74. Johnson, M. E., Elliott, S. J., Baek, K. H. & Garcia-Bonito, J. An equivalent source technique for calculating the sound field inside an enclosure containing scattering objects. *The Journal of the Acoustical Society of America* **104,** 1221–1231 (1998).

75. Kuo, S. M., Mitra, S. & Gan, W.-S. Active noise control system for headphone applications. *IEEE Transactions on Control Systems Technology* **14,** 331–335 (2006).

76. Gan, W. S., Mitra, S. & Kuo, S. M. Adaptive feedback active noise control headset: implementation, evaluation and its extensions. *IEEE Transactions on Consumer Electronics* **51,** 975–982 (2005).

77. Elliott, S. J. & David, A. *A virtual microphone arrangement for local active sound control* in *Proceedings of the 1st International Conference on Motion and Vibration Control* (1992), 1027–1031.

78. Siswanto, A., Chang, C.-Y. & Kuo, S. M. *Active noise control for headrests* in *Signal and Information Processing Association Annual Summit and Conference (APSIPA), 2015 Asia-Pacific* (2015), 688–692.

79. Moreau, D., Cazzolato, B., Zander, A. & Petersen, C. A review of virtual sensing algorithms for active noise control. *Algorithms* **1,** 69–99 (2008).

80. Elliott, S., Stothers, I. & Nelson, P. A multiple error LMS algorithm and its application to the active control of sound and vibration. *IEEE Transactions on Acoustics, Speech, and Signal Processing* **35,** 1423–1434 (1987).

81. Widrow, B. & Stearns, S. D. *Adaptive signal processing* (Pearson Education, London, 1985).

82. Haykin, S. S. *Adaptive Filter Theory* ISBN: 9780133227604 (Prentice Hall, New Jersey, USA, 1996).

83. Morgan, D. An analysis of multiple correlation cancellation loops with a filter in the auxiliary path. *IEEE Transactions on Acoustics, Speech, and Signal Processing* **28,** 454–467 (1980).

84. Banerjee, S. & Roy, A. *Linear Algebra and Matrix Analysis for Statistics* ISBN: 9781420095388 (CRC Press, Florida, USA, 2014).

85. Wall, M. E., Rechtsteiner, A. & Rocha, L. M. in *A practical approach to microarray data analysis* (eds Berrar, D., Dubitzky, W. & Granzow, M.) 91–109 (Springer, Boston, 2003).

86. Wang, A. K. & Ren, W. Convergence analysis of the multi-variable filtered-X LMS algorithm with application to active noise control. *IEEE Transactions on Signal Processing* **47,** 1166–1169 (1999).

87. Shin, K. & Hammond, J. *Fundamentals of signal processing for sound and vibration engineers* ISBN: 9780470725641 (John Wiley & Sons, New Jersey, USA, 2008).

88. Microsoft. *Kinect for Windows Sensor Components and Specifications* Last accessed 13 March 2018. https://msdn.microsoft.com/en-us/library/jj131033.aspx.

89. Roure, A. & Albarrazin, A. *The remote microphone technique for active noise control* in *INTER-NOISE and NOISE-CON Congress and Conference Proceedings* **1999** (1999), 1233–1244.

90. Cazzolato, B. S. *Sensing systems for active control of sound transmission into cavities* PhD thesis (The University of Adelaide, Adelaide, Australia, 2001).

91. Petersen, C. D., Fraanje, R., Cazzolato, B. S., Zander, A. C. & Hansen, C. H. A Kalman filter approach to virtual sensing for active noise control. *Mechanical Systems and Signal Processing* **22,** 490–508 (2008).

92. Moreau, D. J., Cazzolato, B. S. & Zander, A. C. Active noise control at a moving virtual microphone using the SOTDF moving virtual sensing method. *Acoustics 2009* (2009).

93. Behera, S. K., Das, D. P. & Subudhi, B. *Active headrest with moving error microphone for real-time adaptive noise control* in *Control Conference (ICC), 2017 Indian* (2017), 356–363.

94. Kestell, C. D., Cazzolato, B. S. & Hansen, C. H. Active noise control in a free field with virtual sensors. *The Journal of the Acoustical Society of America* **109,** 232–243 (2001).

95. Munn, J. M. *Virtual sensors for active noise control* PhD thesis (The University of Adelaide, Adelaide, Australia, 2003).

96. Halim, D., Cheng, L. & Su, Z. Virtual sensors for active noise control in acoustic-structural coupled enclosures using structural sensing: robust virtual sensor design. *The Journal of the Acoustical Society of America* **129,** 1390–1399 (2011).

97. Das, D. P., Moreau, D. J. & Cazzolato, B. *Performance evaluation of an active headrest using the remote microphone technique* in *Proceedings of Acoustics 2011* (2011), 69–76.

98. Ryu, S. & Lee, Y.-S. Characteristics of relocated quiet zones using virtual microphone algorithm in an active headrest system. *Journal of Sensors* **2016** (2016).

99. Lei, C., Xu, J., Wang, J., Zheng, C. & Li, X. Active headrest with robust performance against head movement. *Journal of Low Frequency Noise, Vibration and Active Control* **34,** 233–250 (2015).

100. Miyazaki, N. & Kajikawa, Y. Head-mounted active noise control system with virtual sensing technique. *Journal of Sound and Vibration* **339,** 65–83 (2015).

101. Adnadjevic, M., Goossens, B. & Botteldooren, D. On the array configuration and accuracy of remote in-ear level sensing for in-vehicle noise control applications. *Applied Acoustics* **129,** 229–238 (2018).

102. Elliott, S. J., Cheer, J., Choi, J.-W. & Kim, Y. Robustness and regularization of personal audio systems. *IEEE Transactions on Audio, Speech, and Language Processing* **20,** 2123–2133 (2012).

103. Petersen, C. D., Cazzolato, B. S., Zander, A. C. & Hansen, C. H. *Active noise control at a moving location using virtual sensing* in *ICSV13: Proceedings of the 13th International Congress of Sound and Vibration* (2006).

104. Moreau, D., Ghan, J., Cazzolato, B. & Zander, A. Active noise control in a pure tone diffuse sound field using virtual sensing. *The Journal of the acoustical Society of america* **125,** 3742–3755 (2009).

105. Treyer, D., Gaulocher, S., Germann, S. & Curiger, E. *Towards the Implementation of the Noise-Cancelling Office Chair: Algorithms and Practical Aspects* in *23rd Int. Congress on Sound & Vibration Proceedings* (2016).

106. Garcia-Bonito, J., Elliott, S. J. & Bonilha, M. Active cancellation of pressure at a point in a pure tone diffracted diffuse sound field. *Journal of sound and vibration* **201,** 43–65 (1997).

107. Chen, H., Samarasinghe, P. & Abhayapala, T. D. *In-car noise field analysis and multi-zone noise cancellation quality estimation* in *Signal and Information Processing Association Annual Summit and Conference (APSIPA), 2015 Asia-Pacific* (2015), 773–778.

108. Zafeiropoulos, N. *et al. Active Noise Control in a Luxury Vehicle* PhD thesis (University of Salford, 2015).

109. Rafaely, B. & Elliot, S. J. A computationally efficient frequency-domain LMS algorithm with constraints on the adaptive filter. *IEEE Transactions on Signal Processing* **48,** 1649–1655 (2000).

110. Kuo, S. M., Tahernezhadi, M. & Ji, L. Frequency-domain periodic active noise control and equalization. *IEEE Transactions on Speech and Audio Processing* **5,** 348–358 (1997).

111. Rout, N. K., Das, D. P. & Panda, G. Computationally efficient algorithm for high sampling-frequency operation of active noise control. *Mechanical Systems and Signal Processing* **56,** 302–319 (2015).

112. Reddy, R. M., Panahi, I. M. & Briggs, R. Hybrid FxRLS-FxNLMS adaptive algorithm for active noise control in fMRI application. *IEEE Transactions on Control Systems Technology* **19,** 474–480 (2011).

113. Wu, L., Qiu, X., Burnett, I. S. & Guo, Y. A recursive least square algorithm for active control of mixed noise. *Journal of Sound and Vibration* **339,** 1–10 (2015).

114. Morgan, D. R. & Thi, J. C. A delayless subband adaptive filter architecture. *IEEE Transactions on Signal Processing* **43,** 1819–1830 (1995).

115. Park, S. J., Yun, J. H., Park, Y. C. & Youn, D. H. A delayless subband active noise control system for wideband noise control. *IEEE transactions on speech and audio processing* **9,** 892–899 (2001).

116. Cheer, J. & Daley, S. An investigation of delayless subband adaptive filtering for multi-input multi-output active noise control applications. *IEEE/ACM Transactions on Audio, Speech, and Language Processing* **25,** 359–373 (2017).

117. Berkhoff, A. P. & Nijsse, G. A rapidly converging filtered-error algorithm for multichannel active noise control. *International Journal of Adaptive Control and Signal Processing* **21,** 556–569 (2007).

118. Wesselink, J. & Berkhoff, A. P. Fast affine projections and the regularized modified filtered-error algorithm in multichannel active noise control. *The Journal of the Acoustical Society of America* **124,** 949–960 (2008).

119. Rafaely, B. & Elliott, S. J. H_2/H_∞ active control of sound in a headrest: design and implementation. *IEEE Transactions on control systems technology* **7,** 79–84 (1999).

120. Rafaely, B. & Jones, M. Combined feedback–feedforward active noise-reducing headset-The effect of the acoustics on broadband performance. *The Journal of the Acoustical Society of America* **112,** 981–989 (2002).

121. Ray, L. R., Solbeck, J. A., Streeter, A. D. & Collier, R. D. Hybrid feedforward-feedback active noise reduction for hearing protection and communication. *The Journal of the Acoustical Society of America* **120,** 2026–2036 (2006).

122. Montazeri, A. & Poshtan, J. GA-based optimization of a MIMO ANC system considering coupling of secondary sources in a telephone kiosk. *Applied Acoustics* **70,** 945–953 (2009).

123. Halim, D., Cheng, L. & Su, Z. Virtual sensors for active noise control in acoustic-structural coupled enclosures using structural sensing: Part II-Optimization of structural sensor placement. *The Journal of the Acoustical Society of America* **129,** 1991–2004 (2011).

124. Glover, J. Adaptive noise canceling applied to sinusoidal interferences. *IEEE Transactions on Acoustics, Speech, and Signal Processing* **25,** 484–491 (1977).

125. Xiao, Y. & Tadokoro, Y. LMS-based notch filter for the estimation of sinusoidal signals in noise. *Signal Processing* **46,** 223–231 (1995).

126. Kuo, S. M. & Ji, M. J. Development and analysis of an adaptive noise equalizer. *IEEE Transactions on Speech and Audio Processing* **3,** 217–222 (1995).